Spatially Resolved Infrared Spectroscopy of Seyfert Galaxies

Thesis by

Robert A. Knop Jr.

In Partial Fulfillment of the Requirements

for the Degree of

Doctor of Philosophy

California Institute of Technology

Pasadena, California

1997

(Submitted May 20, 1997)

Acknowledgements

Completing a PhD research project and writing up the thesis that goes with it is a monumental task which I could never have completed without the tangible and intangible support of numerous others. The wisdom, mentoring, and guidance of advisors and colleagues, as well as the support and faith of family and friends are due a note of recognition.

Primarily I would like to thank my advisor Tom Soifer, for providing me with direction both on the original plan for the building of the spectrometer and on the science to be done with it. He taught me a lot about the collection and reduction of infrared astronomical data, and made sure that there was at least a modicum of clarity in the presentation of my results. Lee Armus was also crucial in the completion of this thesis, with his deep understanding of the science associated with this project, his guidance in planning and performing the observations, and his direction in the analysis. Gerry Neugebauer, the true father of infrared astrophysics at Caltech, was always very willing to provide me with help and advice, and to read what I had done and give thoughtful and productive comments. I would also like to thank Judy Cohen, Sterl Phinney, and Tom Phillips, members of my committee, for their criticism and advice. Finally, recognition is due to Bob Stokstad, who has been something of a mentor to me since my days in college. His continuing faith in me, and his comments on my thesis from the point of view of a physicist who is not an astronomer, have been very important to me.

The spectrometer would never have been completed without the help of Keith Matthews, Sean Lin, and James Larkin. Keith is a genius of instrumentation, and

it was his help and guidance that allowed us to learn how to observe efficiently at Palomar. Sean Lin's engineering efforts provided a lot of the detailed design of the spectrometer and some of the mechanisms inside it. James Larkin, for several years a fellow graduate student and office mate, was often the one who kept the spectrometer moving towards completion when I felt lost. Without his dedication and efforts, the instrument which we designed together would never have been finished. Before, during, and after the completion of the spectrometer, it was very helpful to work together with him on the reduction and analysis of data, not to mention on the development of astronomical software for the Amiga.

For technical support, I am imdebted to many of the support staff at Caltech and Palomar, including the IR/Submm secretaries Susan McCurdy, Lydia Suarez, and Laurel Martin, as well as Palomar night assistants and the rest of the staff at the observatory. Richard Borup's assistance in the machine shop at Caltech was instrumental in the completion of the spectrometer. Finally, no graduate student would ever make it through Caltech without the aid of Donna Driscoll.

Naturally, graduate school was greatly improved by both the scientific assistance and friendship of my comrades in arms. Deepto Chakrabarty, my housemate of several years, ended up, despite all of his efforts to the contrary, providing a certain modicum of sanity, along with all of the ice cream and pizza. From the early days of directing a musical together to the later days of suffering through some thesis-angst together, Deepto's fellowship was valuable. Todd Hunter, my housemate after Deepto had left, was also a helpful friend, whose assistance on style files, digital recording of analog air compression signals, the "gravity is down to 0.8" problem, and appendix B, section 5 will always be appreciated.

In later years, my observing runs were most often accompanied by Tom Murphy. Tom was not only a creative collaborator in the nomenclature of Cowboy shots, but also a very helpful and thoughtful fellow reducer of infrared spectroscopic data (i.e., a "data monkey"). Alycia Weinberger was a good friend, with whom I spent many hours shooting the breeze about various assorted topics, as well about any number of the different problems and procedures (scientific and computational) one comes across

in this sort of business. She did a good job organizing and managing the Downs softball team over the years. Generous thanks are due to Dominic and Trudi Benford, two good friends who provided me support over the years, in addition to helping me learn the true definition of the word "steege." I would also like to acknowledge the camaraderie of Mike Dederian, Erik Stokstad, and Paul Stokstad, friends who have been with me since before graduate school. Paul, in law school at the time, was even able to find room in his busy schedule to proofread a couple chapters of this thesis.

There is a tide in the affairs of men, the full sea of which was brought on in part due to Shirley Marneus and the folks at TACIT, Allen Gross and the members of the Caltech/Occidental orchestra, Delores Bing and various musicians who performed in chamber groups with me, and Bill Salem and the singers in the choir at St. James. These individuals and groups provided me with an invaluable outlet for my other interests, and gave me a much-needed break from the monomania that can envelop a scientific graduate student. Without them, I may not have been able to make it through.

My parents Bob and Nancy, and my sister Linda, are due an immeasurable debt of gratitude for their faith in me, and for emotional support during times of great discouragement. They gave me a home I could always return to for support when things were dark, and always accepted me no matter how things were going. The support of my loving family was a key pillar in my ability to persevere through the trials of graduate school.

Abstract

This thesis presents infrared spectroscopy of the circumnuclear regions of 23 Seyfert galaxies. Observations are spectrally resolved with a resolution of $\lambda/\Delta\lambda \sim 1000$ and spatially resolved to $\sim 1''$, corresponding to $\sim 10^2$ pc for the objects in the sample. The instrument used for the observations, the Palomar Near-Infrared Spectrometer, is described, and problems peculiar to reduction of data from it are discussed. The lines observed include Paβ, Brγ, [FeII] (λ=1.2567μm), and H_2 (λ=2.1213μm). In nine objects, the coronal line [SIX] (λ=1.2524μm) is also detected. Spatially resolved line emission is clearly visible in approximately half of the objects observed. The data for five of the objects showing the best spatially resolved infrared line emission are analyzed in detail. These objects include Seyfert 1.5 galaxy NGC 4151 and Seyfert 2 galaxies Mk 1066, NGC 2110, NGC 4388, and Mk 3. The data for the remaining objects is presented in tabular form, and each object is discussed briefly. The data argue that processes associated with the Seyfert nucleus are responsible for the bulk of the observed [FeII] emission. Kinematic and spatial associations can be drawn between features in the [FeII] line profiles and other processes associated with the active nucleus, such as outflows seen in ionized optical emission and radio lobes. Most of the [FeII] appears to emerge from partially ionized regions excited by nuclear x-rays, with an additional contribution from fast shocks. Some of the H_2 emission also appears to be associated with the nuclear activity. However, in some cases the H_2 emission is observed to have a different spatial distribution from [FeII] and the H^+ emission. The H_2 emission is probably thermally excited. No significant differences are found between the infrared line emission of Seyfert and Seyfert 1.x galaxies.

Contents

List of Figures

List of Tables

Chapter 1

General Introduction

1.1 Introduction: Infrared Spectroscopy of Seyfert Galaxies

Seyfert galaxies are a class of galaxies which host Active Galactic Nuclei (AGN). They are characterized by their morphology and emission line spectrum. In appearance, a Seyfert galaxy has a very small (unresolved or nearly so), very bright core. Its optical spectrum shows emission lines resulting from a wide range of ionization, including strong moderate and high ionization lines. Seyfert galaxies are generally classified into two types, depending on their optical spectrum. Type 1 Seyfert galaxies have very broad permitted hydrogen and helium recombination lines with full widths at half maxima (FWHM) typically greater than 1–3000 km s^{-1}. Forbidden lines, such as those of [NII], [SII], and [OIII], are narrow, with widths less than 1000 km s^{-1}, and typically in the range 300–500 km s^{-1}. Seyfert 2 galaxies have the same narrow forbidden lines, but the permitted lines in these objects are also narrow. Finally, there are intermediate objects, which show both broad and narrow components to the permitted hydrogen recombination lines. These objects are classified as 1.5, 1.8, or 1.9. Seyfert 1.5 galaxies are those objects which have easily identified broad and narrow components to Hα and Hβ. Seyfert 1.8 galaxies show weak wings on both Hα and Hβ, and Seyfert 1.9 galaxies show weak wings on only Hα.

Figure 1.1 is a cartoon of a model of the structure of the circumnuclear regions of a Seyfert galaxy. Models of Seyfert galaxies presume the existence of a Broad Line Region (BLR) and a Narrow Line Region (NLR), from which the broad and narrow lines respectively emerge. Because forbidden lines, which have low critical densities, are not observed to be broad, a lower limit can be set on the density of the BLR. The mean electron density in the BLR is believed to be 10^9–10^{10} cm^{-3} (Osterbrock 1988). The temperature in the BLR is probably on the order of 10^4 K. The size of the BLR is believed to be $\sim 10^{-2}$ pc, which is below the resolution of any current telescope to the distance of even the nearest Seyfert 1 galaxies. Weak spatially resolved broad line emission has been seen in some Seyfert galaxies (e.g., Shields & Filippenko 1988; Sheilds & Filippenko 1996), but this is believed to result from electron scattering of light from the nucleus.

The narrow line region in Seyfert galaxies has been observed to be spatially extended to sizes on the order of 10^2 pc (e.g., Wilson & Tsvetanov 1994). The existence of forbidden lines arising from the NLR places its electron density at $\lesssim 10^4$ cm^{-3}. Optical temperature diagnostics indicate that the temperature in the NLR is 1–2$\times 10^4$ K.

According to unification models of Seyfert galaxies (e.g., Antounucci 1993), Seyfert 1 and Seyfert 2 galaxies are similar objects viewed from different angles. In these models, a broad line region exists in every object. However, it is surrounded by obscuring dust which hides the light from the BLR from view at most angles. Seyfert 1 galaxies are those galaxies observed at an angle such that the BLR is visible, and Seyfert 2 galaxies are those observed at an angle where the BLR is obscured.

Extensive optical spectroscopy, both of just the nucleus and of spatially resolved circumnuclear regions, and narrowband imaging data exist for Seyfert galaxies. These studies have provided much information on the ionization and dynamics of these systems. Optical spectroscopy exists from both ground-based telescopes (e.g., Corbin, Baldwin, & Wilson 1988; Whittle *et al.* 1988) and from the Hubble Space Telescope (HST) (Bower *et al.* 1995). According to the standard model for Seyfert galaxies, the bulk of the optical line emission is the result of photoionization by a compact source of high energy photons in the nucleus (e.g., Osterbrock 1988). An optically thick

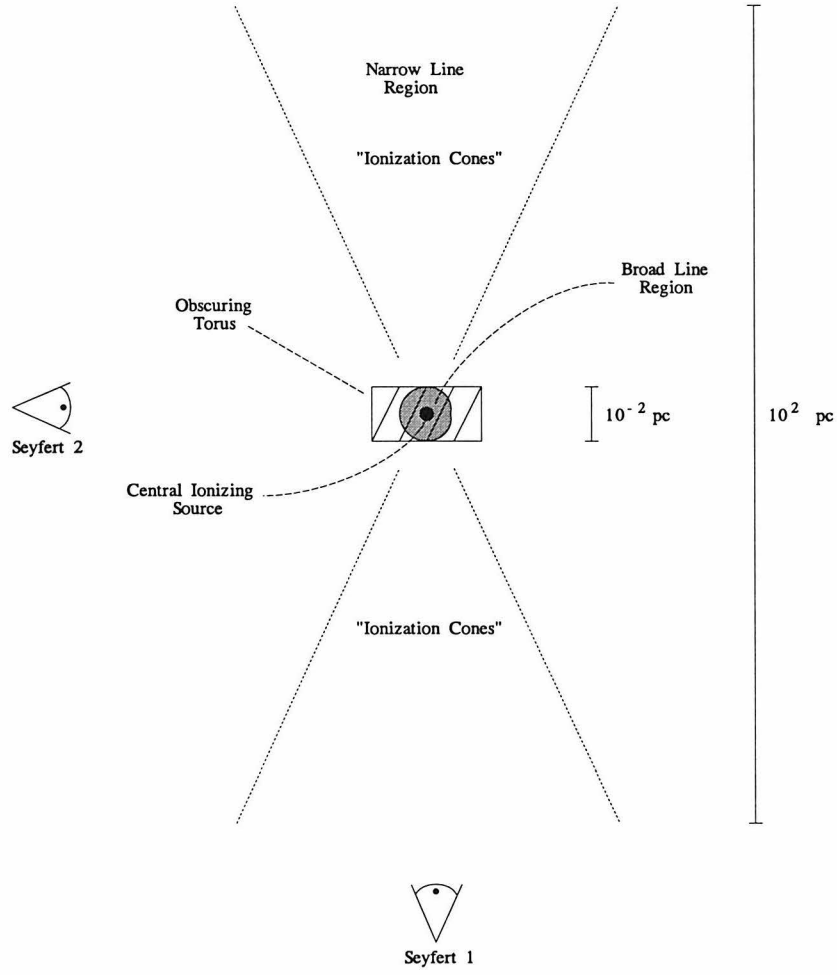

Figure 1.1: Picture of what is believed to be the structure of a Sefyert galaxy. In the unification schemes, Seyfert 1 and Seyfert 2 galaxies are similar objects viewed from different angles. Seyfert 1 galaxies are those observed at such an angle that the broad line region is unobscured.

torus is postulated to surround the central photoionizing source, causing its radiation to emerge anisotropically. The resulting "ionization cones" have been observed in optical line emission in a number of Seyfert galaxies (Wilson & Tsvetanov 1994). Interaction between radio jets or plasma emitted from the nucleus with the interstellar medium may contribute to the structure of the NLR (Pedlar *et al.* 1985; Taylor, Dyson, & Axon 1992). Shocks from the interaction compress and heat the gas. As

the gas cools behind the shock front, it can be photoionized by the nuclear continuum, producing much of the observed NLR emission.

The near-infrared offers valuable probes of the dynamics, composition, and excitation mechanisms present in the circumnuclear gas of AGN. Although most of the emission lines seen from AGN at optical wavelengths are intrinsically stronger than those in the infrared, longer wavelengths are less affected by dust extinction. At near-infrared wavelengths below 2.5μm, there are three filters which correspond to atmospheric windows: J (1.12–1.38μm), H (1.5–1.8μm), and K (2.0–2.4μm). These three windows include strong hydrogen recombination lines, low ionization collisionally excited atomic transitions, and lines from warm molecular gas. The study of the correspondence between infrared and optical spectral characteristics of Seyfert galaxies can thus produce a more complete picture of the physical environment of these systems, including the interactions of the ionized gas with the surrounding molecular material.

Among the near-infrared emission lines which have been observed to be strongest in Seyfert galaxies are the recombination lines of hydrogen, Paβ (λ=1.2818μm) and Brγ (λ=2.1655μm), collisionally excited lines of singly ionized iron, e.g., [FeII] (λ=1.2567μm), and rotational-vibrational lines of molecular hydrogen, e.g., H_2 v = 1 − 0S(1) (λ=2.1213μm). Additionally, there are very high excitation coronal lines such as [SIX] (λ=1.2524μm) and [SiVI] (λ = 1.962μm), which have been seen in a number of Seyfert galaxies (e.g., Moorwood & Oliva 1994). To date, most published infrared spectra of Seyfert galaxies have used single large beams centered on the nucleus (e.g., Goodrich *et al.* 1994); there is very little published data in the infrared of both high spatial and spectral resolution. Some studies have shown that near-infrared line emission is extended over a spatial scale easily probed with ground-based spectroscopy. For example, near-infrared [FeII] and H_2 emission has been seen extended over several arcseconds ($\lesssim$1 kpc) in the nucleus of the Seyfert 2 galaxy NGC 1068 (Blietz *et al.* 1994) and the Seyfert 1.5 galaxy NGC 7469 (Genzel *et al.* 1995). In each case, there were overall spatial and kinematic similarities between the infrared and optical line emission, but differences were also apparent on spatial and velocity scales

within the NLR. Clearly, there is important diagnostic information about the circumnuclear regions of Seyfert galaxies to be gained from spatially resolved near-infrared spectroscopy.

A question which remains to be answered through near-infrared spectroscopy is the source of the near-infrared [FeII] and H_2 line emission in Seyfert nuclei. Because infrared lines of [FeII] are known to be strong in supernova remnants, and since starbursts are known to exist around some Seyfert nuclei, it has been suggested that near-infrared [FeII] emission may trace enhanced near-nuclear star formation (e.g., in NGC 1275, Rudy *et al.* 1993). However, based on the strength and velocity width of infrared [FeII] lines, as well as their spatial correlation with hydrogen recombination lines, others have concluded that in some Seyfert galaxies the [FeII] line emission is associated directly with the narrow line region of the galaxy (e.g., Mouri *et al.* 1993). The two primary proposed mechanisms for producing strong [FeII] emission in this environment are shocks that destroy dust grains, enhance the gas phase density of iron, and ionize the gas; and high energy x-rays which can create extended partially ionized regions. H_2 (λ=2.1213μm) traces warm molecular gas, and may be excited through ultraviolet fluorescence, or may be thermally excited in gas which has been heated by x-ray heating or shocks. Near-infrared spectroscopy can probe all of these processes on arcsecond and sub-arcsecond scales.

1.2 Structure of this Thesis

This thesis is the result of a project designed to obtain spatially resolved infrared spectra of $\sim$ 20 Seyfert galaxies, including Seyfert 2 galaxies as well as Seyfert 1, 1.5, 1.8, and 1.9 galaxies (which together will be referred to as Seyfert 1.x galaxies). Its goal is to understand the origin of the infrared [FeII] and H_2 lines, and to use these as diagnostics to probe the physical processes present in the nuclei and the circumnuclear regions of Seyfert galaxies.

The Palomar Near-Infrared Spectrometer was constructed for the purpose of performing the observations in this thesis and in the thesis of James Larkin (1995).

Chapter 2 describes this instrument. Additionally, it discusses the data reduction procedure used on the data, including discussion in depth of some of the problems peculiar to the reduction of data from this instrument.

Among the first results from this instrument was the first published spatially resolved infrared spectra of the Seyfert 1.5 galaxy NGC 4151. The results for this galaxy are discussed in detail in Chapter 3. This chapter was published in *The Astronomical Journal* (Knop *et al.* 1996a, hereafter Chapter 3). Some of the introduction, as well as the observations and data reduction section from the published paper have been omitted from this thesis, as that information is presented either here or in Chapter 2.

Chapter 4 is a detailed discussion of Mk 1066, NGC 2110, NGC 4388, and Mk 3. These are four Seyfert 2 galaxies for which there is particularly good data from the Palomar Near-Infrared Spectrometer. Of all of the Seyfert 2 galaxies observed for this thesis, these four had among the strongest and spatially most resolved narrow line emission. This chapter will form the nucleus of a paper to be submitted for publication to *The Astrophysical Journal.*

Chapter 5 presents all of the data which are not discussed in either Chapter 3 or Chapter 4. Additionally, all of the data included in this thesis are summarized in tabular form. This chapter forms the bulk of a paper to be submitted to *The Astrophysical Journal Supplement Series.*

Finally, Chapter 6 attempts to bring together the observations presented in earlier chapters, to identify trends, and to draw conclusions based on what has been observed. This chapter forms most of a paper to be submitted for publication to *The Astrophysical Journal.*

Chapter 2

Data Reduction with the Palomar Near-Infrared Spectrometer

2.1 Introduction

Because the techniques of optical and near-infrared spectroscopy are currently very similar, data reduction with the Palomar Near-Infrared Spectrometer follows a procedure very close to that for data reduction of traditional optical spectra. The purpose of this chapter is to describe some of the problems and solutions relevant to reduction of data acquired with the Palomar Near-Infrared Spectrometer. Although most of the information herein is applicable in general to reduction of data with the spectrometer, it is written with data of this thesis in mind. Specifically, the objects observed have bright, core-dominated continuum morphologies. In general, lines are not extended over more than $\sim 10''$. Finally, two primary wavelength ranges at a resolution of $\lambda/\Delta\lambda \sim 1000$ are considered: one within the J-band, centered at 1.27μm, and the other within the K-band, centered at 2.14μm. The wavelength range in the J-band includes the emission lines Paβ and [FeII]; the range in the K-band includes Brγ and H_2 v=1-0S(1). For the observations, the spectrometer is set to a wavelength range appropriately shifted according to the redshift of each object. For all of the objects described in this thesis, the redshift is < 5500 km s^{-1}.

The section following this is a brief description of the instrument. Section 2.3 is a discussion of flatfielding and correction for the atmospheric transfer function. A discussion of the fringing observed in the infrared spectra, which describes when the fringing is a problem and what may be done to correct for it, is in Section 2.5. Section 2.4 briefly discusses optical distortions present in the spectrometer. The last two sections describe, in turn, the wavelength and flux calibration procedures used.

2.2 The Instrument

The Palomar Near-Infrared Spectrometer was designed and built by James Larkin and Robert Knop for the 200-inch Hale telescope at Palomar Observatory (Larkin *et al.* 1996). In order to simplify the design and construction of the instrument, and to reduce the cost of building it, the spectrometer does not contain a detector. Rather, it serves as a reimaging front end for a pre-existing infrared camera. The spectrometer mounts at the Cassegrain focus of the telescope on the infrared mounting platform. The infrared secondary of the telescope provides an F/70 beam to the spectrometer. As the camera was also designed to accept this same F/70 beam, the spectrometer outputs an F/70 beam to the camera. Figure 2.1 is a diagram of the spectrometer and the camera mounted on the back end of the telescope.

The spectrometer has two gratings, which provide resolutions R ($R=\lambda/\Delta\lambda$) of $\sim$ 1000 and $\sim$ 4000 for a slit width of $\sim 0.7''$. A single command accomplishes switching between either grating. For the observations described here, the spectrometer was used with the D80 infrared camera. This camera has a 256×256 HgCdTe array as its detector, with a read noise of $\sim 12e^-$ and a scale of $0.167''$ pixel^{-1}. Four pixels on the array correspond to one resolution element with a slit width of $0.7''$. About 30 rows at the bottom of the detector are vignetted by baffles within the camera assembly, providing about 220 pixels for spectral coverage. This yields a spectral coverage within one exposure of $\sim 0.07\mu$m at 1.27μm and $\sim 0.12\mu$m at 2.14μm. As these spectral coverages do not include the entire J and K bands, the grating may be tilted in order to tune the spectral range observed.

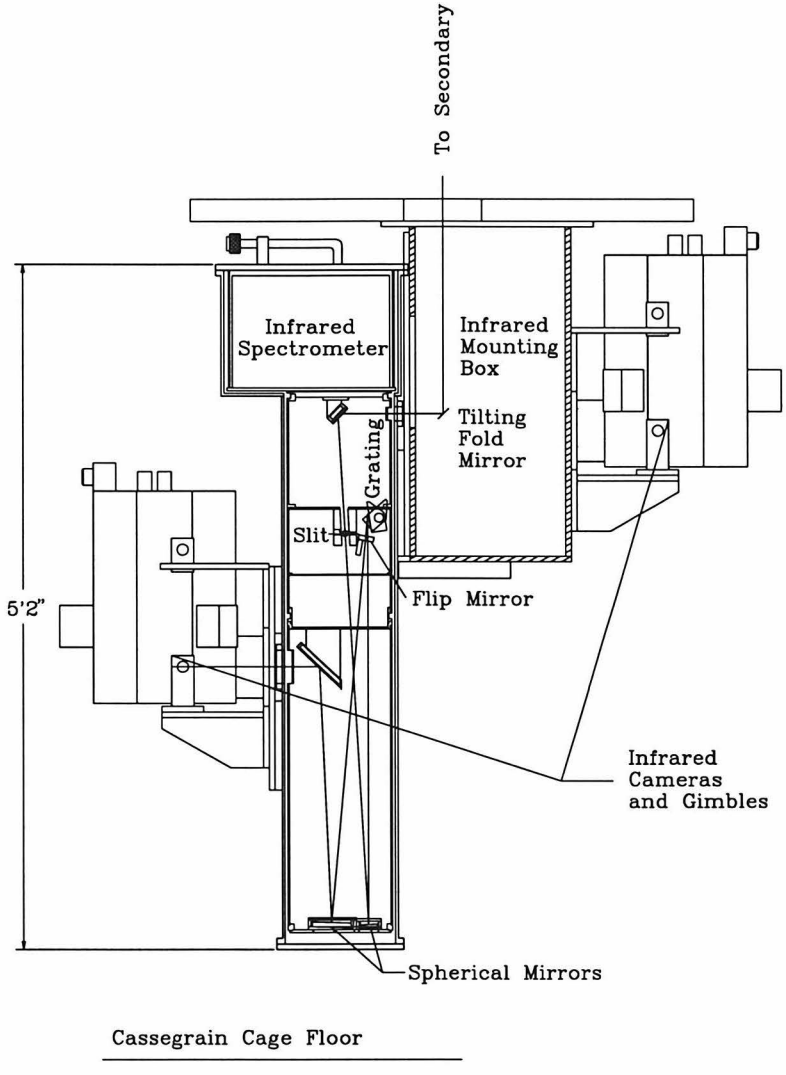

Figure 2.1: A diagram of the Palomar Near-Infrared Spectrometer mounted in the infrared mounting platform. The infrared camera, also used for imaging when mounted directly on the telescope, is shown mounted to the spectrometer, where it serves as a detector for that instrument.

With the R$\sim$ 1000 grating, the spectrometer operates in 2nd order in the K-band (2.0–2.4μm) and in 4th order in the J-band (1.1–1.4μm). The broadband imaging filters within the camera serve as order sorters. In the K-band, a 5% circular variable filter (cvf) provides a better order sorter than the broadband filter. In the K-band, thermal emission from the telescope provides a significant contribution to the background. Because all of the light, both background and of astronomical origin, entering the spectrometer is dispersed by the grating, the background going from the spectrometer into the telescope is reduced by a factor of the resolution. Although the spectrometer and the camera are each individually maintained in vacuum, the interface between the two instruments is a thin gap open to the outside air between two windows. Any motes of dust which collect on these windows will contribute to the thermal background in the K-band. This background is undispersed, and consequently dominates the total background in spectral frames. The 5% cvf matches well the spectral coverage of the spectrometer in the K-band, and rejects the contribution from thermally emitting dust on the camera window outside the spectral range being observed. Because the greatest contribution from these dust motes will be in emission towards the long end of the K-band, in the absence of a 5% filter a Ks filter may reduce the effects of this dust for spectral ranges which do not extend past 2.3μm.

The spectrometer's slit width is continually adjustable from a width of 0″ to 10″. A flat mirror may be flipped into the optical path in front of the grating, allowing imaging of the slit or imaging in a 10″ $\times$ 40″ field of view. This capability allows reproducible centering of the object within the slit.

The performance of the spectrometer has met expectations. For the observations described in this thesis, the efficiency of the entire system (telescope, spectrometer, and camera) was $\sim$ 20%; for comparison, the imaging efficiency of the camera and telescope alone is 30–40%.

2.3 Flatfielding and Atmospheric Transmission

The issues of flatfielding and correction for the spectral transfer function of the atmosphere are linked because in many cases the two are taken care of simultaneously. Naturally, the use of an electronic photon-detecting array makes necessary some form of traditional flatfielding in order to remove pixel-to-pixel gain variations as well as broad changes in sensitivity across the imaging plane. In the imaging mode, twilight sky flats work well as flatfields. For spectroscopy, however, sky flats do not work well because the sky is not spectrally flat; the unresolved OH airglow emission lines limit the sky's utility as a flatfield.

In practice, frames used to flatfield the two-dimensional spectra are either slit spectra of the dome (out of focus), or spectra of the light of a G-dwarf star spread uniformly across the slit. While the incandescent lamps that illuminate the dome do not have features, using a dome spectral flatfield will imprint the spectral shape of those lights into the spectrum. However, the atmospheric transmission will be removed by dividing a G-star spectrum into each spectrum. If dome flatfields are used, they are divided into both the object and G-star spectra, so the spectral shape of the lights illuminating the dome will divide out. If a G-star is used as a flatfield frame, the light of that G-star must be spread uniformly across the slit. The chopping F/70 infrared secondary on the 200-inch telescope allows for this. However, if the angle of the secondary and the slit are slightly misaligned, there may be a gradient in the total amount of light admitted through the slit in the spatial direction along the array, which should be removed.

The atmospheric transfer function must be removed from each spectrum. There are a number of atmospheric absorption lines in the near-infrared which distort the spectral shape of any object observed. These atmospheric transmission features may be removed by dividing each spectrum by the spectrum of an extraterrestrial object whose spectrum is nearly featureless. A G-dwarf star similar to the Sun serves this purpose (Maiolino, Rieke, & Rieke 1996). The G-star used to calibrate observations of a galaxy is observed both close in time and close to the galaxy on the sky, so

that the atmospheric conditions mimic as nearly as possible the conditions during the observation of the galaxy. Because there are atomic hydrogen absorption lines in the spectrum of a G-dwarf star, dividing by that star's spectrum can impress artificial apparent emission lines onto an object spectrum. These absorption lines may be removed through linear interpolation, or by dividing a solar spectrum (Livingston & Wallace 1991) into the spectrum of the G-star before it in turn is divided into an object spectrum. In either event, any features in the regions of the spectrum which correspond to the strongest hydrogen absorption lines in the G-star (Paβ, Brγ) may be corrupted by residual effects from those absorption lines. In addition to the imprinting of false features on the object spectrum due to features in the G-star's spectrum, when the object is divided by a G-star spectrum, its continuum will be affected by the blackbody shape of the G-star's continuum. This blackbody is removed when the G-star is divided by a solar spectrum. If the features of the G-star are instead removed through linear interpolation, then a blackbody of the appropriate temperature must also be divided out of the G-star spectrum.

In many cases, a G-star spectrum spread out along the length of the slit serves as both a flatfield and correction for atmospheric transmission. In some cases, it is necessary to use both a dome flat frame in order to flatten the array and a G-star spectrum to remove atmospheric absorption. Occasionally, due to flexure in the system on the end of the telescope, the wavelength solution will have shifted by $\lesssim$1 pixel between observations of the G-star and the object to be corrected. This can cause artificial absorption and P-Cygni-like profiles at the position of strong atmospheric absorption lines such as the O_2 line at 1.269μm. Because the field of view is spectrally curved (see section 2.4), shifting the G-star spectrum to match the wavelength solution of the object is problematical with two-dimensional spectra. In this case, a dome flat is used to flatten both the G-star and the array, and a one-dimensional wavelength shifted G-star spectrum is divided into each spatial element of the object spectrum. However, there may still be residual artifacts in the spectrum at the position of the O_2 absorption line and the Paβ and Brγ absorption lines in the G-star spectrum. For most of the observations, the redshift of the Seyfert galaxy is such that neither of these

stellar features disrupt the profiles of the interesting nebular infrared emission lines.

2.4 Optical and Spectral Distortions

There are curvatures in the field along both the spatial and spectral axes, which may be corrected in a two step process. There is a small distortion due to the camera optics which leads to the curvature on the array of the spectrum of a point source. The continuum spectra of a point source, obtained at several locations along the length of the slit, may be used to remove this distortion in the data. In addition, the fact that the grating is flat together with the extended slit causes the spectrometer to image monochromatic light at the slit into a curved line at the focal plane of the spectrometer. The night sky OH emission lines of unsubtracted frames were used to measure and remove the curvature of the wavelength solution from the data frames.

2.5 Fringing

A sapphire coating on the front of the NICMOS array inadvertently functions as an interference filter which causes fringing in spectral frames. Figure 2.2a is a dome flatfield image at 2.165 microns which shows this fringing. The amplitude of the fringing is about 2% of the signal in the J-band spectra, and about 5% of the signal in the K-band spectra. In most cases, this fringing is not a problem. It divides out along with other effective gain variations as part of the flatfielding procedure. Occasionally, however, due to flexure, the wavelength solution will shift by $\lesssim 1$ pixel between the observations of the object and the G-star. Empirically, the fringing shift is greater than this; additionally, the shift in the fringing is not a simple linear shift, but rather the fringe spacing is slightly different across the array in the two images. In this case, the fringing does not divide out with other gain variations, and is present in the final image.

In the case where the fringing is a problem, the flatfield correction is performed with dome flats as discussed in section 2.3. The fringes must be removed from the

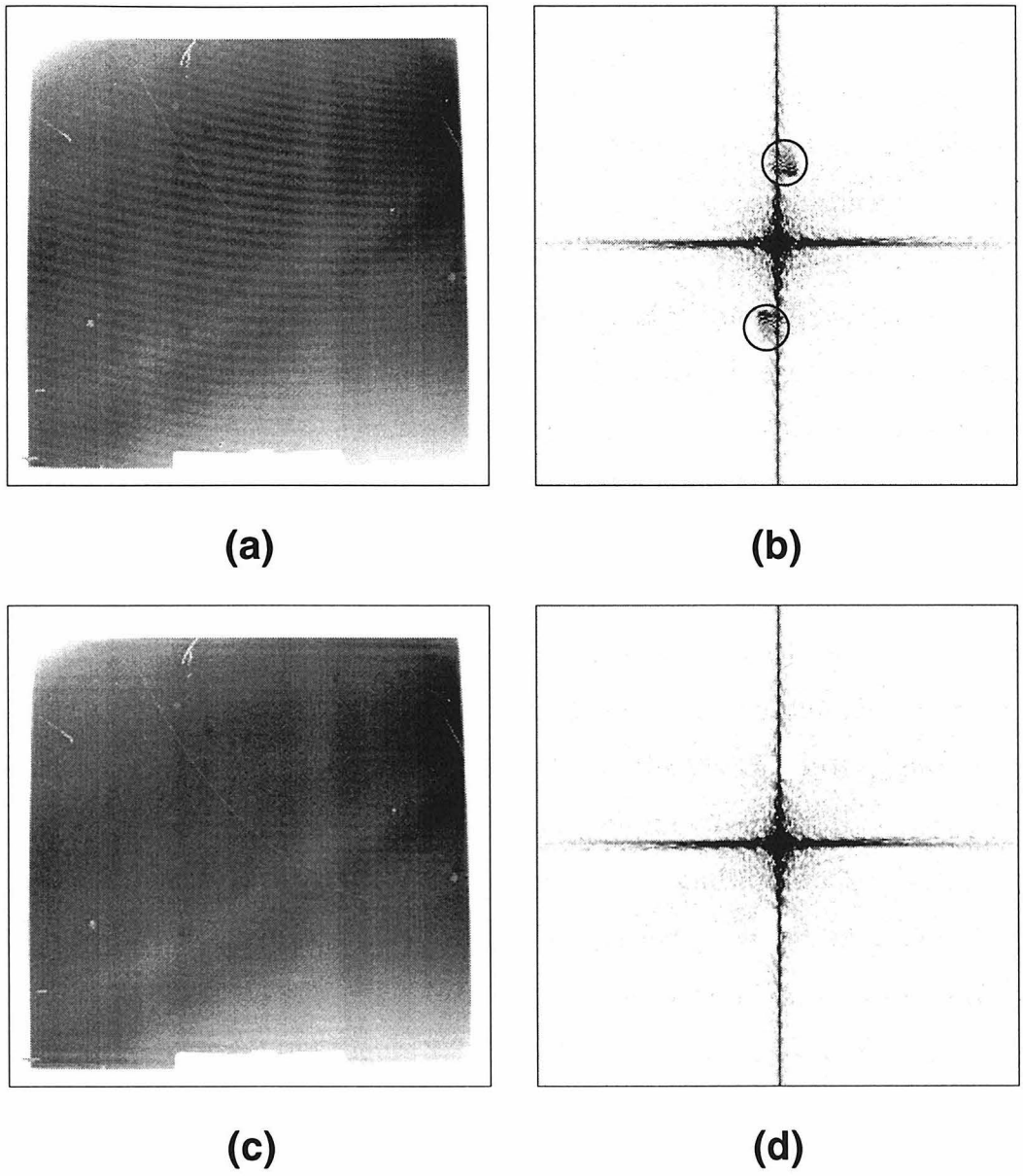

Figure 2.2: Four images demonstrating the fringing at 2.2μm. (a) The original frame, a dome flatfield. The fringes of vertical period $\sim$ 7 pixels are visible here. (b) The amplitude of the Fourier transform of the original frame. The two circled areas are the features which correspond to the fringing. (c) The frame with the fringes removed; this is the inverse Fourier transform of (d), which is the Fourier amplitude frame with the fringe feature removed.

spectral dome flat before it is divided into any other images, and from the G-star spectrum before it is collapsed into a one-dimensional spectrum for division into the object spectrum. Because the fringing is very periodic, it corresponds to a very small region in the Fourier transform of the frame. In contrast, the spectral features one is interested in are either very broad (i.e., the continuum) or located at a single position (an emission line), neither of which will have much power corresponding to the regular frequency of the fringing. It is therefore possible to remove the fringing in the Fourier domain without adversely affecting the rest of the spectrum. Figure 2.2b shows the Fourier amplitudes of the image in Figure 2.2a. The circled regions on the amplitude image are the frequencies due to the fringing. Figure 2.2d is the Fourier amplitude image with these regions interpolated across, and Figure 2.2c is the corresponding dome flat with the fringes removed.

Removing the fringing from the object spectra is more troublesome. Because the fringing is absorptive in nature, fringes will only be present where there is a strong signal. In the dome flats and G-star spectra, this is along the full length of the slit, resulting in the Fourier transform in Figure 2.2b. In the object spectra, however, there is typically only strong signal at the position on the slit corresponding to the nucleus of the galaxy. In the subtracted dithered images, there is additionally a second negative object spectrum at the location of the object during the second exposure. Only at these positions along the slit axis is there signal. This results in a somewhat different Fourier transform, shown in Figure 2.3. This figure shows the Fourier transform of a K-band object spectrum; in the spectra at the J-band, the amplitude of the fringes is usually low enough that it is very difficult to distinguish the power due to the fringes in the Fourier transform frames. Generally, it is only possible and useful to remove the fringes from the K-band object spectra. (However, when it is necessary it is possible and fruitful to remove the fringes from the J-band dome flat and G-star spectra.)

There are other features occasionally present in the raw data which are easy to remove in the Fourier transforms, even if the removal of the fringes is not necessary. Occasionally, electronic problems in the readout can imprint a vertical "pinstriping" with a period of exactly two pixels. In this pinstriping, every other column of the

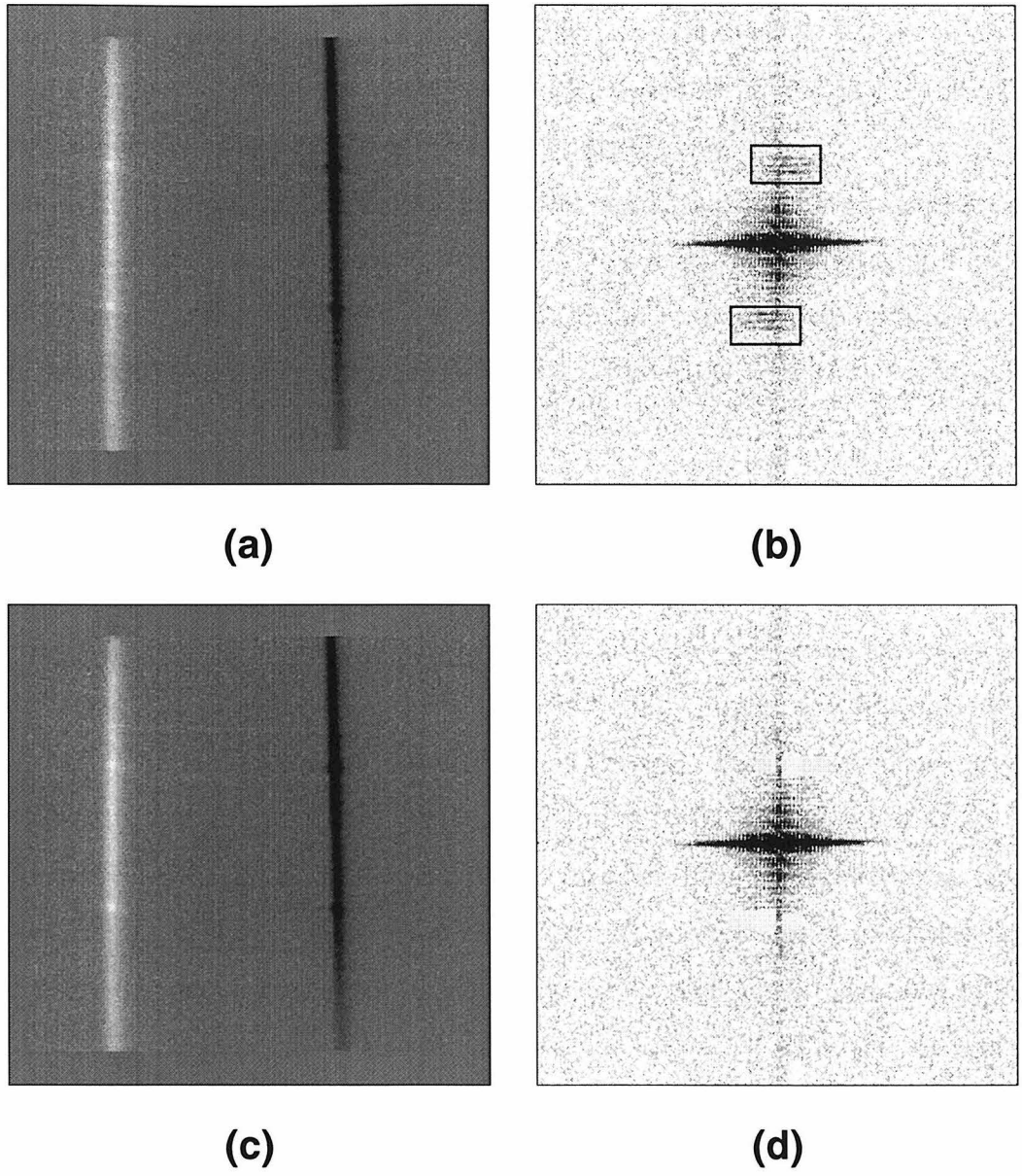

Figure 2.3: Images demonstrating the fringing in an object spectrum. (a) The original frame, a 2.162μm spectrum of NGC 4388. (b) The Fourier transform amplitudes of the original spectrum. The boxed areas in the image indicate the power corresponding to the fringing. (c) The object spectrum with the fringing removed, which is the inverse Fourier transform of (d), the Fourier amplitude frame with the fringe feature removed.

array is somewhat brighter than the ones adjacent. The other feature sometimes seen is a similar diagonal pinstriping at exactly 45°. Both of these features imprint power into the Fourier spectrum in very sharp peaks in regions of the Fourier amplitude image where there is very little power due to the images itself. Removing these peaks completely removes the pinstriping from the original image.

One artifact which is frequently impressed upon the image as a result of this procedure is ringing near the edges (within $\lesssim$ 20 pixels) of the wavelength range of the spectrum. For this reason, it is advantageous to ensure that the grating angle is set so that the spectral features of interest are not near the edge of the spectrum.

2.6 Wavelength Calibration

Two standards may be used for wavelength calibration. The spectrometer is equipped with Ne, Ar, Kr, and Xe lamps, which provide unresolved features at known wavelengths along the full length of the slit. Additionally, there are many unresolved atmospheric OH emission lines between 1 and 2.2μm. These atmospheric features allow direct measurement of the wavelength solution from the object spectrum.

The wavelengths of the atmospheric OH emission lines are tabulated in Oliva & Origlia (1992). Unfortunately, these lines are not suitable for a good wavelength solution for regions of the J-band which include Paβ and [FeII] redshifted by 1000–5000 km s^{-1}. There are no lines which Oliva & Origlia list as single isolated lines "suitable for wavelength calibration."

Tables 2.1 and 2.2 list the wavelengths of the atmospheric lines in the ranges 1.247–1.305μm and 2.090–2.212μm respectively. These wavelengths were measured from a frame which had wavelength calibration information available from lamp spectra. In all cases but one (noted in the table), the lines which Oliva & Origlia list as suitable for wavelength calibration are consistent with the wavelengths measured here. The use of these wavelengths improves the wavelength calibration by a factor of ~4–5 over using mean values from blended lines tabulated by Oliva & Origlia. These wavelengths should only be considered valid for the Palomar near-infrared spectrometer with a

0.5–0.8″ slit.

Table 2.1: Effective Atmospheric OH Emission Wavelengths: 1.247–1.305μm

λ (μm)	$\Delta\lambda^a$ (μm)	$\lambda_0{}^b$ (μm)
1.24791	0.00005	1.24793
1.24990	0.00004	1.24990
1.25688	0.00005	
1.25853	0.00005	1.25855
1.26822[c]	0.00004	
1.26928[c]	0.00004	
1.27221	0.00003	
1.27460	0.00004	
1.27608	0.00003	
1.27786	0.00003	
1.28017	0.00003	
1.29023	0.00003	
1.29178	0.00004	
1.29395	0.00005	
1.29820	0.00004	1.29822
1.30182	0.00004	1.30181
1.30496	0.00005	1.30493

(a) An estimate of the uncertainty of the wavelength of the atmospheric line. Most of these uncertainties correspond approximately to half of the width of a 0.7″ slit. Actual measurements of the pixel centroid in frames will usually be somewhat more uncertain. (b) The wavelength as tabulated by Oliva & Origlia (1992) for those lines they list as suitable for wavelength calibration. (c) These two "lines" are deblended Gaussian components from a 3-Gaussian fit to the atmospheric O_2 line at 1.269μm. The deblending is empirical, and depends strongly on the width of the slit. If possible, this line should be avoided, but occasionally it is the only measurable sky line in the lower part of the array.

The atmospheric wavelength calibration generally requires a second or third order polynomial in order to match the wavelengths of the lines across the array. (With averages of values tabulated in Oliva & Origlia (1992) for blended sky lines, a first order fit provides a good enough calibration within the uncertainty of the wavelengths of the sky lines.) The calibration allows the measurement of the velocity of strong, narrow spectral features to $\lesssim$20 km s^{-1}. Note, however, that the use of the Ne, Ar, Kr, and Xe lamps allows an equivalent or better wavelength calibration. Using the lamps for calibration has the additional advantage of known unresolved lines at

Table 2.2: Effective Atmospheric OH Emission Wavelengths: 2.090–2.212μm

λ (μm)	$\Delta\lambda^a$ (μm)	$\lambda_0{}^b$ (μm)
2.09045	0.00004	2.09039
2.10601	0.00005	
2.11036	0.00004	
2.11709	0.00004	2.11710
2.12434	0.00009	2.12440
2.13165	0.00005	
2.15026	0.00005	
2.15317	0.00006	
2.15761	0.00007	
2.17050	0.00008	2.17052
2.17966	0.00007	2.17965
2.18694[c]	0.00008	2.18676
2.19500[d]	0.00008	2.19498
2.20468	0.00010	2.20464
2.21189	0.00010	2.21197

(a) An estimate of the uncertainty of the wavelength of the atmospheric line, which generally correspond to 0.25–0.5 the width of a 0.7″ slit. Actual measurements of the pixel centroid in frames will usually be somewhat more uncertain. (b) The wavelength as tabulated by Oliva & Origlia (1992) for those lines they list as suitable for wavelength calibration. (c) This is the one line where the measured wavelength and the wavelength tabulated in Oliva & Origlia (1992) disagree by more than the uncertainty in this wavelength determination. (d) There appears to be a break in the continuum coincident with this line in many of the sky spectra. It should be used with caution.

known wavelengths; there is no need to use the secondary "effective" wavelengths in Tables 2.1 and 2.2, and the wavelengths of the lamp lines do not depend on atmopheric conditions or the setting or characteristics of the instrument. Because the time required to obtain sufficient lamp spectra is small in comparison to the time spent integrating on an object, it is always beneficial to obtain lamp spectra for both the object and the G-star. (This conclusion is the result of hindsight. The observations in this thesis were calibrated entirely with atmospheric OH lines.)

2.7 Flux Calibration

Flux calibration of infrared spectra such as those presented in this thesis is difficult partially because there are no good published spectrophotometric standards in the infrared, only broad-band flux standards. Additionally, many of the observations described here were taken under non-photometric conditions. Flux calibration of slit spectra is further hampered by the fact that narrow slits limit the amount of light which gets to the detector. If seeing conditions change, spectra of the same object will have a different number of observed counts in the detector. In the case of observations of point sources where there is a measurement of the point spread function at the time of the observations (e.g., along the spatial axis of a longslit spectrum), this effect can be calibrated out. However, it is impossible to take this effect out for extended objects. Because many of the objects presented in this thesis are extended on scales between one and a few times the atmospheric seeing, it is impossible to determine accurate fluxes of the line which can be reproduced under differing atmospheric conditions. For that reason, the "flux calibration" procedure performed does not try to correct for the spatial extent of the object. Rather, the quoted fluxes are simply observed fluxes, i.e., the flux from the object which passed through our slit given the atmospheric seeing at the time of the observation.

Observations described in this thesis were calibrated according to the following procedure. First, images of the galaxy taken through the spectrometer in its imaging mode were flux calibrated as discussed below. Images of the galaxy through the slit allow a measurement of the fraction of the flux of the galaxy which passed through a known length along the slit. In those cases where an image of the galaxy thorough the slit was not available, an image of the slit taken during the same run (e.g., of a twilight sky) was used to artifically mask the image of the galaxy, thereby producing an effective image through the slit, but also rendering the procedure more uncertain. An assumption about the shape of the continuum of the spectrum across the effective wavelength range of the filter used for the images provided an expected continuum level in the spectra along the same length of the slit. The measured level of the

continuum in electrons thereby corresponded to this expected continuum level, and the flux calibration was complete. The correspondence between electrons and flux varied depending on the photometric conditions of the night.

One of two procedures is used in order to calibrate the images of the galaxy. If the night was photometric, then the galaxy images may be calibrated using images of infrared photometric standard stars (Persson 1996). If the night was not photometric, then prior knowledge of the magnitude of the galaxy is required. In this case, the calibration was determined by integrating the number of electrons within an aperture on the galaxy image. This was then compared to a known flux of the galaxy in the same aperture measured previously (Neugebauer 1996) or as compiled in Gezari *et al.* (1993). Naturally, this procedure will introduce errors into the flux calibration if the object is one whose nuclear flux can significantly vary, such as is the case with NGC 4151. The quoted flux calibration uncertainties in Chapters 3 through 6 are estimates which reflect the total uncertainty in this proceure for each object, including the uncertaintly in the level and slope of the continuum, the photometric quality of the night, possible variation of the continuum flux of the galaxy, the uncertainty in the measurement of the flux through the slit, and the uncertainty in the flux calibration of the images. In some cases, the lack of an image of the galaxy through the slit or variable photometric conditions rendered this procedure highly uncertain, such that flux measurements should be considered good only to order of magnitude. In these cases, the flux calibration uncertainty is quoted as "100%."

2.8 Summary

The infrared spectral data presented here were reduced following a standard reduction procedure. Data were first preprocessed, including subtraction of any bias levels (of which there may be four, as each quadrant of the array in the infrared camera is read out separately). A sky frame was subtracted from each data or calibration frame, or, in the case of small objects which are dithered along the slit, subsequent object frames were subtracted from each other. Frames were flatfielded either using a dome flat or

a G-star spectrum. If necessary, fringing was removed in the Fourier domain. Object spectra were extracted, shifted, and summed together. Wavelength calibration was performed using lamp spectra, or unresolved atmospheric OH emission lines. Finally, the data were flux calibrated using a bootstrap procedure from flux calibrated images of the galaxy, and images of the galaxy through the slit.

Chapter 3

NGC 4151

3.1 Introduction

The nearby galaxy NGC 4151, being one of the brightest and best studied Seyfert galaxies, is an ideal candidate for these spatially resolved infrared spectral studies. NGC 4151 has been classified optically as a Seyfert 1.5 galaxy (Osterbrock & Koski 1976). From measurements of the 21cm HI line in the outer parts of the galactic disk, Pedlar *et al.* (1992) derive a systemic radial velocity of 997±3 km/s. Using a value of 75 km s^{-1} Mpc^{-1} for H_0 yields a distance to NGC 4151 of 13 Mpc, and a spatial scale of 64 pc/″.

Optically, the narrow line region (NLR) of NGC 4151 has been previously observed to be extended by about 4″ or 5″ along a position angle of 60°. Ulrich (1973) and Schulz (1990) spectroscopically identify a number of different velocity components or "clouds" at different distances within about 5″ of the nucleus along this position angle in [OIII] and Hα emission. The NLR is resolved in narrow band [OIII] images taken with the Hubble Space Telescope into a number of individual emission line clouds (Evans *et al.* 1993). These emission line clouds are themselves resolved on scales of less than 1″, and are distributed in northeast-southwest cones with opening angles of 75°±10°.

This chapter presents observations that address the origin of the near infrared [FeII]

emission in NGC 4151. It describes spatially resolved spectroscopy of the near nuclear regions of NGC 4151, focusing on the [FeII] λ=1.2567μm and Paβ λ=1.2818μm lines. It shows that the width of the lines, their central velocities, and the [FeII]/Paβ ratio vary with position along the slit; and that the [FeII] emission is associated with previously identified clouds in the narrow line region of NGC 4151.

3.2 Observations and Data Reduction

Observations and data reduction were performed describing the procedure in Chapter 2. On May 25, 1994, two spectra of 300 seconds each were obtained of NGC 4151 covering the spectral range between 1.24μm and 1.30μm. This spectral range includes Paβ (rest λ=1.2818μm) and [FeII] (rest λ=1.2567μm). The spectra were obtained using a 0.75″ wide slit at a spectral resolution of R$\sim$1000. The nucleus of the galaxy was moved back and forth along the slit by 20″ between observations, to allow for sky subtraction while continuously integrating on the object. The observations were made with the slit oriented at a position angle of 60°, to align it with the [OIII] emission cones observed by the Hubble Space Telescope by Evans *et al.* (1993). Observing conditions were non-photometric. From observations of a point source and the spatial extent of the pointlike Seyfert 1 nucleus in the continuum, the full width at half maximum (FWHM) of the point spread function (psf) was determined to be 1.3″. The G-star used for correction of atmospheric transmission was BS 4785 [G0V].

The largest source of systematic uncertainty in the flux calibration is the assumption that the continuum flux of the galaxy at the time of our observations was the same as it was at the time of the earlier photometric observations. The continuum of the nuclear source has been observed to fluctuate by as much as a factor of 2 at both 2.2μm (Prestwich *et al.* 1992) and 0.5μm (Antonucci and Cohen 1983). We therefore assume that our flux calibration is good to only 50%.

3.3 Results

In Figure 3.1 we present the two dimensional near-infrared spectrum of NGC 4151. The vertical axis covers the 1.24-1.30μm spectral regime, while the horizontal axis covers 7″ along the 0.75″ wide slit. Left corresponds to southwest (PA 240°), and right to northeast (PA 60°) on the sky. In Figure 3.1b, a smoothed continuum and broad emission line of Paβ have been subtracted in order to increase the contrast and visibility of the narrow emission lines (see section 3.6). Three lines are visible in Figure 3.1: Paβ (λ=1.2818μm), [FeII] (λ=1.2567μm), and a line at λ=1.2524μm which we identify as [SIX]. This feature was first seen in the Circinus galaxy by Moorwood & Oliva (1994) and Oliva *et al.* (1994). Both the Paβ and [FeII] lines are spatially extended, and show clear velocity shifts with position (visible as a tilt of the line on the figure). The [SIX] line is visible only on the nucleus, and is spatially unresolved, as distinct from the extended nature of the narrow components of Paβ and [FeII]. This is consistent with the extent of coronal lines observed in the Circinus galaxy (Oliva *et al.* 1994), and in contrast with the prediction of Korista & Ferland (1989) that coronal lines would be extended at least as much as the narrow line region of an active galaxy. The [SIX] line does not show noticeable velocity shifts; the single unresolved component on the nucleus is at a redshift of 973±46 km/s, consistent with the systemic velocity of the nucleus of NGC 4151. The line is not blueshifted with respect to the other lines on the nucleus, as is the case with other coronal lines in several Seyfert galaxies (Penston *et al.* 1984). Its FWHM, corrected for our instrumental resolution, is 170±65 km/s.

Figure 3.2 shows nine one-dimensional spectra, each extracted in 1.33″ wide bins from the spectrum in Figure 3.1. Each spatial bin is offset from adjacent ones by 0.67″, half of the width of a spatial bin. The 1.33″ size of the spatial bin along the slit was chosen to match the seeing at the time of the spectral observations. The emission lines identified in Figure 3.1 are clearly seen in Figure 3.2. The Paβ line shows both broad and narrow components. On the nucleus there is a broad line with a FWHM of 5800±800 km/s, and a total flux in a 1.33″×0.75″ beam of 800×10^{-15} erg cm^{-2} sec^{-1}.

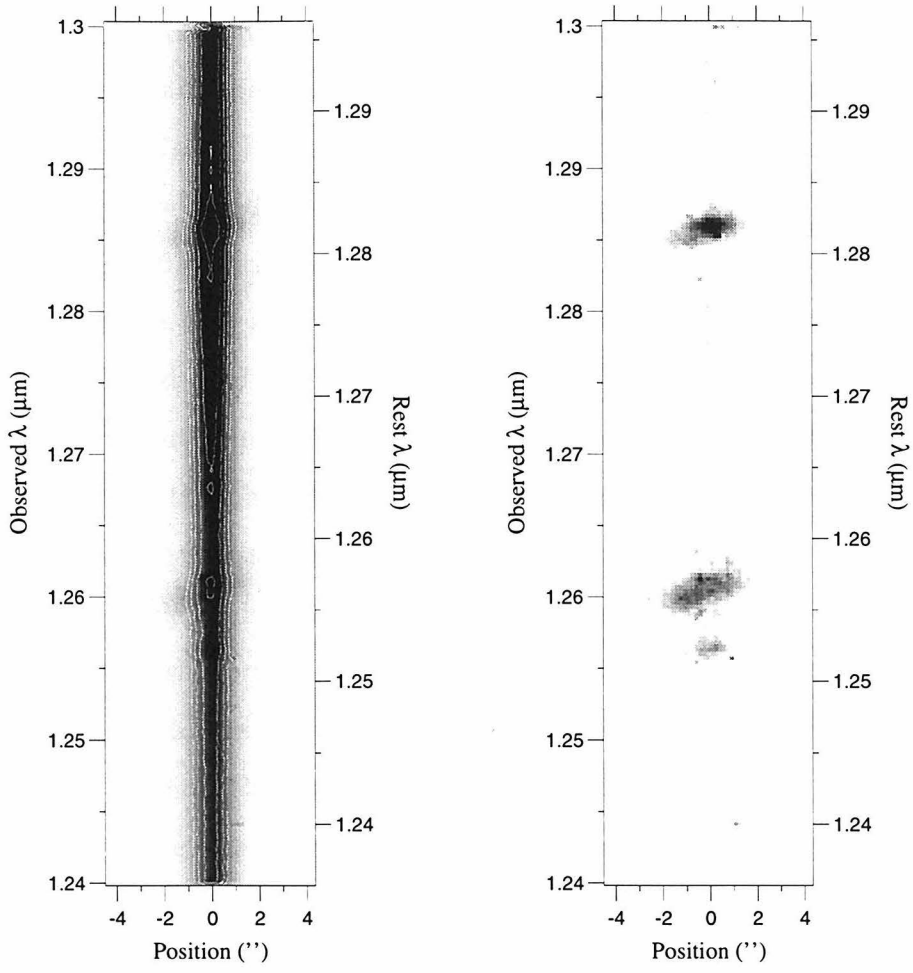

Figure 3.1: A greyscale image showing the reduced 1.24-1.30μm longslit spectrum of NGC 4151. The resolution of the spectrum is 240 km/s. On both spectra, the left axis scale is the observed wavelength, and the right axis is the rest wavelength, assuming a velocity of cz = 997 km/s (Pedlar *et al.* 1992). The left image shows the full spectrum; the image on the right has a smoothed continuum and Paβ broad line subtracted, to increase the contrast of the narrow emission lines. On the left image, the contours are logarithmically scaled; in both images, the greyscale is linearly scaled. Three lines are visible on the plot: the upper line is Paβ (rest λ=1.2818μm), and below that is [FeII] (rest λ=1.2567μm). The line blueward of [FeII] is [SIX] (rest λ=1.2524μm).

The extent of the broad Paβ line is consistent with it being spatially unresolved.

The narrow component of Paβ is slightly resolved in velocity in some of the spatial bins: the spectral resolution is 240±20 km/s, based on unresolved atmospheric OH lines measured simultaneously with NGC 4151, while the typical intrinsic line width of Paβ is 250 km/s (after subtracting the width of an unresolved line in quadrature). The [FeII] (λ=1.2567μm) line has no broad component. It also is clearly spatially resolved and appears broader than the narrow component Paβ, with a typical line width of 400 km/s after correction for our resolution.

To determine the flux and shapes of the narrow lines, we first subtracted the continuum and broad Paβ line from the data to create a spectrum of the narrow lines above a zero continuum. We then fit one or more Gaussian line profiles to each narrow line in each of the nine 0.75″×1.33″ spatial beams spaced by 0.67″ in Figure 3.2. Initially we fit a single Gaussian profile to each line (Paβ and [FeII]) in each spatial bin, allowing the amplitude, width, and center of the Gaussian to vary in a χ^2 minimization fit. The fits were each performed individually and unconstrained; for example, the Gaussian profiles fit to the [FeII] line were not required to have the same profile or velocity as those fit to the Paβ line at the same position on the slit. In many cases, this single Gaussian profile was sufficient to adequately fit the data. Where this provided a statistically unsatisfactory fit, an additional one or two Gaussian components were added. In all cases, we selected the minimum number of components to describe an individual feature. The simplest set of Gaussian profiles which adequately described the data for each line in each spatial bin is listed in Table 3.1. The fits are plotted with the data in Figure 3.3. Section 3.6 discusses in greater detail those cases where more than one Gaussian line profile was required to fit the data. Although fitting the emission lines with Gaussian components does not provide a unique solution, it does allow for a simple means of describing the [FeII] and Paβ line profiles as they change their shapes and centroids with distance from the nucleus.

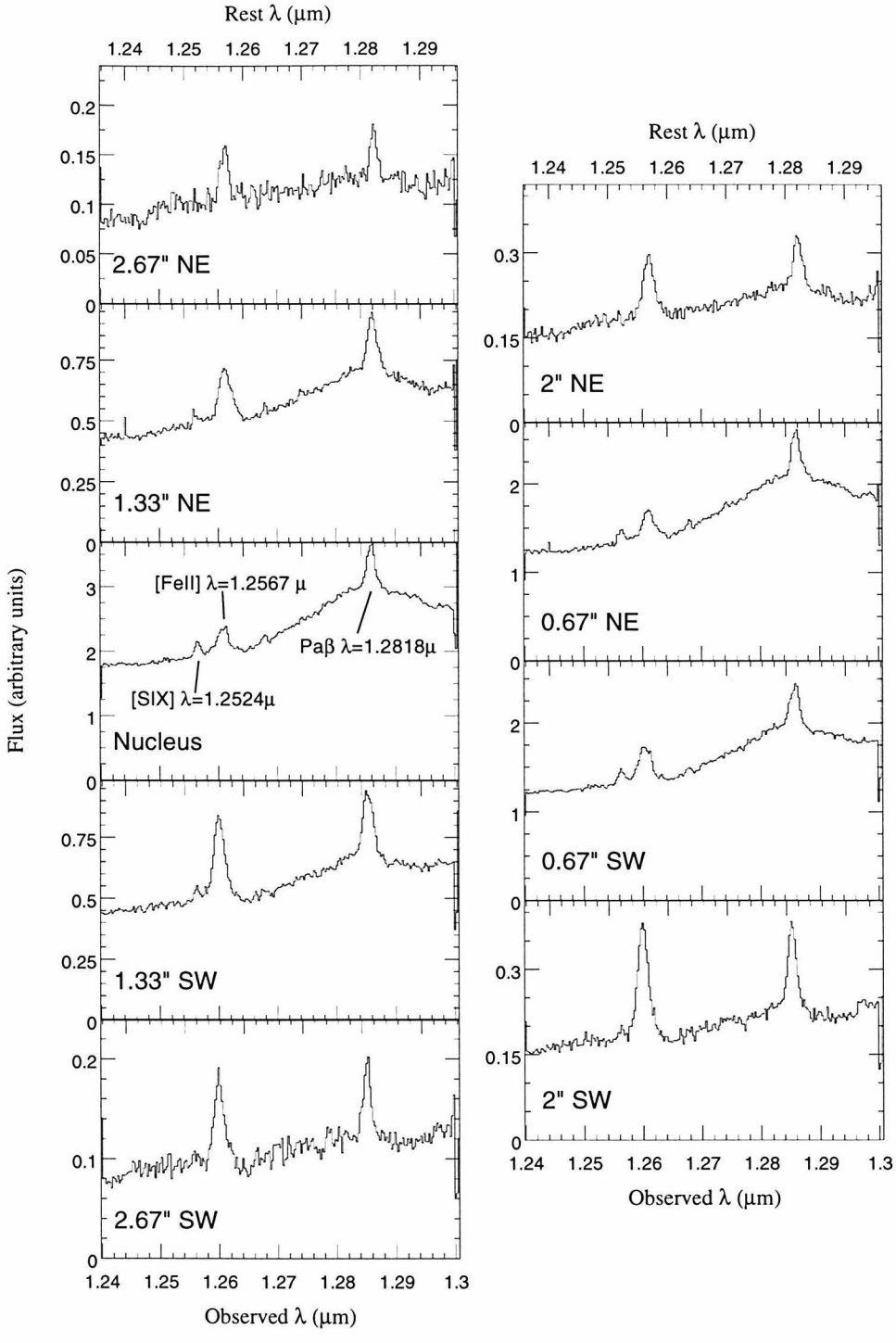

Figure 3.2: One-dimensional infrared 1.24μm-1.30μm spectra of the Seyfert 1.5 galaxy NGC 4151. These spectra show seven 1.33″×0.75″ beams along a slit oriented at a position angle of 60°. On the right are plotted spectra whose bins are offset spatially by half the size of the spatial bin.

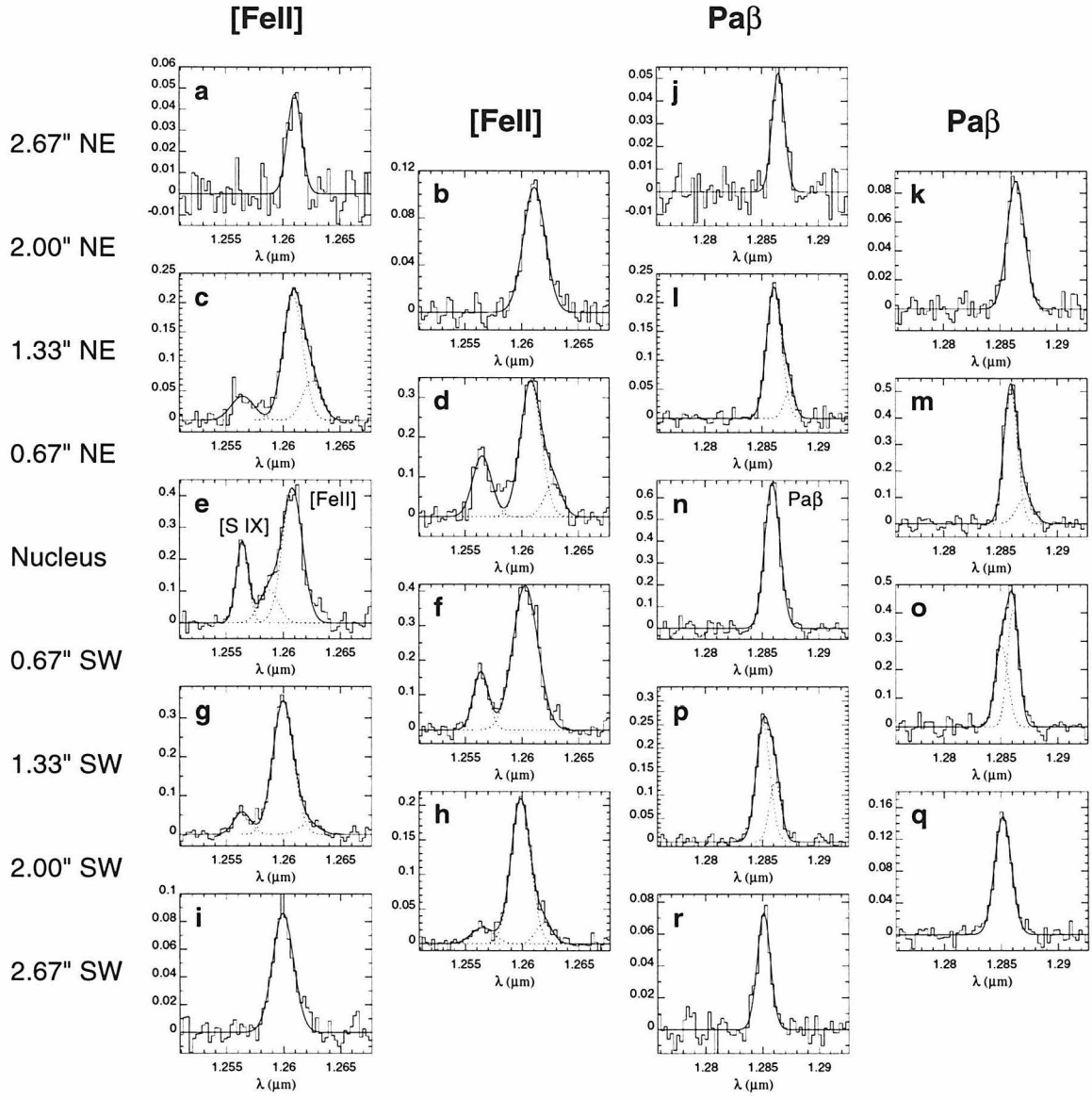

Figure 3.3: Gaussian line profiles used to describe the [FeII] and Paβ lines in each of the spatial bins of Figure 3.2. Individual Gaussian line components are dotted lines, and the solid line is the sum of the individual Gaussian line profiles, indicating our total fit to the data. The narrow emission line on the blue side of [FeII] seen in c, d, e, f, g, and h is [SIX] (rest λ=1.2524μm). These fits are discussed in greater detail in Section sec4151app.

Table 3.1: Gaussian Components fit to Line Profiles

Position	[FeII](λ=1.2567μm)			Paβ(λ=1.2818μm)		
	flux	center	FWHM	flux	center	FWHM
	10^{-15} erg s^{-1} cm^{-2}	km s^{-1}	km s^{-1}	10^{-15} erg s^{-1} cm^{-2}	km s^{-1}	km s^{-1}
2.67″ NE	2.3±0.4	1033±31	260±50	2.3±0.4	1094±38	184±55
2.00″ NE	8.3±1.1	1056±28	490±21	5.5±0.8	1077±37	352±25
1.33″ NE	2.8±1.6	1389±129	405±160	1.8±1.0	1318±63	<180
	16.3±2.8	997±51	455±42	12.1±2.0	1001±39	280±39
0.67″ NE	5.3±3.5	1450±109	365±204	5.7±6.7	1253±204	336±298
	25.1±4.8	975±43	455±59	24.8±7.4	958±45	236±46
Nucleus				800	960±170	5800±800
	29.8±6.8	981±48	434±70	36.2±5.0	960±36	285±24
	6.9±6.0	487±148	402±342			
0.67″ SW	37.2±5.1	855±28	575±20	16.9±6.8	1007±51	<180
				13.3±6.7	763±74	212±115
1.33″ SW	2.0±1.5	1318±167	455±332	5.3±3.0	1014±60	<180
	25.3±3.7	779±30	457±27	12.7±3.4	762±53	257±62
2.00″ SW	1.8±0.8	1245±71	335±148			
	14.6±2.1	752±29	425±31	8.8±1.2	786±36	329±22
2.67″ SW	6.4±0.9	773±29	466±31	3.5±0.5	771±37	228±41

Line fluxes, velocities, and widths for the Paβ and [FeII] emission lines observed in the spectrum of NGC 4151. The effective beam for each line is 1.33″x0.75″, so neighboring spatial bins overlap by 50%. The 0.75″ wide slit was oriented at a position angle of 60°. The uncertainties quoted on the fluxes include those in our flux calibration as well as those resulting from the Gaussian fits described in the text of the paper (see text for detailed discussion). The instrumental resolution of 240 km/s, as measured from unresolved OH sky lines, has been subtracted in quadrature from the FWHM of each of the Gaussians in the table. For comparison, the systemic velocity of NGC 4151, as measured from the 21cm HI line in outer parts of the galaxy, is 997±3 km/s (Pedlar *et al.* 1992).

3.4 Discussion

3.4.1 Identifying Velocity Components in Paβ

The components of the Paβ line producing the observed shapes seen in Figures 3.2 and 3.3 and in Table 3.1 are indicative of multiple, discrete emitting components rather than a continuous distribution of gas exhibiting a smooth velocity gradient. Were there a smooth distribution of gas, the line centers would vary smoothly in velocity with position away from the nuclear velocity. However, superimposed discrete components are visible, which change in relative strength causing the varying Paβ line profiles. A clear illustration of the nature of these multiple components is seen in the Paβ

line southwest of the nucleus (Figures 3.3n, 3.3o, 3.3p, and 3.3q). On the nucleus (Figure 3.3n), the Paβ line is centered at 960 km/s. At a position 2.67″ southwest of the nucleus (Figure 3.3q), the Paβ line is centered at 770 km/s. In the spatial bins 0.67″ and 1.33″ southwest of the nucleus (Figures 3.3o and 3.3p), the Paβ emission can be described as an increasing mixture of the blueshifted 770 km/s component combined with the nuclear 960 km/s component. The nuclear component is stronger in the spatial bin 0.67″ southwest of the nucleus (Figure 3.3o), with the blueshifted component visible as a blue shoulder. In the spatial bin 1.33″ southwest of the nucleus (Figure 3.3p), the blueshifted component is stronger, with the nuclear component a red shoulder.

All of the velocity centers of the narrow Paβ Gaussian components tabulated in Table 3.1 are consistent with one of four basic velocity components: a nuclear component at about 980 km/s, consistent with NGC 4151's systemic velocity of 997 km/s (Pedlar *et al.* 1992), and consistent with the 960 km/s emission we observe on the nucleus; a blueshifted component southeast of the nucleus at about 770 km/s; a redshifted component visible >2″ northeast of the nucleus at about 1070 km/s; and a second redshifted component 1.33″ northeast of the nucleus at about 1380 km/s. From these identifications, a picture emerges of four cloud systems, at different velocities and distances from the nucleus, along the 60° slit. A cartoon of this picture is shown in Figure 3.4. Note that because the data in this paper are from a single slit orientation, we only have one dimension of spatial information.

Kinematically, the Paβ velocity components show correlations with the long slit optical Ha and [OIII] spectroscopy of Schulz (1990) and Ulrich (1973). In the optical data, these authors identify a number of discrete components or "clouds" at velocities similar to the components seen here in the near-infrared lines. Table 3.2 lists the comparison between the kinematic components seen in the optical line and the kinematics seen in the near infrared lines in this paper. The optical data are used to model a nuclear outflow by Ulrich (1973) and Schulz (1990). There is remarkable agreement between the velocities of the optical and infrared emission lines suggesting that the latter are involved in the outflow from the Seyfert nucleus.

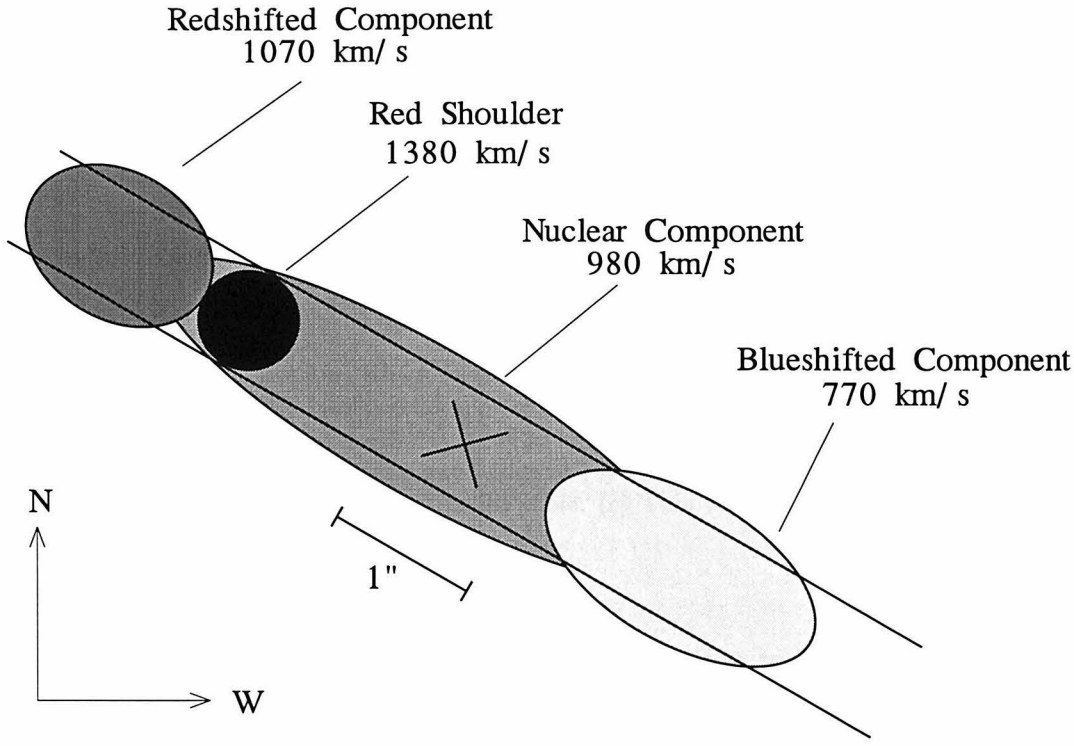

Figure 3.4: A cartoon of the four narrow velocity components identified in Paβ and [FeII] in Tables 3.1 and 2. The 0.75″ wide slit at a position angle of 60° is indicated by the two long parallel lines. The cross indicates the center of the slit and the peak of the continuum emission.

3.4.2 Correlation Between Paβ and [FeII]

The centroids of the components of the Paβ and [FeII] lines as tabulated in Table 3.1 agree quite well with each other. Both are redshifted (relative to the nucleus) northeast of the nucleus, and both are blueshifted southwest of the nucleus. In general, the line shapes are similar within each spatial bin. For example, 1.33″ northeast of the nucleus, both the Paβ and [FeII] lines have a red shoulder. In each spatial bin, with few exceptions there is good correspondence between the velocity centers of the two lines; usually, the components that comprise the [FeII] line share the same redshifts as the components that comprise the Paβ line. One exception is 1.3″ and 2.0″ southwest of the nucleus, where there is a very weak red shoulder identified at approximately 1270 km/s in the [FeII] line, which is not seen in Paβ. Given the ratios of [FeII]/Paβ seen in the other components, it is possible this shoulder may just be too weak at

Table 3.2: Comparison of IR and Optical Velocity Components

Comp.	Ulrich (1973)		Schulz (1990)		this paper	
	position (at 240°)	velocity (km/s)	position (at 240°)	velocity (km/s)	position (at 240°)	velocity (km/s)
1	1.5″ SW	(610)[a]	1-3″ SW	740	1″-3″ SW	770
2	nucleus	970	2″SW-2″ NE	960	1.3″ SW-1.3″ NE	980
3	1″-3″ NE	1120	2″-3″ NE[b]	1130	2″-3″ NE	1070
4	1″ NE	(1470)[c]	...	...	1-2″ NE	1380

(a) This velocity is reported by Ulrich as the "blue edge" of the component. (b) Schulz decomposes a flat-topped profile into two components, one at approximately the nuclear velocity of component 2 and the other at a velocity of 1130 km/s. Schulz identifies the 1130 km/s component with Ulrich's component having a red edge at 1470 km/s; here, that 1130 km/s component is instead identified with component 3 in the table. (c) This velocity is reported by Ulrich the "red edge" of the component.

Paβ to be identified in the spectra. A second exception to the correlation between line centers of Paβ and [FeII] components is the [FeII] emission 0.67″ southwest of the nucleus (Figure 3.3f), which, at a velocity centroid of 855±28 km/s, is intermediate between the nuclear system and the 770 km/s blueshifted system. Given the large width of this line (575±20 km/s) as compared to neighboring lines, this component is consistent with a blend of two Gaussian profiles, one at each the velocities of these two systems. However, we cannot distinguish this blend from a single Gaussian fit. A final [FeII] Gaussian component whose velocity center does not fall within one of the four velocity components identified in Paβ is the 581 km/s component identified on the nucleus (Figure 3.3e). It is possible that this component is associated with the [SIX] line blueward of [FeII] on the nucleus.

Except for the cases cited above, the Gaussian components fit to the [FeII] lines belong to one of the four velocity systems identified in the Paβ line. Moreover, the [FeII] emission components show the same velocity centers at the same locations along the slit as do the Paβ velocity components. The correlations between the Paβ and [FeII] line velocities suggest that the cloud systems responsible for the narrow Paβ line are also producing the bulk of the [FeII] emission. The correlations of the kinematics of the near infrared and optical lines further suggest that the [FeII] emission arises in the narrow line region. Since the HST [OIII] narrow band images of Evans *et al.* (1993)

indicate structure on spatial scales an order of magnitude smaller than our spatial resolution, each velocity component we have identified is likely to be composed of many smaller clouds.

Although the line centroids of the [FeII] and Paβ emission lines are generally well matched, the width of the [FeII] line is consistently broader than that of the Paβ line in every spatial bin, and in every corresponding Gaussian component listed in Table 3.1. Given our spectral resolution of 240$\pm$20 km/s as measured from unresolved OH sky lines, most of the observed narrow Paβ features are unresolved or only marginally resolved in velocity, whereas the majority of the [FeII] lines are clearly resolved in velocity, showing intrinsic widths of 400 km/s or more. The coincidence of the spatial and velocity centers of the Paβ and [FeII] lines argue that the physical regions where each of these emission lines arise share the same large scale dynamics. The differences in the line widths, however, argue that on small scales there may be an additional excitation process acting upon the Fe^+.

Figure 3.5 is a plot of the line center versus the FWHM of the Gaussian components. On this figure are plotted all of the Gaussian profile fits from Table 3.1, excluding those points which, because of their faintness and blending with adjacent components, had an uncertainty in line width greater than 250 km/s and those points with an uncertainty in line centroid greater than 150 km/s. The blueshifted 770 km/s component, and the high velocity 1380 km/s component are all easily distinguished from each other and from the components closer to the nuclear velocity on this plot. The nuclear 980 km/s component and redshifted 1070 km/s component are not readily separated since their velocity difference is small and closer to the uncertainties in the various line centroids. The substantially larger [FeII] line widths are immediately apparent in Figure 3.5.

The infrared Paβ and [FeII] emission is correlated, showing spatial and kinematic similarities which indicate the lines arise from the same or at least from correlated physical locations. Furthermore, the Paβ and [FeII] emission shows similar velocity components to those seen in the optical NLR clouds. Consequently, our data argue that the [FeII] emission arises in the NLR of NGC 4151, so there is no need to invoke

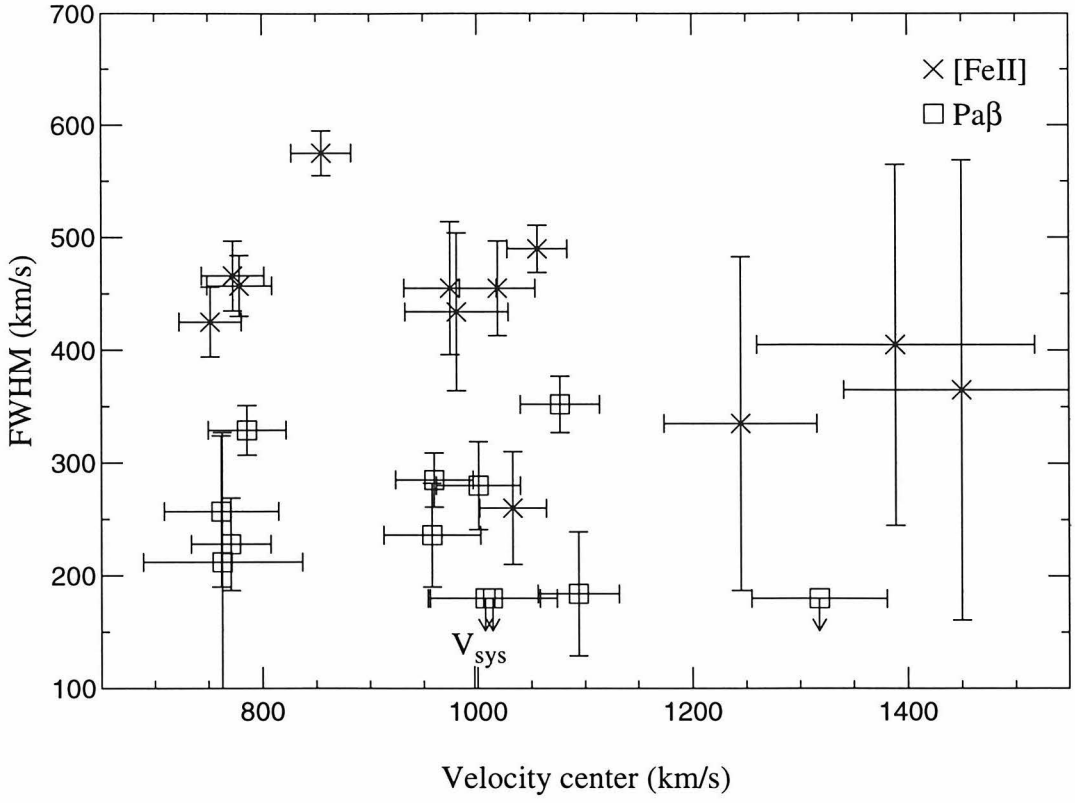

Figure 3.5: Width versus central velocity of the Paβ and [FeII] components tabulated in Table 3.1. Paβ is indicated by boxes and [FeII] is indicated by crosses. For each of the three major velocity groupings, the [FeII] line is broader than the Paβ line by typically 150-200 km/s.

a near-nuclear starburst to explain the [FeII] emission.

3.4.3 [FeII]/Paβ Flux Ratios and [FeII] Emission Processes

The total narrow-line flux ratio of [FeII]/Paβ (excluding the broad Paβ line) in the $0.75'' \times 6.67''$ slit is 1.28 ± 0.04. The ratio of [FeII]/Paβ flux clearly varies as a function of position along the slit, and among the four previously mentioned velocity components. These results are summarized in Tables 3.3 and 3.4. The most noticeable trend evident in these tables is that the [FeII]/Paβ ratio increases with increasing radius from the nucleus. This is true whether one considers just the ratio as a function of position (Table 3.3), or whether one considers the ratio for the four identified velocity components (Table 3.4, where the 980 km/s component is considered nuclear). The

Table 3.3: Variation of Narrow [FeII]/Paβ Flux Ratio with Position

Position	[FeII]/Paβ flux ratio
2.67″ NE	1.01±0.12
2.00″ NE	1.51±0.05
1.33″ NE	1.39±0.04
0.67″ NE	1.00±0.04
Nucleus	1.01±0.05
0.67″ SW	1.24±0.04
1.33″ SW	1.51±0.04
2.00″ SW	1.86±0.06
2.67″ SW	1.84±0.15

[FeII]/Paβ flux ratios we observe are comparable to large-beam [FeII]/Paβ flux ratios observed in other Seyfert galaxies, which typically range from 0.3 to 1.4 (Mouri *et al.* 1990; Goodrich *et al.* 1994).

The large scale kinematical correlation between [FeII] and Paβ observed is a direct indication that the [FeII] emission arises in the NLR of NGC 4151. Additionally, the similarity between the near-infrared emission line components measured here and the optical Hβ and [OIII] emission lines (Schulz 1990; Ulrich 1973) suggests the former arise in the outflowing ionized gas. However, the fact that the [FeII] lines are consistently broader than the narrow Paβ lines argues for an additional excitation mechanism for the [FeII]. This mechanism may be fast shocks associated with the outflow. These shocks could also explain the brightness of the [FeII] emission, as shocks can destroy grains which contain much of the iron in the interstellar medium, thus increasing the gas phase abundance. If shocks do contribute to the [FeII] emission, they ought to contribute to other low-ionization species as well. As such, one might expect other low-ionization species to show similar profiles to [FeII] at the same spatial positions. Schulz (1990) tabulates the FWHM for several optical species, including [SII], [OI], and [NII]. For position angles close to 60° at a distance 2″ from the nu-

Table 3.4: Variation of Narrow [FeII]/Paβ Flux Ratio with Velocity Component

Component	[FeII]/Paβ flux ratio
770 km/s	1.96±0.37
980 km/s	0.83±0.13
1070 km/s	1.84±0.15
1380 km/s	2.53±2.34

cleus, the widths of these species are between 300 km/s and 450 km/s, consistent with the line widths observed for [FeII]. However, the presence of multiple, possible overlapping emission line components in these data are difficult to assess. Multiple, marginally resolved components may be present, for example, in Hα southwest of the nucleus where the linewidth is >350 km/s (Schulz 1990), whereas in Paβ we separate two blended components each with width <250 km/s.

In the nearest Seyfert 2 galaxy, NGC 1068, Blietz *et al.* (1994) observe [FeII] emission which is enhanced along the direction of the outflow from the nucleus. The strength of the [FeII] emission drops where the radio jet flares out. Blietz *et al.* suggest that these features of the [FeII] emission may be partially the product of shocks resulting from the interaction between the nuclear outflow and circumnuclear molecular clouds. Our correlation between [FeII] and Paβ which indicates that the [FeII] emission does arise in the NLR of NGC 4151, suggests that similar conditions may exist in the circumnuclear regions of both NGC 1068 and NGC 4151, and that similar processes may be giving rise to the [FeII] emission.

Although shocks are a natural mechanism which can explain the enhanced [FeII] emission in NGC 4151, we cannot rule out x-ray photoionization. From the flux ratio of [FeII](λ=1.644μm)/Brγ in the Crab Nebula, Graham *et al.* (1990) argue that power-law photoionization of the filaments in the nebula produces enough partially ionized gas to account for all of the [FeII] emission, and that there is no need for shocks to dissociate dust grains. From similarities between the [FeII] to hydrogen recombination line flux ratios in the Crab Nebula and in NGC 4151, these authors further argue that

photoionization in the NLR can entirely account for the [FeII] emission in NGC 4151, with no need for shocks either from supernova or from the NLR itself. However, the fact that the [FeII] line is systematically broader than the Paβ line in NGC 4151 suggests that another mechanism, possibly shocks, are important in the narrow line region for the generation of [FeII] emission.

3.5 Summary and Conclusions

We have presented spatially resolved near-infrared spectroscopic data on the Seyfert 1.5 galaxy NGC 4151. There is a spatially unresolved broad component of Paβ, a spatially unresolved component that we identify with [SIX] and spatially resolved narrow components of Paβ and [FeII] (λ=1.2567μm). From these data, we have identified individual velocity components in each of these lines, which have a finite number of discrete velocity centroids consistent with individual cloud systems, not with a smooth distribution of gas. The velocity centroids of the [FeII] and Paβ lines agree well in spatial and velocity structure, indicating that these two species share similar bulk kinematics. In addition, the velocity components identified in our near-infrared data correspond well to velocity components previously identified in optical spectroscopy of NGC 4151. The correspondence in the kinematics of the [FeII] line to the kinematics of the Paβ and optical Hβ and [OIII] lines indicates that the [FeII] emission is associated directly with the Seyfert narrow line region. Despite the strong correlation between the [FeII] and Paβ velocity centroids, the [FeII] narrow lines are consistently broader than the Paβ narrow lines. This suggests that the [FeII] emission has an additional excitation source, possibly high velocity shocks associated with a nuclear outflow. The increase in the [FeII]/Paβ line flux ratio with radius may reflect the increasing importance of this shock excitation to the [FeII] with distance from the nucleus along the direction of the outflow.

3.6 Appendix to Chapter 2: Discussion of Individual Gaussian Fits

This appendix discusses in greater detail the fits to the observed line profiles displayed in Figures 3.2 and 3.3.

2.67″, 2.00″ northeast of the nucleus (Figure 3.3a, b, j, k)

Both the [FeII] line and the Paβ line were acceptably fit by a single Gaussian line profile in each of these spatial bins.

1.33″ northeast of the nucleus (Figure 3.3c,l)

Both the Paβ and [FeII] lines in this spatial have a non-Gaussian shape clearly visible in Figure 3.2. Both lines appear to have a small "shoulder" on the long wavelength side. This red shoulder is also visible in the 0.67″ northeast bin in Figure 3.2. Both lines were fit with two Gaussian line profiles. The fit was done by a χ^2 minimization of two profiles: one with a centroid near the peak in intensity of the entire line, and a second which fits the red shoulder. This procedure produces a significantly better fit (with a lower χ^2 per degree of freedom) to both line profiles than does a single Gaussian profile.

0.67″ northeast of the nucleus (Figure 3.3d, m)

The [SIX] blueward of [FeII] is present in this bin (Figure 3.3d). It was fit with a single Gaussian profile. The [FeII] line shows enhanced emission along its red shoulder. This was fit with a second, Gaussian profile redward of the primary [FeII] component. In this spatial bin, the [FeII] line was fit independently from the unidentified line.

The Paβ line (Figure 3.3m), similar to the [FeII] line, shows a small amount of enhanced emission on its red side. It also was fit with a second Gaussian profile redward of the primary Paβ component.

Nucleus (Figure 3.3e, n)

Three Gaussian line profiles were required to adequately fit the [FeII]/[SIX] line complex. The first is for the [SIX] line, which appears both in the nuclear spectrum, and the spectra 1.33″ northeast and southwest of the nucleus. The other two Gaussian profiles used to fit the profile of the [FeII] line itself were centered on the peak of the emission, and a weaker "shoulder" necessary to fit the flux to the blue side of the peak. Figure 3.3e shows the results of this fit.

The broad Paβ line was fit to the unsubtracted spectrum of Figure 3.2. One large source of uncertainty in the shape and the derivation of the integrated flux of the broad line is the shape of the continuum. To estimate the shape of the broad Paβ line and the uncertainties in the parameters that describe it, we used two different fits for the continuum: one, a flat and horizontal line (F_λ=const) at the level of the continuum at the left of the middle panel of Figure 3.2, and two, a line sloping gently upward ($F\lambda \propto \lambda$). Two Gaussians were simultaneously fit in a χ^2 minimization procedure over each of these continua, one to fit the broad line, one to model the narrow line. The results of these fits for the broad line are reported in Table 3.1. The results of these fits for the narrow line were consistent with the single Gaussian fit to the continuum and broad line subtracted spectrum.

0.67″ southwest of the nucleus (Figure 3.3f, o)

One Gaussian profile for the [FeII] line and one Gaussian profile for the [SIX] line was sufficient to fit the [FeII]/[SIX] complex (Figure 3.3f).

The Paβ line (Figure 3.3o) has an asymmetric shape, with a steeper drop redward of the peak than blueward of the peak. A good fit to the line included two Gaussian profiles of comparable amplitude.

1.33″ southwest of the nucleus (Figure 3.3g, p)

Similar to the [FeII] line 1.33″ northeast of the nucleus, this [FeII] line appears to have a very weak red shoulder. A second Gaussian line profile was included in the

χ^2 minimization fit to model this shoulder. In this case, the shoulder is at a velocity consistent with the redshift of the [FeII] line on the nucleus, and the bulk of the [FeII] emission is blueshifted relative to the nucleus.

The Paβ line (Figure 3.3p) shows an asymmetry opposite that of the Paβ line 0.67″ southwest of the nucleus. As with the Paβ line 0.67″ southwest of the nucleus, it was fit with two Gaussian profiles of comparable amplitude.

2.00″ southwest of the nucleus (Figure 3.3h, q)

One Gaussian profile was sufficient to fit the unidentified line blueward of [FeII]. The [FeII] line itself (Figure 3.3h) shows enhanced emission in the red wing. It was fit with two Gaussian profiles: a strong one comprising the bulk of the line, and a weak second Gaussian profile redward of the center of the line to describe the enhanced wing emission.

The Paβ line (Figure 3.3q) was satisfactorily fit with a single Gaussian profile.

2.67″ southwest of the nucleus (Figure 3.3i, r)

The [FeII] line and the Paβ lines were each adequately fit by a single Gaussian line profile.

Chapter 4

Seyfert 2 Galaxies Mk 1066, NGC 2110, NGC 4388, and Mk 3

4.1 Introduction

This chapter presents longslit near-infrared spectra of the Seyfert 2 galaxies Mk1066, NGC 2110, NGC 4388, and Mk3, in the lines Paβ, Brγ, [FeII] (λ=1.2567μm), H_2 v=1-0 S(1), and [SIX](λ=1.2524μm). The observations reported in this chapter are of the four Seyfert 2 galaxies with the best detected large extended circumnuclear emission line regions in the near-infrared. This chapter will comprise the bulk of a paper to be submitted to *The Astrophysical Journal* for publication. The data for the remaining Seyfert galaxies is presented in Chapter 5. The results of all of the data are summarized and discussed in Chapter 6.

4.2 Observations and Data Reduction

The data discussed in this chapter were obtained and reduced according to the procedure described in Chapter 2. Table 4.1 is a log of the observations, including the resolution (in km s^{-1}), on-source integration time, and position angle of the slit for each observation. Since we are interested in exploring the near infrared emission line

flux ratios and dynamics as a function of distance from the Seyfert nucleus, we chose slit position angles to coincide with the position angle of known ionization cones or other anisotropy previously mapped through narrow band optical emission line imaging. In the case of two of the galaxies (Mk1066 and NGC4388), there are additional observations along a secondary slit through the nucleus, perpendicular to the primary position angle. In order to accurately center the nucleus in the slit, a fold mirror inside the spectrometer, but in front of the grating, allows infrared imaging with a $10'' \times 40''$ field of view.

Galaxy	Wavelength	On-Source Integration	Slit PA	Res. km s^{-1}	psf FWHM	Date of Observation
Mk1066	1.25μm-1.31μm	2400s	135°	242±15	0.7″	1995/09/09
Mk1066		2400s	45°	228±15	0.6″	1996/09/10
Mk1066	2.10μm-2.23μm	2400s	135°	289±19	0.6″	1995/09/08
Mk1066		2400s	45°	289±19	0.5″	1995/09/10
NGC2110	1.25μm-1.31μm	2400s	160°	229±16	$\sim$ 1.1″	1996/01/05
NGC2110	2.09μm-2.22μm	1800s	160°	285±19	$\sim$ 1.1″	1996/01/05
NGC4388	1.25μm-1.31μm	2400s	30°	229±15	$\sim$ 0.8″	1996/01/03
NGC4388		2400s	120°	244±15	0.8″	1996/04/08
NGC4388	2.10μm-2.23μm	2400s	30°	261±19	$\sim$ 0.7″	1996/01/03
NGC4388		1800s	120°	303±19	0.8″	1996/04/08
Mk3	1.26μm-1.32μm	3000s	113°	243±15	$\sim$ 1.0″	1995/11/06
Mk3	2.14μm-2.27μm	1800s	113°	292±19	$\sim$ 1.0″	1995/11/07

Table 4.1: Observation log. References for position angles are: Mk1066: Bower *et al.* (1995); NGC2110: Mulchaey *et al.* (1994); NGC4388: Corbin, Baldwin, & Wilson (1988); Mk3: Mulchaey *et al.* (1996). The resolution column indicates the FWHM of an unresolved line measured from OH sky lines in one of the galaxy frames.

During the observations of Mk1066 and the April 1996 observations of NGC4388, we determined the atmospheric seeing tabulated in Table 4.1 by observing a star halfway through the relevant spectra observations. These observations of the star were guided using the same offset guiding procedures as were used for the spectral observations. For the other observations, we do not have as accurate a measurement of the point spread function (psf). In the case of Mk3, it was estimated based on

2.2μm imaging of a quasar somewhat later than the observations of Mk3. In the case of NGC 2110 and the January 1996 observations of NGC 4388, unguided G-star and photometric standard star images were used to estimate the seeing at the time of the spectral observations.

4.3 Results and Discussion: Individual Objects

4.3.1 Mk1066

Mk1066 is an inclined SB0+ galaxy with a systemic velocity of 3625 km s^{-1} (Bower *et al.* 1995). With $H_0 = 75$ km s^{-1} Mpc^{-1}, this yields a spatial scale of 234 pc/$''$. HST imaging of the nuclear regions shows a narrow "jetlike" feature in a narrow band image which includes [OIII] and Hβ. This jet is oriented at 315° and extends $\sim 1.4''$ northwest of the nucleus. In Hα and [NII], the jet is observed on both sides of the nucleus. The nuclear radio source is linear, and extended over $2.6''$. The 5 GHz radio emission is oriented at the same position angle as the optical line emission (Ulvestad & Wilson 1989).

Mk1066 shows strong infrared line emission, concentrated on the nucleus. Four emission lines are visible in the spectra shown in Figures 4.1, 4.2, and 4.3: Paβ and [FeII] in the J-band spectra, and Brγ and H_2 in the K-band spectra. The 135° angle of the slit was chosen to align with the position angle of the optical ionization cones (Bower *et al.* 1995). In addition, there is data along a 45° slit chosen to be perpendicular to the primary slit. The infrared lines are visible over a spatial extent of $\sim 5''$ (1.2 kpc) along the 135° slit, in comparison to the FWHM of the nuclear continuum which was $\sim 1.8''$ at 1.25μm and $\sim 1.1''$ at 2.15μm in our spectra. In contrast, the lines are less spatially extended along the 45° slit, and are only visible over an extent of $\lesssim 3''$. The Brγ line is strongest on the nucleus, but the Paβ, [FeII], and H_2 lines peak about $0.5''$ northwest of the nucleus.

Figure 4.1 shows two greyscale plots of the reduced $1.25 - 1.31\mu$m spectra along both slits. The horizontal axis is observed wavelength, and the vertical axis is position

along the slit in arcseconds from the nucleus. The Paβ and [FeII] lines are spatially resolved along both position angles in Figure 4.1. The tilt in the lines indicates that there is a spatial velocity gradient in the [FeII] and Paβ lines along the 135° slit; this will be discussed in section 4.3.1. Along the 45° slit, no velocity gradient is visible.

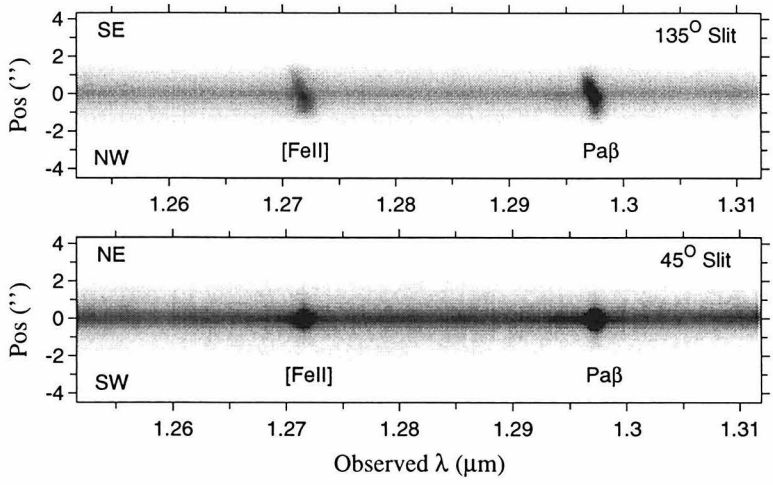

Figure 4.1: Spectra of Mk1066 in the 1.25−1.31μm range. Position is distance from the nucleus in arcseconds along the indicated position angle of the slit.

Figures 4.2 and 4.3 are one-dimensional projections in various spatial bins extracted from the two-dimensional data. Figure 4.2 shows the spectra along the 135° slit, and Figure 4.3 along the 45° slit. The size of each spatial bin used in the extractions is 4 pixels, or 0.67″. This matches the point spread function (psf) at the time of the observations (0.5″–0.7″).

The Paβ profile near the nucleus shows enhanced emission blueward of the line center. These blueward features on Paβ are visible not only in Mk 1066, but also in many other Seyfert galaxies (Chapter 5). Were this Paβ emission, it would be at a velocity of ~ -700 km s^{-1} relative to the centroid of the Paβ emission, which is higher than the other velocities observed in Mk 1066. These blue features on Paβ are probably primarily due to a blend of two HeI lines at 1.2785μm and 1.2791μm, which has been resolved from Paβ in high resolution spectroscopy of the planetary nebula BD+30°3639 (Goodrich *et al.* 1994). There may also be some contribution

from [FeII] ($\lambda = 1.2788\mu$m). For $T_e \sim 10^4$ K and $n_e \sim 10^4$ cm^{-3}, the strength of the $\lambda = 1.2788\mu$m line is expected to be < 0.1 of the strength of the λ=1.2567μm line (Goodrich *et al.* 1994). In Mk 1066, [FeII] ($\lambda = 1.2788\mu$m) could account for at most half of the emission on the blue side of Paβ.

Integrated Line Flux Ratios

Table 4.2 lists the equivalent widths and flux ratios of the lines observed in Mk 1066. Because [FeII] and Paβ were observed simultaneously and are close in wavelength, we can obtain accurate [FeII]/Paβ flux ratios which are relatively insensitive to uncertainties in flux calibration or differential reddening. Similarly, we may obtain reliable H_2/Brγ flux ratios from our K-band spectra. Figure 4.4 shows these ratios as a function of position along the slit, using the total integrated fluxes for each species in each spatial bin to derive the line flux ratios.

Table 4.2: Mk1066 Equivalent Widths and Flux Ratios

Pos[a]	Equivalent Width ($10^{-4}\mu$m)				Flux Ratios	
(″)	[FeII]	Paβ	H_2	Brγ	[FeII]/Paβ	H_2/Brγ
			Mk 1066, 135° slit			
2.67	6.7±4.5	17.1±12.4	...	...	0.43±0.14	...
2	4.7±1.7	5.8±1.9	4.0±1.9	<4.3	0.79±0.21	>0.87
1.33	18.4±3.2	15.3±2.6	9.4±2.0	10.3±2.7	1.17±0.08	0.86±0.09
0.67	23.0±2.6	29.0±2.6	12.6±1.7	18.7±2.8	0.75±0.03	0.63±0.05
0	20.8±1.9	27.4±2.1	13.0±1.2	14.0±1.5	0.75±0.04	0.89±0.06
-0.67	39.0±3.8	33.0±4.6	17.8±2.6	20.6±3.8	1.20±0.04	0.85±0.06
-1.33	21.6±3.4	23.2±4.6	9.0±2.7	16.7±6.3	0.99±0.05	0.56±0.09
-2	5.3±2.2	6.7±2.5	<4.4	11.5±6.1	0.85±0.17	<0.40
			Mk 1066, 45° slit			
1.33	5.0±1.3	4.2±1.1	13.0±5.3	<2.7	1.30±0.32	>4.41
0.67	11.2±1.6	10.3±1.3	12.6±2.7	6.7±1.1	1.06±0.09	1.74±0.21
0	17.2±1.4	29.1±2.7	11.5±1.5	13.7±1.4	0.57±0.03	0.76±0.06
-0.67	15.9±2.6	17.9±2.7	12.6±2.3	10.0±2.0	0.87±0.07	1.21±0.10
-1.33	5.2±1.4	8.9±2.6	9.0±4.0	<4.7	0.64±0.16	>1.83
-2	...	...	5.6±3.7	<5.3	...	>0.91

a Positive positions are towards the position angle of the slit as quoted.

The most striking feature of Figure 4.4 is the rapid rise of the H_2/Brγ flux ratio with distance from the nucleus along the 45° slit, perpendicular to the position angle of the optical ionization cones. The H_2 line may be seen 2″ away from the nucleus

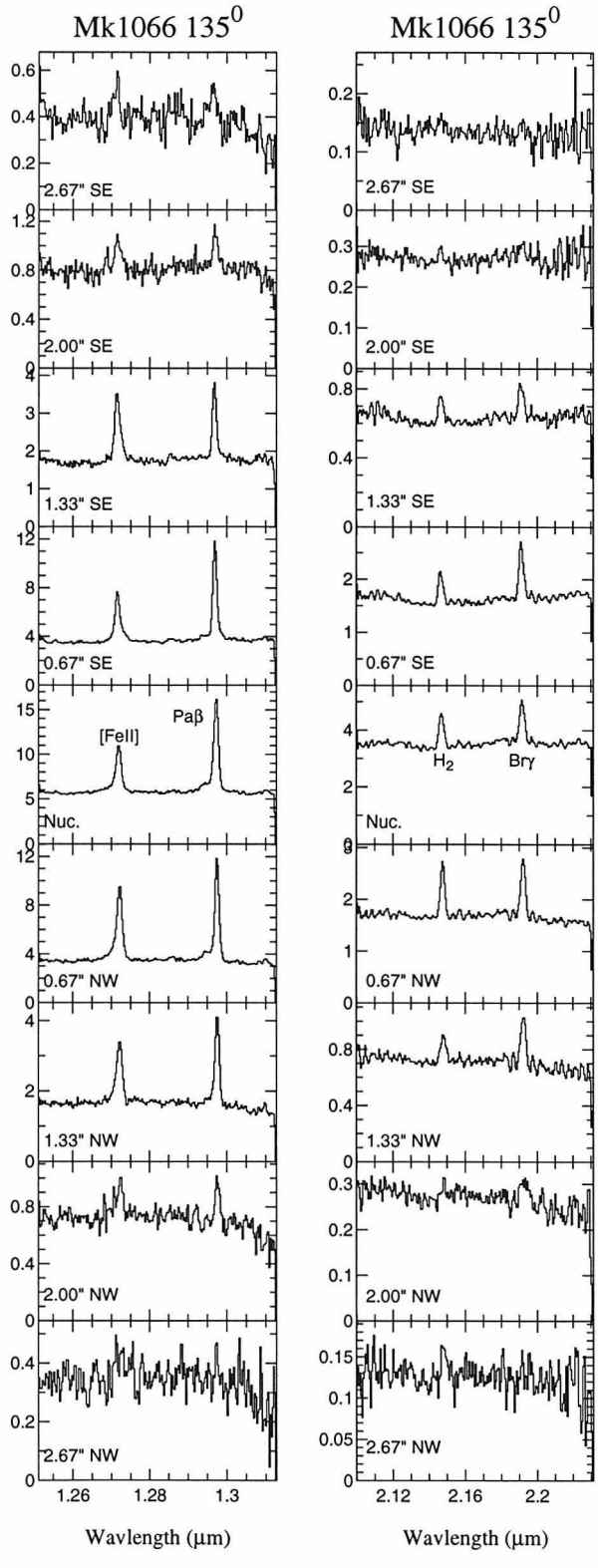

Figure 4.2: Spectra of Mk1066 along the 135° slit. Each spectrum represents the spectrum in a rectangular beam which is 0.67″ along the slit by the width of the slit $\sim$ 0.6″. Spatial bins are adjacent.

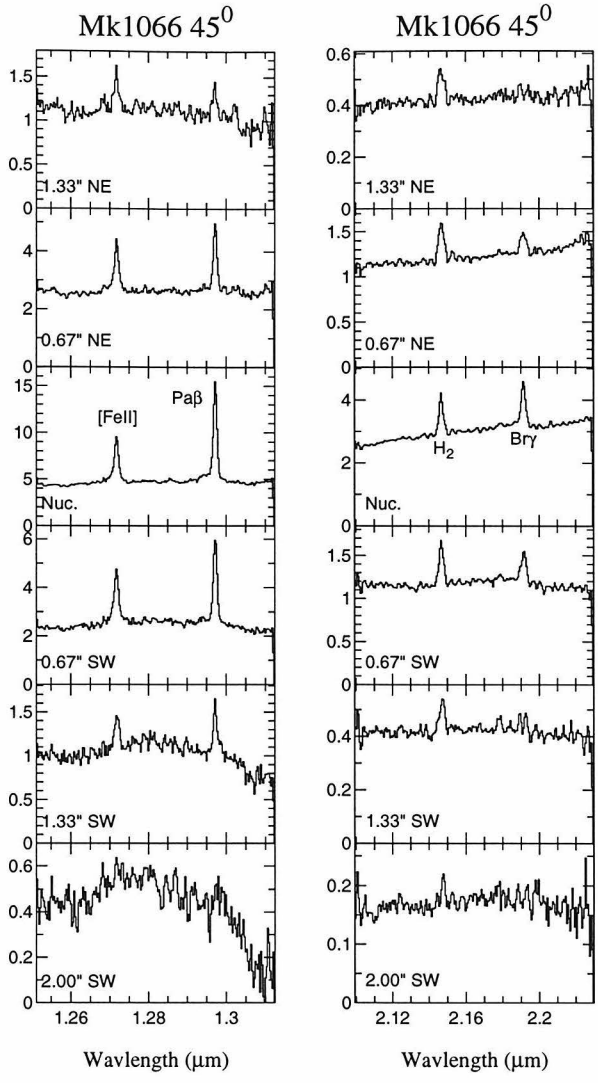

Figure 4.3: Spectra of Mk1066 along the 45° slit. Each spectrum represents the spectrum in a rectangular beam which is 0.67″ along the slit by the width of the slit $\sim$ 0.6″. Spatial bins are adjacent.

in both directions, while the Brγ line is detected only within 0.67″ of the nucleus. The H_2/Brγ flux ratio 1.33″ from the nucleus along the 45° slit is >3, in contrast to the nuclear value of 0.8. Along the 135° slit, the H_2/Brγ flux ratio does not change so dramatically, always remaining between about 0.4 and 0.9, although there is an indication of a gradient across the nucleus. The [FeII]/Paβ flux ratio, although it shows variations with position, does not show as rapid changes as does the H_2/Brγ flux ratio along the 45° slit. However, there is a clear local minmum in the [FeII]/Paβ ratio at the nucleus along both slits.

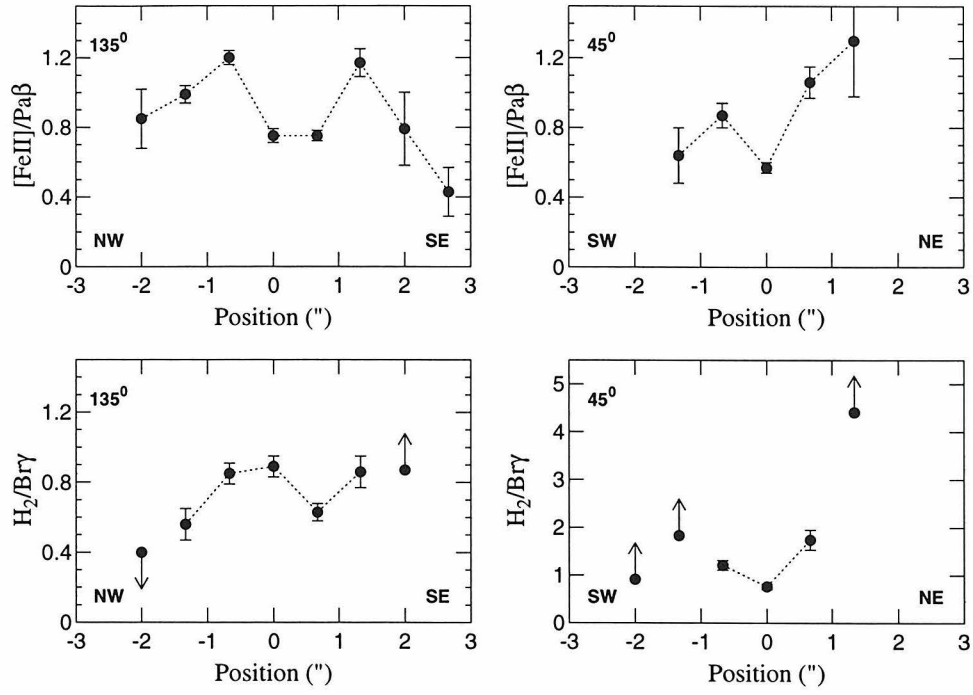

Figure 4.4: Flux ratios for Mk1066. The two plots on the left are for the 135° slit, the two plots on the right for the 45° slit.

Velocity structure

Figure 4.5 is a set of position versus velocity plots along the 135° slit for each of the four lines identified in Figures 4.2 and 4.3. In each case, a smoothed continuum has been subtracted from the spectrum. Velocity is plotted relative to 3625 km s^{-1}, the systemic velocity of Mk1066 (Bower *et al.* 1995), and position is distance in arcseconds on the sky from the continuum peak. A velocity gradient is visible in each of the lines, in the sense that the lines are blueshifted southeast of the nucleus and redshifted northwest of the nucleus. The slope of the velocity gradient does not appear to be the same for all of the lines. Specifically, the H_2 line appears to have a steeper gradient (~300 km $s^{-1}/''$, or ~1300 km s^{-1}/kpc) in comparison to the other three lines (whose gradients are ~200 km $s^{-1}/''$, or ~900 km s^{-1}/kpc). In addition, Brγ appears to have a slightly steeper gradient (by ~50 km $s^{-1}/''$) than Paβ southeast of the nucleus. The gradients of the [FeII] and Paβ lines are similar.

Another feature apparent in Figure 4.5 is that all of the lines, except for Brγ, peak

northwest of the nucleus. This is discussed in section 4.3.1.

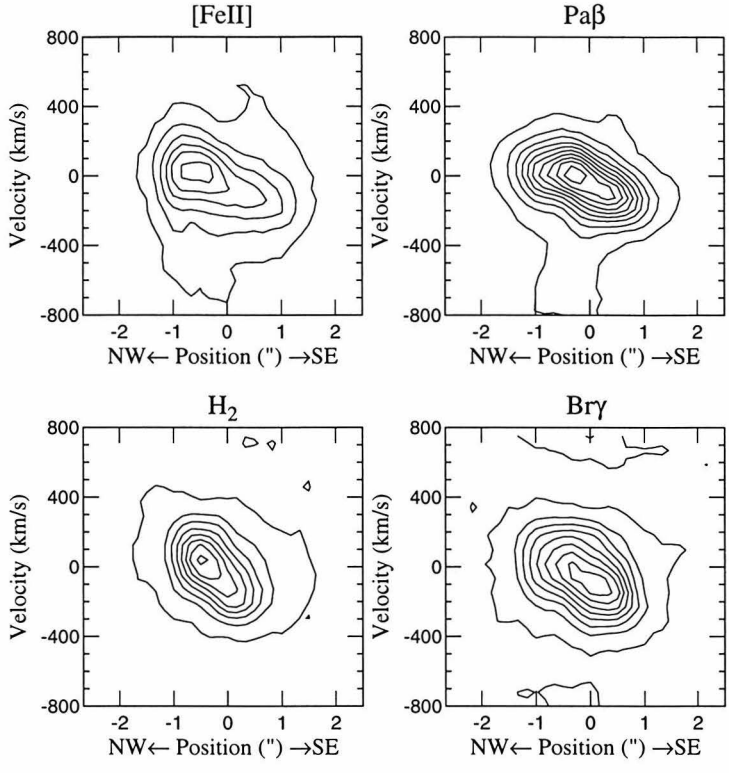

Figure 4.5: Position versus velocity plots for Mk1066. Position along a 135° slit. Velocity is relative to 3625 km s^{-1}, the systemic velocity of Mk1066 (Bower *et al.* 1995).

Table 4.3 lists the velocity centroids and total full widths at half maximum of the lines observed in Mk 1066 along both slits in each spatial bin. Many of the lines show a complicated asymmetric profile. These lines were decomposed into the smallest number of Gaussian components necessary to statistically describe the line profile. Figure 4.6 shows plots of the velocity of the strongest narrow Gaussian component of each line as a function of position along the slit. Usually, this is equivalent to a plot of the mode (peak) of the line profile as a function of position, because most of the line profiles in Mk 1066 are dominated by a strong, central narrow component. For reference, a line connecting the Brγ velocity peaks is drawn on each plot, and the Hα velocity curve (Bower *et al.* 1995) is shown on the Paβ plot.

The steeper velocity gradient in Brγ than in Paβ southeast of the nucleus as seen

Table 4.3: Mk 1066 Line Centroids and Widths

	[FeII]		Paβ		H_2		Brγ	
Pos[a] "	Centroid[b] km s^{-1}	FWHM[c] km s^{-1}	Centroid km s^{-1}	FWHM km s^{-1}	Centroid km s^{-1}	FWHM km s^{-1}	Centroid km s^{-1}	FWHM km s^{-1}
Mk 1066, 135° slit								
2.67	-118±24	< 154	-233±41	677±194	...	...	...	...
2	-68±25	267±109	-58±20	221±83	-72±35	< 190	...	...
1.33	-59±14	294±53	-77±19	< 154	-45±15	328±46	-90±19	383±34
0.67	-38±14	240±32	-67±14	< 154	-45±15	321±50	-73±18	237±46
0	-125±16	296±41	-20±15	205±50	3±13	353±29	-19±18	329±27
-0.67	-54±14	289±54	51±14	< 154	89±13	223±37	51±19	269±32
-1.33	-8±15	341±62	32±16	167±74	143±20	360±78	70±20	308±44
-2	109±18	218±75	70±18	202±65	...	...	133±46	715±196
Mk 1066, 45° slit								
1.33	-34±17	222±73	-50±19	179±93	-6±15	491±59	...	...
0.67	-52±14	179±52	-20±10	< 150	-12±11	392±35	-43±17	429±62
0	-74±12	179±38	-41±13	< 150	-14±12	192±61	-83±17	250±44
-0.67	-54±15	219±46	-24±11	< 150	-21±10	277±33	-49±14	313±51
-1.33	-10±19	247±83	64±49	< 150	39±18	329±82	...	...
-2	...	...	...	...	107±23	< 190	...	...

a Positive position is towards the position angle of the slit as quoted.
b Centroids are relative to 3625 km s^{-1}, the systemic velocity of Mk1066.
c The resolution has been subtracted in quadrature.

in Figure 4.5 is also visible in Figure 4.6. The slope of the [FeII] velocity gradient is similar to that of Paβ. The velocity gradient seen in H_2, although similar to the other lines, is steeper. The H_2 velocity gradient is marginally steeper than that for Brγ; the difference is greater between H_2 and Paβ. Two arcseconds south of the nucleus, all of the lines except for Brγ (which is undetected) show a local velocity reversal of 50–75 km/s.

In addition to the primary narrow components whose centroid velocities are plotted in Figure 4.6, the Mk1066 line profiles show weaker components which are displaced in velocity relative to the center of the lines. Southeast of the nucleus, where the peaks of the line profiles are blueshifted relative to the systemic velocity, all of the lines show a noticeable enhanced red wing (although it is very weak in H_2). On the nucleus and to the northwest where the peaks of the line profiles are redshifted, the Paβ and [FeII] lines show an enhanced blue wing. While this blue wing is almost certainly a feature of the [FeII] line profile itself, the blue wing of the Paβ line suffers the contamination from other species discussed above.

For illustration, Figure 4.7 shows the profiles of the [FeII], Paβ, and Brγ lines on the nucleus and 1.33″ northeast and southwest of the nucleus. Southeast of the

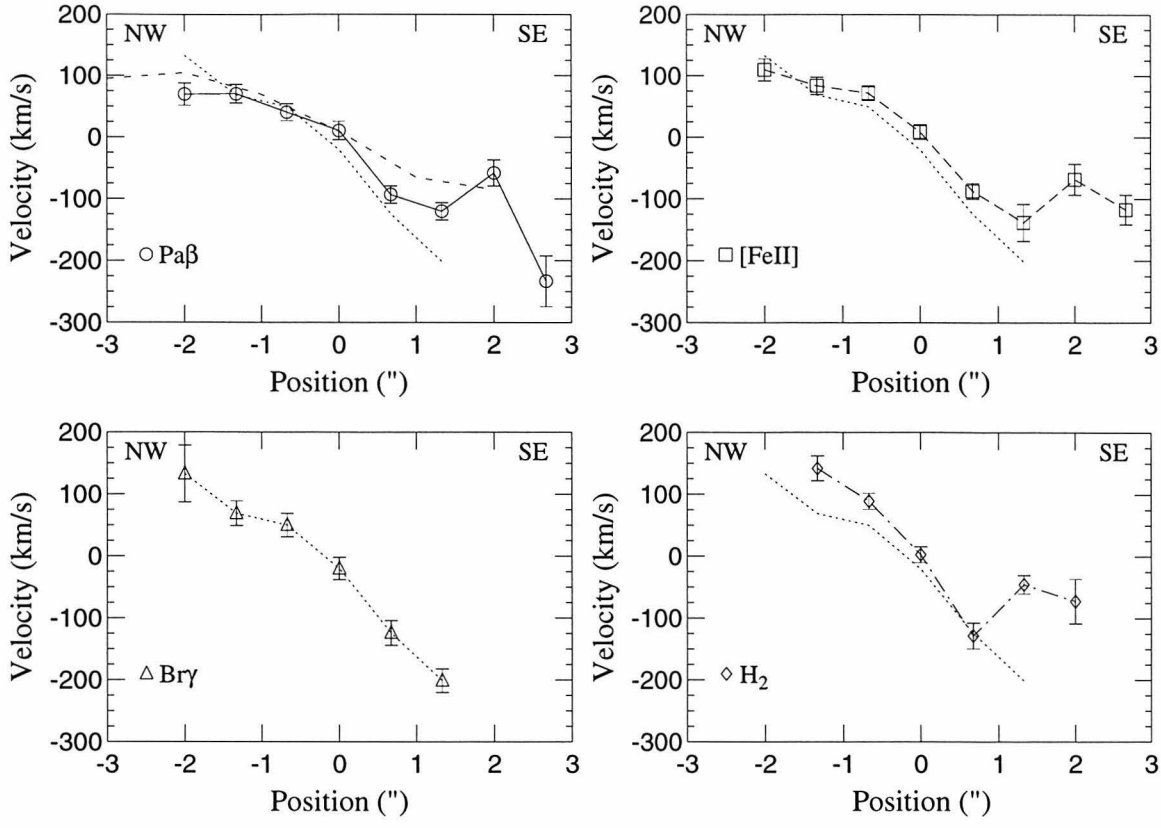

Figure 4.6: Velocity of the primary narrow component of each line versus position along the 135° slit for Mk1066. The data for Brγ are shown as a dotted line in each plot. The dashed line on the Paβ plot is the Hα data of Bower *et al.* (1995).

nucleus, the red wing is stronger relative to the rest of the line in [FeII] and Brγ than it is in Paβ. Similarly, northwest of the nucleus, the blue wing is most prominent in [FeII]. It is not visible in the Brγ line, and in Paβ it may be contaminated by the aforementioned HeI and [FeII] lines.

Comparison with Optical Spectroscopy

Bower *et al.* (1995) present longslit optical spectroscopy of Mk1066 along a 134° slit. The Hα, Hβ, [NII], [SII], and [OI] lines all have a velocity gradient extending from +100 km s^{-1} 2-3″ northwest of the nucleus to -90 km s^{-1} 2-3″ southeast of the nucleus. This is similar to the velocity structure seen in the infrared lines (see Figure 4.6), although the peaks of the Paβ and particularly the Brγ lines are slightly

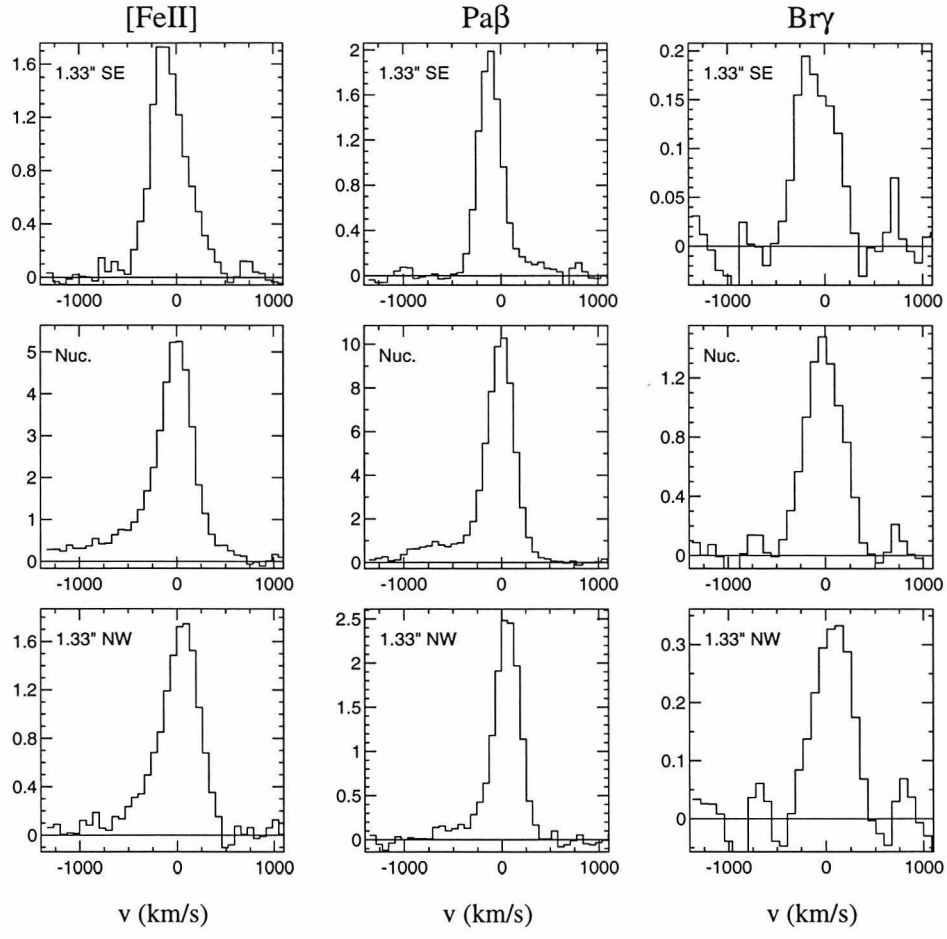

Figure 4.7: Selected line profiles of Mk1066 along the 135° slit, chosen to illustrate shoulders seen in asymmetrical line profiles.

blueshifted relative to the optical lines to the southeast of the nucleus.

In addition to the primary kinematic component seen in optical emission lines, Bower *et al.* (1995) identify a second kinematical component, seen in [OIII]. The [OIII] emission is slightly blueshifted relative to the other lines northwest of the nucleus and redshifted by as much as 200 km s^{-1} relative to the other lines southeast of the nucleus. This structure is qualitatively similar to the enhanced wings seen in the infrared lines discussed in section 4.3.1. Specifically, the infrared lines show an enhancement blueward of the peak on the nucleus and to the northwest, and they show an enhancement redward of the peak to the southeast. It is likely that some of the wings seen on the infrared emission lines are associated with the kinematic component

Bower *et al.* (1995) identify in [OIII].

Extinction

Paβ and Brγ are both hydrogen recombination lines (n=5–3 and n=7–4 respectively), and should arise in the same physical locations. Their intrinsic flux ratio is well known (assuming radiative transfer effects are negligible). Because of reddening, in dusty regions the observed Paβ line will be suppressed relative to the observed Brγ line. If the dust is intermixed with the line emitting clouds and there are strong velocity gradients, the two lines can appear to have different velocity structures. In Mk 1066, both the infrared and optical data indicate that extinction effects are stronger to the southeast than they are to the northwest.

A difference in both the spatial and velocity distribution of Paβ and Brγ is visible in Figure 4.5. The peak of the Paβ emission is shifted to the northwest in position relative to that of the Brγ emission, which is very close to the continuum peak. The Brγ line is stronger relative to Paβ to the southeast than it is to the northwest. The simplest explanation of this difference is a larger extinction due to dust in the southeast. Spatially variable extinction may also be responsible for the slightly different Paβ and Brγ velocity gradients seen in Figure 4.5. To the southeast, where dust extinction appears greater, the discrepancy between the velocity gradients for the Paβ and Brγ lines is larger. Extinction could also explain the difference between the velocities of the infrared lines and the optical Hα line southeast of the nucleus (Bower *et al.* 1995). The Hα-infrared slope discrepancy is in the same direction as the Paβ–Brγ slope discrepancy, i.e., lines at shorter wavelengths have shallower gradients; see Figure 4.6.

This same extinction effect is seen in the red wing of the Paβ and Brγ line southeast of the nucleus as discussed in section 4.3.1; the wing was relatively more prominent in Brγ than in Paβ suggesting that the extinction to the region where the wings originate is greater than the extinction to the region where the bulk of the line emission originates. If the wings represent outflowing gas, then the redshifted receding gas,

which may be partially obscured by dust in the disk of the galaxy, would show higher extinction. There is also evidence from optical wavelengths that the outflowing gas is heavily extincted. The optical line emission is seen emerging from the nucleus in ionization cones at position angles of 135°/315°. The [OIII]+Hβ narrowband image shows suppressed emission to the southeast, being much stronger to the northwest. The 5 GHz radio emission (Ulvestad & Wilson 1989) indicates that the strength of the outflow is slightly asymmetric, but the difference in the strength of the radio emission northwest and southeast of the nucleus is not as great as the difference in the strength of the [OIII] emission which Bower *et al.* (1995) associate with the outflow. Dust in the disk of the galaxy to the southeast which obscures the outflow can explain the suppressed [OIII] emission.

Extinction cannot explain the discrepancies between the H_2 and Brγ lines, since the differential extinction between the two is negligible. In Figure 4.5, the H_2 line shows a different velocity gradient than Brγ and the peak of the H_2 emission is shifted to the northwest relative to the peak of the Brγ emission. The differences in their appearance may indicate that the emission seen from each species originates from different clouds which are projected along the same line of sight; i.e., the ionized atomic and warm molecular gas are not cospatial. Additionally, there may be a systematic variation in the physical conditions along the cone axis of the galaxy.

A Picture of the Nuclear Regions of Mk1066

Based on their optical spectroscopy, Bower *et al.* (1995) describe the nucleus of Mk1066 as a combination of two systems. A rotating disk, seen in Hα, [NII], [SII], and other species is the locus of low-excitation emission. A second component showing different velocity structure, seen in [OIII], represents high excitation outflowing gas. The features seen in the infrared spectral lines are consistent with these two kinematic systems.

Figure 4.8 is a cartoon drawing of the system based on the optical and infrared data. In this picture, there is an inclined disk with a major axis of 135° projected

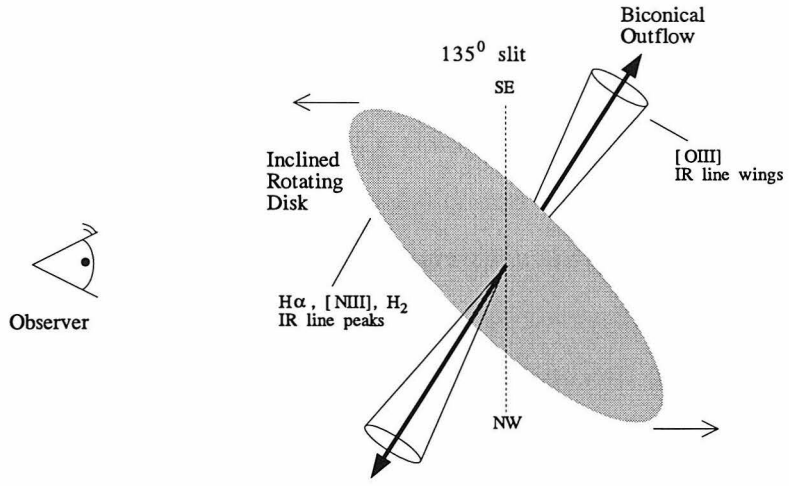

Figure 4.8: Cartoon drawing of the nuclear regions of Mk1066. The rotating disk is the source of low excitation emission, and the source of the primary velocity gradient seen in most optical and infrared lines. The outflow is higher excitation emission, and shows up as wings in the infrared lines.

on the sky. This orientation explains both the greater spatial extent and the larger velocity gradient in the infrared lines along the 135° slit. The plane of the disk is dusty, explaining the extinction effects discussed in section 4.3.1. There is a biconical outflow associated with the higher-excitation gas, as drawn. To the northwest, this outflow is relatively unobscured, as it is in front of the plane of the galaxy. This explains the blueshifted [OIII] emission seen by Bower *et al.* (1995). The blue wings seen on the infrared lines to the northwest are associated with this outflow. To the southeast, the outflow is obscured by the plane of the galaxy, suppressing the [OIII] emission observed in that direction. Extinction resulting from this obscuration enhances the Brγ/Paβ ratio on the red side of the line profile southeast of the nucleus (see Figure 4.7).

[FeII] and H_2 Emission Processes

The fact that various features of the [FeII] emission line profiles correspond with those identified with the active nucleus in other species, such as the wings seen in [OIII] Bower *et al.* (1995), suggest that the [FeII] emission is dominated by processes associated directly with the Seyfert nucleus. In addition, the [FeII] emission shows

some interesting spatial associations with the radio emission of Mk1066 (Bower *et al.* 1995). Similar to the optical and infrared emission, the radio emission is "linear" and elongated along a position angle of 134°. This radio emission appears to represent two oppositely directed radio jets, and spatially corresponds with the outflow seen in [OIII]. The [FeII] emission is relatively stronger than the Paβ emission in the outflow, indicated by the fact that the wings associated with the outflow in [FeII] are stronger, relative to the rest of the line profile, than the wings in Paβ (see Figure 4.7). Shocks resulting from the interaction of outflowing radio plasma with the ambient gas are a natural mechanism for the production of [FeII] emission. Fast shocks can both destroy dust grains, increasing the gas phase abundance of iron, and create large partially ionized regions, two conditions which enhance [FeII] emission. This suggests that there is a contribution to the [FeII] emission from the interaction of the radio jets with surrounding gas.

The most striking feature of the H_2 emission is that its strength does not drop off as quickly with distance from the nucleus perpendicular to the outflow axis as compared to the other infrared lines. While Brγ is only detected out to 150pc from the nucleus at a position angle of 45°, H_2 is detected to >300pc. That H_2 is visible along both slits indicates that warm molecular gas is ubiquitous in the near-nuclear disk of Mk 1066. Since the H_2 is not as confined to the cone axis as the other lines, it is evidently not as directly dependent on ionization from the active nucleus or the radio jets for its excitation. There is probably little H_2 emission associated with the high excitation outflow, since the wings seen in the infrared [FeII] and Paβ lines which we associated with this outflow were small to nonexistent in the H_2 line profiles.

Heating by x-rays from the Seyfert nucleus cannot explain the H_2 emission extended perpendicular to the ionization cone axis. The existence of the ionization cone implies that the ionizing nuclear radiation only escapes in that direction. Slow ($v< 25$ km s^{-1}) shocks originating in the nucleus may propagate outward and heat molecular clouds in the disk of the galaxy. Alternatively, there may be a local source of heating for the molecular gas in the regions within $\sim$ 500 kpc of the nucleus of Mk 1066.

Summary

1. The infrared Paβ, Brγ, and [FeII] lines are extended over 1.2 kpc along a 135° position angle coincident with the direction of the optically identified ionization cones. Along a perpendicular angle, their intensity drops off faster with distance from the nucleus; 300 pc away from the nucleus at 45°, the intensity of the lines relative to the nucleus is 20% of their value along a position angle of 135°.

2. The infrared lines have strongly peaked narrow components. These peaks have a rotation curve similar to the optical Hα *et al.* lines along a position angle of 135°, which Bower *et al.* (1995) identify as part of a rotating, LINER-like disk.

3. There are secondary components in the form of enhanced wings in the infrared lines whose kinematics differ from the strong, narrow components in a manner similar to the difference between the kinematics of [OIII] and the other optical lines. The [OIII] emission and the near infrared line wings are likely assocaited with a nuclear outflow which produces blueshifted emission to the northwest of the nucleus.

4. The relative spatial distributions of Brγ and Paβ indicate that there is greater extinction to the southeast of the nucleus than there is to the northwest. This may explain differences seen in the velocity centers of hydrogen recombination lines to the southeast, which is most likely due to partial obscuration of the gas by an inclined disk in Mk 1066.

5. The H_2 line is more extended than the other lines along an angle perpendicular to the ionization cone. Along the axis of the cone, it shows a steeper velocity gradient than Paβ, Brγ or [FeII].

6. We propose that there is a measurable contribution to the [FeII] emission from shocks associated with the nuclear outflow. It may have a direct link to the radio jets seen at 3.6cm. The H_2 emission, on the other hand, arises primarily from the inner (500pc) disk of Mk 1066, most of which is presumably shielded from

direct illumination of the nucleus. This warm molecular gas may be heated by local sources such as star formation.

4.3.2 NGC 2110

NGC 2110 is an S0 galaxy with a systemic velocity of 2342 km s^{-1} (de Vaucouleurs *et al.* 1991), which gives a spatial scale of 150 pc/″. HST narrowband imaging of optical Hα+[NII] and [OIII] emission shows a narrow jetlike feature near the nucleus extending to the north at a position angle of ~340°, and a weaker opposing feature extending to the south at ~160° (Mulchaey *et al.* 1994). The feature curves into an "S" shape 4″ away from the nucleus in each direction. At 1.49 GHz, NGC 2110 shows a triple radio source extended over 4″ with a position angle of ~0° (Ulvestad & Wilson 1984a), slightly different from the position angle of the optical line emission. The curvature of the "S" of the optical line emission is towards the direction of the radio emission. In x-rays, NGC 2110 has a 2-10 keV luminosity of 1.4×10^{43} erg/s with a comparatively high absorbing column density of 7.4×10^{22} cm^{22} (Reichert *et al.* 1985). This luminosity is closer to a typical value for a moderate luminosity Seyfert 1 galaxy than for Seyfert 2 galaxies ($\sim 5 \times 10^{41}$ erg/s) (Kriss *et al.* 1980). ROSAT High Resolution Imager (HRI) data show a spatially extended x-ray source, with secondary x-ray emission 4″ north of the nucleus which may be responsible for the soft x-ray excess (Weaver *et al.* 1995).

Our longslit spectra of NGC 2110 along a position angle of 160° (Figure 4.9) show four strong infrared emission lines in the observed spectral regions: [FeII], Paβ, H_2(v=1-0 S1), and Brγ. These lines are visible on the nucleus, and are seen to be extended by $\gtrsim$ 6″ (900 pc). By comparison, the FWHM of the continuum is 2.4″ at 1.2μm and 1.5″ at 2.2μm, while the seeing at the time of the observations was ~ 1.1″. The spectra in Figure 4.9 represents the summed spectrum in spatially adjacent 1″ bins along the slit. The most striking feature of the NGC 2110 J-band spectrum is the strength of the [FeII] line. On the nucleus, the [FeII]/Paβ flux ratio is 8.1, which is greater than that observed in any other Seyfert galaxy in this thesis. The implications

of this will be discussed later in this section.

Integrated Line Flux Ratios

Table 4.4 tabulates the equivalent widths and flux ratios of the lines observed in NGC 2110. The [FeII]/Paβ and H_2/Brγ line ratios are very large on and near the nucleus. These flux ratios as a function of position along the slit are plotted in Figure 4.10. Near the nucleus, the H_2/Brγ flux ratio is close to 3, locally rising at a position 2″ north of the nucleus, and dropping off in the furthest spatial bins. The [FeII]/Paβ flux ratio is 8.1±0.8 on the nucleus, falling rapidly with radius, to ∼1 at 3″ south of the nucleus and ∼3 at 3″ north of the nucleus.

Table 4.4: NGC 2110 Equivalent Widths and Flux Ratios

Pos[a] (″)	Equivalent Width ($10^{-4}\mu$m)				Flux Ratios	
	[FeII]	Paβ	H_2	Brγ	[FeII]/Paβ	H_2/Brγ
3	3.5±1.0	3.3±0.8	3.8±1.3	2.1±0.9	1.09±0.25	1.89±0.78
2	6.2±1.3	2.9±0.7	7.2±1.4	1.9±0.6	2.19±0.42	4.08±1.08
1	15.4±1.4	3.1±0.5	6.2±0.8	2.0±0.4	5.02±0.48	3.23±0.53
0	24.7±1.6	3.1±0.4	4.8±0.4	1.6±0.3	8.11±0.78	3.17±0.63
-1	22.5±2.3	3.2±0.5	6.6±0.7	2.0±0.4	7.36±0.74	3.59±0.69
-2	11.7±2.3	2.8±0.6	8.4±1.7	1.4±0.4	4.43±0.53	6.50±1.50
-3	8.7±2.0	3.1±0.9	5.5±1.2	2.8±1.0	2.93±0.54	2.14±0.51
-4	5.8±2.8	<2.7	3.6±1.5	<9.7	>2.24	>0.39

a Positive positions are toward the southeast at a position angle of 160°.

For most Seyfert galaxies, values of [FeII]/Paβ typically range between 0.5 and 2.0 (e.g., Goodrich *et al.* 1994; Simpson *et al.* 1996b), while for the H_2 v=1-0 S(1)/Brγ flux ratio the typical range is between 0.5 and 1.5 (e.g., Moorwood & Oliva 1988). The flux ratios observed in NGC 2110 are significantly higher than these, with the [FeII] line in particular being unusually strong in comparison to the Paβ line. Indeed, the value of 8.1 for the [FeII]/Paβ flux ratio on the nucleus is higher than that observed in any Seyfert galaxy to date (e.g, Goodrich *et al.* 1994; Forbes and Ward 1993; Mouri *et al.* 1993). This high [FeII]/Paβ ratio is due to both a strong [FeII] line and a weak Paβ line in comparison to other Seyfert galaxies. The equivalent width of the [FeII] line on the nucleus, $25\times10^{-3}\mu$m, is larger by a factor of 2-4 than that typically seen

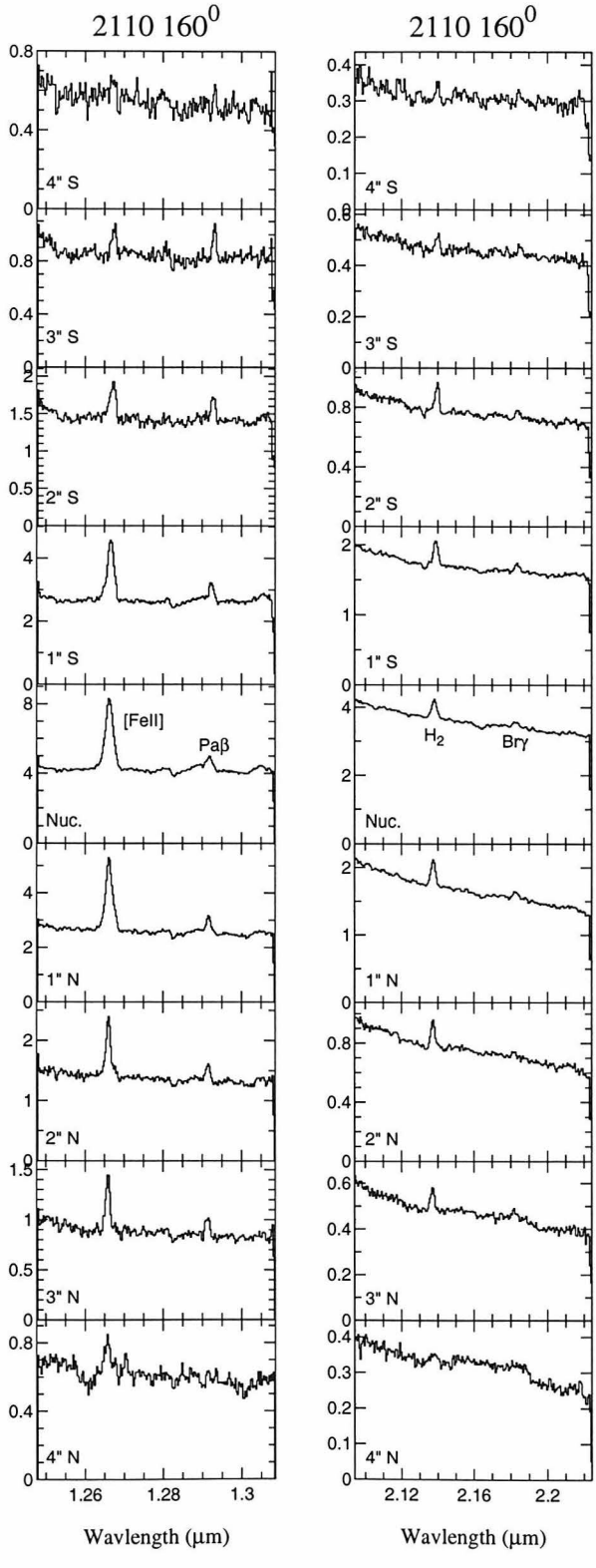

Figure 4.9: Spectra of NGC 2110 along the 160° slit. Each spectrum is produced from a 1.0 × 0.6″ rectangular beam. Spatial bins are adjacent. The distance of each spatial bin from the nucleus in a southerly direction is indicated in each panel. Note the strength of [FeII] and the large [FeII]/Paβ flux ratio on the nucleus.

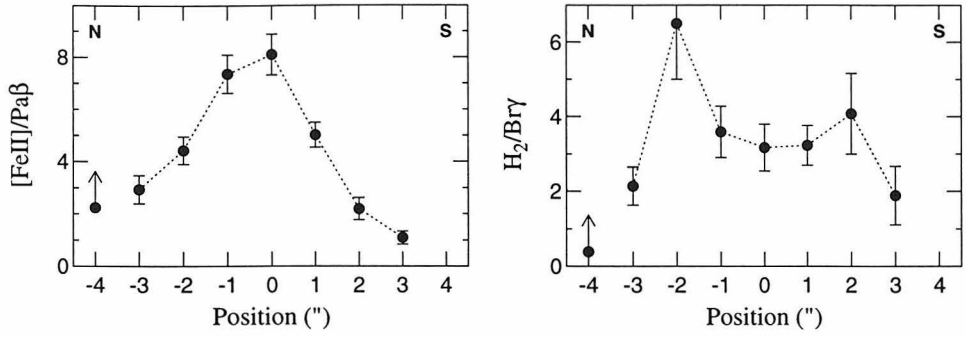

Figure 4.10: NGC 2110 flux ratios as a function of position along the 160° slit. Positive positions are to the south.

in Seyfert galaxies, although it is not the largest known equivalent width of [FeII] in a Seyfert 2 galaxy (Chapter 5).

Velocity structure

In Figure 4.11, we show a set of position versus velocity plots for each of the four near-infrared lines seen in NGC 2110. A smoothed continuum has been subtracted from the data in each case. Velocity is plotted relative to 2340 km s^{-1}, the systemic velocity of NGC2110 (de Vaucouleurs *et al.* 1991).

All of the lines in Figure 4.11 show a velocity gradient which has increasing velocity to the south and decreasing velocity to the north. Unlike Mk1066, the slope of all the gradient appears to be quite similar for all of the infrared lines in NGC 2110. Figure 4.12 is a plot of the velocity centroid of each line profile as a function of position for each of the four lines. The centroids for Paβ are only for the line flux which can be identified as arising from Paβ; the flux due to the contamination from HeI and [FeII] on the blue side of Paβ (as discussed in section 4.3.1) has not been included in the centroid calculation. Table 4.5 tabulates these velocity centroids, as well a the full widths at half maximum of each of the line profiles. The velocity structure in Figure 4.12 is dominated by the gradient from north to south which is visible in Figure 4.11. The slope of the gradient is steeper to the south than it is to the north. North of the nucleus, the lines reach a velocity of about -100 to -150 km s^{-1}

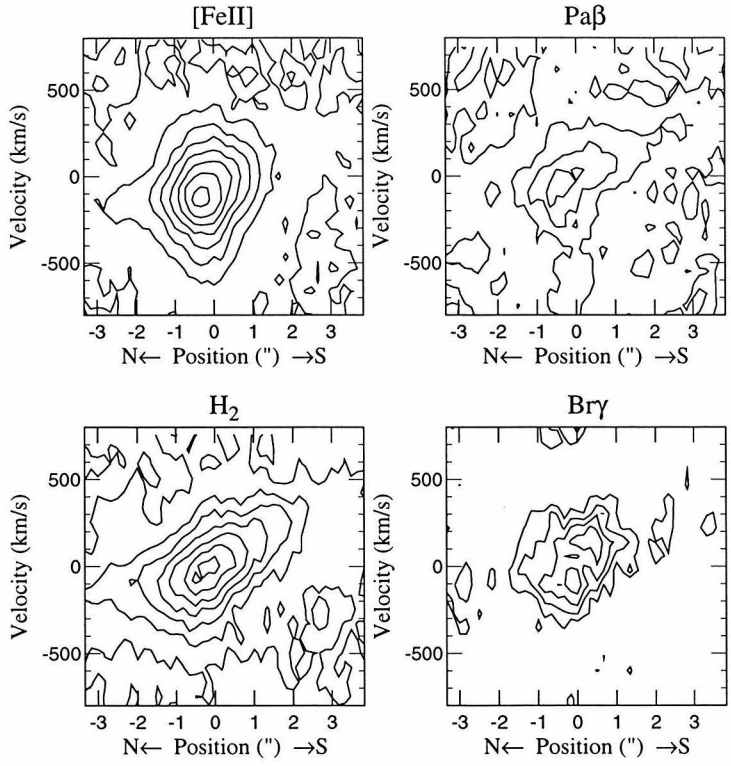

Figure 4.11: Velocity versus position along 160° slit for NGC 2110. Velocity is relative to 2340 km s^{-1}, the systemic velocity of NGC 2110.

relative to the systemic velocity of NGC2110 at a distance of 3″. South of the nucleus, the lines reach velocities of +250 to 300 km s^{-1} at a distance of 3″.

A second feature of the velocity structure of the infrared line radiation apparent in Figure 4.12 is that the [FeII] line is systematically at a lower velocity than the other lines. This effect is strongest south of the nucleus, although here the strong blue wings in [FeII] pull the centroids to lower velocities. The slope of the [FeII] velocity gradient is similar to the slope for the other lines, but in each spatial bin the velocity peak of the [FeII] line is shifted to the blue by about $50 - 100$ km s^{-1}, which is several times the uncertainty in the wavelength calibration.

In many cases, the lines are asymmetric, although in most of these cases the asymmetries are small enough that the velocity centroids plotted in Figure 4.12 are very close to the velocities of the peaks of the lines. On the nucleus and 1″ south of

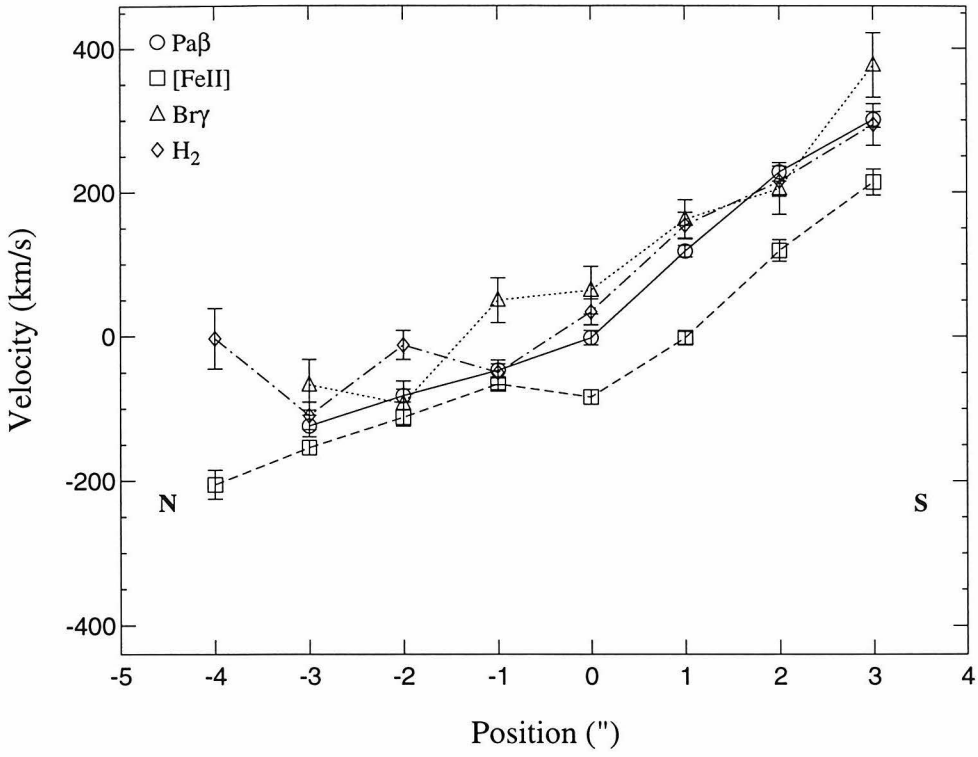

Figure 4.12: Velocity centroid of the whole line profile versus position for each line at each position along the 160° slit. Velocity is relative to 2340 km s^{-1}, the systemic velocity of NGC2110.

the nucleus, there is a blue wing seen in Paβ and [FeII] (see Figure 4.9), although in Paβ this is due at least in part to contamination from HeI and [FeII] ($\lambda = 1.2788\mu$m) mentioned in section 4.3.1. The Brγ line 1″ north of the nucleus shows a strong enhanced red wing, and appears to be the superposition of two narrow components comparable in strength. Two arcseconds north of the nucleus the [FeII] and H_2 lines show a red shoulder. South of the nucleus, these lines show a blue shoulder.

The [FeII] line is significantly broader than the other lines, particularly close to the nucleus. On the nucleus, the FWHM of the [FeII] line is 500 km s^{-1}, as compared to 340 km s^{-1} for the Paβ line. In addition, the [FeII] line has wings with FWHM $\sim$ 850 km s^{-1} which are not visible in the Paβ line. The [FeII] line is narrower at larger radii, having a FWHM of $<$ 400 km s^{-1}, 3″ away from the nucleus. At 3″ south of the nucleus, the [FeII] line remains $\lesssim$ 100 km s^{-1} broader than the Paβ line, while north of the nucleus the line widths are comparable.

Table 4.5: NGC 2110 Line Centroids and Widths

	[FeII]		Paβ		H_2		Brγ	
Pos[a] "	Centroid[b] km s^{-1}	FWHM[c] km s^{-1}	Centroid km s^{-1}	FWHM km s^{-1}	Centroid km s^{-1}	FWHM km s^{-1}	Centroid km s^{-1}	FWHM km s^{-1}
3	212±18	219±88	299±11	< 150	292±29	223±132	375±45	< 189
2	117±15	334±44	226±13	< 150	213±21	< 189	203±36	213±169
1	-4±9	373±36	116±8	213±41	152±18	275±35	160±27	259±92
0	-86±10	496±34	-4±10	338±43	32±18	359±36	62±33	391±116
-1	-68±8	383±25	-49±9	186±51	-52±17	273±34	48±31	304±111
-2	-114±11	171±54	-84±9	176±53	-14±20	238±52	-95±31	< 189
-3	-156±10	197±31	-126±15	203±82	-112±19	205±61	-69±35	313±136
-4	-207±20	347±87	...	...	-5±42	546±226	...	...

a Positive position is southeast along the 160° slit.
b Centroids are relative to 2342 km s^{-1}, the systemic velocity of NGC 2110.
c The resolution has been subtracted in quadrature.

Comparison With Other Observations

The velocity structure seen in Hα, Hβ, and [OIII] (Wilson *et al.* 1985) is quite similar to the velocity structure seen in the infrared lines plotted in Figures 4.11 and 4.12. Line velocities vary from about -100 km s^{-1} relative to the systemic velocity a few arcseconds north of the nucleus to approximately the systemic velocity on the nucleus. A few arcseconds south of the nucleus, velocities rapidly rise to +200 to 300 km s^{-1} relative to the systemic velocity. Wilson *et al.* (1985) and Wilson & Baldwin (1985) describe this velocity field as a rotating disk with a projected major axis of 161°.

Near the nucleus, the [OIII] line has a higher root mean square (RMS) width than the Hβ line by 100-200 km s^{-1}. Wilson *et al.* (1985) state that this may be the result of the greater flux of [OIII], allowing weak wings to be visible in that line which are not visible in Hβ. South of the nucleus, [OIII] shows a tendency toward enhanced blue wings; this behavior is similar to what is observed in [FeII], and to a lesser extent in H_2. These enhanced wings show some spatial similarities with the 2 cm emission (Ulvestad & Wilson 1984a). The blue wings are strongest in [FeII], H_2, and [OIII] 2″ south of the nucleus, which is the approximate position of one of the radio peaks. The second radio peak is 2″ north of the nucleus, where we see a red shoulder in [FeII] and H_2. This suggests that, as with Mk1066, there may be two kinematical components: a rotating disk, and a second velocity field, possibly an outflow associated with the radio jets.

[FeII] and H_2 Emission Processes

The fact that the [FeII]/Paβ ratio is very large on the nucleus and rapidly drops with distance from the nucleus suggests that the [FeII] emission is associated with the Seyfert nucleus itself. There is indirect evidence that the physical process responsible for the [FeII] emission in NGC 2110 is x-ray heating and ionization. NGC 2110 has a 2–10 keV x-ray flux which is an order of magnitude greater than what is typical for a Seyfert 2 galaxy. On the nucleus, the [FeII]/Paβ ratio is also nearly an order of magnitude greater than the typical value for Seyfert 2 galaxies. Out to radii 3–4″ north of the nucleus, the [FeII]/Paβ ratio remains atypically large for a Seyfert 2 galaxy. About $\sim 4''$ north of the nucleus lies the secondary 0.1–2.4 keV x-ray emission peak identified by Weaver *et al.* (1995). At this position, we have a lower limit on the [FeII]/Paβ flux ratio of ≥ 2. South of the nucleus, opposite the direction of the extended x-ray emission, the [FeII]/Paβ ratio drops to unity.

Although the [FeII] excitation may be dominated by x-ray ionization in NGC2110, there is likely to be an additional contribution due to fast shocks resulting from the interaction of outflowing radio plasma with surrounding gas. This would explain the enhanced red and blue wings respectively north and south of the nucleus which are spatially coincident with the radio peaks seen by Ulvestad & Wilson (1984a) at 1.49 GHz.

Nuclear x-ray heating of molecular clouds may also be the primary mechanism responsible for the H_2 emission, although the enhanced H_2 is not as dramatic as is the case with [FeII] in this galaxy. The H_2/Brγ ratio in NGC2110 is large for Seyfert galaxies, yet the H_2/Brγ ratio is not strongly peaked on the nucleus as is the case for the [FeII]/Paβ ratio. The H_2/Brγ flux ratio is nearly constant over the 6″ (900pc) where the lines are detected. In contrast to Mk1066, the presence of the wings in the H_2 line profiles indicates that there may be warm molecular gas in the outflowing clouds.

Summary

1. In NGC 2110, the [FeII]/Paβ flux ratio is unusually large near the nucleus, reaching a value of 8.1 on the nucleus and dropping off rapidly with distance from the nucleus. The H_2/Brγ ratio is also large, being $\gtrsim 3$ within 2″ of the nucleus. The H_2/Brγ ratio, however, does not vary as strongly with position, except for a local maximum located 2″ north of the nucleus.

2. In general, the infrared lines show a smooth velocity gradient with lines blueshifted to the north and redshifted to the south of the nucleus. This is similar to the velocity gradient seen in optical emission by Wilson *et al.* (1985).

3. The infrared [FeII] line has a velocity gradient with the same slope as the other infrared lines. However, in each spatial bin it is shifted by about 50-100 km s^{-1} to the blue. Additionally, the [FeII] line is $\sim$ 160 km s^{-1} broader than the other infrared lines near the nucleus.

4. There are enhanced wings on the infrared lines. To the south, where line centroids are redshifted, there are enhanced blue wings. To the north, where line centroids are blueshifted, there are enhanced red wings.

We suggest that the [FeII] excitation is dominated by nuclear x-ray photoionization. However, the enhanced off-nuclear wings which are spatially coincident with the radio peaks indicate that there is some emission associated with outflowing gas. Fast shocks may contribute to the [FeII] emission at these locations. The H_2 emission may also result from molecular clouds heated by nuclear x-rays. The distribution of warm molecular gas is not as strongly centralized on the nucleus as is the distribution of partially ionized [FeII]-emitting gas.

4.3.3 NGC 4388

NGC 4388 is a highly inclined spiral galaxy at a systemic velocity of 2525 km s^{-1} (Petitjean & Durret 1993). Although its Hubble type is uncertain (de Vaucouleurs *et*

al. 1991), Corbin, Baldwin, & Wilson (1988) classify it as SB(s)b pec. It is generally considered to be a member of the Virgo cluster (Helou *et al.* 1980), implying that the distance to the galaxy is probably ~14 Mpc (Pierce & Tully 1988). This yields a spatial scale of 68 pc/″. Optical narrowband imaging (Corbin, Baldwin, & Wilson 1988) shows an Hα+[NII] extent of $> 40''$ east and west of the nucleus, aligned with the major axis of the galaxy at position angle $\sim 90°$. This emission originates in the spiral arms of the galaxy, and is probably due to HII region complexes. Close to the nucleus on a spatial scale of $\sim 5''$, the [OIII] emission is extended about the nucleus in a halo-like distribution that has a major axis at a position angle of $\sim 30°$. High resolution radio maps at 4.86 GHz show emission which is elongated southwest of the nucleus at a similar position angle of 200° (Hummel & Saikia 1991). The source is double peaked, with a primary peak on the nucleus and a secondary peak 2.5″ southwest of the nucleus. There is a weak tertiary peak about 1″ northeast of the nucleus. NGC 4388 has also been detected in x-rays, with a 2-10 keV luminosity of $\sim 2 \times 10^{42}$ erg/s (assuming a distance of 14.1 Mpc to the galaxy) (Hanson *et al.* 1990). The soft (0.1-2.4 keV) x-ray emission of NGC 4388 is extended over $\gtrsim 15''$ (Matt *et al.* 1994).

Figure 4.13 is a two-dimensional greyscale plot of the 1.25μm-1.31μm spectrum of NGC 4388 along two slits at position angles of 30° and 120°. The horizontal axis is observed wavelength, and the vertical axis is position along the slit. The 30° slit was chosen to align with the major axis of the distribution of [OIII] emission near the nucleus (Corbin, Baldwin, & Wilson 1988). The 120° slit was chosen perpendicular to this first slit. Apparent from this figure are the strong Paβ and [FeII] lines, which are detected over a spatial extent of 8″ (540 pc) at 30°. Along the same position angle, at 2.2μm we detected the Brγ and H_2 over a similar spatial extent. Along the perpendicular position angle of 120°, the lines drop off more quickly with distance from the nucleus, but are still visible out to a radius of 2–3″.

Because Hα emission is extended over $> 40''$ along a position angle of 120° (Corbin, Baldwin, & Wilson 1988), we obtained a sky frame distant from the center of the galaxy. Subtracting this sky frame from spectra of the galaxy verified that no infrared

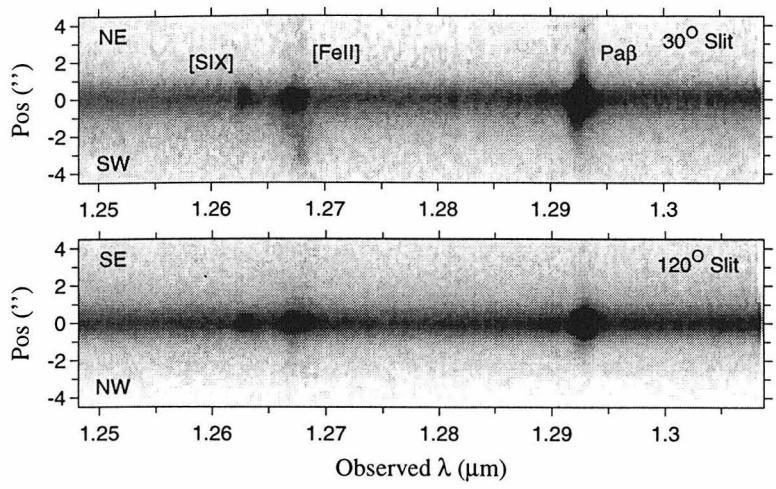

Figure 4.13: $1.25 - 1.31\mu$m spectra of NGC4388.

emission lines were detected at a radius greater than $5''$ in this direction to a 3σ flux limit of $\sim 2 \times 10^{-16}$ erg cm^{-2}s^{-1} in a $1.0'' \times 0.6''$ spatial beam.

In addition to the [FeII], Paβ, Brγ, and H_2 lines, there is a narrow line seen on the nucleus blueward of [FeII], which is identified as the fine structure line [SIX] at a rest wavelength of 1.25249μm (Kuhn, Penn, & Mann 1996). Oliva *et al.* (1994) identify this line as [SIX] in the Circinus galaxy. However, Simpson *et al.* (1996b) and Thompson (1995) identify this line as HeI ($\lambda = 1.2528\mu$m) with some contamination from [SIX] in NGC 1068 and NGC 4151 respectively.

The arguments in favor of this line being primarily [SIX] are threefold. First, the HeI line is not strong enough to account for the observed flux in the objects where this line is seen. Recombination cascade calculations (Robbins 1968) indicate that the strength of this line should be $\lesssim 20\%$ of the strength of the HeI ($\lambda = 1.2785\mu$m) line. The latter line, blended with HeI ($\lambda = 1.2791\mu$m) and [FeII] ($\lambda = 1.2788\mu$m), comprises emission which is frequently seen as a weak blue wing on the Paβ line profile. However, when seen, the line blueward of [FeII] is of comparable strength or stronger than the blend blueward of Paβ, arguing against its identification as HeI.

The second argument is that the observed wavelength centroid, as compared to the observed wavelengths of the [FeII] and Paβ lines, is more consistent with [SIX] than

with HeI. Since the ionization potential of He is only 24.5 eV, we would expect He to show a similar spatial and velocity structure to the H^+ lines. S^{7+}, on the other hand, has a much larger ionization potential of 328 eV (West *et al.* 1985), and may arise from very different physical regions than does most of the Paβ and Brγ emission.

The final argument in favor of the line's identification as [SIX] is that the line is only seen in a small number of galaxies for which infrared spectra are available (Chapter 5). A HeI line would be expected to be seen with a similar strength relative to Paβ in most Seyfert galaxies, as the two lines should arise from similar physical regions. The strength of a high ionization coronal line may vary greatly between objects, however, due to variations in the ionization conditions, as well as differences in extinction to the regions responsible for the H^+ emission and the coronal emission. For these three reasons, we therefore assume that the line observed at a rest wavelength of 1.252μm is [SIX].

The [SIX] line is very strong on the nucleus. Its equivalent width of $4.5\times10^{-4}\mu$m is nearly half that of [FeII]. It is not as spatially extended as the other infrared lines along the position angle of either slit. It is marginally resolved spatially along the 30° slit, showing a stronger flux (0.39±0.08 of the nuclear flux) in the $\pm1''$ spatial bins than would be expected for atmospheric seeing of 0.8″ (0.08 of the nuclear flux). It is not resolved along the 120° slit.

Figures 4.14 and 4.15 are one-dimensional projections in various spatial bins of the data along the slits oriented at position angles of 30° and 120° respectively. The size of each spatial bin used in the extractions is 6 pixels (1″), slightly larger than the psf at the time of the observations, which was 0.7–0.8″ for the spectra at both position angles.

Inspection of Figures 4.14 and 4.15 reveals subtle differences between the emission observed in the nuclear bin on the two different slits. Notably, the [FeII] line shows a different profile in the two spectra, having a stronger red wing in the nuclear bin of the PA=120° data (Figure 4.15) as compared to the nuclear bin in the PA=30° data (Figure 4.14). Additionally, Paβ, Brγ, and [FeII] are redshifted by $\lesssim$ 70km s^{-1} in the nuclear bin of the 120° slit relative to their velocity in the nuclear bin of the 30° slit.

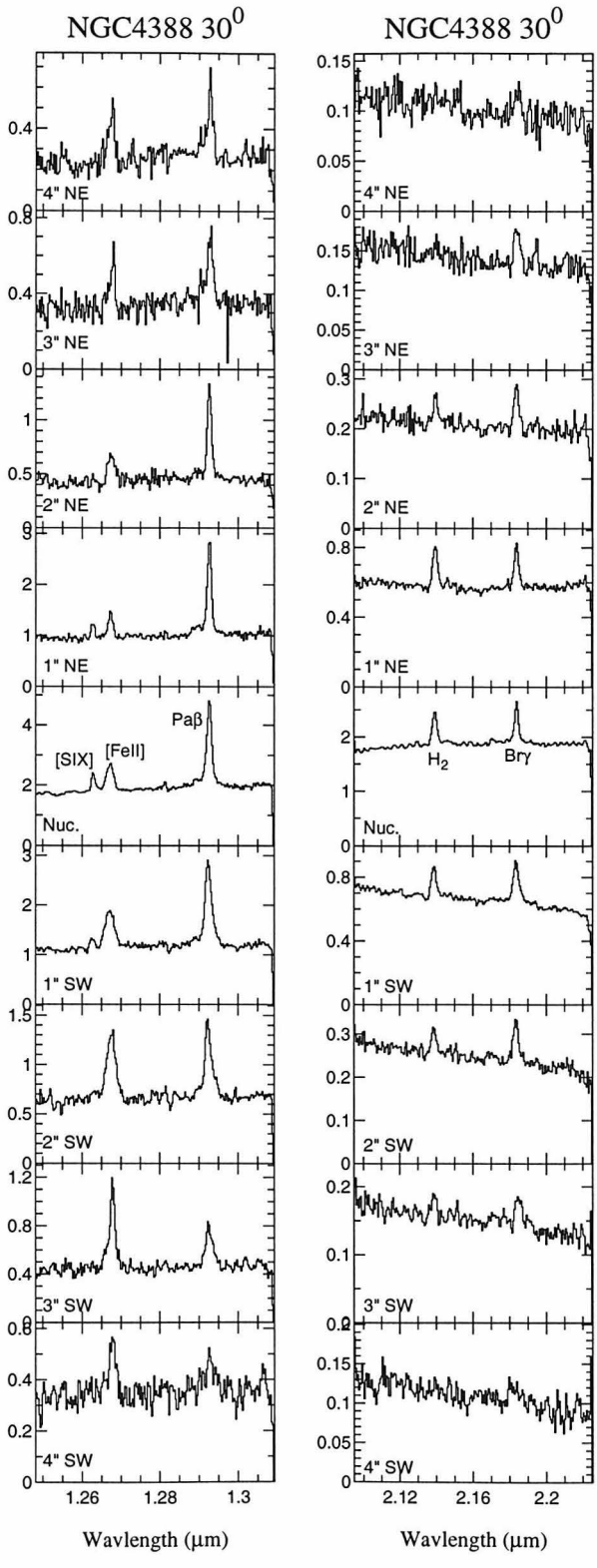

Figure 4.14: Spectra of NGC4388 along the 30° slit. Each spectrum is within a rectangular beam which is 1″ along the slit by the width of the slit (∼ 0.6″). Spatial bins are adjacent. The distance of each spatial bin from the nucleus along a position angle of 30° is indicated in each spectrum.

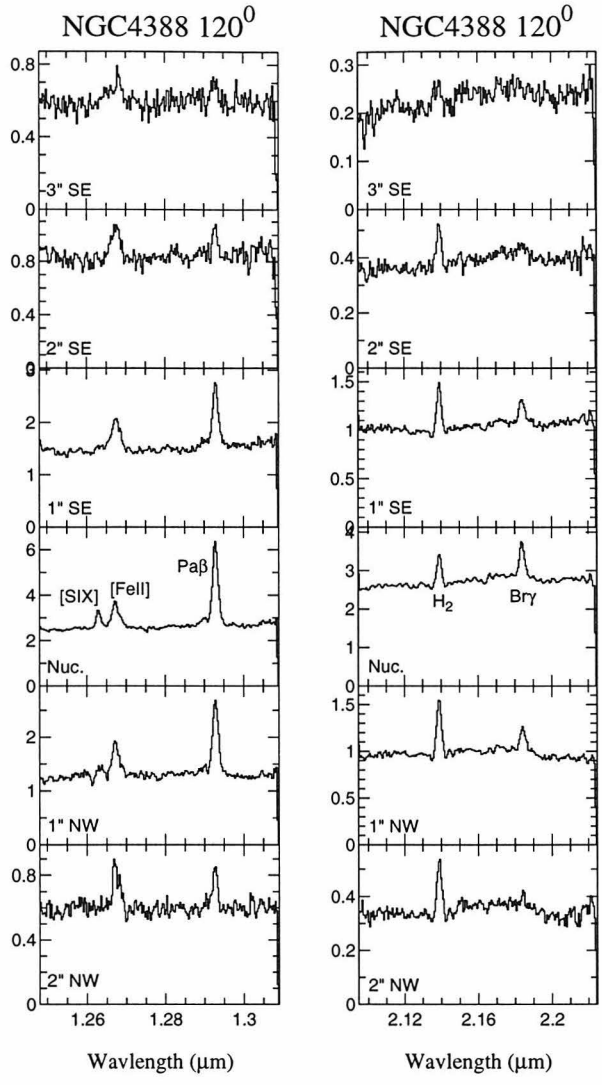

Figure 4.15: Spectra of NGC4388 along the 120° slit. Each spectrum is within a rectangular beam which is 1″ along the slit by the width of the slit (∼ 0.6″). Spatial bins are adjacent. The distance of each spatial bin from the nucleus along a position angle of 120° is indicated in each spectrum.

These discrepancies are probably due to the fact that the rectangular sections of the slits which represent the nuclear bin in each case sample slightly different regions of the galaxy. The asymmetry of the synthetic beam together with any variations in the seeing (which is similar in size to the slit), as well as slight differences in positioning between the two observations (which were made on different days), make it likely that slight differences would be seen between the two observations.

Integrated Line Flux Ratios

Table 4.6 lists the equivalent widths and flux ratios of the infrared lines detected in NGC 4388 along both slits. Figure 4.16 shows the [FeII]/Paβ and H_2/Brγ flux ratios along both slits. On the nucleus, the [FeII]/Paβ flux ratio is about 0.4, a relatively low value for a Seyfert 2 galaxy. The [FeII]/Paβ flux ratio rises off of the nucleus along the directions of both slits; this is opposite from the trend observed in NGC 2110 (Section 4.3.2). It is largest where the [FeII] velocity centers are most discrepant from the Paβ velocity centers, specifically to the southwest along the 30° slit and to the southeast along the 120° slit (see section 4.3.3).

Table 4.6: NGC 4388 Equivalent Widths and Flux Ratios

Pos[a]	Equivalent Width ($10^{-4}\mu$m)					Flux Ratios		
(″)	[FeII]	Paβ	H_2	Brγ	[SIX]	[FeII]/Paβ	H_2/Brγ	[SIX]/Paβ
				NGC 4388, 30° slit				
4	22.8±19.1	19.0±14.9	<7.4	13.0±12.8	...	0.99±0.25	<0.67	...
3	15.5±9.5	18.2±9.1	<7.0	13.3±9.9	...	0.71±0.17	<0.57	...
2	13.4±6.0	26.1±7.0	6.5±3.1	12.7±6.7	...	0.47±0.08	0.56±0.13	...
1	7.7±1.9	25.7±5.5	13.6±4.1	12.7±3.2	3.6±1.0	0.28±0.03	1.05±0.15	0.13±0.02
0	11.2±1.7	26.3±4.2	9.5±1.2	10.6±1.5	4.5±0.8	0.40±0.03	0.88±0.08	0.16±0.02
-1	18.8±4.6	32.2±6.8	8.4±1.6	17.1±3.9	2.4±0.8	0.57±0.04	0.51±0.06	0.07±0.01
-2	31.0±9.4	26.8±7.4	6.3±2.7	14.7±6.5	...	1.13±0.11	0.46±0.09	...
-3	29.7±11.8	17.8±7.1	6.1±3.6	13.6±10.5	...	1.64±0.22	0.49±0.14	...
-4	12.5±6.6	4.8±2.7	<6.9	<11.7	...	2.52±0.84	...	...
				NGC 4388, 120° slit				
2	9.0±2.5	4.0±1.3	12.4±5.3	<4.9	...	2.18±0.53	>2.29	...
1	12.7±2.1	16.8±3.1	14.1±2.9	9.4±2.0	...	0.72±0.07	1.39±0.18	...
0	11.5±1.4	24.1±2.7	8.4±1.1	11.6±1.8	4.4±0.6	0.46±0.03	0.67±0.07	0.17±0.01
-1	10.1±2.0	19.9±3.5	19.6±4.6	8.0±1.7	...	0.50±0.05	2.34±0.25	...
-2	8.9±3.0	7.2±2.2	18.0±5.9	3.2±1.5	...	1.26±0.24	5.23±1.60	...

a Positive positions are towards the position angle of the slit as quoted.

Along the 30° slit, which is coincident with the major axis of the optical [OIII] emission (Corbin, Baldwin, & Wilson 1988), the H_2/Brγ ratio is $\lesssim$1, with the value dropping off slowly away from the nucleus. Along the perpendicular slit, however, the flux of the H_2 line does not drop off nearly as fast as the flux from the Brγ line; i.e., the H_2/Brγ flux ratio rises rapidly with distance from the nucleus. At a distance 2″ southeast and northwest of the nucleus, the Brγ line is < 1/25 of its nuclear strength,

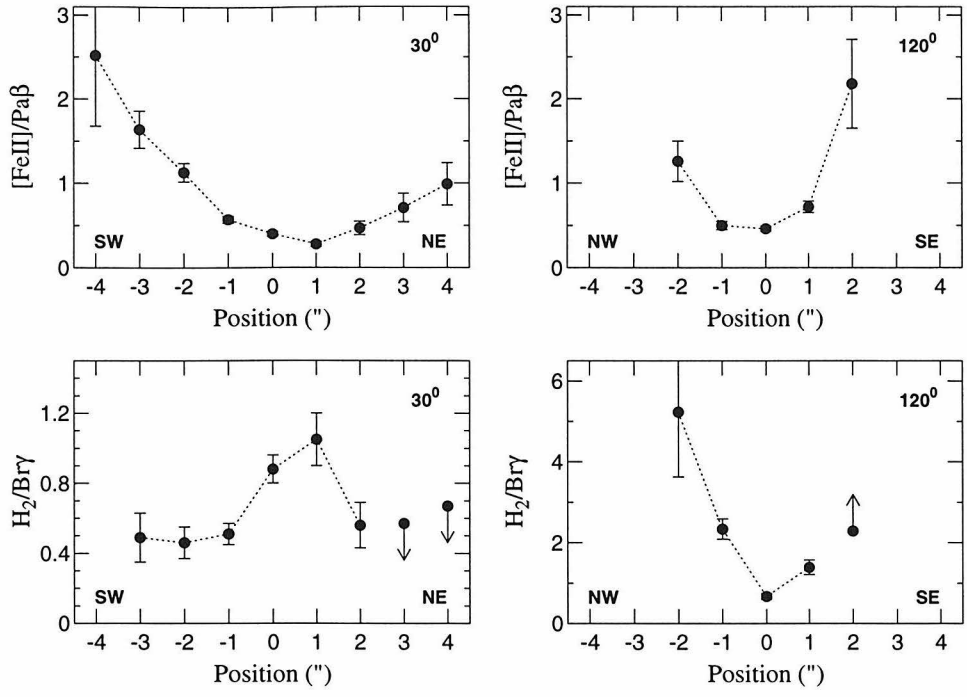

Figure 4.16: Flux ratios for NGC 4388. The two plots on the left are for the 30° slit; the two plots on the right, for the 120° slit.

while the H_2 line is 1/8 of its nuclear strength (see Figure 4.15). This behavior is qualitatively similar to that seen in Mk 1066.

Velocity structure

Figure 4.17 is set of continuum-subtracted position/velocity contour plots for the emission lines observed along the 30° slit for NGC 4388. Velocity is relative to 2525 km s^{-1}, the systemic velocity of NGC 4388 (Petitjean & Durret 1993). There is an enhanced blue wing of Paβ on the nucleus. This emission is probably dominated by the contamination from HeI (λ=1.2786μm) and [FeII] (λ=1.2788μm) discussed in section 4.3.1.

Table 4.7 lists the centroid and width of each line in each spatial bin along both slit. Figures 4.18 and 4.19 shows the velocity centroid of the line profiles as a function of position along the 30° and 120° slits respectively.

Northeast of the nucleus along the 30° slit, the Paβ, Brγ, and [FeII] lines agree in velocity centroid, and show only a small increase in velocity with distance from the

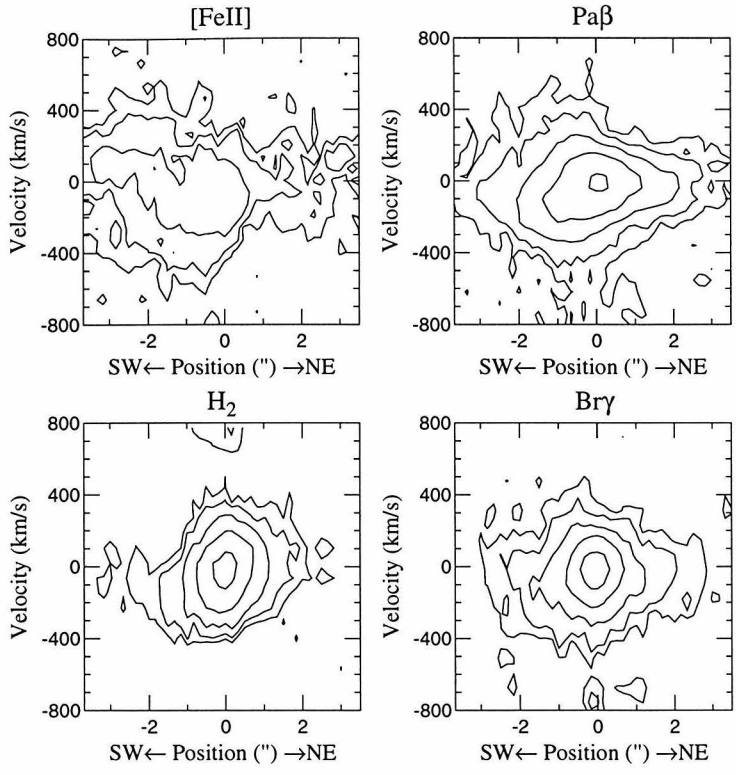

Figure 4.17: Position versus velocity plots for NGC 4388. Position is along a 30° slit. Velocity is relative to 2525 km s^{-1}, the systemic velocity of NGC 4388. Contours in this figure are logarithmic and separated by a factor of two.

nucleus. The H_2 line is slightly redshifted relative to the other lines. Southwest of the nucleus, however, the lines show very different velocity structures. The Paβ, Brγ, and [FeII] lines turn towards increasing velocity with radius to the southwest, while the velocity gradient of H_2 flattens. The [FeII] line curves back more sharply than the Paβ line, until its peak is about 100 km s^{-1} redward of Paβ 3″ south of the nucleus. Brγ also differs from Paβ southwest of the nucleus, increasing in velocity closer to the nucleus than does Paβ.

Along the 120° slit, the infrared line fluxes drop off faster with radius than they do along the 30° slit. Along the 120° slit, there is no evidence for significant velocity changes in the Paβ line. Where it was detected, the velocity peak of the Brγ line is marginally consistent with that of the Paβ line; the [FeII] line is also at a similar

Table 4.7: NGC 4388 Line Centroids and Widths

	[FeII]		Paβ		H_2		Brγ		[SIX]	
Pos[a] ″	Centroid[b] km s^{-1}	FWHM[c] km s^{-1}	Centroid km s^{-1}	FWHM km s^{-1}	Centroid km s^{-1}	FWHM km s^{-1}	Centroid km s^{-1}	FWHM km s^{-1}	Centroid km s^{-1}	FWHM km s^{-1}
				NGC 4388, 30° slit						
4	18±20	353±60	60±20	192±75	...	...	109±53	454±237	...	...
3	35±37	< 150	45±16	334±64	...	...	35±33	424±139	...	...
2	38±23	443±94	2±10	206±30	80±21	197±114	1±18	284±71	...	...
1	-2±13	249±42	4±11	168±40	48±14	338±53	7±14	286±52	-70±17	< 150
0	-42±17	479±67	-12±12	249±43	8±10	306±34	6±15	< 182	-5±28	< 150
-1	-51±12	606±34	-21±11	366±48	-60±11	316±40	23±35	403±84	-110±22	204±95
-2	52±12	624±31	12±28	321±62	-63±19	272±86	-38±15	392±53	...	...
-3	76±17	195±64	16±18	383±70	-50±27	278±173	158±29	524±98	...	...
-4	138±22	357±91	24±27	< 150	...	...	...	...	...	...
				NGC 4388, 120° slit						
2	34±23	601±103	49±19	218±81	3±16	253±80	...	...	...	...
1	10±21	624±75	91±20	291±54	2±10	221±34	56±17	404±41	...	...
0	28±13	380±60	54±5	267±56	-4±11	211±40	54±16	286±62	-29±11	201±36
-1	14±17	332±100	47±6	333±20	-37±9	284±30	71±15	331±58	...	...
-2	13±21	252±140	1±13	240±67	-42±12	249±442	67±34	< 194	...	...

a Positive position is towards the position angle of the slit as quoted.
b Centroids are relative to 2525 km s^{-1}, the systemic velocity of NGC 4388.
c The resolution has been subtracted in quadrature.

velocity as the Paβ line everywhere except for 1″ southeast of the nucleus, where [FeII] is blueshifted by 80 km s^{-1} relative to Paβ. The H_2 line is always blueshifted relative to the Brγ line by 50–100 km s^{-1}.

In addition to different variations in centroid with position, the lines have differing profiles. Along the 30° slit, not only is [FeII] generally wider than Paβ, and at a different velocity centroid southwest of the nucleus, but the asymmetries in the lines are different. For instance, Figure 4.20 shows that 2–3″ southwest of the nucleus the [FeII]/Paβ ratio is preferentially enhanced at redshifted velocities. These asymmetries suggest that systems of clouds with different flux ratios at different velocities are superimposed along the line of sight. Along the 120° slit, the [FeII] line has an enhanced red shoulder to the northwest of the nucleus. Again, the Paβ line is redshifted relative to the [FeII] line, so this enhanced red shoulder may correspond to a component which is associated with the Paβ peak.

Comparison with other observations

Filippenko & Sargent (1985) report a faint broad (Full Width at "Zero Intensity" of 6000 km s^{-1}) Hα line on the nucleus, while Shields & Filippenko (1988; 1996) report

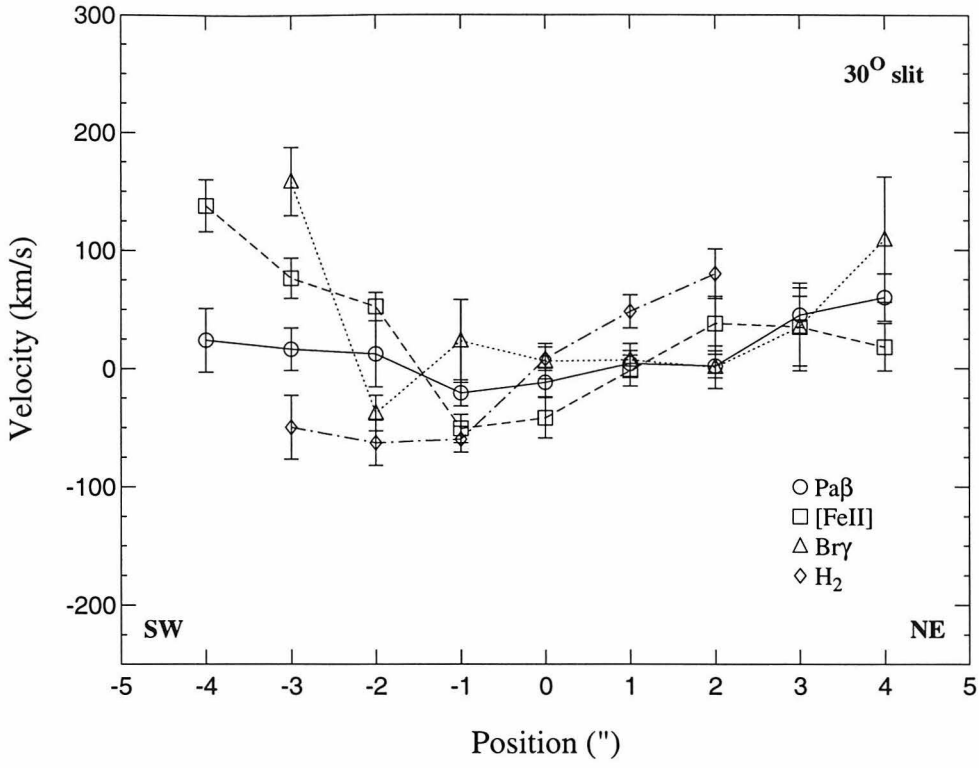

Figure 4.18: Velocity centroid of each line versus position along the 30° slit for NGC4388. Positive distance is to the northeast.

the detection of a broad line in scattered Hα flux within 5″ of the nucleus. Figures 4.14 and 4.15 show no convincing evidence of a broad Paβ or Brγ line. The flux of a FWHM$\sim$ 2700km s^{-1} broad Paβ line on the nucleus is $< 3 \times 10^{-15}$ erg cm^{-2} s^{-1}, corresponding to an upper limit in its equivalent width of $1.6 \times 10^{-3} \mu$m.

Petitjean & Durret (1993) report on optical spectroscopy in slits oriented at a number of position angles, including two angles, 0° and 60°, which straddle our 30° slit. To the north and east, within 5″ of the nucleus, the optical lines show a shallow gradient to the red with all line velocities within 100 km s^{-1} of the systemic velocity, consistent with the infrared emission lines. Optically, this gradient continues to the south and west, with lines more distant from the nucleus at lower velocity, in contrast to the increasing velocity seen in infrared Brγ and [FeII] emission.

In order to compare the infrared spectroscopy with radio maps of NGC 4388, it is important to register the slit with the radio coordinates. Given that the optical

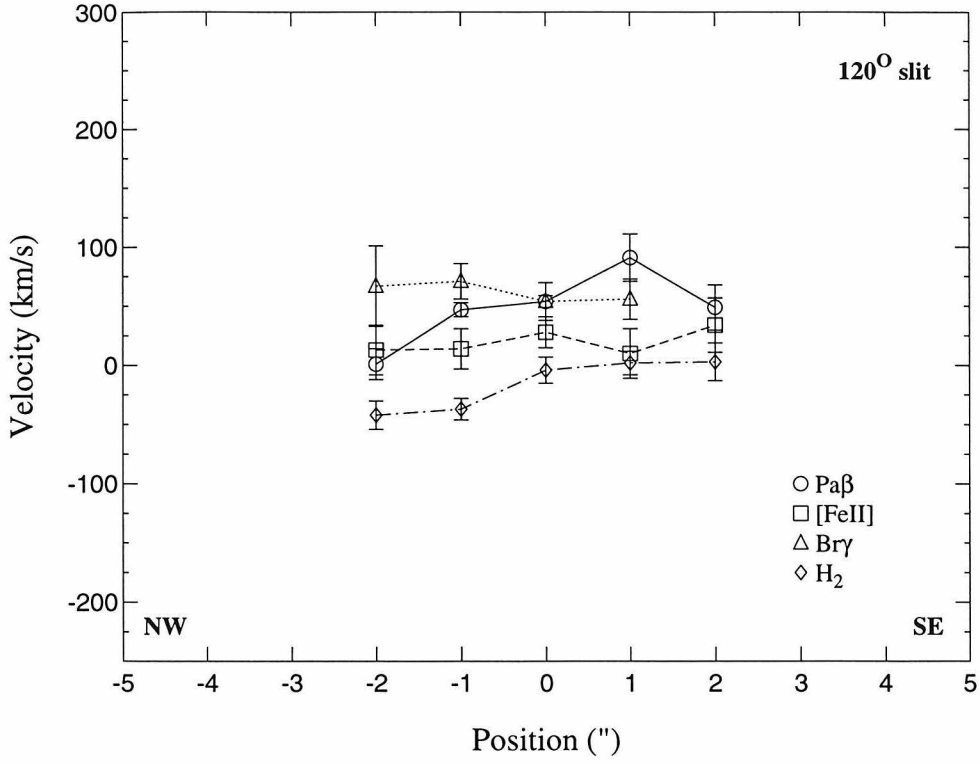

Figure 4.19: Velocity centroid of each line versus position along the 120° slit for NGC4388. Positive distance is to the southeast.

continuum and lines (Corbin, Baldwin, & Wilson 1988; Colina *et al.* 1987) show complicated morphologies, it is not necessarily true that the peak of the flux distribution at one wavelength will be coincident with the peak at another wavelength. Based on the offset between the centroid of the IR continuum image of NGC 4388 obtained with the spectrometer and a star from the Hubble Guide Star Catalog 3′ away, which was used as a guide star for the observations, the peak of the infrared continuum emission corresponds to the brighter, northeastern radio peak of two peaks separated by $\sim 2''$ in the 4.86 GHz map of Hummel & Saikia (1991).

As with Mk1066 (section 4.3.1), there is a spatial correspondence in NGC 4388 between enhanced [FeII] emission and extended radio emission. To the southwest close to the extended radio emission (Hummel & Saikia 1991), the [FeII]/Paβ ratio increases to values > 1.5 (see Figure 4.16), whereas within $1''$ of the nucleus the [FeII]/Paβ ratio is $\lesssim 0.5$. To the northeast, the [FeII]/Paβ ratio is also higher than it

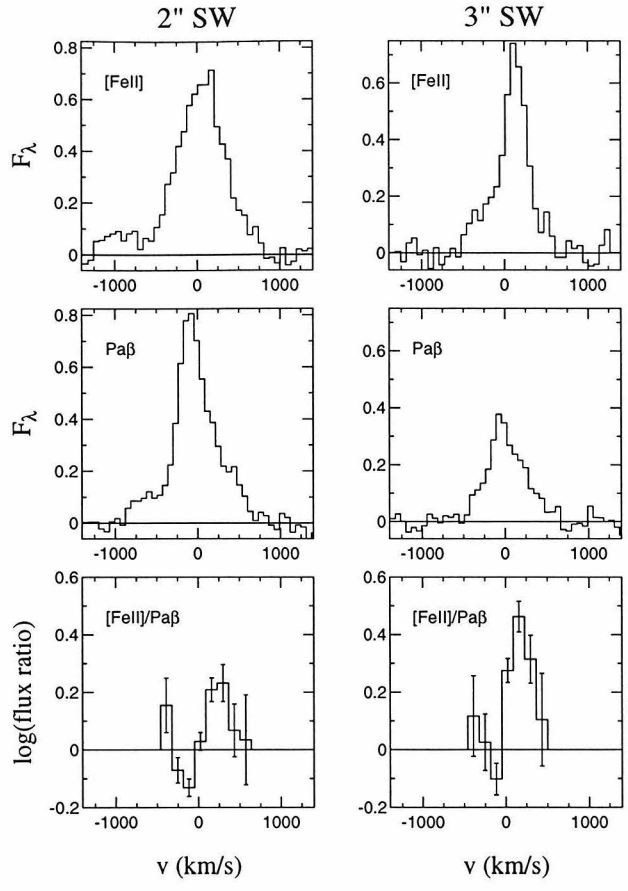

Figure 4.20: Line profiles of [FeII] and Paβ in NGC4388 2-3″ southwest of the nucleus on the 30° slit, and the log of the [FeII]/Paβ ratio as a function of velocity. Points with greater than 50% uncertainty in the flux ratio have been omitted from the latter plot.

is on the nucleus, but is still not as large as the values to the southwest. Additionally, to the southwest the [FeII] line profiles are most disparate from the Paβ lines profiles, where the peak of the [FeII] emission is redshifted relative to the peak of the Paβ emission.

[FeII] and H_2 emission mechanisms

The velocity field of NGC 4388 is known to be complicated. There is a rotating disk with major axis at position angle $\sim 60°$ and inclination $\sim -70°$ (Petitjean & Durret 1993). However, in addition to this, there is blueshifted gas out of the plane of the galaxy to the north and south, as well as other localized sites within 20″ where the velocities of the gas observed with optical spectroscopy is discrepant from the rotation (Corbin, Baldwin, & Wilson 1988).

In the infrared, we are probably observing at least two kinematic components within 4″ of the nucleus of NGC 4388. One kinematical component is the rotating disk, which is responsible for the velocities of the lines in Figure 4.18 northeast of the nucleus, and for the velocities of the Paβ and H_2 lines southwest of the nucleus. These velocities match most closely the velocities of the optical lines which Petitjean & Durret (1993) identify with the rotation curve of the galaxy.

In addition to this rotating component, there may be a receding outflow to the southwest, associated with the radio emission (Hummel & Saikia 1991). This receding outflow has a higher [FeII]/Paβ ratio than the gas in the disk of the galaxy. Colina *et al.* (1987) observed red components in the [OIII] lines profiles along a 23° slit; to the southwest, the mean [OIII] velocities are redshifted from the peak [OIII] velocities by 50-80km s^{-1}. The Brγ velocities southwest of the nucleus in Figure 4.18 probably include contributions from both the disk and outflow components. They are redshifted relative to Paβ, and relative to optical emission lines that correspond to the rotation of the disk. Additionally, the Brγ/Paβ ratio is higher to the southwest than it is to the northeast (although it is highest on the nucleus). This suggests that the emission associated with the outflow is viewed through substantial extinction in the disk of the galaxy.

The [FeII] emission also increases off the nucleus along the 120° slit which is perpendicular to the putative outflow axis. This increased emission does not correspond to notable differences in emission at other wavelengths. It is likely that this strong [FeII] emission is associated with the disk of the galaxy, as it shares a similar (although not identical) velocity gradient with the other lines (Figure 4.19).

The H_2 emission appears to be originating primarily in the disk of the galaxy, as its velocity as plotted in Figures 4.18 and 4.19 follows closely the Paβ and optical velocities identified with the rotating disk (Petitjean & Durret 1993). The H_2/Brγ emission drops off away from the nucleus along the direction of the radio emission, suggesting that the H_2 emission is not associated with the radio jets or the outflow. Similar to Mk1066, the H_2/Brγ ratio shows a striking increase along the slit perpendicular to the outflow axis. Along this direction, the H_2 emission appears to share a similar spatial

structure to the [FeII] emission. The ratios of both lines to hydrogen recombination lines (Figure 4.16) and the velocity curve of both lines (Figure 4.19) along a position angle of 120° share the same shape (although the H_2 emission increases faster relative to Brγ than the [FeII] emission does relative to Paβ). The mechanism of excitation of the [FeII] and H_2 lines in the disk of NGC4388 at radii of >150pc are probably related.

Summary

1. Strong Paβ, Brγ, [FeII], and H_2 emission is seen from NGC 4388. These lines are observed to be extended by $\sim 8''$ along the major axis of the spatial distribution of optical [OIII] emission. Infrared line emission is seen extended by $\sim 5''$ perpendicular to this direction.

2. We identify a line at the rest wavelength of 1.252μm with the infrared coronal line [SIX]. This line is less spatially extended than the other lines. On the nucleus, its flux is 1/6 the flux of Paβ.

   There is infrared [SIX] coronal line emission on the nucleus with a flux that is 1/6 the flux of Paβ.

3. The [FeII]/Paβ flux ratio is lowest on the nucleus with a value of 0.4. It rises to values $\gtrsim 2$ southwest of the nucleus where the velocity centers of the Paβ and [FeII] lines are most different. The H_2/Brγ flux ratio is highest (>2-3) away from the nucleus along the 120° slit, perpendicular to the major axis of the [OIII] spatial distribution. Along this direction, the H_2/Brγ and [FeII]/Paβ ratios both increase away from the nucleus. Along the 30° slit, the two line ratios show opposite trends from each other, with the H_2/Brγ ratio increasing and the [FeII]/Paβ ratio decreasing with distance from the nucleus.

4. Northeast of the nucleus, the infrared lines in NGC 4388 show structure which is similar to the optical line measured by Petitjean & Durret (1993). Southwest

of the nucleus, the Brγ and [FeII] lines are redshifted relative to Paβ by 50-150 km s^{-1}.

5. In some cases, where different lines have different velocity centroids, there is substructure suggestive that the same velocity components may be present in every line with different strengths. Specifically, southeast of the nucleus where the [FeII] emission is redshifted relative to the Paβ emission, there are enhanced blue wings in [FeII] and enhanced red wings in Paβ.

A possible explanation for the velocity structures seen in the infrared lines is that there are at least two kinematical components. Most velocities are governed primarily by a rotating disk. There may additionally be an obscured redshifted outflow southwest of the nucleus. The coincidence of strong, redshifted [FeII] emission to the southwest may be evidence of shock-excited [FeII] emitting gas associated with this outflow.

4.3.4 Mk3

Mk3 is an S0 galaxy at a systemic velocity of 4046 km s^{-1} (Whittle *et al.* 1988), yielding a spatial scale of 262 pc/″. Narrowband optical imaging with the HST shows that the NLR of the galaxy is S-shaped (Capetti *et al.* 1995). On small spatial scales of $\sim$ 1″, the NLR is at a position angle of 86°. On larger spatial scales of a few arcseconds, the apparent position angle of the NLR is 113° (Pogge & de Robertis 1993). Radio observations at 14.9 GHz show a linear structure oriented at a position angle of 86° (Kukula *et al.* 1993). There are two radio peaks, the stronger one 1.1″ west of the nucleus, the weaker one 0.4″ east of the nucleus. Higher resolution maps of the source at 5 GHz resolve the linear structure into a number of components. In particular, the eastern lobe is resolved into three components aligned along the axis of the source, together with a third component coincident with the core of the galaxy. Mk3 is also quite bright in x-rays, with an x-ray luminosity of 3×10^{42} erg/s (with $H_0 = 75$ km s^{-1} Mpc^{-1}), and a very high absorbing column of 6×10^{23} cm^{-2} (Awaki

et al. 1990). The 0.1–2 keV x-ray source is unresolved with the ROSAT HRI on a scale of $\sim 4''$ (Morse *et al.* 1995).

The reduced 1.29μm and 2.21μm spectra of Mk 3 along a 113° slit are plotted in Figure 4.21, in spatial bins along the slit separated by $1''$. The position angle of the 113° slit was chosen to align with the major axis of the [OIII] distribution on scales of $\sim 1''$ (Mulchaey *et al.* 1996). The [FeII] and Paβ emission lines are visible in the 1.2μm spectra, and the H_2 and Brγ emission lines are visible in the 2.2μm spectra. Note that for these observations, the Brγ line was centered in the K-band spectrum so that the H_2 line is near the blue edge of the spectrum. This may lead to inaccuracies in placing the continuum on the blue side of the H_2, resulting in underestimates of the flux of the H_2 line and any blue wings in the profile of the H_2 line.

The [FeII], Paβ, H_2, and Brγ lines are extended along the slit by $\lesssim 7''$ (1.8kpc). The equivalent width of the nuclear lines are $40 \times 10^{-4}\mu$m for Paβ, $52 \times 10^{-4}\mu$m for [FeII], $16\times10^{-4}\mu$m for Brγ, and $5.1 \times 10^{-4}\mu$m for H_2. These equivalent widths are larger by a factor of $\gtrsim 2$ than what is seen in most Seyfert 2 galaxies (Chapter 5).

Most of the extended line emission is characteristically narrow (FWHM$<$ 500 km s^{-1}), yet on the nucleus the infrared lines are quite broad. The FWHM of the nuclear Brγ line is $\sim$700 km s^{-1}, that of Paβ is $\sim$1000 km s^{-1}, and that of [FeII] is $\sim$1150 km s^{-1}. These lines are also markedly asymmetric, with strong blue wings. The peak of the Paβ line on the nucleus is at a velocity $\sim$ 200 km s^{-1} greater than the line centroid. Although [SIX] is not obvious, it could easily be hidden within the broad blue wings of the [FeII] line profile

While the observed width of the Paβ line on the nucleus is comparable to the FWHM of broad Paβ lines seen in some Seyfert 1 galaxies (Chapter 5), the observed line profiles in Mk3 probably do not indicate the detection of a canonical broad line region, since [FeII] and Paβ lines are both broad and have similar profiles. Because the critical density of [FeII] is only $n_e \sim 10^5 cm^{-3}$, the broad [FeII] emission cannot be produced in a high density ($n_e \sim 10^8 - 10^{10} cm^{-3}$) broad line region. Some or all of the high velocity Paβ line flux is therefore probably coming from the NLR.

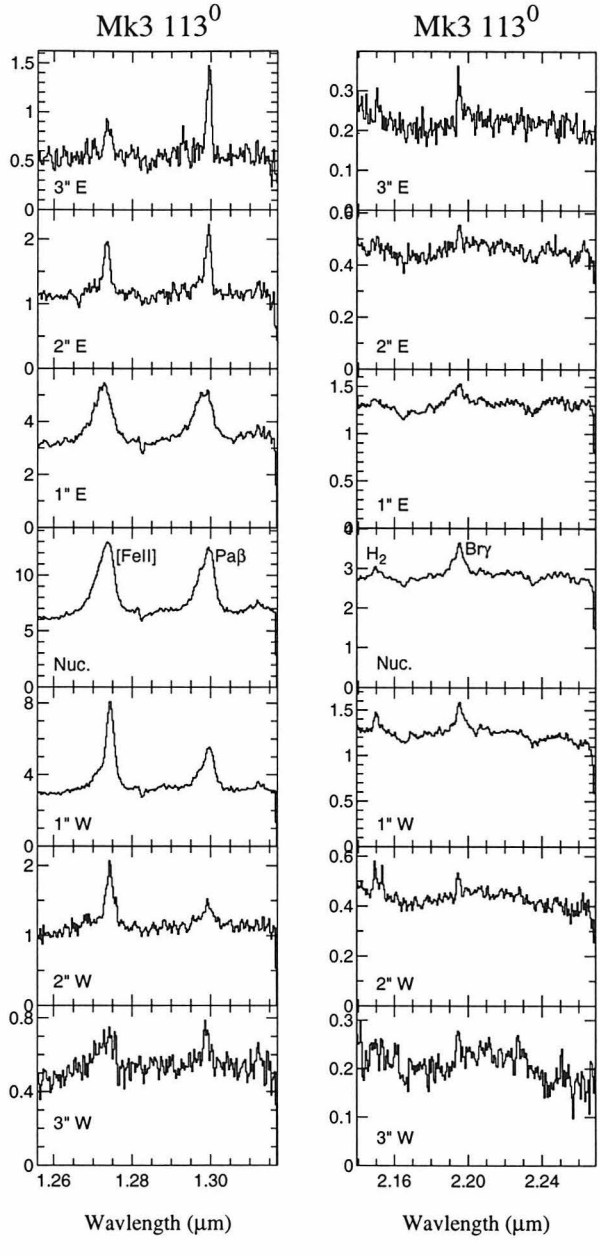

Figure 4.21: Spectra of Mk3 along the 113° slit. Each spectrum is within a rectangular beam which is 1.0″ along the slit by the width of the slit ($\sim 0.6''$). Spatial bins are adjacent. The distance of each spatial bin from the nucleus in an easterly direction is indicated in the spectrum.

Flux Ratios

Table 4.8 lists the equivalent widths and flux ratios of the lines observed in Mk 3. Figure 4.22 shows the flux ratios of [FeII]/Paβ and H_2/Brγ as a function of position along the slit. The H_2/Brγ flux ratio, close to $0.3 - 0.4$ in all but one spatial bin, is relatively low for Seyfert galaxies. The H_2/Brγ flux ratio is anomalously large 2″ west of the nucleus. The strong, double-peaked H_2 emission responsible for this enhanced flux ratio is visible in Figure 4.21. The higher velocity peak is unresolved, and is at a velocity of 450 km s^{-1} relative to the systemic velocity of Mk 3. Although the reality of the peak cannot be ruled out, it is probably the result of an artifact rather than real H_2 emission. If this is the case, then the H_2Brγ ratio would be $\lesssim 1.5$, which is still higher than it is in every other spatial bin.

Table 4.8: Mk 3 Equivalent Widths and Flux Ratios

Pos[a] (″)	Equivalent Width ($10^{-4}\mu$m) [FeII]	Paβ	H_2	Brγ	Flux Ratios [FeII]/Paβ	H_2/Brγ
3	11.6±4.3	24.5±8.6	5.8±4.2	12.0±8.4	0.47±0.10	0.49±0.24
2	13.0±3.5	17.7±4.7	...	4.0±1.4	0.74±0.12	...
1	37.6±4.2	31.3±3.5	3.4±1.2	11.5±2.6	1.17±0.07	0.29±0.11
0	52.2±5.1	39.3±3.2	5.3±0.7	16.7±2.1	1.24±0.04	0.31±0.04
-1	46.3±6.2	26.4±3.0	4.6±0.8	12.8±2.2	1.72±0.08	0.35±0.05
-2	17.9±5.7	9.5±2.9	13.1±4.5	4.4±1.6	1.88±0.43	2.94±0.54
-3	17.6±7.7	4.3±1.7	...	...	3.75±1.15	...

a Positive positions are east towards the 113° position angle of the slit.

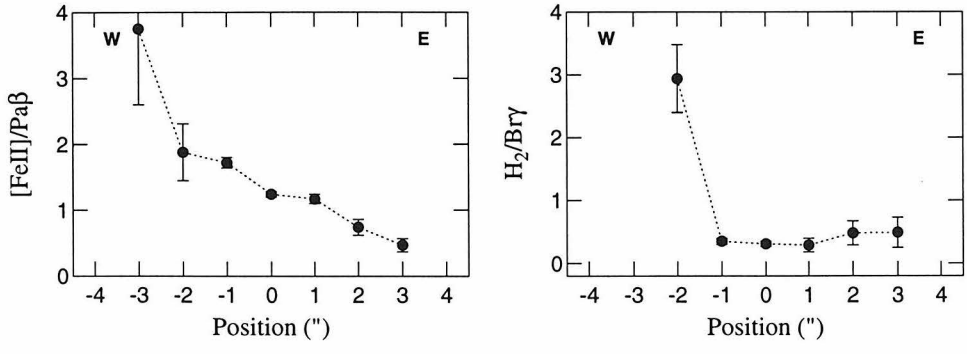

Figure 4.22: Mk3 flux ratios as a function of position along the 113° slit. Positive positions are to the east. Fluxes are integrated over the entire line profile in each spatial bin.

The [FeII]/Paβ ratio changes by a factor of nearly 4 along the slit. This change is a monotonic increase from east to west, although it is poorly determined 3″ west of the nucleus due to the low signal to noise ratio in the Paβ line. This general trend is also visible in Figure 4.23 (section 4.3.4), where the [FeII] emission is suppressed to the east and enhanced to the west relative to the Paβ emission.

Velocity Structure

Figure 4.23 shows position versus velocity plots for each of the four emission lines seen in Mk 3. A smoothed continuum has been subtracted from the data in each case. Velocity is plotted relative to 4046 km s^{-1}, the systemic velocity of Mk 3 (Whittle *et al.* 1988). Table 4.9 lists the velocity centroids and total full widths at half maximum of the lines in each of the 1″ spatial bins for which spectra are plotted in Figure 4.21.

To the east, the Paβ line is narrow and stronger than any narrow Paβ emission to the west. A very shallow velocity gradient at the limit of our resolution is marginally visible in this narrow component. The Paβ line is redshifted by $\sim$ 100 km s^{-1} $\gtrsim$ 3″ east of the nucleus. The Brγ line is not as cleanly detected as the Paβ line, but appears to share a similar velocity structure, although the shallow velocity gradient is not apparent in Brγ. The Brγ is slightly blueshifted relative to the Paβ line east of the nucleus. Both the Paβ and Brγ lines appear to continue a shallow velocity trend from east to west, i.e., the line peak shifts to the blue with distance to the west. The total blueshift of the lines is $\lesssim$ 100 km s^{-1} west of the nucleus.

Table 4.9: Mk 3 Line Centroids and Widths

	[FeII]		Paβ		H_2		Brγ	
Pos[a] ″	Centroid[b] km s^{-1}	FWHM[c] km s^{-1}	Centroid km s^{-1}	FWHM km s^{-1}	Centroid km s^{-1}	FWHM km s^{-1}	Centroid km s^{-1}	FWHM km s^{-1}
3	19±26	382±105	73±12	200±65	72±60	< 191	24±28	265±145
2	-44±16	367±51	-58±36	255±125	...	...	74±23	< 191
1	-363±19	1165±102	-306±14	1201±122	-22±79	710±335	-153±46	899±210
0	-190±13	1137±41	-109±11	991±46	-2±49	639±99	-15±21	564±169
-1	54±13	501±56	-4±13	695±53	81±34	< 191	127±19	446±85
-2	162±16	394±83	-84±61	532±220	165±32	745±430	3±18	< 191
-3	-77±45	1117±248	-75±21	< 155	...	...	...	...

a Positive position is east towards the 113° position angle of the slit.
b Centroids are relative to 4046 km s^{-1}, the systemic velocity of Mk 3.
c The resolution has been subtracted in quadrature.

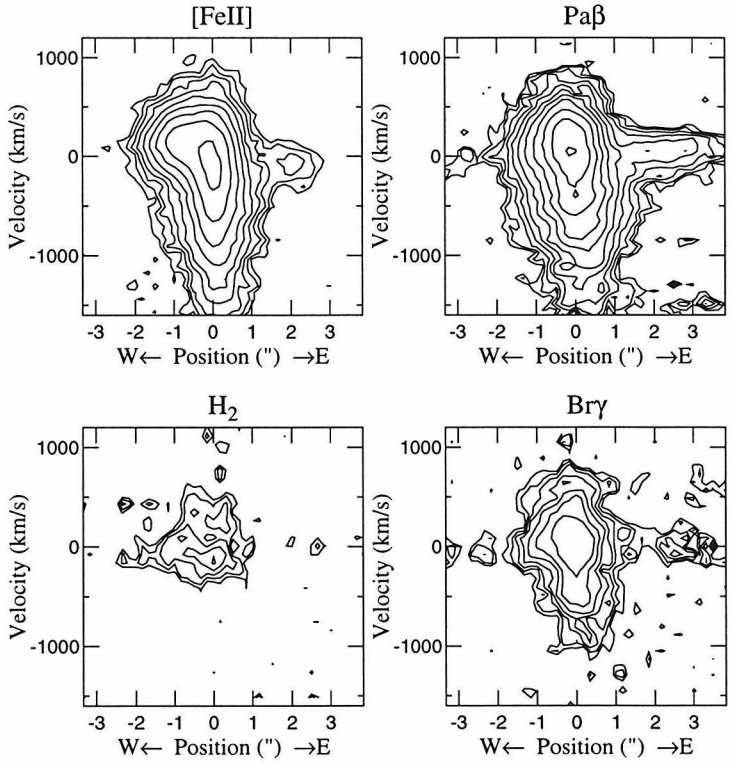

Figure 4.23: Position versus velocity plots for Mk 3. Position is along a 113° slit. Velocity is relative to 4046 km s^{-1}, the systemic velocity of Mk 3 (Whittle *et al.* 1988). Contours are logarithmic, separated by a factor of $\sqrt{2}$.

The velocity structure of the [FeII] line to the east is different from that of the hydrogen recombination lines. To the east of the nucleus and on the nucleus, the peak of the [FeII] line is blueshifted relative to the Paβ and Brγ lines. West of the nucleus, the velocity of the [FeII] line is closer to that of the hydrogen recombination lines. The H_2 line is only barely detected east of the nucleus. West of nucleus by 2″, the H_2 line shows a peculiar double-peaked shape (see Figure 4.21). It is unclear whether this is a real effect of localized H_2 emission, or an artifact.

On the nucleus, the [FeII], Paβ, and Brγ lines all have qualitatively similar profiles. All three lines show strong enhanced emission to the blue of the peak. However, as is visible in Figure 4.24, the profiles differ in detail. The blue wings are not as strong relative to the peak of the line in Brγ, yielding a lower overall FWHM for Brγ than

for the other two lines. The peak of the [FeII] line profile is shifted to the blue of the Paβ line profile by 80 km s^{-1}, and the FWHM of [FeII] is about 100 km s^{-1} larger than the FWHM of Paβ. Since the red side of the [FeII] profile matches Paβ (see Figure 4.24), this apparent peak shift is the result of enhanced emission on the blue wing of [FeII].

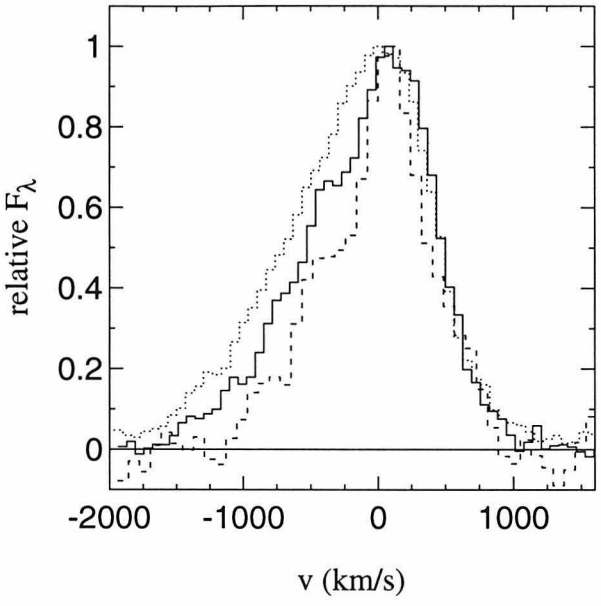

Figure 4.24: Profiles of nuclear lines in Mk 3. The lines are normalized to the same peak flux. The solid line is Paβ, the dotted line [FeII], and the dashed line Brγ.

While the profiles to the east of the nucleus are narrow, Figure 4.23 clearly shows that 1–2″ west of the nucleus the lines are broader, with the FWHM of Paβ line equal to 500–600 km s^{-1}, though not as broad as the lines are on the nucleus. Figure 4.25 shows the profiles of the Brγ, Paβ, and [FeII] lines 1″ west of the nucleus. Two features are apparent from this plot. First, the red wing of the Brγ line is stronger relative to the amplitude of the line core than red wing of Paβ. This may indicate that there is receeding gas obscured behind dust, as the longer wavelength Brγ is less affected by extinction than Paβ. Second, the [FeII]/Paβ ratio is largest with a value of $\sim$ 2.2 at a redshifted velocity near $\sim$ 150 km/s. The blue hump on the Paβ and [FeII] line profiles has an [FeII]/Paβ ratio of about 1, close to the nuclear flux ratio (see section 4.3.4).

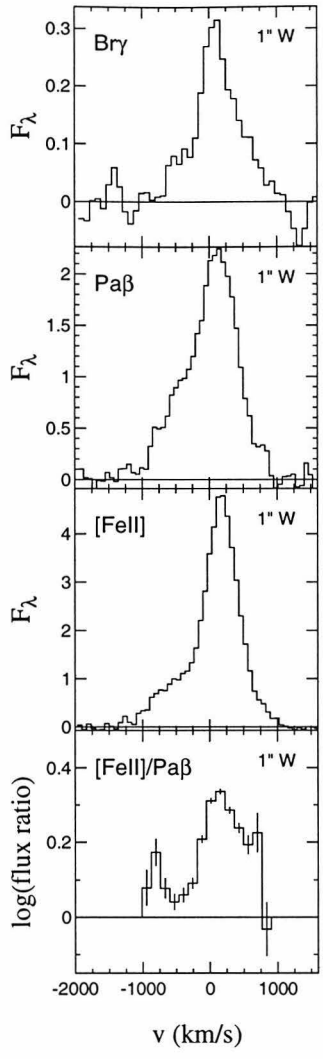

Figure 4.25: Line profiles of Brγ, [FeII], and Paβ, and the log of the [FeII]/Paβ flux ratio as a function of velocity, 1″ west of the nucleus of Mk 3 at a position angle of 293°. Points with uncertainty greater than 20% have been omitted from the latter plot.

Comparison with Other Observations

The velocity gradient seen in the off-nuclear narrow Paβ line is generally consistent with the rotation curve seen in optical Hβ and [OIII] emission by Whittle *et al.* (1988). However, the optical slit position angle is 86°, while the infrared data presented here was obtained through a slit at a position angle of 113°. East of the nucleus, the [OIII] line peaks at 120 km s^{-1}, while west of the nucleus it peaks at -120 km s^{-1}, similar to the limiting off-nuclear velocities of $\pm$100 km s^{-1} in the infrared lines. Whittle *et al.* (1988) also saw a similar increase in the FWHM of the optical Hβ and [OIII] lines near the nucleus of Mk3. This broader emission is blueshifted relative to the

peak of the lines, again consistent with that seen in the infrared lines. In addition, a red wing in the [OIII] and Hβ profiles is similar to the enhanced red emission seen in the infrared lines in Figure 4.25, which was also strongest 1″ west of the nucleus. A Gaussian decomposition of the optical lines placed the relative velocity of the redshifted component at $\sim$ 300 km s^{-1}; our Gaussian decomposition of the infrared lines places the velocity of the reddened component of the infrared lines at somewhat higher velocity, closer to $\sim$ 500 km s^{-1}, although this is uncertain given the complex blended line profiles in Mk 3 (see Figure 4.25).

The spatial location of this red wing is coincident with the stronger of two radio peaks seen at 2cm (Ulvestad & Wilson 1984a). This stronger radio peak is 1.1″ west of the nucleus along a position angle of 86°. The relatively high extinction seen for this reddened component in the infrared Brγ and Paβ lines is consistent with the picture of this radio peak as a lobe coincidental with a receding outflow of ionized gas which is obscured behind the plane of the galaxy. The weaker radio lobe is 0.4″ east of the nucleus along the same position angle. Whittle *et al.* (1988) do not identify any component in the optical spectra with the eastern radio lobe. However, the enhanced blue wings seen on the nucleus in both the infrared and [OIII] emission lines may be part of an approaching outflow associated with the eastern radio lobe.

[FeII] and H_2 Emission Processes

As with Mk1066 and NGC4388, and to a lesser extent NGC2110, the [FeII] emission in Mk 3 shows spatial correlations with the radio emission which suggests that processes involving the radio jet's interaction with circumnuclear gas are significantly enhancing the [FeII] emission. West of the nucleus at the position of the western radio peak (Kukula *et al.* 1993), the [FeII] line shows enhanced redshifted emission, which is also seen in Paβ and Brγ lines as well as in the optical lines (Whittle *et al.* 1988). At the position of this radio peak west of the nucleus, the [FeII]/Paβ ratio is higher than it is to the east of the nucleus where the radio emission is much weaker. This enhanced redshifted emission 1″ west of the nucleus also has a larger Brγ/Paβ flux

ratio, suggesting higher extinction to the region which is the source of the enhanced [FeII] emission. This is consistent with the picture of the region as a receding outflow which is partially obscured by the intervening galaxy.

The eastern radio peak is too close (0.4″) to the nucleus to distinguish infrared line emission spatially coincident with it from emission directly on the nucleus. However, if the two knots of radio emission represent the radio lobes of a biconical outflow, the enhanced blue wings in the infrared and optical lines on the nucleus may in fact be correlated with the second radio lobe. Higher resolution 5 GHz maps of Mk3 (Kukula *et al.* 1993) resolve the eastern lobe into a number of individual linearly spaced components. The infrared lines near the nucleus show a complicated, evidently multi-component structure in velocity (see Figure 4.21). The multicomponent nature of the emission in both radio emission (in space) and infrared line emission (in velocity) is consistent with the identification of the broad blue wings on the infrared lines near the nucleus with the eastern radio lobe. The [FeII] emission on the nucleus is blueshifted relative to the Paβ emission, suggesting that the [FeII]/Paβ flux ratio may be enhanced at the position of the eastern radio peaks. Given this spatial correspondence, it is likely that the [FeII] emission is enhanced by fast shocks resulting from the interaction between the radio jet and the circumnuclear gas.

Except for the anomalously high value 2″ west of the nucleus, the H_2/Brγ ratio is lower in Mk3 than it is in most Seyfert galaxies. West of the nucleus, the narrow Paβ and perhaps Brγ emission may be associated with the rotation of a galactic disk, based on similarities with optical lines (Whittle *et al.* 1988). At these positions, the H_2 emission is suppressed relative to the Brγ emission, indicating that in contrast to the other galaxies discussed in this paper, the circumnuclear disk of the galaxy contains less warm molecular gas in comparison to ionized gas.

Summary

1. At a position angle of 113°, the infrared line emission is observed to be extended by $\lesssim 7''$.

2. There is a FWHM$\sim$1000 km s^{-1} blue wing visible on the nucleus of Mk 3, most most prominent in [FeII] and Paβ but also seen in Brγ. There is a red wing on the line profiles, arising from a region of relatively high extinction, $\sim 1''$ west of the nucleus. This red wing corresponds to a redshifted component seen in optical emission (Whittle *et al.* 1988). Both wings are spatially consistent with the position of two radio peaks (Kukula *et al.* 1993).

3. The Paβ and Brγ narrow line peaks may follow a barely resolved smooth rotation curve which lies at +100 km s^{-1} east of the nucleus and -100 km s^{-1} west of the nucleus. East of the nucleus, the Brγ line is marginally blueshifted relative to Paβ. The [FeII] emission is blueshifted relative to the Paβ emission both east of the nucleus, and significantly so on the nucleus.

4. The [FeII]/Paβ flux ratio monotonically increases from $\sim$ 0.5 3″ east of the nucleus to $\sim$ 2 2″ west of the nucleus. The H_2/Brγ flux ratio is close to 0.3 – 0.4 everywhere except where it is anamalously high, possibly as a result of an artifact, 2″ west of the nucleus.

We propose that emission associated with an outflow of ionized gas contributes significantly to the infrared line emission in Mk 3. The [FeII]/Paβ ratio is enhanced in components identified with this outflow and coincident with the 2cm radio lobes, suggesting a possible shock contribution to the [FeII] emission. The low H_2/Brγ ratio indicates that in contrast to other Sefyert galaxies, the circumnuclear disk is relatively depleted in warm molecular gas.

4.4 General Discussion

4.4.1 [FeII] Emission Processes

One obvious conclusion from the data presented here is that the [FeII]/Paβ ratio in Seyfert galaxies varies significantly with position on scales of $\leq 1''$. Of the four galaxies observed, each showed a different dependence of [FeII]/Paβ on position,

whether it was monotonically increasing across the nucleus (Mk3), highest at the nucleus (NGC2110), lowest at the nucleus (NGC4388), or close to constant with point-to-point variations (Mk1066). These data show that flux ratios integrated over large nuclear beams may be of limited value for drawing conclusions about the excitation processes of the infrared lines. The flux ratios are observed to vary significantly on scales of $\lesssim 10^2$ pc.

Circumnuclear starbursts and processes associated with the central AGN directly have both been implicated in the generation of [FeII] emission lines seen in Seyfert galaxies (e.g., Moorwood & Oliva 1988; Mouri *et al.* 1993). Our data in general support the active nucleus as the power source of [FeII] in the Seyfert galaxies observed here. Despite the differences in the details of the velocity structure of the infrared lines, the velocity gradients of [FeII] tend to match those for the other lines. The [FeII] line can generally be kinematically associated with other spectral features linked with the nuclear activity (e.g., [OIII]), or sites of enhanced radio emission. The one exception is the extended [FeII] emission along position angle 120° in NGC4388.

There are two proposed mechanisms for [FeII] emission associated with the AGN itself. Because the ionization potential of Fe^+ is only 16.2 eV, the [FeII] line will be strong in partially ionized regions. If clouds illuminated by the Seyfert nucleus have a high enough column density, only that side of the cloud facing the nuclear ionizing source will be fully ionized. Because the ionization cross section for high-energy x-rays is relatively small, x-rays can penetrate deeply into these dense clouds, creating large warm partially ionized regions suitable for [FeII] emission (Graham *et al.* 1990). Fast shocks can also produce partially ionized regions heated to 6000 K (Shull & Draine 1987). Models indicate that these shocks may also destroy dust grains (Seab & Shull 1983). Because much of the iron in the local interstellar medium is locked up in dust grains, the destruction of those grains would enhance the gas phase Fe abundance, thereby increasing the infrared [FeII] emission.

Simpson *et al.* (1996b) saw a slightly stronger correlation between infrared [FeII] and 6cm radio emission than between Paβ and 6cm emission. Based on the difference in the correlations, Simpson *et al.* concluded that $\sim$ 20% of the [FeII] emission in

Seyfert galaxies is due to the action of fast shocks, and that the bulk of it is due to x-ray photoionization. Photoionization models indicate that a solar abundance of iron illuminated by the nuclear source would actually create a [FeII]/Paβ ratio which is several times higher than what Simpson *et al.* observe. From this, they conclude that shocks cannot be primarily responsible for the [FeII] emission observed in Seyfert galaxies, because shocks would destroy dust grains, increasing the gas phase abundances of iron and creating [FeII]/Paβ line ratios significantly larger than what is typically observed.

The data presented here for Mk 1066, NGC 2110, NGC 4388, and Mk 3 generally support the conclusions of Simpson *et al.* Except for the nucleus of NGC 2110, the flux ratios observed at various positions in the galaxies are within the range of those seen in integrated nuclear spectra by Simpson *et al.* While the [FeII]/Paβ flux ratios show variations with position, in most cases the [FeII] emission tends to be spatially associated with Paβ emission, and the primary component of [FeII] often shares the same velocity structure as the Paβ line. Thus, most of the [FeII] emission probably comes from gas physically and kinematically associated with the Paβ emission. Since optical hydrogen recombination lines are believed to originate in NLR clouds illuminated by the nucleus, much of the [FeII] emission may likewise arise from clouds illuminated by the nucleus. One exception is NGC 2110, with its very large [FeII]/Paβ ratio on the nucleus. The [FeII] emission on the nucleus of this galaxy may be dominated by shocks.

The variation in the [FeII]/Paβ flux ratios and the differences in the [FeII] and Paβ line profiles can be explained by additional [FeII] emission produced through the action of shocks associated with the expanding radio plasma. In all four of the galaxies, features were identified in the [FeII] emission line profile which appeared to correspond to the spatial position of peaks of non-thermal radio emission. In many cases, these features showed relatively high [FeII]/Paβ ratios. Also, in Mk 3 and NGC 4388, the [FeII] emission was enhanced relative to the Paβ emission, or showed the largest kinematical differences from the Paβ emission, at positions spatially coincident with radio peaks. This suggests that processes associated with radio jets are contributing

measurably to the [FeII] emission. The most probable explanation of this is fast shocks resulting from the interaction of outflowing radio plasma with the circumnuclear gas.

4.4.2 H_2 Emission Processes

Molecular hydrogen emission can result from ultraviolet fluorescence of hydrogen molecules in photodissociation regions illuminated by photons from OB stars or by a nuclear UV continuum source. Alternatively, the H_2 emission may be excited thermally, through either slow (v< 25 km/s) shocks (Shull & Draine 1987), or through x-ray heating of dense molecular clouds (Draine & Woods 1990). Observations of the flux ratio between H_2 (v=1-0 S1) (λ=2.1213μm) and H_2 (v=2-1 S1) (2.2471μm) rule out ultraviolet fluorescence as a significant mechanism in most Seyfert galaxies (Moorwood & Oliva 1990).

In all four of the galaxies discussed here, we have identified features in [FeII] and hydrogen recombination line profiles which we associate with outflows or other interactions with radio lobes and jets. Except for NGC 2110, these features are weaker or invisible in the H_2 line profile; the kinematics of the H_2 are usually better explained by galactic rotation. In addition, in those two galaxies where we have data perpendicular to the outflow axis (Mk1066 and NGC4388), the H_2 is significantly more extended than the atomic hydrogen recombination lines.

Although x-ray heating of molecular clouds that cross into the ionization cones can give rise to the extended H_2 emission along the cone axes, it is unlikely that the nucleus is responsible for the enhanced H_2 emission along the axis perpendicular to the cones. According to the standard model of Seyfert galaxies, the radiation from the central source is obscured except along the axis of the ionization cones; thus, nuclear x-rays cannot penetrate significantly into the gas perpendicular to the cone axis to produce the extended H_2 emission. While these X-rays would heat the inner face of the obscuring molecular torus, the size of that torus is believed to be on the order of a few parsecs, so this cannot explain the extended H_2 emission that we observe. Also, if molecular hydrogen emission does emerge from photodissociation regions heated

by x-rays from a central source, we would expect strong Brγ emission at the same positions as the H_2 emission.

Shocks driven directly or indirectly by the nucleus are another possible explanation for the excitation of the H_2 emission. Shocks moving through a higher density medium will be slower than those moving through a lower density medium. Such slow shocks moving through high density molecular clouds in the disk of the galaxy could excite molecular hydrogen emission. Where the shocks encounter lower density clouds, they should be faster, and produce substantial [FeII] emission. The [FeII]/Paβ ratio does rise with distance from the nucleus, at least initially, in both Mk1066 and NGC4388 perpendicular to the primary direction of extended high-excitation gas. Alternatively, secondary shocks in molecular clouds circumscribing radio outflows might give rise to enhanced H_2 emission. This process might produce the differing [FeII] and H_2 spatial morphologies observed in NGC 1068 by Blietz *et al.* (1994). One problem with this scenario is that, in contrast to the axis of ioniziation cones where outflowing radio plasma may be accelerated by radiation pressure from the nucleus into the surrounding gas, there is nothing to drive nuclear shocks to distances of $\sim$1 kpc perpendicular to the cone axis.

It is also possible that there is some local source of heating which is contributing to the H_2 emission. NGC 4388 has a bar oriented at position angle $\sim 90°$ (Corbin, Baldwin, & Wilson 1988). Dynamical processes associated with this bar may be creating shocks which give rise to the observed H_2 emission. In Mk1066, it is also possible that the bulk motions of clouds which do not move completely with the rotation of the disk are colliding with other clouds, creating slow shocks which excite the H_2 emission. Another local source which might give rise to the H_2 emission is young stars heating molecular clouds. While this may contribute to the H_2 emission, it is unlikely to be the sole dominant source, as the H_2/Brγ ratios observed in the extended H_2 gas tend to be higher than the values $\lesssim 0.5$ typically observed in starburst galaxies (Moorwood & Oliva 1988; Moorwood & Oliva 1990; Kawara *et al.* 1988).

4.5 Summary and Conclusions

1. We have observed strong infrared Paβ, Brγ, [FeII], and H_2 line emission which is spatially extended on scales of a few hundred parsecs in Mk1066, NGC2110, NGC4388, and Mk3.

2. We have detected the near infrared coronal line [SIX] (λ=1.2524μm) in the nucleus of NGC4388. In contrast to the other infrared lines, this line is only marginally spatially extended. There is no apparent [SIX] emission from Mk 1066, NGC 2110, or Mk 3.

3. While often showing similar velocity trends over the central few arcseconds, the [FeII], H_2, and H^+ lines have profiles which differ in detail from each other over the full spatial range probed by these observations. The peaks of lines are shifted relative to each other at some spatial positions in some galaxies, and some species show enhanced blue and red wings relative to other species.

4. The [FeII]/Paβ and H_2/Brγ flux ratios can vary dramatically on scales of 10^2 pc near the nuclei of Seyfert 2 galaxies.

5. The [FeII] emission appears to be associated with the nuclear activity in the galaxies, not requiring the invocation of a circumnuclear starburst in any of these four galaxies. The [FeII] can be kinematically and spatially linked to processes dominated by the active nucleus. In all of these galaxies, there are correlations between features in the [FeII] emission and both radio jets and optically identified outflows, suggesting that some [FeII] emission is produced by fast shocks resulting from interactions between radio jets and circumnuclear gas.

6. The H_2 emission, although peaked on the nucleus, is relatively strong compared to hydrogen recombination and [FeII] emission perpendicular to the axis of ionization cones or the major axis of high-excitation gas in Mk 1066 and NGC 4388. The spatial distribution and line profile of H_2 generally differs from that of [FeII].

A local source such as bar-driven shocks or circumnuclear star formation may be partially responsible for the H_2 emission in these galaxies.

Chapter 5

Summary of Data

5.1 Introduction

This chapter presents the longslit infrared spectroscopic data of 18 Seyfert galaxies obtained for this thesis which have not been presented in Chapters 3 and 4. There is a brief discussion for each object, in addition to tables which summarize the fluxes and profiles of the lines observed in all 23 objects. This chapter forms the core of a paper to be submitted to *The Astrophysical Journal Supplement Series*. All of the data from this chapter and previous chapters will be summarized and analyzed in Chapter 6.

5.2 Observations and Data Reduction

Table 5.1 lists all of the observations obtained for this thesis, including those observations which were discussed in greater detail in Chapters 3 and 4. The observations and reductions were performed according to the procedure described in Chapter 2. The goal of the project was to search for spatially extended near-infrared line emission, and to relate structures in this emission to structures observed at optical and radio wavelengths in the hope of shedding new light on the interaction of the Seyfert nucleus with the circumnuclear gas. Because desirable targets were those likely to show extended emission, Seyfert galaxies visible from Palomar Observatory ($\delta > -20°$) were

selected with redshift cz<5400 km s^{-1}, corresponding to a spatial scale of 350 pc/″ for H_0=75 km s^{-1} Mpc^{-1}. Galaxies with known extended optical ionized gas were preferentially observed, followed in priority by galaxies with spatially extended radio emission on scales of $\gtrsim$ 1″. The final sample of galaxies observed includes 11 Seyfert 1.x (1, 1.5, and 1.9) galaxies and 12 Seyfert 2 galaxies. This sample is not meant to address the presence of infrared emission from Seyfert galaxies in a statistical sense. Rather, these data are suitable to test correlations between infrared, optical, and radio emission in a sample of nearby, bright galaxies.

Table 5.1: Observation Log

Name	Alt. Name	Type	v^b_{sys} km s^{-1}	λ (μm)	On-Src t_{int}	Slit PA	Res. km s^{-1}	psf FWHM	Flux[a] Unc.	Date of Obs.	Fig.
NGC262	Mk348	2	4540	1.29	2400s	15°	237±15	0.8″	25%	95/09/08	5.15
				2.18	1800s	15°	302±19	0.7″	25%	95/09/08	
				1.29	1800s	270°	166±15	~ 0.6″	35%	94/08/22	5.16
				2.18	1800s	270°	228±19	~ 0.6″	35%	94/08/22	
NGC449	Mk1	2	4780	1.29	2400s	156°	250±15	0.7″	25%	95/09/09	5.9
				2.18	1800s	156°	308±19	0.6″	25%	95/09/09	
Mk993	UGC00987	1/1.9	4658	1.29	2400s	150°	234±15	0.8″	25%	95/09/10	5.22
				2.18	1800s	150°	297±19	0.7″	25%	95/09/10	
Mk359	UGC01032	1.5	5012	1.29	2400s	20°	234±15	$\lesssim$ 0.7″	35%	95/09/10	5.14
NGC591	Mk1157	2	4547	1.29	2400s	152°	237±15	0.7″	75%	95/09/08	5.10
				2.18	1800s	152°	302±19	0.7″	100%	95/09/08	
Mk1066	UGC02456	2	3625	1.28	2400s	135°	242±15	0.7″	20%	95/09/09	...[c]
				2.17	2400s	135°	289±19	0.6″	25%	95/09/08	
				1.28	2400s	45°	228±15	0.6″	20%	95/09/10	
				2.17	2400s	45°	289±19	0.5″	25%	95/09/10	
NGC1667		2	4547	1.29	2400s	164°	235±15	~ 1.5″	30%	96/03/08	5.26
NGC2110		2	2342	1.28	2400s	160°	229±15	~ 1.1″	20%	96/01/05	...[c]
				2.16	1800s	160°	285±19	~ 1.1″	50%	96/01/05	
Mk3		2	4046	1.29	3000s	113°	243±15	~ 1.0″	20%	96/11/06	...[c]
				2.20	1800s	113°	292±19	~ 1.0″	20%	96/11/07	
NGC2273	Mk620	2	1840	1.27	2400s	120°	230±15	1.6″	50%	96/03/08	5.17
				2.15	1800s	120°	292±19	1.3″	30%	96/03/08	
NGC2992		2/1.9	2314	1.28	2400s	15°	229±15	~ 1.8″	25%	96/03/08	5.1
				2.16	1800s	15°	290±19	~ 1.8″	25%	96/03/08	
				1.28	2400s	118°	229±15	1.7″	25%	96/03/07	5.2
				2.16	600s	118°	299±19	1.5″	30%	96/03/07	
NGC3227		1.5	1157	1.27	1800s	40°	229±15	~ 1.0″	100%	95/03/14	5.12
				2.16	1200s	40°	268±19	~ 1.0″	100%	95/03/14	
NGC3516		1.5	2649	1.28	2400s	35°	227±15	1.8″	25%	96/03/08	5.19
				2.16	1800s	35°	299±19	< 1.8″	25%	96/03/08	
NGC4051		1	725	1.27	1800s	81°	248±15	~ 1.3″	100%	95/03/15	5.11
				2.16	1000s	81°	289±19	~ 1.3″	100%	95/03/15	

Table 5.1: Observation Log (continued)

Name	Alt. Name	Type	v^b_{sys} km s^{-1}	λ (μm)	On-Src t_{int}	Slit PA	Res. km s^{-1}	psf FWHM	Flux[a] Unc.	Date of Obs.	Fig.
NGC4151		1.5	997	1.27	600s	60°	236±22	$\sim 1.3''$	50%	94/05/25	...[c]
NGC4388		2	2525	1.28	2400s	30°	229±15	$\sim 0.8''$	25%	96/01/03	...[c]
				2.16	2400s	30°	261±19	$\sim 0.7''$	25%	96/01/03	
				1.28	2400s	120°	244±15	$0.8''$	25%	96/04/08	
				2.16	1800s	120°	303±19	$0.7''$	25%	96/04/08	
NGC5273		1.9	1054	1.28	1200s	10°	173±15	$\sim 0.6''$	50%	94/08/20	5.23
NGC5347		2	2335	1.28	2400s	270°	168±15	$\sim 0.8''$	60%	94/08/21	5.27
				2.17	1200s	270°	233±19	$\sim 0.7''$	40%	94/08/22	
NGC5929		2	2561	1.28	2400s	50°	229±15	$0.8''$	50%	95/09/07	5.7
				2.16	1800s	50°	289±19	$0.7''$	50%	95/09/07	
				1.28	2400s	140°	237±15	$0.9''$	25%	95/09/09	5.8
				2.16	1800s	140°	299±19	$0.9''$	25%	95/09/09	
NGC6814		1	1563	1.27	1500s	180°	222±15	$\sim 1.6''$	35%	94/05/25	5.24
				2.16	600s	180°	280±19	$\sim 1.6''$	100%	94/05/25	
NGC7450	Mk1126	1.5	3191	1.28	2400s	107°	246±15	$0.9''$	25%	95/09/10	5.25
				2.16	1800s	107°	311±19	$0.8''$	25%	95/09/10	
NGC7469	Mk1514	1	4898	1.29	1200s	240°	166±15	$\lesssim 1.1''$	50%	94/07/26	5.21
				2.19	1500s	240°	249±19	$\lesssim 1.1''$	50%	94/07/27	
NGC7682		2	5120	1.29	2400s	60°	237±15	$< 1.6''$	50%	95/09/07	5.18
				2.18	1800s	60°	301±19	$< 1.6''$	40%	95/09/07	
				2.27	1800s	60°	283±19	$< 1.6''$	25%	95/09/08	

a The uncertainty in the flux calibration. This does not reflect the uncertainty in the number of electrons collected by the detector, but rather the error in converting the data to an absolute flux. Equivalent widths and ratios of lines observed simultaneously are not affected by this uncertainty. A flux calibration uncertainty of 100% indicates the flux calibration is highly uncertain, and probably good only to an order of magnitude (i.e., an uncertainty of ±1 in the log of line fluxes).

b Systemic velocities are from: Mk993, NGC3227, NGC4051, NGC6814, NGC7450, NGC1667, NGC2273, NGC2992, and NGC7682, de Vaucouleurs *et al.* (1991); Mk359 and NGC262, Fisher *et al.* (1995); NGC3516, NGC7469, NGC449 and NGC5929, Keel (1996); NGC591, Wegner *et al.* (1993); NGC5347, Huchra *et al.* (1995).

c NGC4151 is described in Chapter 3; MK 1066, NGC 2110, NGC 4388, and Mk 3 are described in Chapter 4.

The width of the slit during the observations ranged from $0.5''$–$0.7''$. This corresponds to a spectral resolution of about 235 km s^{-1} in the 1.27μm wavelength range, and a resolution of about 290 km s^{-1} in the 2.16μm wavelength range. The atmospheric seeing ranged from $0.6''$ to $1.8''$. The angle of the slit in most objects was chosen to align with extended structures in ionized gas which have been published

in the literature. Where this was not available, the slit was aligned with extended radio emission, or optical or infrared continuum emission. For two early observations (NGC 5347 and one slit of NGC 262), the slit was arbitrarily oriented at 270°. For five of the objects, there are observations at two slit position angles. The secondary slit is perpendicular to the primary slit in three of these objects (Mk 1066, NGC 4388, and NGC 5929). In NGC 2992, the two slits are oriented along two directions of extended Hα emission.

5.3 Results

We have detected narrow components of the four primary lines ([FeII], Paβ, H_2, and Brγ) in most of the galaxies in Table 5.1. Although the narrow [FeII], H_2, and Brγ lines are isolated at our resolution, frequently there is some enhanced emission on the blue wing of the narrow Paβ line. (See, for example, the nuclear bin on NGC 2273 in Figure 5.17, or NGC 5929 in Figure 5.7.) This enhanced emission is not in the form of a single narrow line, but rather a weak, broadened emission with a FWHM of $\sim$ 600 km s^{-1}, centered 500-700 km s^{-1} blueward of Paβ. As discussed in Chapter 4, the probable dominant contributers to this emission are a blend of two HeI lines at 1.2785μm and 1.2791μm, which have been resolved from Paβ in high resolution spectroscopy of the planetary nebula BD+30°3639 (Goodrich *et al.* 1994). There may be some additional contribution from [FeII] (λ = 1.2788μm) (Thompson 1995). While this emission may confuse the identification of additional components in the blue wing of Paβ, and possibly lead to the misidentification of a blueshifted broad line, it is generally weak enough that it does not significantly affect measurements of the flux or the velocity of the peak of the Paβ line. Finally, a broad Paβ line was detected on the nucleus of every Seyfert 1.x galaxy in the sample except for NGC 6814, but not in any Seyfert 2 galaxies.

In addition to the four primary lines, in nine of the objects (including NGC 4151 and NGC 4388, which were discussed in Chapters 3 and 4 respectively), there is a line blueward of [FeII] which we identify as the coronal line [SIX] (λ=1.2524μm)

(Chapter 4; Chapter 6). This line is always observed to be narrow, and generally is seen concentrated on the nucleus. It was seen in five Seyfert 2 galaxies and in four Seyfert 1.x galaxies.

A summary of the lines detected follows. In section 5.3.1, Table 5.2 describes the nuclear broad lines. In section 5.3.2, equivalent widths, line ratios, line centroids, and line widths are tabulated in Tables 5.3 and 5.4 for the narrow components of the lines in each object in Table 5.1 at each spatial resolution element. Finally, there is a more detailed discussion for each object which has not already been discussed in Chapters 3 and 4.

5.3.1 Summary of Broad Lines Detected

Detections and upper limits on broad components of the Paβ and Brγ lines in the Seyfert 1.x galaxies are tabulated in Table 5.2. The FWHM of these broad components are all >1000 km s^{-1}, with five of the nine showing a FWHM >3000 km s^{-1}. Only in six of the objects was a broad component of the Brγ line detected. In four of the six objects, the FWHM of the Brγ line is consistent with the FWHM of the Paβ line. In NGC 3516, the broad Brγ line is narrower than the broad Paβ line by 950 km s^{-1}. This is probably a result of the non-Gaussian shape of the broad line in NGC 3516 coupled with the lower signal-to-noise ratio of the Brγ line data, which together allow weak wings to be lost in the noise.

In most cases, the fluxes of the broad and narrow hydrogen recombination lines were separated by a Gaussian decomposition. Two or more Gaussian profiles were fit to the observed line, at least one to fit the broad line, and at least one to fit the narrow line. The fit that used the minimum number of Gaussians which adequately described the data was accepted.

5.3.2 Summary of Narrow Lines Detected

The equivalent widths and flux ratios of the narrow Paβ, Brγ, [FeII], H_2 v=1-0S(1), and [SIX] lines observed are tabulated in Table 5.3. In each case, the size of the

Table 5.2: Broad Lines Detected in Seyfert 1.x Galaxies

Galaxy	Type	Beam (″)	Paβ		Brγ	
			Eq. Width $10^{-4}\mu$m	FWHM km s^{-1}	Eq. Width $10^{-4}\mu$m	FWHM km s^{-1}
Mk993	1/1.9	0.6×1.3	12.7±3.0	3321±794	7.9±3.1	2596±1039
Mk359	1.5	0.6×0.7	17.9±1.6	1143±78		
NGC2992	2/1.9	0.6×1.7	8.5±1.9	2452±550	8.8±1.7	1984±351
NGC3227	1.5	0.5×1.0	22.1±2.4	3122±284	7.7±1.9	1634±427
NGC3516	1.5	0.5×1.7	47.9±2.9	2976±210	7.5±1.2	2263±351
NGC4051	1	0.5×1.3	18.5±1.0	1327±43	4.7±0.7	756±105
NGC4151	1.5	0.6×1.3	12.4±3.3	5800±800		
NGC5273	1.9	0.5×1.0	27.4±5.1	3810±664		
NGC6814	1	...				
NGC7450	1.5	0.6×1.0	16.4±4.9	3633±1242		
NGC7469	1	0.6×1.0	43.3±2.9	2393±83	7.5±1.6	2153±462

beam used to compute the line flux is the width of the slit by an extracted number of pixels along the slit which corresponds to the estimate of the seeing as tabulated in Table 5.1. Data are tabulated for all positions on each object where any narrow line was detected. Spatial bins are offset by the length of the beam along the slit.

The most robust flux ratios obtainable from these data are between lines observed simultaneously in a single observation (see Section 4.3.1). The wavelength ranges in these observations are each small enough that relative extinction effects between lines observed simultaneously should be negligible. Table 5.3 shows the narrow line flux ratios [FeII]/Paβ, H_2/Brγ, and [SIX]/Paβ. The flux of any broad Paβ or Brγ lines are not included in these flux ratios. Equivalent widths of lines are also given in Table 5.3 because they are not sensitive to flux calibration uncertainties. Flux ratios tabulated are the ratios of the integrated flux of the line, not the ratio of the equivalent widths. Flux ratios will differ slightly from equivalent width ratios when there is a slope in the continuum.

Table 5.3: Equivalent Widths and Flux Ratios of Narrow Lines

Pos[a]	Equivalent Width ($10^{-4}\mu$m)					Flux Ratios		
(″)	[FeII]	Paβ	H_2	Brγ	[SIX]	[FeII]/Paβ	H_2/Brγ	[SIX]/Paβ
				NGC 262, 15° slit				
1	15.2±6.0	2.2±2.0	5.8±2.1	5.0±2.9	...	5.52±5.12	1.26±0.64	...
0	27.7±3.7	15.9±2.4	7.5±1.2	8.2±1.7	2.7±0.9	1.46±0.22	0.96±0.19	0.14±0.05
-1	10.5±4.4	8.5±2.7	8.3±2.1	5.3±2.7	...	1.12±0.46	1.70±0.76	...
				NGC 262, 270° slit				
0	18.8±3.7	17.1±4.1	4.8±1.4	3.8±1.7	2.7±0.9	1.01±0.15	1.26±0.53	0.15±0.04
				NGC 449, 156° slit				
0.67	44.9±18.8	35.1±17.4	15.1±7.9	11.9±7.7	...	1.36±0.23	1.28±0.34	...
0	99.2±21.9	76.8±18.0	23.5±5.1	29.7±7.6	6.1±4.1	1.39±0.08	0.84±0.05	0.09±0.05
-0.67	45.1±21.1	39.2±18.7	22.2±11.0	13.0±7.5	4.9±2.7	1.39±0.21	1.91±0.51	0.15±0.05
				Mk 993, 150° slit				
0	4.4±0.7	1.7±0.6	3.0±0.8	1.2±1.8	...	2.79±1.03	2.75±4.29	...
				Mk 359, 20° slit				
0.67	<0.9	9.8±2.3	...	...	...	<0.09	...	...
0	0.9±0.2	4.6±0.7	...	...	3.7±0.5	0.21±0.05	...	0.85±0.13
-0.67	1.6±0.6	4.5±1.3	...	...	...	0.39±0.15	...	...
				NGC 591, 152° slit				
1	11.4±3.6	6.6±1.7	13.6±4.9	5.2±2.2	...	1.77±0.31	2.80±0.70	...
0	16.9±2.5	14.5±1.8	17.9±3.0	8.6±2.1	1.7±0.5	1.26±0.09	2.34±0.28	0.13±0.03
-1	14.6±4.1	9.6±2.2	11.9±5.5	5.0±2.5	...	1.74±0.38	2.63±1.00	...
				Mk 1066, 135° slit				
2.67	6.7±4.5	17.1±12.4	...	...	...	0.43±0.14	...	...
2	4.7±1.7	5.8±1.9	4.0±1.9	<4.3	...	0.79±0.21	>0.87	...
1.33	18.4±3.2	15.3±2.6	9.4±2.0	10.3±2.7	...	1.17±0.08	0.86±0.09	...
0.67	23.0±2.6	29.0±2.6	12.6±1.7	18.7±2.8	...	0.75±0.03	0.63±0.05	...
0	20.8±1.9	27.4±2.1	13.0±1.2	14.0±1.5	...	0.75±0.04	0.89±0.06	...
-0.67	39.0±3.8	33.0±4.6	17.8±2.6	20.6±3.8	...	1.20±0.04	0.85±0.06	...
-1.33	21.6±3.4	23.2±4.6	9.0±2.7	16.7±6.3	...	0.99±0.05	0.56±0.09	...
-2	5.3±2.2	6.7±2.5	<4.4	11.5±6.1	...	0.85±0.17	<0.40	...
				Mk 1066, 45° slit				
1.33	5.0±1.3	4.2±1.1	13.0±5.3	<2.7	...	1.30±0.32	>4.41	...
0.67	11.2±1.6	10.3±1.3	12.6±2.7	6.7±1.1	...	1.06±0.09	1.74±0.21	...
0	17.2±1.4	29.1±2.7	11.5±1.5	13.7±1.4	...	0.57±0.03	0.76±0.06	...
-0.67	15.9±2.6	17.9±2.7	12.6±2.3	10.0±2.0	...	0.87±0.07	1.21±0.10	...
-1.33	5.2±1.4	8.9±2.6	9.0±4.0	<4.7	...	0.64±0.16	>1.83	...
-2	...	...	5.6±3.7	<5.3	...	...	>0.91	...
				NGC 1667, 164° slit				
0	5.0±1.2	<1.8	...	...	...	>2.96	...	...

continued on next page

Table 5.3: Equivalent Widths and Flux Ratios of Narrow Lines (continued)

Pos	Equivalent Width ($10^{-4}\mu$m)					Flux Ratios		
(″)	[FeII]	Paβ	H_2	Brγ	[SIX]	[FeII]/Paβ	H_2/Brγ	[SIX]/Paβ
				NGC 2110, 160° slit				
3	3.5±1.0	3.3±0.8	3.8±1.3	2.1±0.9	...	1.09±0.25	1.89±0.78	...
2	6.2±1.3	2.8±0.6	7.2±1.4	1.9±0.6	...	2.19±0.42	4.08±1.08	...
1	15.4±1.4	3.1±0.5	6.2±0.8	2.0±0.4	...	5.02±0.48	3.23±0.53	...
0	24.6±1.6	3.1±0.4	4.8±0.4	1.6±0.3	...	8.11±0.78	3.17±0.63	...
-1	22.4±2.3	3.2±0.5	6.6±0.7	2.0±0.4	...	7.36±0.74	3.59±0.69	...
-2	11.7±2.3	2.8±0.6	8.4±1.7	1.4±0.4	...	4.43±0.53	6.50±1.50	...
-3	8.7±2.0	3.1±0.9	5.5±1.2	2.8±1.0	...	2.93±0.54	2.14±0.51	...
-4	5.8±2.8	<2.7	3.6±1.5	<9.7	...	>2.24	>0.39	...
				Mk 3, 30° slit				
3	11.6±4.3	24.5±8.6	5.8±4.2	12.0±8.4	...	0.47±0.10	0.49±0.24	...
2	13.0±3.5	17.7±4.7	...	4.0±1.4	...	0.74±0.12	...	...
1	37.6±4.2	31.3±3.5	3.4±1.2	11.5±2.6	...	1.17±0.07	0.29±0.11	...
0	52.2±5.1	39.3±3.2	5.3±0.7	16.7±2.1	...	1.24±0.04	0.31±0.04	...
-1	46.3±6.2	26.4±3.0	4.6±0.8	12.8±2.2	...	1.72±0.08	0.35±0.05	...
-2	17.9±5.7	9.5±2.9	13.1±4.5	4.4±1.6	...	1.88±0.43	2.94±0.54	...
-3	17.6±7.7	4.3±1.7	...	...	...	3.75±1.15	...	...
				NGC 2273, 120° slit				
1.33	4.2±1.1	3.3±0.7	4.5±0.9	1.8±0.7	...	1.39±0.33	2.63±0.92	...
0	5.2±0.6	5.8±0.6	7.0±0.7	3.3±0.6	...	0.91±0.10	2.20±0.34	...
-1.33	6.4±1.2	6.2±1.1	4.7±0.9	3.6±1.2	...	1.07±0.18	1.40±0.41	...
				NGC 2992, 15° slit				
5	6.2±3.6	10.1±5.2	<5.6	7.6±3.8	...	0.78±0.30	<0.75	...
3.33	5.9±2.1	2.8±1.2	6.5±1.9	3.6±1.2	...	2.25±1.03	1.68±0.55	...
1.67	7.1±1.2	3.0±0.7	8.2±1.3	3.2±1.0	...	2.48±0.55	2.40±0.71	...
0	8.5±0.9	4.1±0.6	7.6±0.8	3.2±0.6	...	2.24±0.28	2.33±0.45	...
-1.67	8.8±1.4	3.3±0.7	5.7±0.8	2.6±0.6	...	2.97±0.63	2.22±0.50	...
-3.33	12.6±3.4	3.9±1.2	3.9±1.4	4.4±1.4	...	3.90±1.12	0.88±0.34	...
-5	8.2±4.1	6.9±3.7	6.2±3.2	7.4±5.0	...	1.62±0.67	0.90±0.48	...
				NGC 2992, 118° slit				
1.67	4.2±1.1	2.6±0.9	6.1±1.8	<2.7	...	1.68±0.65	>2.47	...
0	9.7±1.3	4.6±0.7	7.3±1.0	2.7±0.7	...	2.15±0.32	2.80±0.77	...
-1.67	7.5±1.5	5.6±1.2	8.0±2.2	<8.7	...	1.53±0.27	>1.02	...
				NGC 3227, 40° slit				
2	2.8±1.2	<2.2	16.1±9.2	<14.9	...	>1.36	>0.96	...
1	7.8±1.1	4.6±0.9	8.2±1.5	<2.4	...	1.67±0.33	>3.29	...
0	7.0±0.6	3.4±1.0	6.2±0.8	<2.7	...	2.05±0.59	>2.23	...
-1	6.2±1.2	2.4±0.7	8.6±1.9	<3.8	...	2.59±0.81	>2.32	...
-2	5.2±2.1	<2.3	...	...	...	>2.39	...	...
				NGC 3516, 35° slit				
1.67	1.4±0.3	...	...	...	...	...	...	...
0	<1.2	...	...	...	...	...	...	...

continued on next page

Table 5.3: Equivalent Widths and Flux Ratios of Narrow Lines (continued)

Pos	Equivalent Width ($10^{-4}\mu$m)					Flux Ratios		
(″)	[FeII]	Paβ	H_2	Brγ	[SIX]	[FeII]/Paβ	H_2/Brγ	[SIX]/Paβ
				NGC 4051, 81° slit				
1.33	1.3±0.3	2.2±1.3	4.4±0.9	<3.9	1.5±0.5	0.65±0.40	>1.25	0.74±0.48
0	2.3±0.4	7.0±0.7	2.8±0.4	...	3.1±0.3	0.34±0.07	...	0.46±0.04
-1.33	2.4±0.5	1.9±0.7	4.1±0.8	...	2.7±1.0	1.37±0.53	...	1.55±0.76
				NGC 4151, 60° slit				
2.67	22.8±4.2	9.2±1.5	...	...	...	1.93±0.32	...	...
1.33	18.7±1.5	9.2±0.8	...	...	1.5±0.4	1.60±0.11	...	0.13±0.03
0	6.3±0.6	5.6±0.4	...	...	1.9±0.3	1.01±0.11	...	0.30±0.05
-1.33	12.0±1.3	7.9±0.8	...	...	...	1.41±0.10	...	...
-2.67	6.9±1.5	5.8±1.2	...	...	...	1.02±0.21	...	...
				NGC 4388, 30° slit				
4	22.8±19.1	19.0±14.9	<7.4	13.0±12.8	...	0.99±0.25	<0.67	...
3	15.5±9.5	18.2±9.1	<7.0	13.3±9.9	...	0.71±0.17	<0.57	...
2	13.4±6.0	26.1±7.1	6.5±3.1	12.7±6.7	...	0.46±0.08	0.56±0.13	...
1	7.7±1.9	25.7±5.5	13.6±4.1	12.7±3.2	3.6±1.0	0.28±0.03	1.05±0.15	0.13±0.02
0	11.2±1.7	26.3±4.2	9.5±1.2	10.6±1.5	4.5±0.8	0.40±0.03	0.88±0.08	0.16±0.02
-1	18.8±4.6	32.2±6.8	8.4±1.6	17.1±3.9	2.4±0.8	0.57±0.04	0.51±0.06	0.07±0.01
-2	31.0±9.4	26.8±7.4	6.3±2.7	14.7±6.5	...	1.13±0.11	0.46±0.09	...
-3	29.7±11.8	17.8±7.1	6.1±3.6	13.6±10.5	...	1.64±0.22	0.49±0.14	...
-4	12.5±6.6	4.8±2.7	<6.9	<11.7	...	2.52±0.84	...	...
				NGC 4388, 120° slit				
2	9.0±2.5	4.0±1.3	12.4±5.3	<4.9	...	2.18±0.53	>2.29	...
1	12.7±2.1	16.8±3.1	14.1±2.9	9.4±2.0	...	0.72±0.07	1.39±0.18	...
0	11.5±1.4	24.1±2.7	8.4±1.1	11.6±1.8	4.4±0.6	0.46±0.03	0.67±0.07	0.17±0.01
-1	10.1±2.0	19.9±3.5	19.6±4.6	8.0±1.7	...	0.50±0.05	2.34±0.25	...
-2	8.9±3.0	7.2±2.2	18.0±5.9	3.2±1.5	...	1.26±0.24	5.23±1.60	...
				NGC 5273, 10° slit				
0	3.1±0.9	1.8±0.6	...	...	...	1.76±0.56	...	...
				NGC 5347, 270° slit				
0	1.1±0.5	5.0±1.2	4.5±1.2	<2.7	2.1±0.7	0.23±0.10	>1.55	0.43±0.16
				NGC 5929, 50° slit				
1	6.0±1.4	7.6±1.9	6.2±3.0	11.1±5.6	...	0.80±0.17	0.54±0.25	...
0	7.3±1.2	6.0±0.8	6.7±2.1	2.7±0.8	...	1.18±0.19	2.35±0.88	...
-1	11.6±2.1	8.9±2.0	15.7±5.6	4.7±2.6	...	1.40±0.22	3.23±1.11	...
				NGC 5929, 140° slit				
0	6.7±0.8	5.3±0.8	3.8±0.8	4.0±1.0	...	1.41±0.20	1.02±0.26	...
				NGC 6814, 180° slit				
0	4.0±0.7	0.7±0.4	4.1±0.9	<3.5	...	5.86±3.62	>1.13	...
				NGC 7450, 107° slit				
0	4.8±1.5	2.6±0.7	5.0±1.1	2.7±1.0	2.6±0.7	1.81±0.64	1.80±0.68	1.00±0.29

continued on next page

Table 5.3: Equivalent Widths and Flux Ratios of Narrow Lines (continued)

Pos	Equivalent Width ($10^{-4}\mu$m)					Flux Ratios		
(″)	[FeII]	Paβ	H_2	Brγ	[SIX]	[FeII]/Paβ	H_2/Brγ	[SIX]/Paβ
				NGC 7469, 240° slit				
3	6.4±2.1	13.6±4.6	17.9±16.0	12.6±10.5	...	0.47±0.10	1.53±0.86	...
2	8.0±1.2	16.8±2.4	8.6±3.0	11.4±2.8	...	0.48±0.04	0.79±0.21	...
1	3.8±0.5	7.0±0.7	4.2±0.8	3.7±0.7	...	0.56±0.07	1.17±0.27	...
0	3.0±0.3	4.5±0.4	2.2±0.4	1.3±0.6	...	0.70±0.08	1.67±0.81	...
-1	4.8±0.5	8.7±1.4	4.8±0.7	4.2±0.7	...	0.60±0.04	1.12±0.21	...
-2	6.8±1.5	12.2±2.7	6.1±2.1	9.7±2.8	...	0.57±0.06	0.64±0.19	...
-3	9.5±6.7	3.2±2.1	<13.2	<14.5	...	2.62±1.71	...	...
				NGC 7682, 60° slit				
1	8.0±5.1	<6.4	10.1±5.2	<9.3	...	>1.22	>1.05	...
0	5.4±1.3	7.7±1.5	21.5±6.5	6.4±2.5	...	0.73±0.13	3.39±0.66	...
-1	...	...	18.1±11.0	<6.0	...	...	>3.08	...

a Positions are relative to the nucleus (continuum peak) of the galaxy. Positive positions are towards the position angle of the slit as quoted.

The velocity centroids and full widths at half maximum (FWHM) of the lines are tabulated in Table 5.4. Velocity centroids listed are relative to the systemic velocity of each galaxy as tabulated in Table 5.1. In most cases, the lines are symmetric and well described by a single Gaussian profile. Significant exceptions to this are noted in section 5.4 or in Chapter 3 or Chapter 4. In Table 5.4, the widths listed for each line are for the entire narrow line profile, i.e., including all components together. The spatial region of the galaxy sampled for these data are the same as those sampled for the equivalent widths and flux ratios tabulated in Table 5.3.

Of the 23 objects observed, eight have spatially resolved narrow emission lines; eight more have marginally resolved narrow line regions. The spatially resolved line emission of each object is discussed in section 5.4, and in Chapters 3 and 4.

Table 5.4: Line Velocities and Widths

	[FeII]		Paβ		H_2		Brγ		[SIX]	
Pos[a]	Centroid[b]	FWHM[c]	Centroid	FWHM	Centroid	FWHM	Centroid	FWHM	Centroid	FWHM
″	km s^{-1}	km s^{-1}	km s^{-1}	km s^{-1}	km s^{-1}	km s^{-1}	km s^{-1}	km s^{-1}	km s^{-1}	km s^{-1}
					NGC 262, 15° slit					
1	-194±62	421±287	22±28	< 153	-80±32	234±175	-130±86	564±430	...	...
0	-52±19	342±50	-34±19	305±31	-65±17	217±78	-27±28	510±113	-97±29	204±148
-1	18±70	732±333	30±26	320±122	-43±27	327±122	24±82	617±378	...	...

continued on next page

Table 5.4: Line Velocities and Widths (continued)

	[FeII]		Paβ		H_2		Brγ		[SIX]	
Pos	Centroid	FWHM	Centroid	FWHM	Centroid	FWHM	Centroid	FWHM	Centroid	FWHM
$''$	km s^{-1}	km s^{-1}	km s^{-1}	km s^{-1}	km s^{-1}	km s^{-1}	km s^{-1}	km s^{-1}	km s^{-1}	km s^{-1}
NGC 262, 270° slit										
0	-90±16	334±56	-47±28	186±82	-43±20	< 171	-60±61	455±257	-76±28	278±50
NGC 449, 156° slit										
0.67	-226±37	686±107	-114±31	468±114	-65±19	278±68	49±55	857±255	...	...
0	-124±37	708±64	-137±9	610±38	-36±15	288±25	-105±22	602±79	-179±50	520±181
-0.67	1±13	669±46	-109±37	629±162	3±37	266±307	-20±45	688±195	-42±32	249±154
Mk 993, 150° slit										
0	-18±20	432±72	-305±40	435±193	77±42	541±150	211±260	896±376	...	...
Mk 359, 20° slit										
0.67	...	...	101±24	264±68	...	...	...	...	...	...
0	40±22	< 152	4±8	< 152	...	...	...	...	-152±16	371±58
-0.67	95±36	168±207	11±12	< 152	...	...	...	...	...	...
NGC 591, 152° slit										
1	30±14	381±55	-48±12	186±69	-5±17	417±69	37±28	214±155	...	...
0	-39±13	364±60	-38±6	232±59	-21±10	< 194	9±17	264±69	-23±27	228±129
-1	-28±40	218±76	-30±14	321±66	-17±24	239±115	89±37	< 194	...	...
Mk 1066, 135° slit										
2.67	-118±24	< 154	-233±41	677±194	...	...	...	...	...	...
2	-68±25	267±109	-58±20	221±83	-72±35	< 190	...	...	...	...
1.33	-59±14	294±53	-77±19	< 154	-45±15	328±46	-90±19	383±34	...	...
0.67	-38±14	240±32	-67±14	< 154	-45±15	321±50	-73±18	237±46	...	...
0	-125±16	296±41	-20±15	205±50	3±13	353±29	-19±18	329±27	...	...
-0.67	-54±14	289±54	51±14	< 154	89±13	223±37	51±19	269±32	...	...
-1.33	-8±15	341±62	32±16	167±74	143±20	360±78	70±20	308±44	...	...
-2	109±18	218±75	70±18	202±65	...	...	133±46	714±197	...	...
Mk 1066, 45° slit										
1.33	-34±17	222±73	-50±19	179±93	-6±15	491±59	...	...	...	...
0.67	-52±14	179±52	-20±10	< 150	-12±11	392±35	-43±17	429±62	...	...
0	-74±12	179±38	-41±13	< 150	-14±12	192±61	-83±17	250±44	...	...
-0.67	-54±15	219±46	-24±11	< 150	-21±10	277±33	-49±14	313±51	...	...
-1.33	-10±19	247±83	64±49	< 150	39±18	329±82	...	...	...	...
-2	...	...	...	...	107±23	< 190	...	...	...	...
NGC 1667, 164° slit										
0	18±34	551±152	...	...	...	...	...	...	...	...
NGC 2110, 160° slit										
3	212±18	219±88	299±11	< 150	292±29	223±132	375±45	< 189	...	...
2	117±15	334±44	226±13	< 150	213±21	< 189	203±36	213±169	...	...
1	-4±9	373±36	116±8	213±41	152±18	275±35	160±27	259±92	...	...
0	-86±10	496±34	-4±10	338±43	32±18	359±36	62±33	391±116	...	...
-1	-68±8	383±25	-49±9	186±51	-52±17	273±34	48±31	304±111	...	...
-2	-114±11	171±54	-84±9	176±53	-14±20	238±52	-95±31	< 189	...	...
-3	-156±10	197±31	-126±15	203±82	-112±19	205±61	-69±35	313±136	...	...
-4	-207±20	347±87	...	...	-5±42	546±226	...	...	...	...

continued on next page

Table 5.4: Line Velocities and Widths (continued)

	[FeII]		Paβ		H_2		Brγ		[SIX]	
Pos	Centroid	FWHM	Centroid	FWHM	Centroid	FWHM	Centroid	FWHM	Centroid	FWHM
$''$	km s^{-1}	km s^{-1}	km s^{-1}	km s^{-1}	km s^{-1}	km s^{-1}	km s^{-1}	km s^{-1}	km s^{-1}	km s^{-1}
Mk 3, 30° slit										
3	19±26	382±105	73±12	200±65	72±60	< 191	24±28	265±145	...	...
2	-44±16	367±51	-58±36	255±125	...	...	74±23	< 191	...	...
1	-363±19	1165±102	-306±14	1201±122	-22±79	710±335	-153±46	899±210	...	...
0	-190±13	1137±41	-109±11	991±46	-2±49	639±99	-15±21	564±169	...	...
-1	54±13	501±56	-4±13	695±53	81±34	< 191	127±19	446±85	...	...
-2	162±16	394±83	-84±61	532±220	165±32	745±430	3±18	< 191	...	...
-3	-77±45	1117±248	-75±21	< 155	...	...	...	...	...	...
NGC 2273, 120° slit										
1.33	-37±21	310±92	41±13	< 151	61±16	< 191	22±40	193±230	...	...
0	-28±11	281±38	43±7	< 151	57±12	212±47	69±19	< 191	...	...
-1.33	-69±18	452±74	13±10	188±46	73±16	202±84	76±46	547±201	...	...
NGC 2992, 15° slit										
5	-396±41	316±184	-209±15	< 150	...	...	-233±45	335±214	...	...
3.33	-131±38	414±165	-114±32	< 150	-53±23	348±109	-184±39	345±183	...	...
1.67	-11±19	283±53	-52±18	206±91	-43±12	301±52	-26±52	627±230	...	...
0	-88±14	311±33	4±11	224±40	24±10	253±39	81±27	448±102	...	...
-1.67	57±21	276±66	41±21	269±81	114±13	288±56	154±26	307±124	...	...
-3.33	202±52	344±145	175±20	< 150	202±36	220±205	233±26	< 191	...	...
-5	168±24	175±127	200±29	< 150	192±45	265±234	220±68	461±314	...	...
NGC 2992, 118° slit										
1.67	39±27	412±117	-17±44	413±201	81±29	323±131	...	...	...	...
0	-7±15	408±115	31±11	271±54	15±16	233±68	18±30	< 193	...	...
-1.67	-61±14	375±55	26±14	269±64	-38±30	335±136	...	...	...	...
NGC 3227, 40° slit										
2	-18±23	< 150	...	...	6±31	297±133	...	...	...	...
1	-37±15	556±56	-176±27	667±115	-7±21	294±72	...	...	...	...
0	-30±12	606±24	-17±44	354±76	13±19	308±56	...	...	...	...
-1	12±27	678±103	-15±32	365±144	73±23	439±79	...	...	...	...
-2	241±51	530±267	...	...	...	...	...	...	...	...
NGC 3516, 35° slit										
1.67	-193±28	323±82	...	...	...	...	...	...	...	...
0	...	...	...	...	...	...	...	...	...	...
NGC 4051, 81° slit										
1.33	-36±26	251±126	-101±30	363±163	-30±22	285±103	...	...	-105±46	525±205
0	-79±43	231±148	-122±7	343±23	-26±20	349±86	...	...	-233±12	208±72
-1.33	-45±17	162±98	-23±18	< 156	14±23	303±111	...	...	-90±80	921±131
NGC 4151, 60° slit										
2.67	-184±37	396±106	-229±37	226±58	...	...	...	...	...	...
1.33	-194±29	442±58	-166±36	426±58	...	...	...	...	-110±32	< 188
0	-107±39	496±78	-40±36	284±30	...	...	...	...	-59±31	< 188
-1.33	96±31	546±99	36±37	336±51	...	...	...	...	...	...
-2.67	40±32	250±73	94±38	< 188	...	...	...	...	...	...

continued on next page

Table 5.4: Line Velocities and Widths (continued)

	[FeII]		Paβ		H_2		Brγ		[SIX]	
Pos	Centroid	FWHM	Centroid	FWHM	Centroid	FWHM	Centroid	FWHM	Centroid	FWHM
"	km s^{-1}	km s^{-1}	km s^{-1}	km s^{-1}	km s^{-1}	km s^{-1}	km s^{-1}	km s^{-1}	km s^{-1}	km s^{-1}
					NGC 4388, 30° slit					
4	18±20	353±60	60±20	192±75	...	...	109±53	454±237	...	...
3	35±37	< 150	45±16	334±64	...	...	35±33	424±139	...	...
2	38±23	443±94	2±10	206±30	80±21	197±114	1±18	284±71	...	...
1	-2±13	249±42	4±11	168±40	48±14	338±53	7±14	286±52	-70±17	< 150
0	-42±17	479±67	-12±12	249±43	8±10	306±34	6±15	< 182	-5±28	< 150
-1	-51±12	606±34	-21±11	366±48	-60±11	316±40	23±35	403±84	-110±22	204±95
-2	52±12	624±31	12±28	321±62	-63±19	272±86	-38±15	392±53	...	...
-3	76±17	195±64	16±18	383±70	-50±27	278±173	158±29	524±98	...	...
-4	138±22	357±91	24±27	< 150	...	...	...	...	...	...
					NGC 4388, 120° slit					
2	34±23	601±103	49±19	218±81	3±16	253±80	...	...	...	...
1	10±21	624±75	91±20	291±54	2±10	221±34	56±17	404±41	...	...
0	28±13	380±60	54±5	267±56	-4±11	211±40	54±16	286±62	-29±11	201±36
-1	14±17	332±100	47±6	333±20	-37±9	284±30	71±15	331±58	...	...
-2	13±21	252±140	1±13	240±67	-42±12	249±442	67±34	< 194	...	...
					NGC 5273, 10° slit					
0	-3±28	315±161	95±15	< 133	...	...	...	...	...	...
					NGC 5347, 270° slit					
0	39±31	< 131	63±21	344±79	84±29	287±66	...	...	-21±35	242±169
					NGC 5929, 50° slit					
1	-278±17	204±73	-217±15	< 150	-219±40	< 190	-238±74	680±366	...	...
0	-131±23	524±109	-92±14	399±30	16±59	495±186	133±40	< 190	...	...
-1	31±14	219±45	45±13	192±60	33±28	299±76	61±43	< 190	...	...
					NGC 5929, 140° slit					
0	-34±17	< 153	-61±17	634±54	84±22	332±79	1±33	636±111	...	...
					NGC 6814, 180° slit					
0	-54±23	444±93	-58±75	274±350	-22±25	< 188	...	...	...	...
					NGC 7450, 107° slit					
0	8±69	464±227	-16±20	168±74	54±25	352±115	114±54	451±249	-127±20	< 155
					NGC 7469, 240° slit					
3	44±19	187±71	50±13	155±35	-61±78	649±343	20±63	366±276	...	...
2	26±13	239±26	32±11	143±20	40±43	610±177	77±19	190±63	...	...
1	9±14	297±36	18±12	213±21	40±25	346±84	104±25	305±90	...	...
0	-33±15	364±41	-24±12	255±23	2±27	349±93	70±56	480±248	...	...
-1	-38±12	268±21	-38±11	175±17	72±23	313±78	28±21	332±69	...	...
-2	-49±14	203±33	-37±11	171±22	92±37	397±144	-92±42	301±131	...	...
-3	-134±69	572±305	-56±47	173±164	...	...	...	...	...	...

continued on next page

Table 5.4: Line Velocities and Widths (continued)

	[FeII]		Paβ		H_2		Brγ		[SIX]	
Pos	Centroid	FWHM	Centroid	FWHM	Centroid	FWHM	Centroid	FWHM	Centroid	FWHM
$''$	km s^{-1}	km s^{-1}	km s^{-1}	km s^{-1}	km s^{-1}	km s^{-1}	km s^{-1}	km s^{-1}	km s^{-1}	km s^{-1}
					NGC 7682, 60° slit					
1	281±141	1065±584	...	...	-8±32	< 194	...	...	...	...
0	45±19	284±73	-10±15	< 153	-13±19	< 194	-12±33	240±123	...	...
-1	...	...	...	...	-19±22	< 194	...	...	...	...

a Positive positions are towards the position angle of the slit as quoted.
b Centroids are relative to the systemic velocity for each galaxy.
c The resolution has been subtracted in quadrature.

5.4 Individual Objects

The following sections plot the spectra of each object and describe the observations tabulated in Tables 5.2 through 5.4 in greater detail. The objects with the most interesting results are presented first.

5.4.1 NGC 2992 (Seyfert 2/1.9)

Figures 5.1 and 5.2 show the infrared spectra of NGC 2992 along the 15° and 118° slits respectively. The nuclear region of this galaxy shows complicated extended structure in Hα (Wehrle & Morris 1988). The two slits were chosen to align with two axes of this extended structure. The 15° slit also coincides with the brightest extent of the radio emission in the 6cm image of the nucleus of NGC 2992.

Spatially extended [FeII], Paβ, H_2, and Brγ emission was detected over 10″ along the 15° slit, and over 3″ along the 118° slit. In comparison, the seeing was 1.5″–1.8″ during the observations.

Broad Hydrogen Recombination Lines

NGC 2992 is frequently classified as a Seyfert 2 galaxy. However, the presence of faint FWHM$\sim$2600 km s^{-1} broad wings on the Hα line argues that it would be better classified as a Seyfert 1.9 galaxy (Veron *et al.* 1980; Shuder 1980). Rix *et al.* (1990)

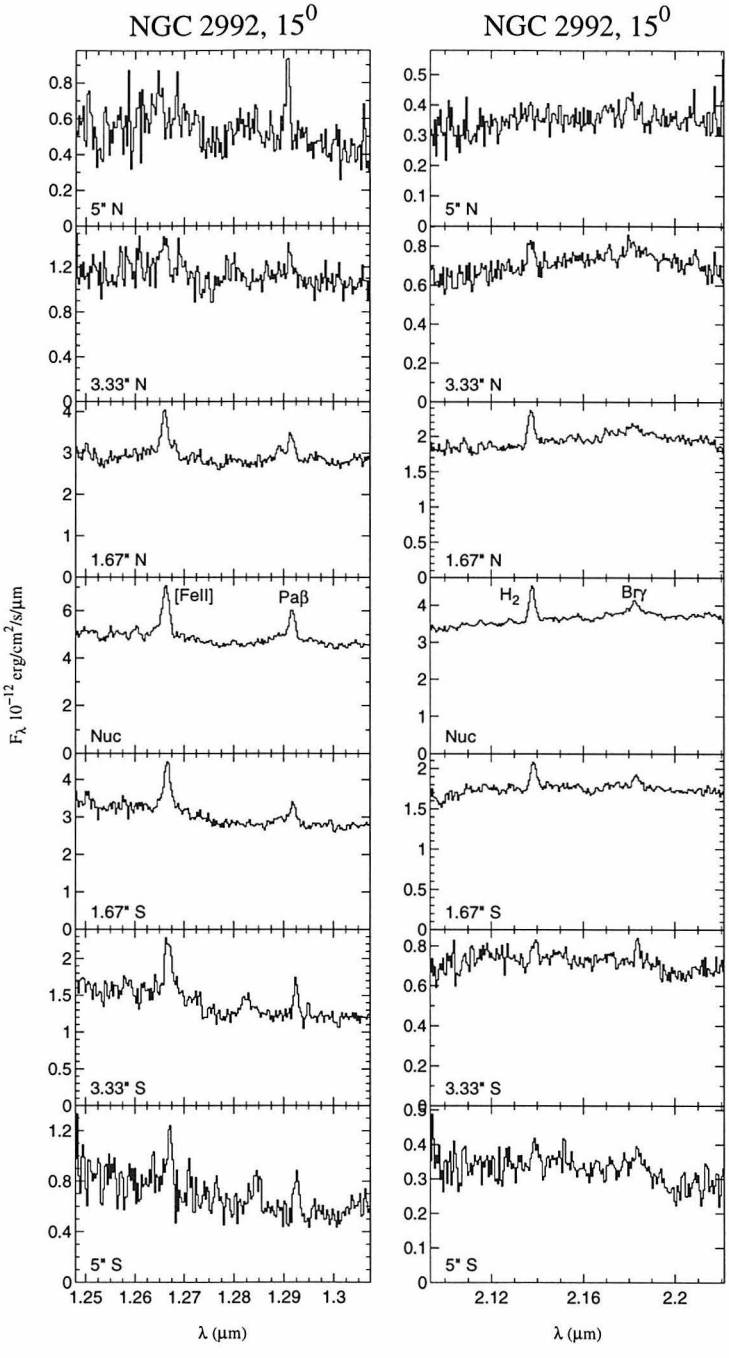

Figure 5.1: Spectra of NGC 2992 along a 15° slit. Each spatial bin is 1.67″ along the slit by 0.6″, the width of the slit.

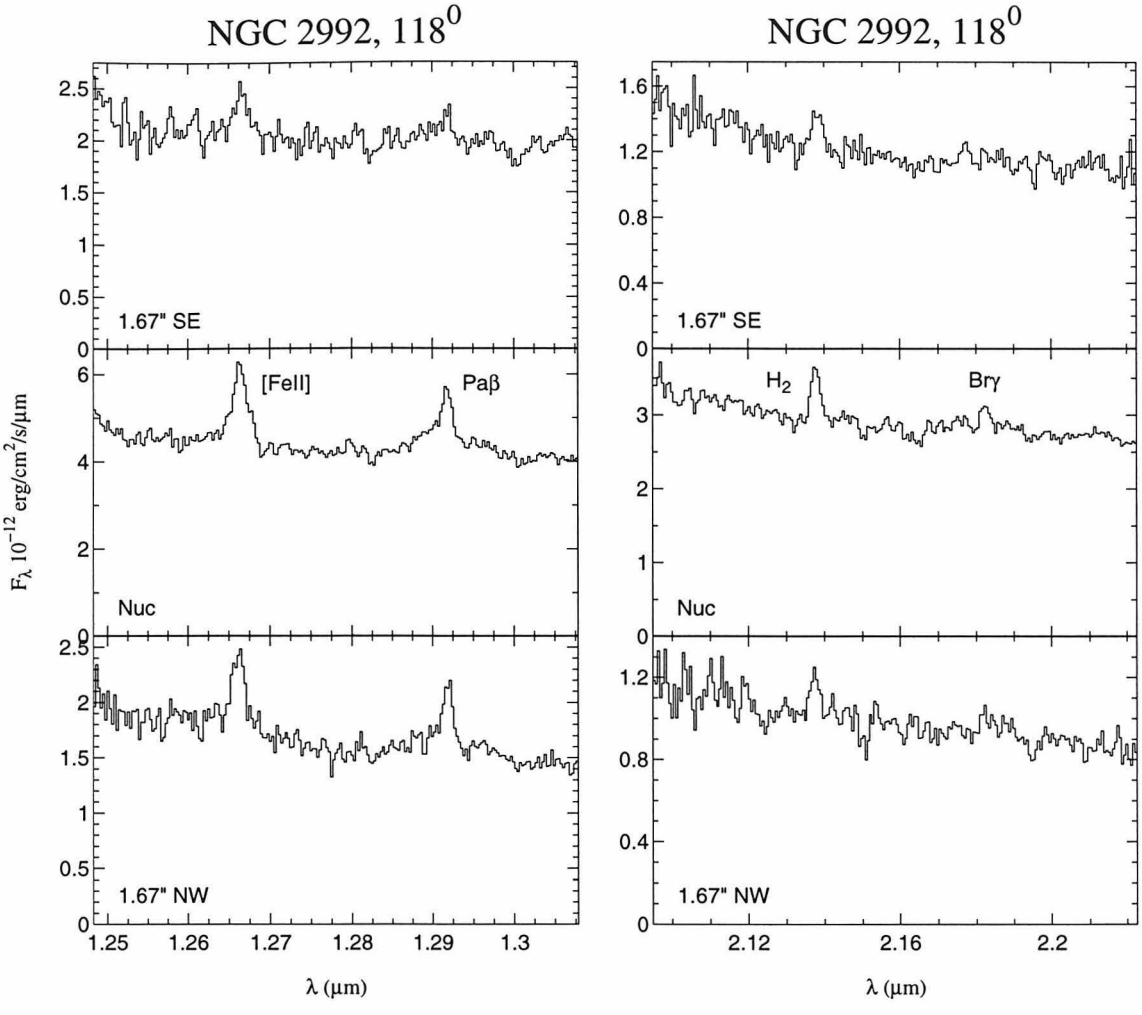

Figure 5.2: Spectra of NGC 2992 along a 118° slit. Each spectrum represents the emission in a region of the slit 0.6″ wide by 1.67″ long.

and Goodrich *et al.* (1994) report the detection of a FWHM$\sim$2900 km s^{-1} broad Paβ line in NGC 2992, with a flux equal to four times the flux of the narrow Paβ line.

Our data show broad components in both the Paβ and Brγ lines. The lines are visible in the nuclear bin of both slits. In order to deblend the broad Paβ line from both the narrow component and the blended HeI and [FeII] emission on the blue side of the Paβ line discussed in section 5.3, we have fit the line profile on the nucleus with three Gaussian components. Figure 5.3 shows the results of these fits to the Paβ line profile in the nuclear bin of the 15° slit. The result is a broad line with a FWHM of 2500$\pm$600 km s^{-1} with a flux 2.1$\pm$0.5 times the flux of the narrow line. Although Rix

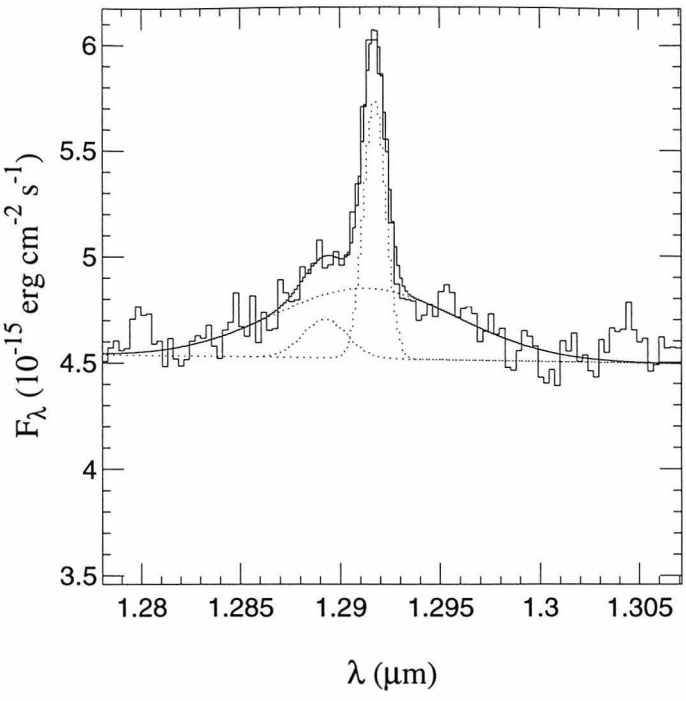

Figure 5.3: Gaussian decomposition of the Paβ line profile in the nuclear bin of the 15° slit on NGC 2992.

et al. (1990) include flux in a larger circular beam, the broad-to-narrow Paβ line flux ratio is smaller here, which may in part be explained by the fact that Rix *et al.* (1990) did not account for the excess emission on the blue side of Paβ from HeI and [FeII], thereby increasing the effective amplitude of their observed broad line.

A fit of two Gaussians to the Brγ line profile in the nuclear bin of the 15° slit produces a broad component with a FWHM of 2000±400 km s^{-1}. The broad Brγ line has 5.0±1.7 times the flux of the narrow Brγ line. The narrow/broad flux ratios of the Paβ and Brγ may be used to derive a differential extinction to the broad line region and the narrow line region on the nucleus. Using the standard interstellar extinction law (Savage & Mathis 1979), the extinction A_V to the broad line region is greater than that to the narrow line region by 5.7±2.7 magnitudes.

Spatially Extended Velocity Structure

All four of the infrared lines detected in NGC 2992 show a velocity gradient along the 15° slit. The full extent of this velocity gradient may be seen in Figure 5.4, which is a

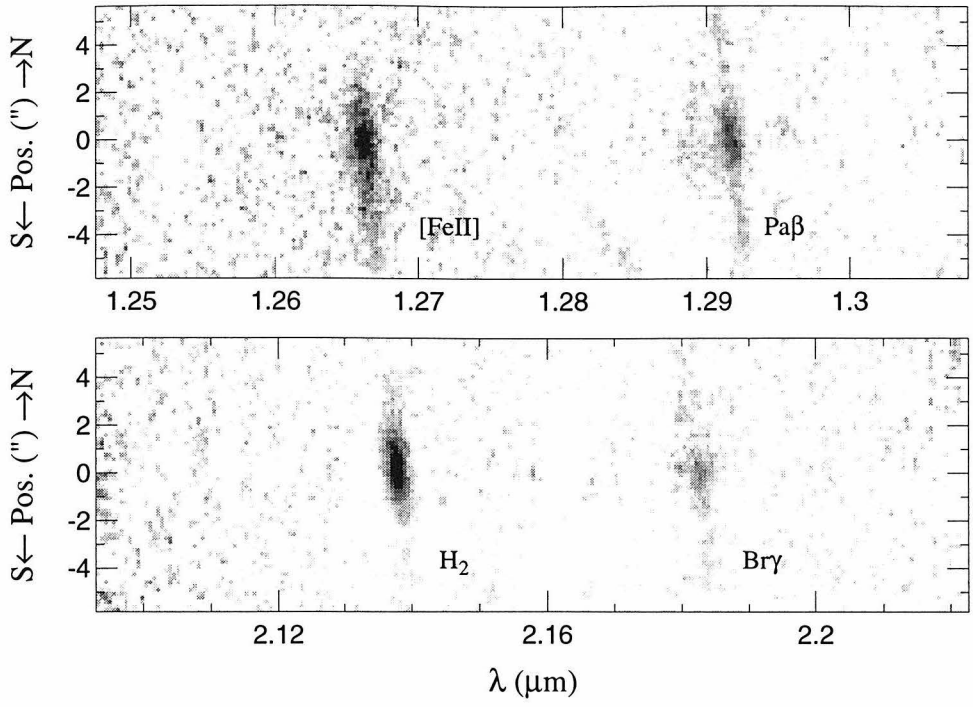

Figure 5.4: Greyscale plot of the spectra of NGC 2992. Position is in arcseconds along the 15° slit. A smoothed continuum (including the broad Paβ and Brγ lines) has been subtracted from each spectrum.

two-dimensional greyscale plot of the spectra along the 15° slit. A smoothed spline fit to the continuum and weak broad Paβ line has been subtracted from each row in this figure in order to increase the visibility of the extended lines. Figure 5.5 is a contour plot of the velocity of each line versus position. Line centroids change from about -200 km s^{-1} relative to the systemic velocity, 5″ north of the nucleus to $+200$ km s^{-1}, 5″ south of the nucleus. The slope is reasonably uniform, and with one exception is the same in all four of the lines. North of the nucleus, in Figure 5.4 the H_2 line appears to have a constant velocity that does not vary with position.

The velocities of the peaks of the narrow lines versus their positions are plotted in Figure 5.6. The peak of the [FeII] line is slightly blueshifted relative to the Paβ line north of the nucleus. South of the nucleus, both the Brγ and H_2 lines are redshifted relative to the Paβ line.

Colina *et al.* (1987) plot the velocity of the optical [OIII] line along a 26° slit, close

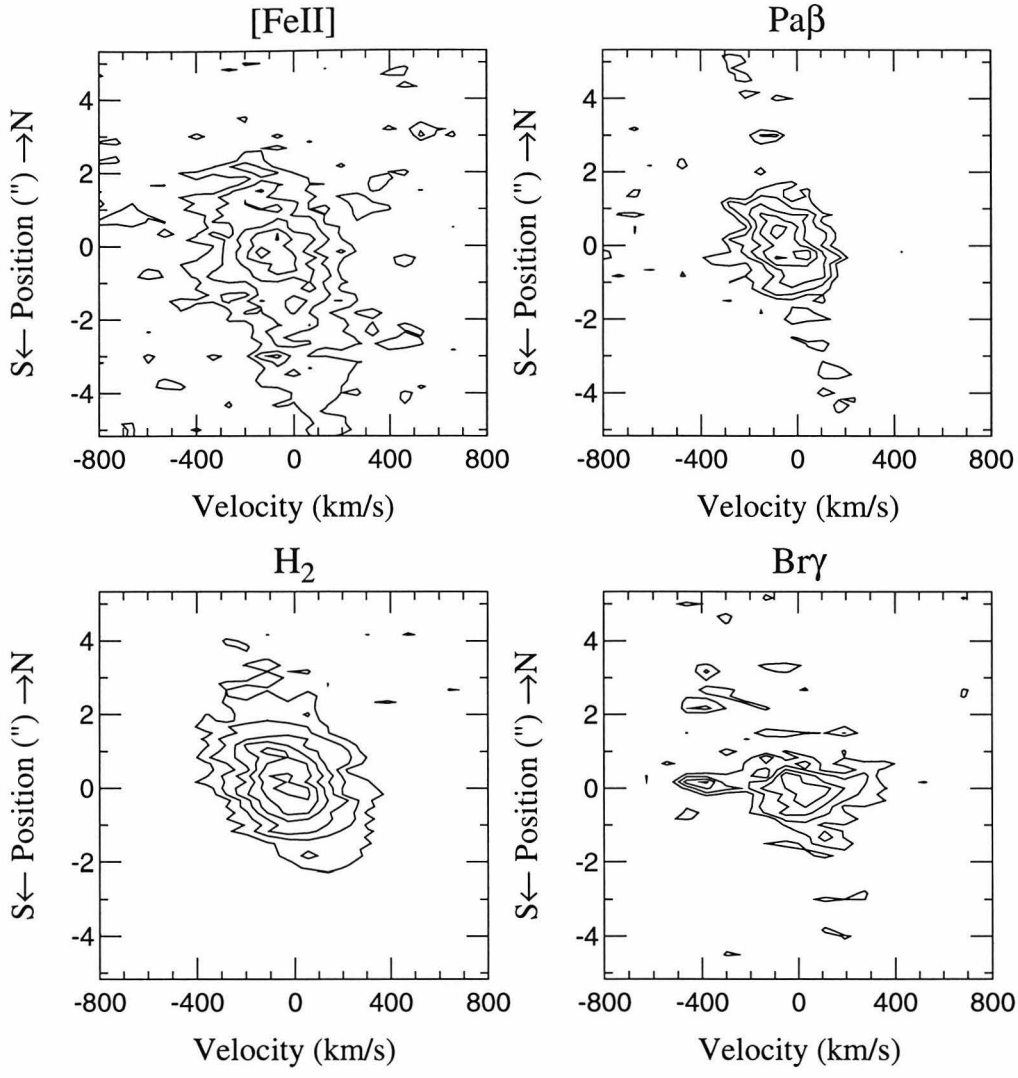

Figure 5.5: Position versus velocity contour plot for NGC 2992. The continuum and broad lines have been subtracted from each spectrum. Position is in arcseconds along a 15° slit. The lowest contour in each plot corresponds to a pixel brightness of approximately 2σ.

to the angle of our 15° slit. Southeast of the nucleus, the [OIII] velocities are consistent with the infrared velocities. However, northeast of the nucleus, the peaks of the infrared lines are blueshifted relative to the peaks of the [OIII] line by ~ 100 km s^{-1}. The [OIII] line shows a blue asymmetry northeast of the nucleus, while the infrared lines are symmetric to within the resolution of the data. (Although there appears to be a reddened component of [FeII] 1.67″N of the nucleus, this is coincident with the wavelength of a strong atmospheric O_2 absorption line, and may be the result of

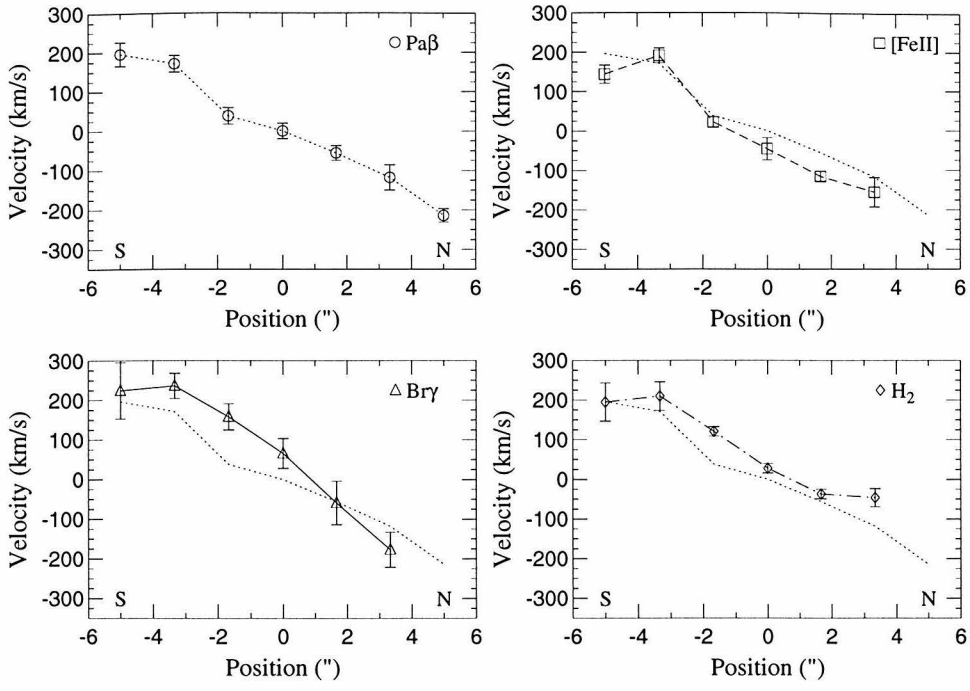

Figure 5.6: Position versus velocity for the peak of the narrow components of the lines along the 15° slit on NGC 2992. For reference, the velocity curve for Paβ appears on each of the other plots.

poor atmospheric correction.) Colina *et al.* (1987) explain the profiles with a radial infall which becomes more obscured by a dust lane with increasing distance from the nucleus. As infrared lines are less affected by dust extinction, this picture is consistent with the blueshift of the infrared lines relative to the [OIII] line. It is also consistent with the trend in the Brγ/Paβ flux ratio within 3.33″ of the nucleus, which is $\gtrsim 2''$ higher off of the nucleus than on the nucleus, and which is marginally higher north of the nucleus than south of the nucleus.

5.4.2 NGC 5929 (Seyfert 2)

The infrared spectra of NGC 5929 are shown in Figures 5.7 and 5.8. The 50° slit was chosen to align with extended [OIII] and Hα+[NII] emission. Narrowband HST imaging in these lines showed that the ionized gas is located parimarily in two peaks separated by $\sim 1''$ at 50° (Bower *et al.* 1994). This angle is also close to the $\sim 60°$ position angle of the two radio peaks which are separated by 1.3″ (Ulvestad & Wilson

1984a). The 140° slit is perpendicular to the primary slit.

Large velocity differences are evident over the 3″ observed extent of the Paβ, Brγ, [FeII], and H_2 lines along the 50° slit. Northeast of the nucleus, the lines appear to be dominated by a narrow (FWHM$\lesssim$ 300km s^{-1}) blueshifted component at -230 km s^{-1} relative to the systemic velocity of the system (2561 km s^{-1}). The [FeII] line is further blueshifted by an additional -75 km s^{-1}. Southwest of the nucleus, the lines are dominated by a narrow redshifted component at +40 km s^{-1}. On the nucleus, the lines appear to be composed of an overlap of two components at the velocities of the the two off-nuclear lines. In the nuclear bin of both slits, the Paβ line appears to have a double-peaked profile, although the two peaks are at the limit of the spectrum's resolution. A Gaussian decomposition of the line profiles on the nucleus indicate that the profiles of the lines are consistent with two narrow components at the velocities of the off-nuclear lines. Along the perpendicular 140° slit, the lines are not extended.

Both the [FeII]/Paβ and H_2/Brγ ratios are larger in the redshifted, southwestern component than in the blueshifted, northeastern component. This is apparent both from the nuclear and off-nuclear line profiles. On the nucleus, the redshifted component of [FeII] is stronger than its blueshifted component, whereas they are of approximately equal strength in the Paβ line. In the off-nuclear bins, the [FeII] and H_2 lines are stronger relative to the Paβ and Brγ lines respectively to the southwest than they are to the northeast.

Determining the velocity and flux of the [FeII] line in the redshifted component is hampered by the presence of strong atmospheric O_2 lines (seen in both emission and absorption) at the wavelength of the redshifted component in [FeII]. This problem is exacerbated by the fact that the observations of NGC 5929 occurred at the beginning of the night while the sky was still rapidly changing. In order to correct for the contribution of this atmospheric line to the [FeII] line flux, a flux of the residual sky line as measured at a radius further than the spatial extent of the infrared lines was subtracted from the measured flux of the redshifted component of [FeII] at each position. The typical flux of the residual O_2 sky line blend is $\sim 10^{-15}$ erg cm^{-2} s^{-1}, which is comparable to the flux observed in the [FeII] line. Despite the subtraction

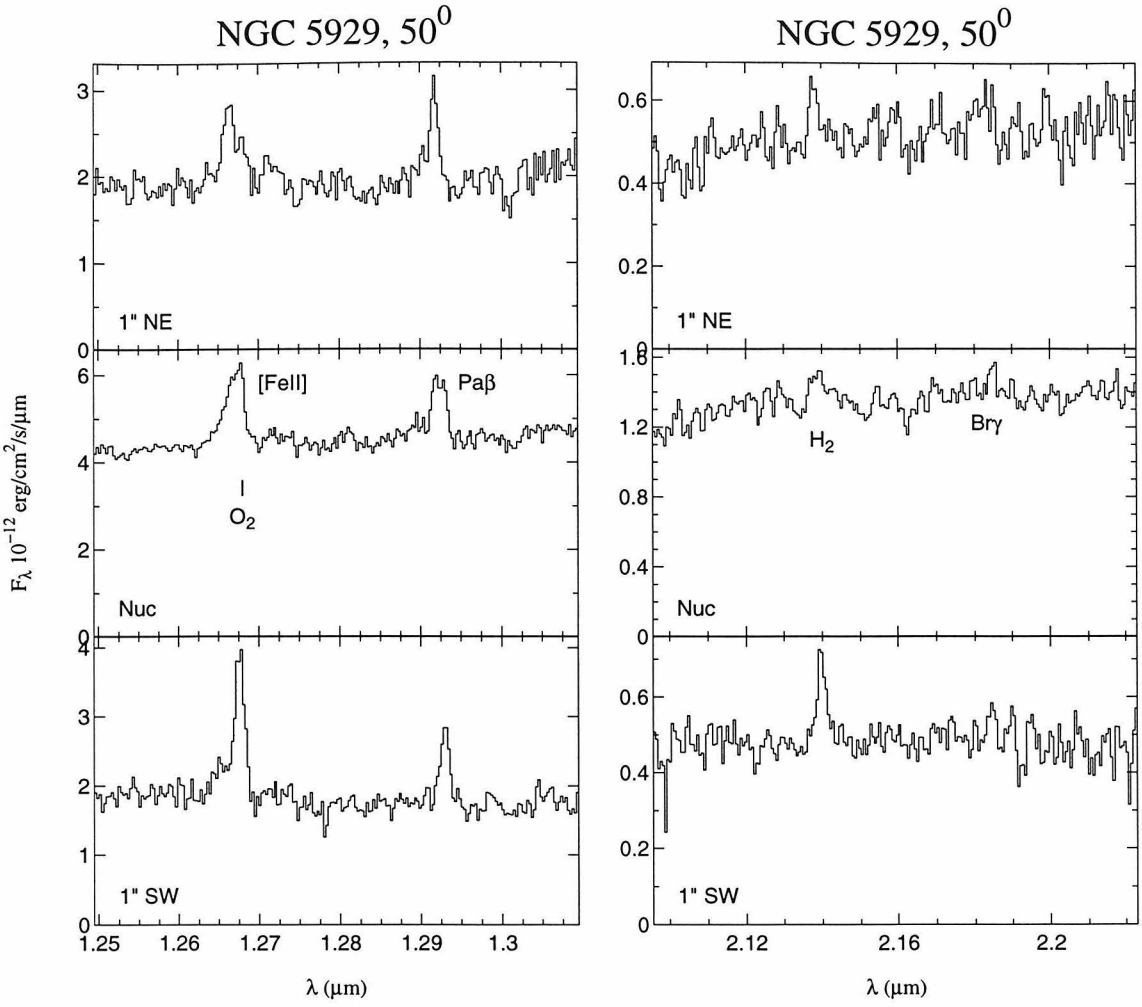

Figure 5.7: Spectra of NGC 5929 along a 50° slit. Each spatial bin is 1.0″ along the slit by 0.6″ wide. The position indicated with O_2 on the nuclear spectrum is the position of an atmospheric sky absorption line poor correction for which leaves significant residuals in the spectrum.

of the residual O_2 sky lines, there may be systematic errors in the flux of the [FeII] line, and the Gaussian decomposition may yield erroneous positions and widths for the components of the [FeII] line.

The spatial and velocity structure seen in the infrared lines corresponds to structure seen in the optical and radio emission of NGC 5929. In all three wavelengths, the morphology of NGC 5929 appears to be dominated by two spatially separated components. A 6cm radio map of NGC5929 shows two unresolved components separated by 1.3″ along a position angle of $\sim 50°$ (Ulvestad & Wilson 1984a). Narrowband imaging

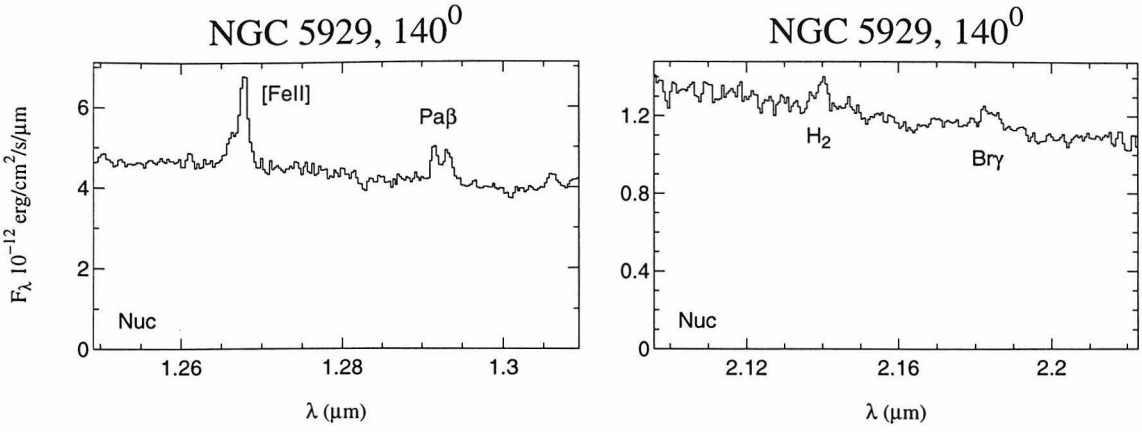

Figure 5.8: Spectra of NGC 5929 along a 140° slit. Each spatial bin is 1.0″ along the slit by 0.6″ wide.

of Hα+[NII] and [OIII] with HST (Bower *et al.* 1994) shows the ionized gas similarly resolved into individual components. The northeastern "cloud" or component appears to be bisected by a dust lane. Spectroscopy of [OIII] along a 60° slit shows two components spatially coincident with the two radio peaks, and similar in velocity to the infrared components (Whittle *et al.* 1986). To the northeast, the [OIII] emission is blueshifted by -250 km s^{-1} relative to the systemic velocity (see Table 5.1). To the southwest, the [OIII] is redshifted by $+60$ km s^{-1} relative to the systemic velocity. These velocities are similar to the velocities observed in the IR lines, which are shifted by -200–300 km s^{-1} northeast of the nucleus and $+40$ km s^{-1} southwest of the nucleus.

5.4.3 NGC 449=Mk 1 (Seyfert 2)

Figure 5.9 shows the infrared spectra of NGC 449 along a 156° slit chosen to align with the radio emission, which is slightly extended by $\sim$ 0.9″ along this angle (Ulvestad *et al.* 1981). The infrared lines are only slightly spatially extended, visible 0.67″ northwest and southeast of the nucleus. They do not show any appreciable velocity shifts. Narrowband imaging of [OIII] (Mulchaey *et al.* 1996) shows that the [OIII] emission is extended along the major axis of the galaxy (67°) rather than along the radio axis.

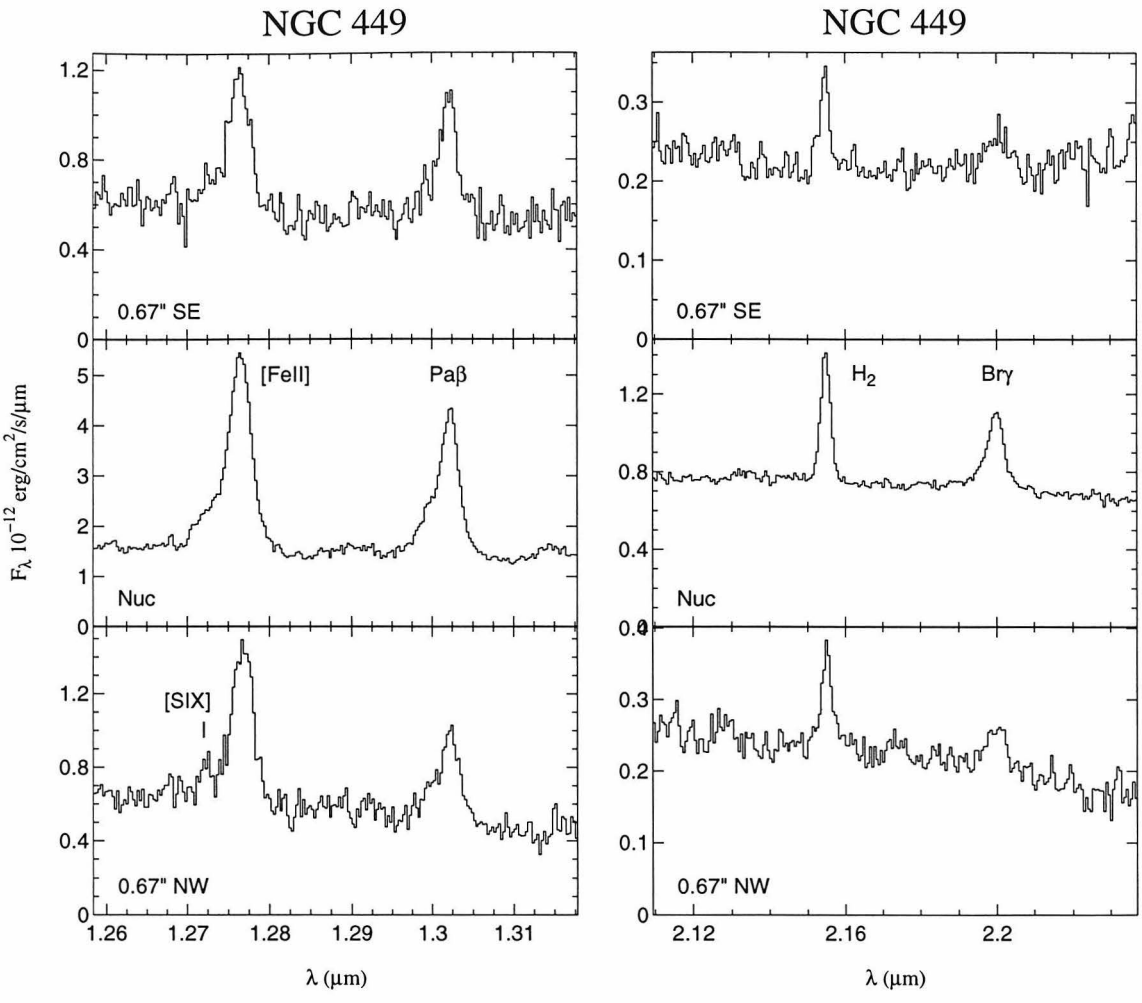

Figure 5.9: Spectra of NGC 449 along a 156° slit. Each spectrum represents the emission in a region of the slit 0.6″ wide by 0.67″ long.

The equivalent widths of the nuclear lines are unusually large in comparison to other Seyfert galaxies. These equivalent widths, found in Table 5.3, are an order of magnitude larger than typical nuclear equivalent widths tabulated in Table 5.3, and are 2–3 times greater than those in other galaxies with "strong" lines, e.g., Mk 1066, NGC 4388, and Mk 3. The [FeII], Paβ, and Brγ lines show profiles similar to the nuclear profiles observed in Mk 3 (Chapter 4). A Gaussian decomposition of these lines (Table 5.5) produced a two-Gaussian fit to each line, with a broader, blueshifted base and a narrow peak. No constraints were placed on any of the Gaussians in the fit. The fit to the [FeII] line included a third Gaussian to represent a faint line on

Table 5.5: Nuclear Gaussian Decomposition of NGC 449.

	[FeII]	Paβ	Brγ	H_2	[SIX]
Flux[a]	8.2±2.6	7.4±0.3	1.6±0.2		
Center[b]	-209±91	-211±16	-170±37		
FWHM[c]	1180±190	1180±30	1230±80		
	6.7±1.2	3.4±0.2	0.9±0.1	2.1±0.1	0.9±0.4
	-22±12	24±9	5±22	-36±15	-180±51
	530±40	380±20	430±50	301±30	430±210

(a): Flux of the Gaussian component in 10^{-15} erg cm^{-2} s^{-1} (b): Centroid of the Gaussian component in km s^{-1} (c): FWHM of the Gaussian component in km s^{-1}.

the blue side of the profile which we identify as [SIX]. A [SIX] line is visible 0.67″ northwest of the nucleus. Other galaxies with [SIX] emission show it concentrated on the nucleus. It is likely that [SIX] emission in the nuclear spectrum is lost within the strong blue wing on [FeII].

Although the broader components of Paβ, Brγ, and [FeII] have widths of 1200 km s^{-1}, they may not be produced in a canonical broad line region. The broad components of Paβ and Brγ are of comparable width to the broad component of [FeII]; the critical density of [FeII] is $\sim 10^5$ cm^{-3}, which is much lower than values usually derived for the broad line region of Seyfert 1.x galaxies. Thus, kinematically the high velocity width components of Paβ and Brγ appear to be associated with a low density environment. In contrast to the other three lines, the H_2 line does not show any evidence for a broad component.

The narrow component of [FeII] on the nucleus is blueshifted relative to the narrow component of Paβ by $\sim$ 45 km s^{-1}. The FWHM of the narrow [FeII] component is also $\sim$ 140 km s^{-1} larger than that of the narrow Paβ component. The Brγ profile is more symmetric than the Paβ profile, represented by less of a velocity difference between the two Gaussian components in its fit. The FWHM of the H_2 line is 290 km s^{-1},

comparable to the FWHM of the narrow component of Paβ. The optical Hβ and [OIII] lines show similar profiles to the Paβ and [FeII] lines, with enhanced blueshifted emission (Bergeron & Durret 1987).

5.4.4 NGC 591=Mk 1157 (Seyfert 2)

Figure 5.10 shows the infrared spectra of NGC 591 along a 152° slit which was chosen to align with the elongation of the [OIII] emission (Mulchaey *et al.* 1996). The optical emission shows increasing excitation (stronger [OIII] as compared to Hα+[NII]) to the southeast than to the northwest. In radio continuum emission, NGC 591 shows a double peaked source separated by 0.6″ at 160° (Ulvestad & Wilson 1989).

In the infrared spectra, there is a weak [SIX] line visible on the nucleus. The other four lines are extended by ±1″ along the slit. At both positions 1″ off of the nucleus along the 152° slit, the Paβ line's velocity is consistent with its nuclear velocity. The [FeII] line does, however, show a velocity gradient along the slit, being redshifted relative to Paβ by 80 ± 20 km s^{-1} 1″ southeast of the nucleus. On the nucleus, in addition to its primary narrow component, the [FeII] line has a FWHM$\sim$ 800 km s^{-1} broad base. No such broad base is visible in Paβ, although Paβ is slightly asymmetric, showing more emission on the red side of the peak.

The Brγ and H_2 lines also show a different velocity structure. While the H_2 line shows no velocity gradient across the slit, the Brγ line redshifted by 80 ± 40 km s^{-1} relative to its nuclear velocity 1″ northwest of the nucleus. The H_2/Brγ ratio is everywhere $\sim$ 2.5, which is higher than the typical value of $\sim$ 1, but not unique among Seyfert galaxies observed in this study.

5.4.5 NGC 4051 (Seyfert 1)

Figure 5.11 shows the spectra of NGC 4051 along an 81° slit. The slit was chosen to align with the radio continuum emission of NGC 4051, which is slightly resolved by $< 1''$ along a position angle of 81° (Kukula *et al.* 1995). Narrowband images of [OIII] also show a small spatial extent similar to the extent of the radio emission along 81°

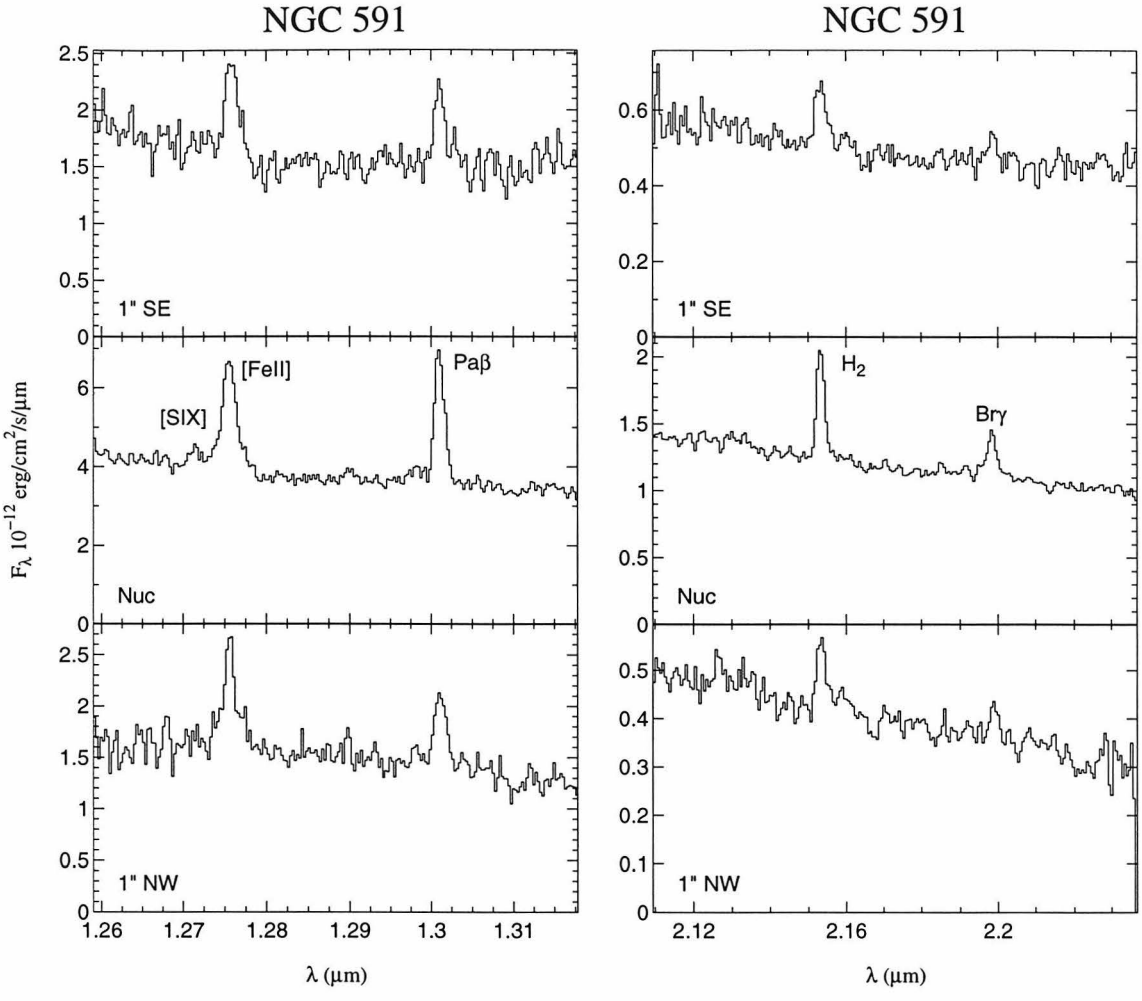

Figure 5.10: Spectra of NGC 591 along a 152° slit. Each spectrum represents the emission in a region of the slit 0.6″ wide by 1.0″ long.

(Haniff *et al.* 1988).

NGC 4051 is optically classified as a Seyfert 1 galaxy (Dahari & DeRobertis 1988), but in the infrared strong broad and narrow components of Paβ are clearly detected. The broad line, with a FWHM of 1300 km s^{-1}, is relatively narrow in comparison to the other broad lines discussed in this paper. The apparent spatial extent of the broad component of Paβ is consistent with spillover resulting from the estimated 1.3″ atmospheric seeing.

The most striking feature of the nuclear spectrum of NGC 4051 is the strength of the [SIX] line and the weakness of the [FeII] line. On the nucleus, the narrow

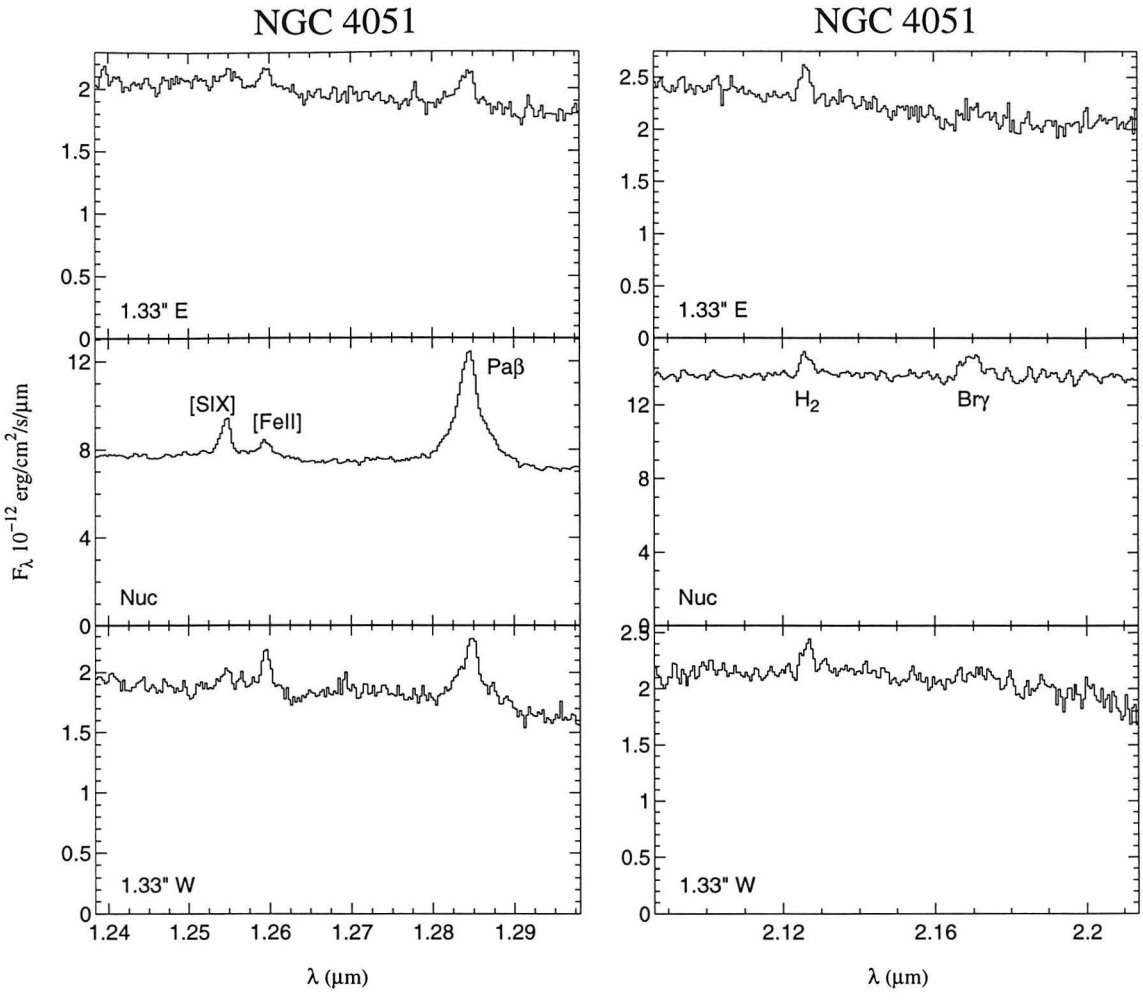

Figure 5.11: Spectra of NGC 4051 along an 81° slit. Each spectrum is within a slit that is 0.5″ wide by 1.33″ long.

[FeII]/Paβ ratio is 0.34, which is one of the lowest values observed in any Seyfert galaxy in this project. The [SIX] line is 1.5 times as bright as the [FeII] line, which is uncharacteristic of other galaxies where [SIX] is detected. While the spatial extent of the infrared lines is marginal, off the nucleus to the west the [FeII] line is brighter than the [SIX] line, indicating that [FeII] is more spatially extended than [SIX]. The narrow [FeII]/Paβ ratio also increases off the nucleus.

The Paβ and H_2 lines are both redshifted 1.33″ west of the nucleus. The Paβ line is redshifted by $+100 \pm 20$ km s^{-1}, and the H_2 line is marginally shifted by $+40 \pm 30$ km s^{-1}. The velocity of the [FeII] line on the nucleus is indistinguishable from the

velocity 1.33″ west of the nucleus, and is consistent with the velocity of Paβ 1.33″ west of the nucleus.

5.4.6 NGC 3227 (Seyfert 1.5)

The infrared spectra of NGC 3227 are plotted in Figure 5.12. The 40° position angle of the slit is similar to the extended optical [OIII] emission, which is extended by $\sim$ 7″ along a position angle of 30°. In the infrared, both a broad (3100 km s^{-1}) and narrow Paβ line are apparent on the nucleus in Figure 5.12. A weak broad Brγ line is also present; Figure 5.13 shows the nuclear spectrum of H_2 and Brγ together with the fits to the two lines in which the weak $\sim$ 1600 km s^{-1} broad Brγ line is visible.

The Paβ line is visible 1″ off the nucleus in both directions along the slit, while the [FeII] line is visible up to 2″ off the nucleus in both directions. The narrow [FeII]/Paβ ratio increases weakly with distance from the nucleus to the southwest, although the signal-to-noise ratio of the data does not make this a strongly significant effect. No narrow Brγ line is detected on or off the nucleus. The H_2 line is distinctly detected between 1″ SW of the nucleus and 2″ NE of the nucleus.

None of the off-nuclear lines shows a velocity centroid appreciably different from their velocity on the nucleus. To the northeast, Mundell *et al.* (1995) report that the FWHM of the Hα and [NII] lines are 450-600 km s^{-1}, whereas to the southwest lines are narrower. In contrast, in the infrared, where the signal-to-noise ratio is good enough to allow a reliable measurement, the narrow line widths do not vary significantly with position, but are rather generally within the range of 350-600 km s^{-1}. The [FeII] line is narrower to the northeast, but the detection of the line and the measurement of its width here is marginal.

5.4.7 Mk 359 (Seyfert 1.5)

Figure 5.14 shows the 1.29μm spectra of Mk 359 along a 20° slit oriented perpendicular to the major axis of the galaxy. The strongest line visible in the spectrum is the Paβ line. The [FeII] line is weak. The [SIX] line is visible in this galaxy, and is stronger on

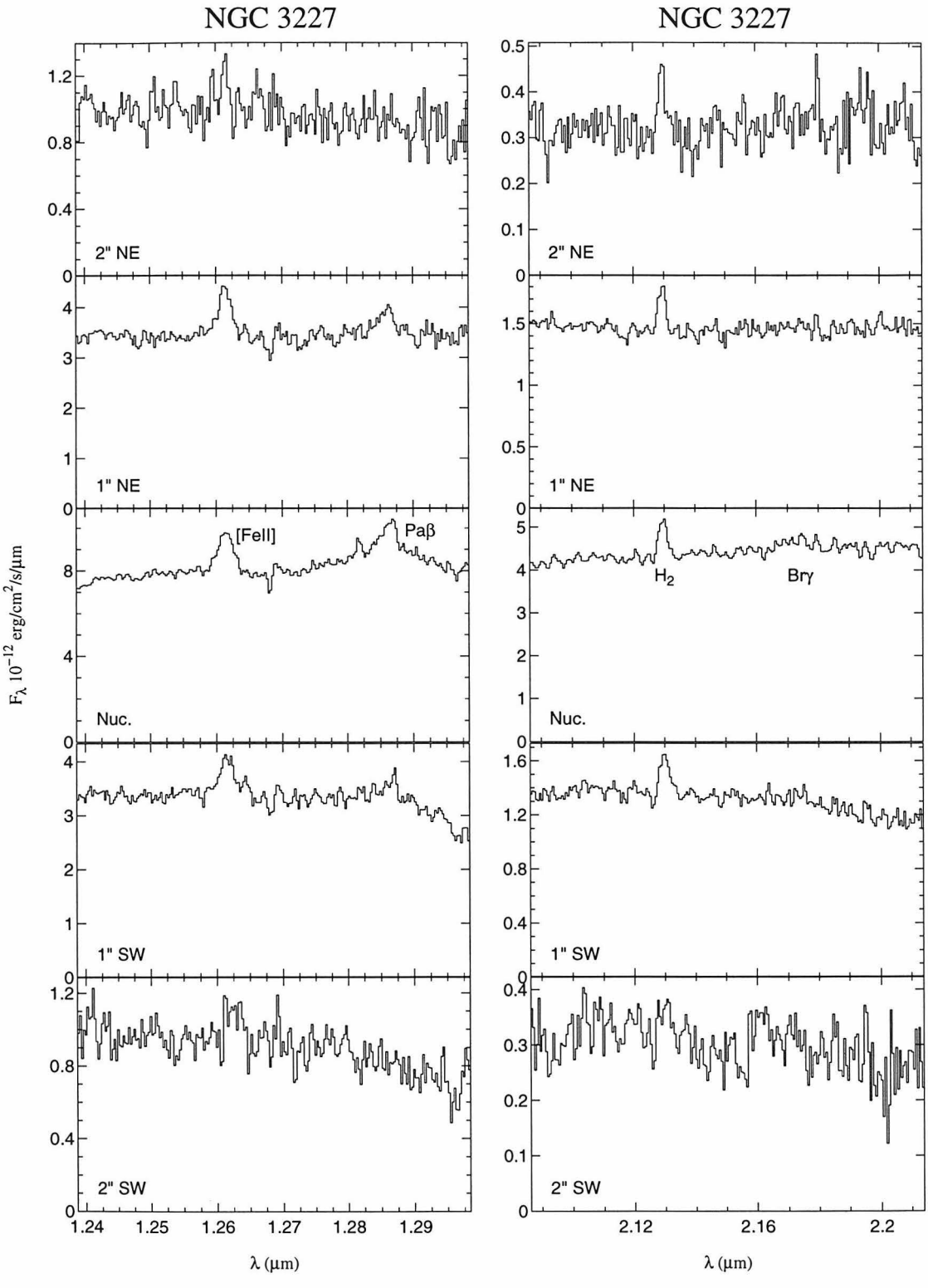

Figure 5.12: Spectra of NGC 3227 along a 40° slit. Each spectrum is within a spatial region that is the width of the slit, 0.5″, by 1.0″ along the slit.

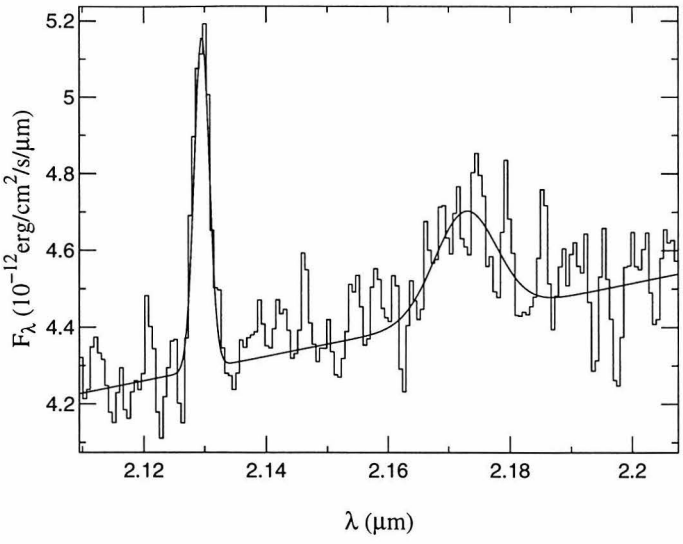

Figure 5.13: Zero-suppressed nuclear spectrum of NGC 3227. The line drawn through the data shows the two single Gaussian fits to the narrow H_2 and broad Brγ lines, over a linear continuum.

the nucleus than the [FeII] line. The apparent P-Cygni-like profiles blueward of [SIX] and redward of [FeII] (each marked with an X in Figure 5.14) are the result of poor atmospheric correction. The Paβ and [FeII] lines are marginally spatially extended. The [FeII] line is stronger than the [SIX] line 0.67″ south of the nucleus, indicating that the spatial extent of the [FeII] emission is greater than that of the [SIX] emission.

A broad Paβ line is visible on the nucleus. At 1100 km s^{-1}, this broad line is narrower than most of the broad lines seen in Seyfert 1 and intermediate type galaxies, although it is comparable in width to the strong broad line of NGC 4051 (Figure 5.11). The optical broad lines are also relatively narrow at $\sim$ 800 km s^{-1} (Veilleux 1991). This broad Paβ line also appears to be redshifted relative to the narrow line. It may not actually represent a classical broad line region (BLR), but rather it is possible that the red wings on the Paβ profile may result from additional narrow components blended with the main profile. Unlike broad lines characteristic of a classical BLR, the broad redshifted Paβ emission is extended to the north. However, unlike the case of Mk 1 (section 5.4.3), the broadened emission is only seen in hydrogen recombination emission. The [FeII] line is narrow with a FWHM of $<$ 150 km s^{-1}, and the optical forbidden and narrow permitted lines are narrow with FWHM near $\sim$ 100 km s^{-1} (Veilleux 1991).

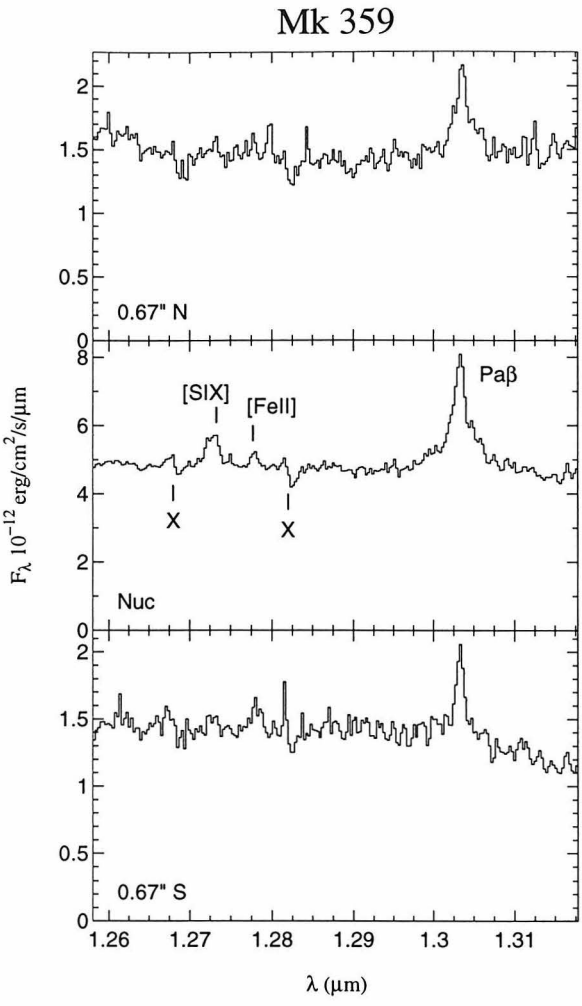

Figure 5.14: Spectra of the MK359 along a 20° slit. Each spatial bin is 0.67″ along the slit by 0.6″, the width of the slit.

5.4.8 NGC 262=Mk 348 (Seyfert 2)

Figures 5.15 and 5.16 show the spectra of NGC 262 taken a 15° slit and a 270° slit respectively. The 15° slit was chosen to nearly align with the 6cm radio emission, which is extended by $\sim 18''$ along a position angle of $\sim 13°$ (Baum *et al.* 1993). The Paβ, Brγ, [FeII], and H_2 lines are strong on the nucleus, and marginally extended along the slit oriented at 15°. None of the lines are extended along the slit at PA 270°. On the nucleus, a weak [SIX] line is visible. Narrowband [OIII] emission shows that the ionized gas has a halo morphology extended along a similar position angle of $\sim 12°$ (Mulchaey *et al.* 1996). Simpson *et al.* (1996a) detect a biconical structure in an image of the ratio of [OIII] and Hα+[NII]. Along a position angle of $\sim 170°$ they

identify regions of high excitation $\sim 2''$ north and south of the nucleus. Although the angle of the 15° infrared slit is 25° different from the angle to the identified regions of high excitation, there are no infrared lines visible in the regions of the slit which overlap these regions.

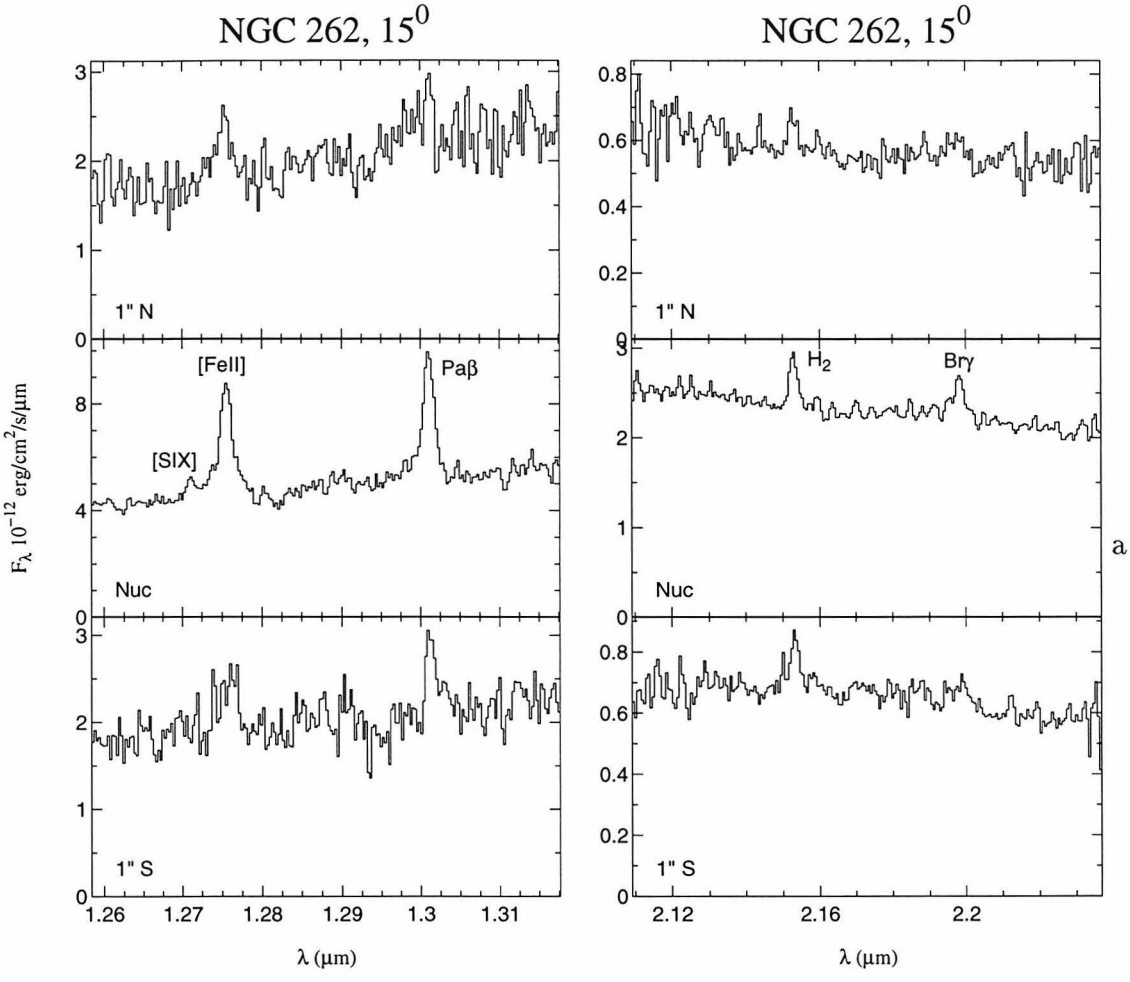

Figure 5.15: Spectra of NGC 262 along a 15° slit. Each spectrum represents the emission in a region of the slit $0.6''$ wide by $1.0''$ long.

Miller & Goodrich (1990) reported the detection of a broad Hα line in NGC 262 in polarized flux with a FWHM of 7400 km s^{-1}. There is no evidence of a line that broad in either the Paβ or Brγ data presented here. Ruiz *et al.* (1994) report a FWHM=884 km s^{-1} broad line in Paβ in NGC262. However, this line is shifted to the blue of the narrow Paβ line, and is probably dominated by the HeI and [FeII]

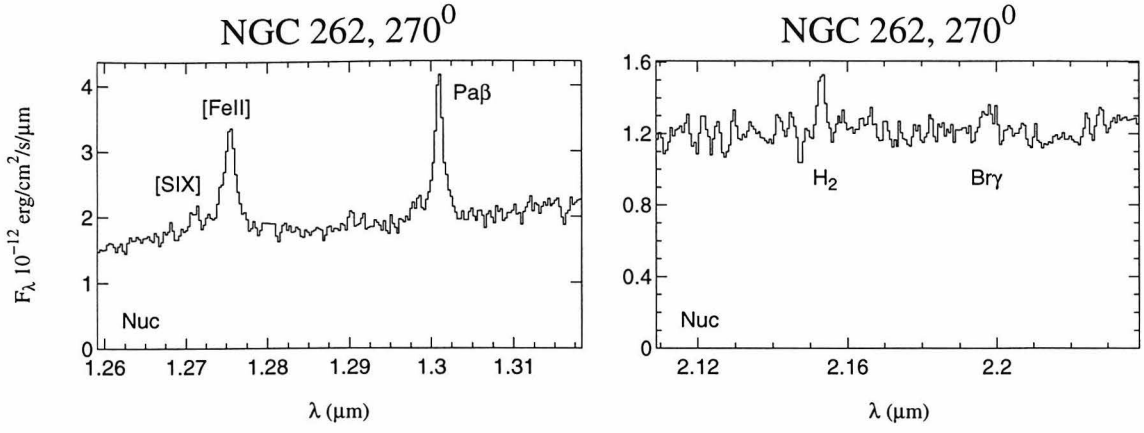

Figure 5.16: Spectra of NGC 262 along a 270° slit. Each spectrum represents the emission in a region of the slit 0.5″ wide by 1.0″ long.

emission discussed in section 5.3. In Figures 5.15 and 5.16, the Paβ line profile also shows an enhanced red wing, suggestive of a broad $\sim$ 800 km s^{-1} base with $\sim$ 30% of the flux in the Paβ line. As is the case with NGC 449, a similar broad base is visible in the profile of the [FeII] line.

5.4.9 NGC 2273=Mk 620 (Seyfert 2)

Figure 5.17 shows the infrared spectra of NGC 2273. The 120° slit was chosen to align with the position angle of a region of Hα+[NII] emission located $\sim$ 13″ away from the nuclueus (Mulchaey *et al.* 1996), but no infrared line emission was observed at this position. Rather, the infrared lines are extended by $< 1.5''$. There are no strong variations in the flux ratios or velocities of the infrared lines along the slit.

On the nucleus, the [FeII]/Paβ ratio is 0.91±0.10, a typical value for Seyfert 2 galaxies. The H_2/Brγ ratio, however, is 2.20±0.34, somewhat larger than that seen in most of the observations presented here. The nuclear [FeII] line is blueshifted relative to the Paβ line by 71 ± 13 km s^{-1}. The Paβ, Brγ, and H_2 lines are all consistent with unresolved lines, but the [FeII] line is marginally resolved with a width of 280 km s^{-1}.

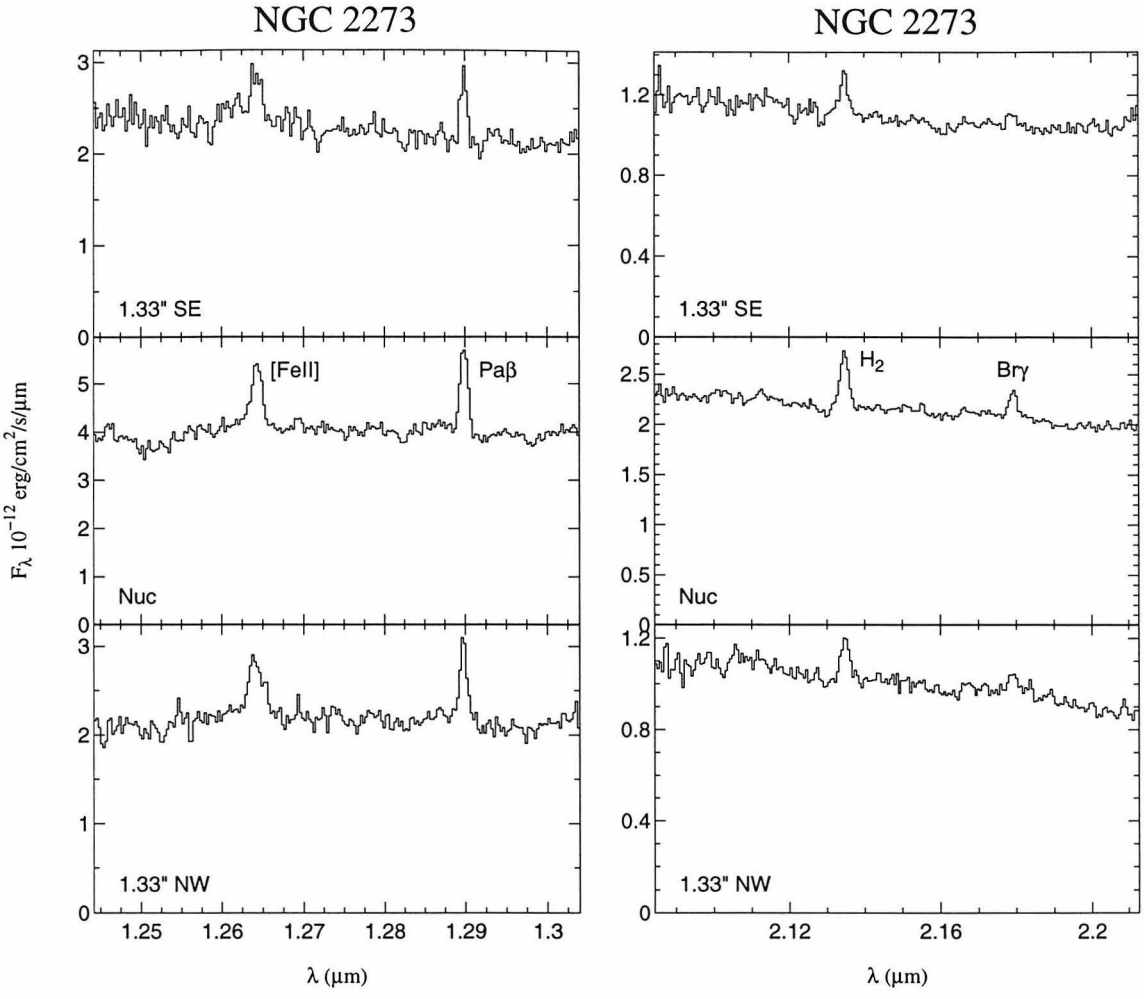

Figure 5.17: Spectra of NGC 2273 along a 120° slit. Each spectrum represents the emission in a region of the slit 0.6″ wide by 1.33″ long.

5.4.10 NGC 7682 (Seyfert 2)

Figure 5.18 shows the infrared spectra of NGC 7682. The slit was oriented at 60° to align it with the strongest of several weak HII regions visible within 10–15″ of the nucleus. The ionized gas around the nucleus itself is unresolved (Brodie *et al.* 1987), as is the radio emission (Kukula *et al.* 1995). No emission lines were seen in the infrared at the position of the HII region.

The dominant feature of this spectrum is the large nuclear $H_2/Br\gamma$ ratio of 3.4±0.4. Although not the largest $H_2/Br\gamma$ ratio observed, it is among the largest $H_2/Br\gamma$ flux

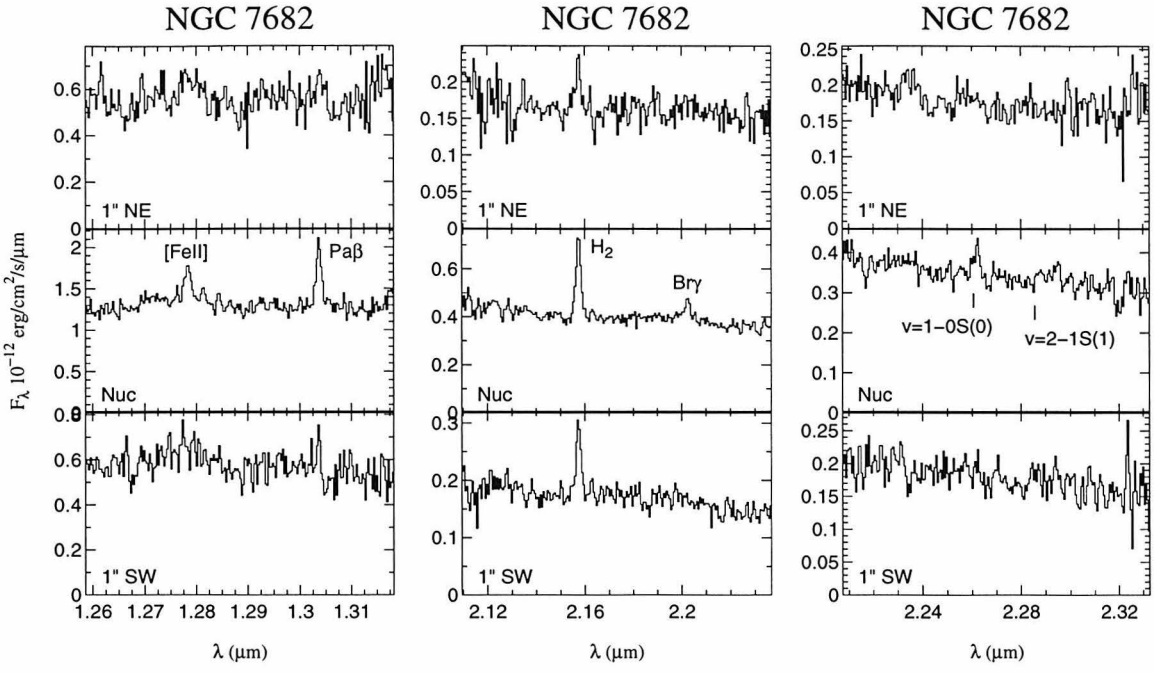

Figure 5.18: Spectra of NGC 7682 along a 60° slit. Each spatial bin is 1.0″ along the slit by 0.6″ wide.

ratios seen in the seyferts of this sample. The large ratio results from a strong H_2 line, whose equivalent width is a factor of 2–10 greater than that observed in most of the galaxies tabulated in Table 5.3, and is exceeded only slightly by the equivalent width of H_2 on the nucleus of NGC 449 (section 5.4.3). The H_2 line is the only emission line which is spatially resolved, showing emission at $\pm 1''$ along the 60° slit.

Because of the strength of the H_2 emission, NGC 7682 was also observed at a third range wavelength which covers rest wavelengths of 2.21μm–2.33μm. This third range includes two additional lines of molecular hydrogen: v=1-0S(0) ($\lambda = 2.2227\mu$m) and v=2-1S(1) ($\lambda = 2.2471\mu$m). The v=1-0S(0) line is detected at a flux level of 0.26±0.04 the v=1-0S(1) line. The v=2-1S(1) line is undetected to a limit of < 0.2 of the strength of the v=1-0S(1) line. This implies that ultraviolet fluorescence cannot be responsible for the bulk of the H_2 emission in NGC 7682, because it predicts a v=2-1S(1)/v=1-0S(1) ratio of ~ 0.5 (Moorwood & Oliva 1990). Rather, the H_2 emission must be excited thermally, probably through either x-ray or shock heating of molecular clouds.

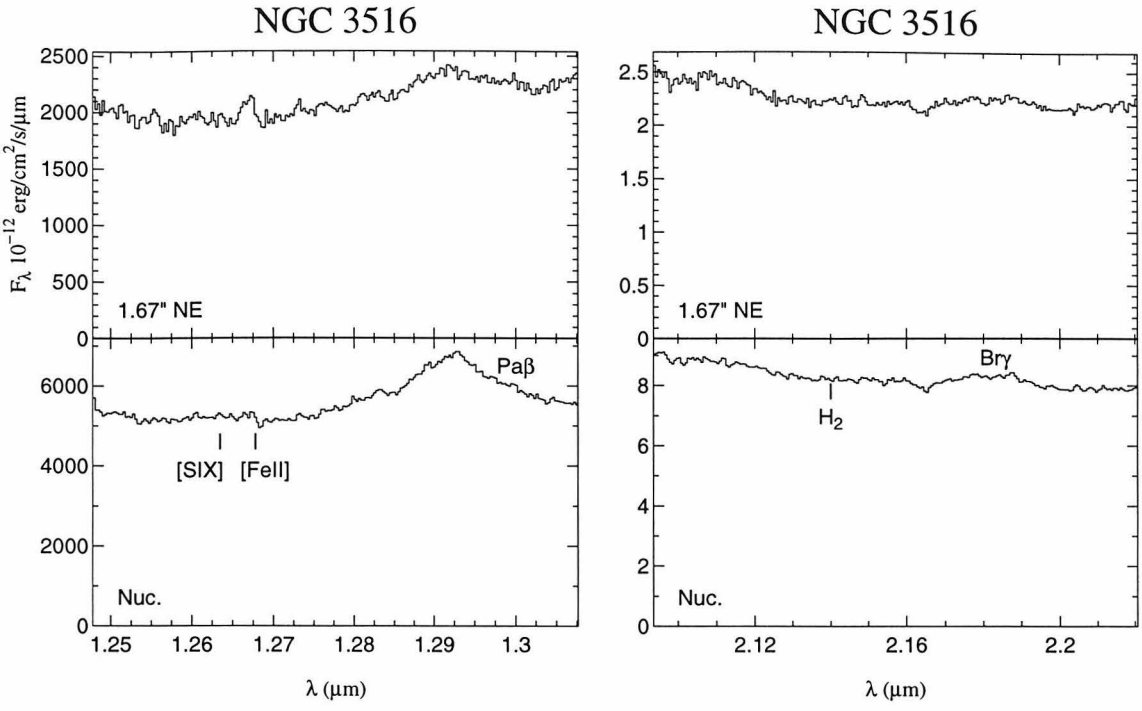

Figure 5.19: Spectra of NGC 3516 in a 0.6″ wide by 1.67″ long beam along a 35° slit.

5.4.11 NGC 3516 (Seyfert 1.5)

The nuclear spectrum of NGC 3516 through a 35° slit (Figure 5.19) shows a strong broad Paβ line. Although NGC 3516 is optically classified as a Seyfert 1.5 galaxy (Osterbrock & Martel 1993), the Paβ line does not show a well defined narrow component. The line has a non-Gaussian shape, but may be described by three Gaussian components with FWHM of 4500 km s^{-1}, 2000 km s^{-1}, and 700 km s^{-1}. A weak broad Brγ line is also present, and was successfully fit with a single Gaussian of width 2300 km s^{-1}. Because of the strength of the continuum, the broad Brγ line is not immediately apparent in Figure 5.19. Figure 5.20 is a zero-suppressed spectrum in which the broad Brγ line is visible. (The apparent absorption line on the blue side of the broad Brγ line is the result of poor correction for Brγ absorption in the G-star used to calibrate the atmospheric transmission.) The broad Brγ line appears $\sim$ 1000 km s^{-1} narrower than the broad Paβ line, although this is probably an effect of the weaker wings corresponding to the 4500 km s^{-1} component of the Paβ line being lost in the

noise.

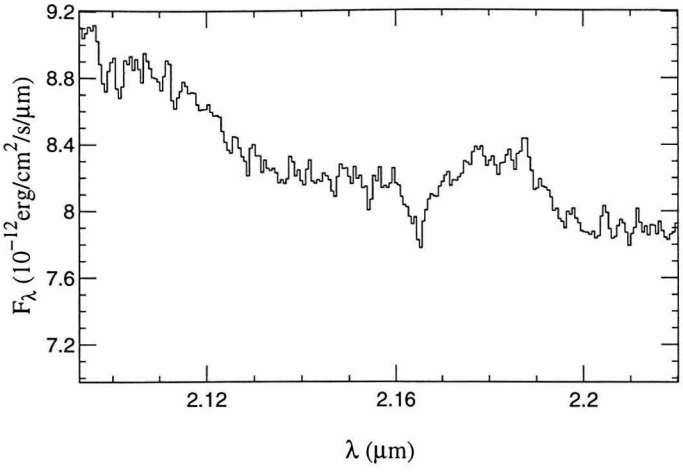

Figure 5.20: Zero-suppressed nuclear spectrum of NGC 3516, plotted in order to bring out the broad Brγ line.

No strong narrow lines are visible on the nucleus. Because the continuum on the nucleus is so bright, the upper limit on the flux of [FeII] on the nucleus is 1.8×10^{-15} erg cm^{-2} s^{-1}; the detection of an [FeII] line is hampered by the presence of a strong atmopsheric O_2 absorption line which overlaps the red side of the wavelength of [FeII]. The only off nuclear line detected is [FeII] which is present 1.67″ NE of the nucleus with a strength of 0.8×10^{-15} erg cm^{-2} s^{-1}. Optical narrowband imaging of Hα performed by Veilleux *et al.* (1993) shows that the NLR of NGC 3516 is extended in a Z-shaped structure, extended intially at a position angle of 30–35°. The Hα emission extends out as far as 20″, with most of the flux being within 10″ of the nucleus. The surface brightness of Hα near the nucleus is $\sim 10^{-14}$ erg cm^{-2} s^{-1} arcsec^{-1}. Under case B conditions, assuming no dust extinction, we would predict a Paβ flux of $\sim 0.6 \times 10^{-15}$ erg cm^{-2} s^{-1} within one of our spatial bins, which is comparable to or lower than the limits on the detection of a narrow Paβ line near the nucleus.

5.4.12 NGC 7469=Mk 1514 (Seyfert 1)

The infrared spectrum of NGC 7469 has been studied extensively by Genzel *et al.* (1995), so the observations of this galaxy will be discussed only briefly here. NGC 7469 is believed to be a composite system, showing signs of both Seyfert activity and active circumnuclear star formation within a radius of $\sim 5''$ of the nucleus. In particular,

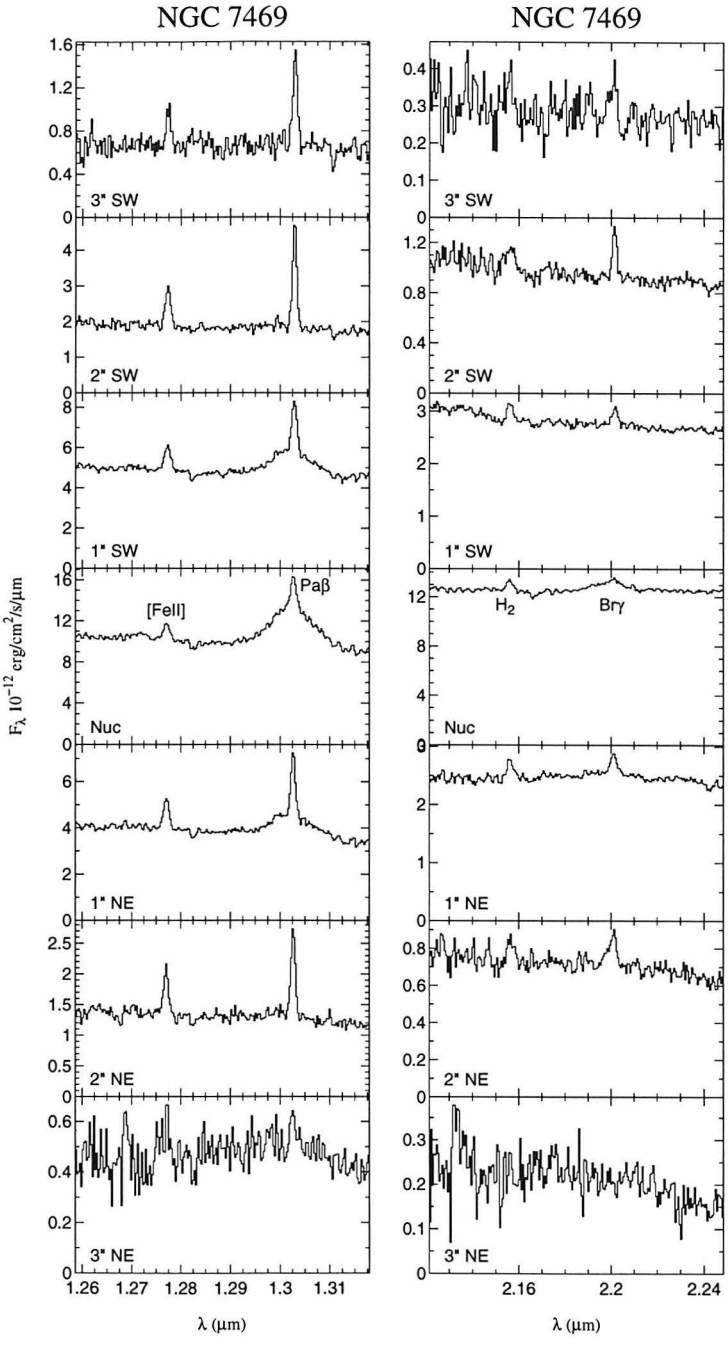

Figure 5.21: Spectra of the NGC 7469 along a 240° slit. Each spatial bin is 1.0″ along the slit by 0.6″, the width of the slit.

there is a ring of star formation at a radius of $\sim 1.5''$.

Figure 5.21 shows the spectra of NGC 7469 along a slit oriented at position angle 240°. A strong broad Paβ line with a FWHM of 2430 ± 80 km s^{-1} is visible on the nucleus, as is a weaker broad Brγ line with a FWHM of 2200 ± 500 km s^{-1}. [FeII], Paβ, H_2, and Brγ lines are visible extended over $6''$ along a position angle of 240°. Although weak infrared coronal [SiX] and [SiVI] emission has been observed in this galaxy (Thompson 1996; Genzel *et al.* 1995), the [SIX] line is undetected.

The [FeII]/Paβ ratio off the nucleus is $\lesssim 0.6$, which is lower than that seen in most Seyfert galaxies, but is within the range seen in starburst galaxies (Simpson *et al.* 1996b). On the nucleus, the [FeII]/Paβ ratio is marginally higher at 0.7. The H_2/Brγ ratio is ~ 1 along the length of slit. It is higher on the nucleus, but the ratio is uncertain due to potential errors in deblending the broad and narrow components of Brγ. This H_2/Brγ ratio is a factor ~ 1.7 greater than the ratio of the fluxes of the two lines listed by Genzel *et al.* (1995); the reason for the discrepancy is unknown.

The velocities of the narrow components of [FeII] and Paβ lines are consistent, and show a monotonic velocity gradient with increasing velocity to the southwest. The [FeII] line is in general 30–80 km s^{-1} broader than Paβ. Both lines are narrower off the nucleus than on the nucleus. The H_2 and Brγ lines do not share this velocity structure, but instead are generally redshifted as well as broader in comparison to [FeII] and Paβ. Note, however, that the detections of H_2 and Brγ are not as clean.

5.4.13 Mk 993 (Seyfert 1/1.9)

Mk993 was originally classified as a Seyfert 2 system. However, between 1983 and 1991, a variable broad line was observed in the galaxy so that it might be classified as a Seyfert 1, 1.5, or 1.9 (Tran *et al.* 1992), depending on the epoch of the observation. Based on this variation, Osterbrock & Martel (1993) give it the median classification of Seyfert 1.5.

Figure 5.22 shows the nuclear infrared spectra of Mk 993 through a slit oriented at 150°, the position angle of the major axis of the 2.2μm continuum (McLeod & Rieke

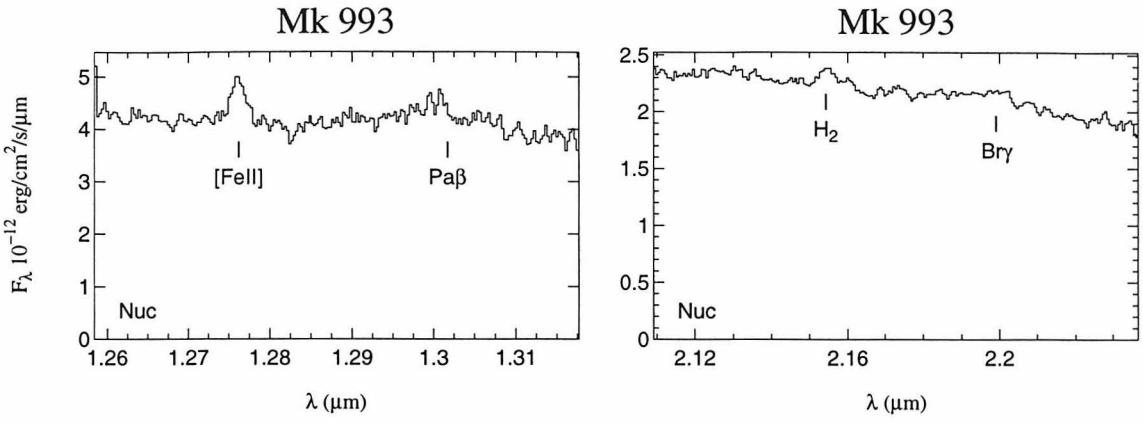

Figure 5.22: Spectra of the nucleus of Mk993 in a $0.6'' \times 1.3''$ slit.

1995). The [FeII] line is clearly detected, and the H_2 line is weakly detected. The narrow component of the Paβ line is weak, and the [FeII]/Paβ flux ratio for Mk 993 is 2.5±0.8, a value relatively high in comparison to most Seyfert galaxies. In addition to the narrow Paβ line, there is a weak broad component of Paβ. A weak broad Brγ line is also marginally detected, although its amplitude is comparable to the level of variation in the continuum. No lines were detected off of the nucleus in Mk 993.

5.4.14 NGC 5273 (Seyfert 1.9)

The spectra of NGC5273 (Figure 5.23) along the major axis of the galaxy (10°) show narrow [FeII] emission, as well as weak narrow and broad components of Paβ. The [FeII] emission is slightly extended along the 10° slit, although the off-nuclear detections are marginal. This object does not show any extent in narrowband images centered on optical [OIII] lines (Mulchaey *et al.* 1996). In 6cm radio flux, Ulvestad & Wilson (1984a) report that the weak core is slightly elongated at 0^0.

5.4.15 NGC 6814 (Seyfert 1)

NGC 6814 (Figure 5.24) is the only Seyfert 1.x galaxy presented here which did not show a broad Paβ or Brγ line. Between 1983 and 1985 the strength of the broad Hβ line in 6814 varied by more than a factor of two (Sekiguchi & Menzies 1990), changing

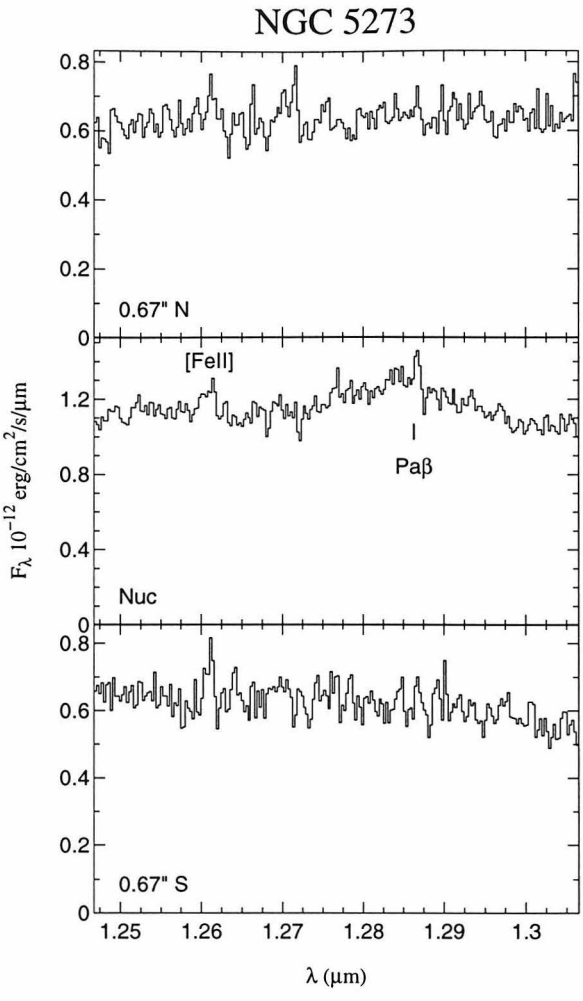

Figure 5.23: Spectra of NGC 5273 along a 10° slit. Each spatial bin is 1.33″ along the slit by 0.6″, the width of the slit.

its classification from a type 1 Seyfert galaxy to a type 1.8. It is possible that the non detection of a broad Paβ line is due to the fact that NGC 6814 was in a quiescent state at the time of the observations.

The [FeII] line is much stronger on the nucleus than the Paβ line, whose detection is marginal at best. The [FeII]/Paβ flux ratio is 5.8±4.2, although the uncertainty in that flux ratio is dominated by the uncertainty in the narrow Paβ detection. The lower limit on the [FeII]/Paβ flux ratio is 2.9, which is higher than every other Seyfert galaxy observed here except for NGC 2110 (Chapter 4).

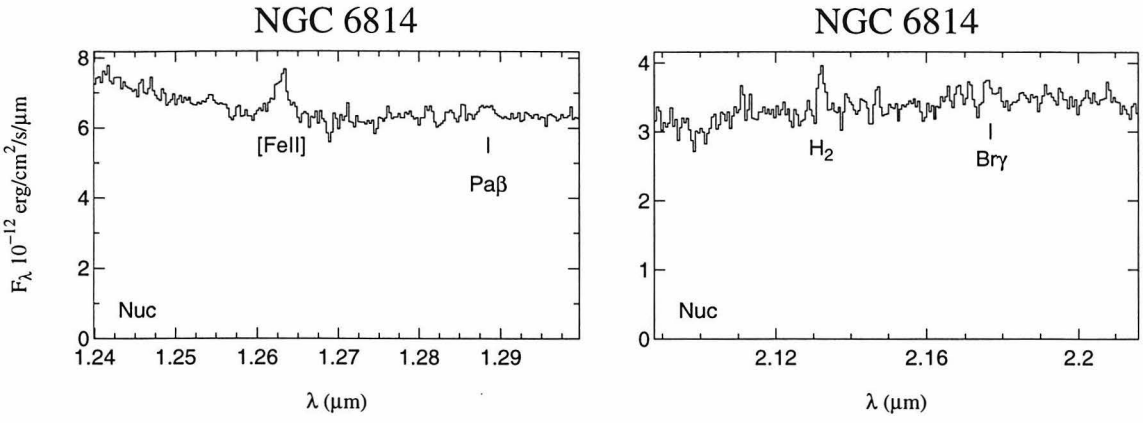

Figure 5.24: Spectra of the nucleus of 6814 in a $0.7'' \times 2.0''$ slit.

5.4.16 NGC 7450=Mk 1126 (Seyfert 1.5)

The spectrum of NGC 7450 along a 107° slit (Figure 5.25) shows a noisy broad Paβ line on the nucleus with a FWHM of 3600±1200 km s^{-1}. This broad line detection should be considered marginal because its amplitude is close to the level of low frequency variations in the continuum. The fit width to Paβ is not significantly broader than the 2500 km s^{-1} broad Hβ line reported by Osterbrock & Pogge (1985). Narrow Paβ, [FeII], and [SIX] lines are all visible on the nucleus. The [FeII] line has broad ($\sim$ 1000km s^{-1}) wings on the nucleus, but its profile is uncertain due to the presence of a strong atmospheric O_2 absorption line at the wavelength of [FeII] in NGC 7450. The [SIX] line is very strong in comparison to the narrow component of Paβ on the nucleus, with the two lines of comparable strength.

The H_2 and [FeII] lines are marginally detected $1''$ west of the nucleus. The narrowband Hα and [OIII] emission of the nucleus of NGC 7450 is spatially unresolved on scales of $\sim 1''$ (Pogge 1989). The radio continuum emission is extended by $\gtrsim 2''$ along a position angle of 107° (Ulvestad & Wilson 1989), coincident with that of our slit.

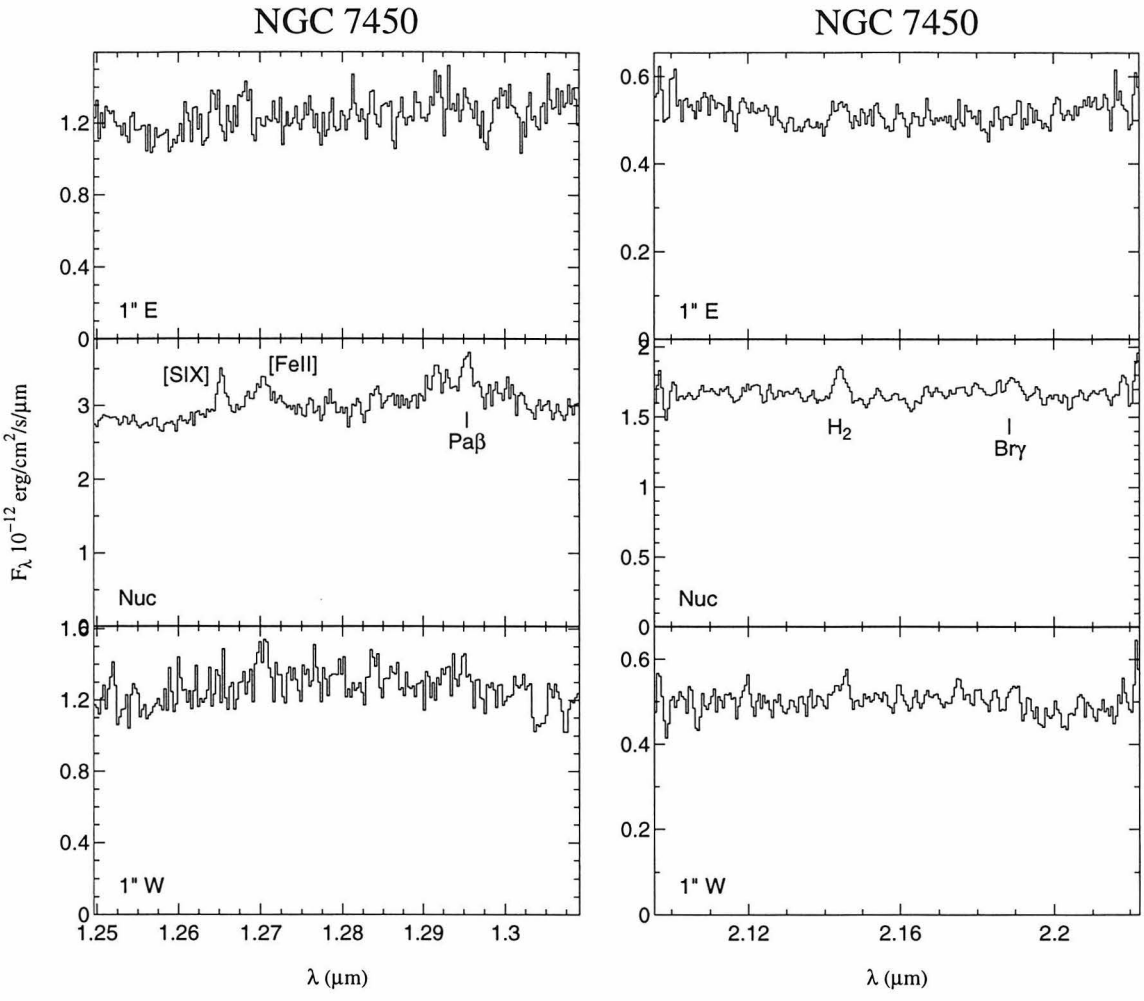

Figure 5.25: Spectra of NGC 7450 along a 107° slit. Each spectrum represents the emission in a region of the slit 0.6″ wide by 1.0″ long.

5.4.17 NGC 1667 (Seyfert 2)

The only emission line seen in NGC 1667 (Figure 5.26) is a noisy detection of [FeII] on the nucleus. Paβ is not visible, with an upper limit on its equivalent width of $1.8 \times 10^{-4}\mu$m. The [FeII]/Paβ flux ratio, with a lower limit of 2.3, is relatively high for the Seyfert galaxies presented here. There are no data available in the 2.16μm wavelength range.

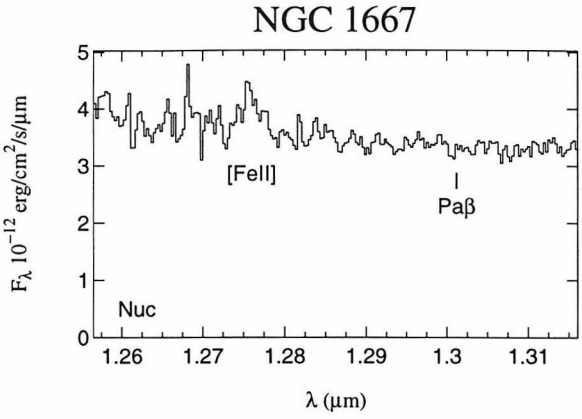

Figure 5.26: Spectra of the nucleus of NGC 1667 with a 164° slit. The spectrum represents data within a slit that is 0.6″ wide by 1.67″ long.

5.4.18 NGC 5347 (Seyfert 2)

Figure 5.27 shows the nuclear spectra of NGC 5347. There are clear detections of Paβ and H_2, and weak detections of [SIX] and [FeII]. The redshift of NGC 5347 is such that the atmospheric O_2 line degrades the quality of the detection of [FeII], and may lead to an underestimate of the [FeII] flux. The measured [FeII]/Paβ flux ratio in NGC 5347 is lower than it is for any other Seyfert 2 galaxy, although the significance of this result is limited by the uncertainty in the [FeII] flux. The lower limit on the H_2/Brγ flux ratio is 1.5.

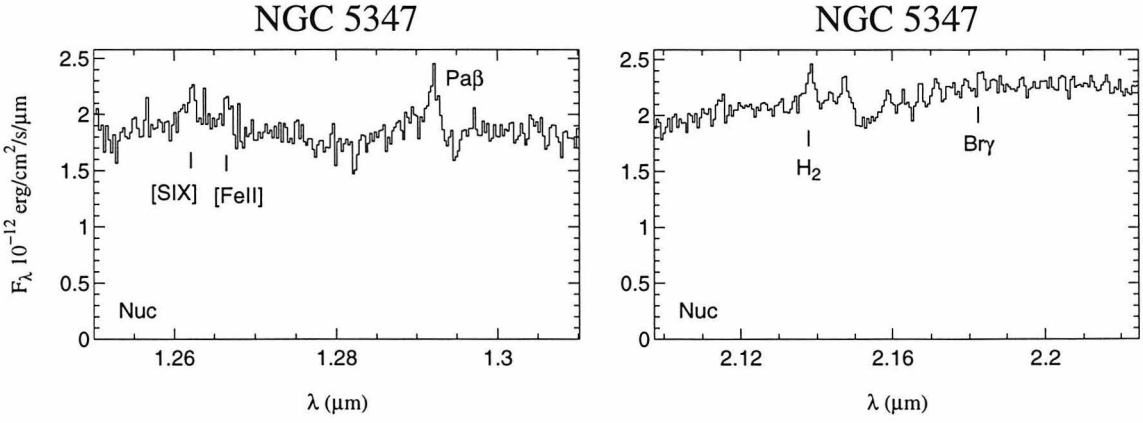

Figure 5.27: Spectra of NGC 5347 along a 270° slit. Each spatial bin is 1.0″ along the slit by 0.5″ wide.

The lines are not detectably extended along the slit, which was arbitrarily oriented

at 270°. Narrowband imaging of NGC 5347 shows that the [OIII] distribution in the center of the galaxy is extended to the northeast along a position angle of ~40°, with a knot of [OIII] 3.6″ away from the nucleus in that direction. The 270° slit of the infrared data does not intersect this knot.

Chapter 6

Summary of Results

6.1 Introduction

This chapter summarizes the results of the program designed to probe the infrared line emission of the nuclear and circumnuclear regions of Seyfert galaxies. Longslit spectra with spectral resolutions $\lambda/\Delta\lambda \sim 1000$ and spatial resolutions of $\sim 10^2$ pc have been presented earlier in Chapters 3 through 5. The selection of the sample and the list of galaxies observed is described in those chapters. The purpose of this chapter is to pull together the observations in order to identify global trends, and to attempt to draw conclusions from the results. This chapter will form the core of a paper to be submitted for publication to *The Astrophysical Journal.*

6.2 Results

As was discussed in earlier chapters, most of the objects showed narrow emission lines of Paβ (λ=1.2818μm), Brγ (λ=2.1655μm), [FeII] (λ=1.2567μm), and H_2 (λ=2.1213μm). In many of these objects, narrow emission lines were observed to be extended by 1–8″ along the slit. Detected broad hydrogen recombination lines are presented in section 5.3.1. Detected narrow hydrogen recombination lines are discussed in section 5.3.2.

In addition to the Paβ, [FeII], H_2, and Brγ lines, nine of the objects, including five Seyfert 2 galaxies and four Seyfert 1.x galaxies, show detections of a line on the blue side of [FeII] which is identified as the fine structure line [SIX], whose wavelength was measured in the solar corona to be 1.25249μm (Kuhn, Penn, & Mann 1996). The identification of this line as [SIX] is argued in Section 4.3.3 in Chapter 4. Although many of the objects do not have strong spatially extended emission in any infrared line observed, the [SIX] line appears to be less spatially extended along the slit than the other lines in the 1.27μm wavelength band. This concentration on the nucleus is characteristic of what is observed for both infrared and optical coronal lines (e.g., Genzel *et al.* 1995; Oliva *et al.* 1994).

6.2.1 Nuclear Kinematics

It is worth comparing the Paβ and Brγ velocities, because both lines are part of the hydrogen recombination cascade. Any differences in the kinematics of the two lines may indicate the presence of dust, as the longer wavelength Brγ is less affected by extinction than Paβ. In general, the velocities of the peaks of the Brγ and Paβ lines are consistent with each other to within the resolution of the data. In some objects, however, the Brγ line is slightly shifted relative to the Paβ line. Figure 6.1 is a histogram of the difference between the peak velocity of the narrow Brγ and Paβ lines. Typical uncertainties on the difference between the Brγ and Paβ velocity peaks are 20–40 km s^{-1}.

As Figure 6.1 shows, there is a marginal trend for the Brγ line on the nucleus to be redshifted relative to the Paβ line by < 150 km s^{-1}. The average difference between Brγ and Paβ velocity centroids is ~ 30 km s^{-1}. The same trend is present in the off-nuclear data. This trend suggests that outflows contribute to the observed velocity gradients in many objects. If receding gas is behind the disk of the galaxy, more of the higher velocity Brγ than Paβ would penetrate dust in the disk, yielding a Brγ profile shifted to the red of the Paβ profile. Because of limited statistics, it is impossible to determine if there is a difference in the trend for the two different types

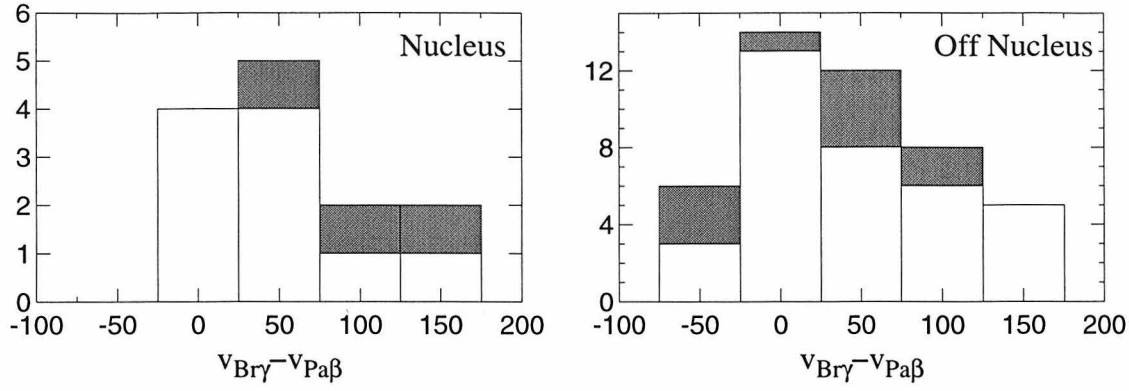

Figure 6.1: Histogram of the velocity difference (in km s^{-1}) between the narrow components of the Brγ and Paβ lines. Shaded bars are for Seyfert 1.x galaxies, and open bars are for Seyfert 2 galaxies. The left plot has the results on the nucleus; the right plot has the the results for resolved off-nuclear positions.

of object, although the data suggest that a systematic redshift of Brγ relative to Paβ is present in both Seyfert 2 and Seyfert 1.x galaxies.

Because the nature of the [FeII] and H_2 emission in Seyfert galaxies is less well understood than that of the hydrogen recombination lines, it is of interest to compare the kinematics of these two species with those of the Paβ and Brγ lines. Because the [FeII] and Paβ lines are observed simultaneously, the spectra are guaranteed to sample the same projected spatial region at the same resolution for the two different species. In addition, the lines are close enough in wavelength that differential extinction effects should be negligible. As such, comparisons between the kinematics of these two species should be fairly robust. Similarly, H_2 and Brγ are observed simultaneously, allowing for robust comparisons between those two species.

Figure 6.2 shows the difference between the full width at half maxima (FWHM) of the [FeII] and Paβ lines versus the difference in their peak velocities for the nuclear and off-nuclear spectra. One feature immediately apparent from these plots is that the [FeII] line appears to be systematically wider than the Paβ line on the nucleus. For Seyfert 2 galaxies, the [FeII] line is typically wider by 60–150 km s^{-1}, with some off-nuclear differences as great as 300–400 km s^{-1}. For Seyfert 1.x galaxies, both the scatter and the uncertainties are greater, but the trend remains that the [FeII] line is

$\sim$ 100 km s^{-1} wider than the Paβ line. Off of the nucleus, the scatter is greater, but [FeII] remains on average $\sim$ 70 km s^{-1} wider than Paβ.

There is also a marginal trend in Seyfert 2 galaxies for the peak of the [FeII] line to be blueshifted by $\lesssim$100 km s^{-1} relative to the Paβ line, both on and off of the nucleus. (A blueshift of [FeII] relative to Paβ corresponds to a positive $v_{\mathrm{Pa}\beta} - v_{[FeII]}$ in Figure 6.2.) Although in many of the objects the difference is not much greater than the uncertainty in the differences, the locus of the scatter plots in Figure 6.2 is shifted to a positive difference between the Paβ and [FeII] peak velocities. The average difference between the [FeII] and Paβ velocity centroids is $\sim$ 40 km s^{-1} on the nucleus, and $\sim$ 25 km s^{-1} off of the nucleus. The average difference is slightly ($\sim$ 10 km s^{-1}) greater for Seyfert 2 than Seyfert 1.x galaxies both on and off of the nucleus.

Figure 6.3 shows the difference in FWHM versus the difference in velocity peak for the H_2 and Brγ lines in the nuclear and off-nuclear spectra. There is no trend in the

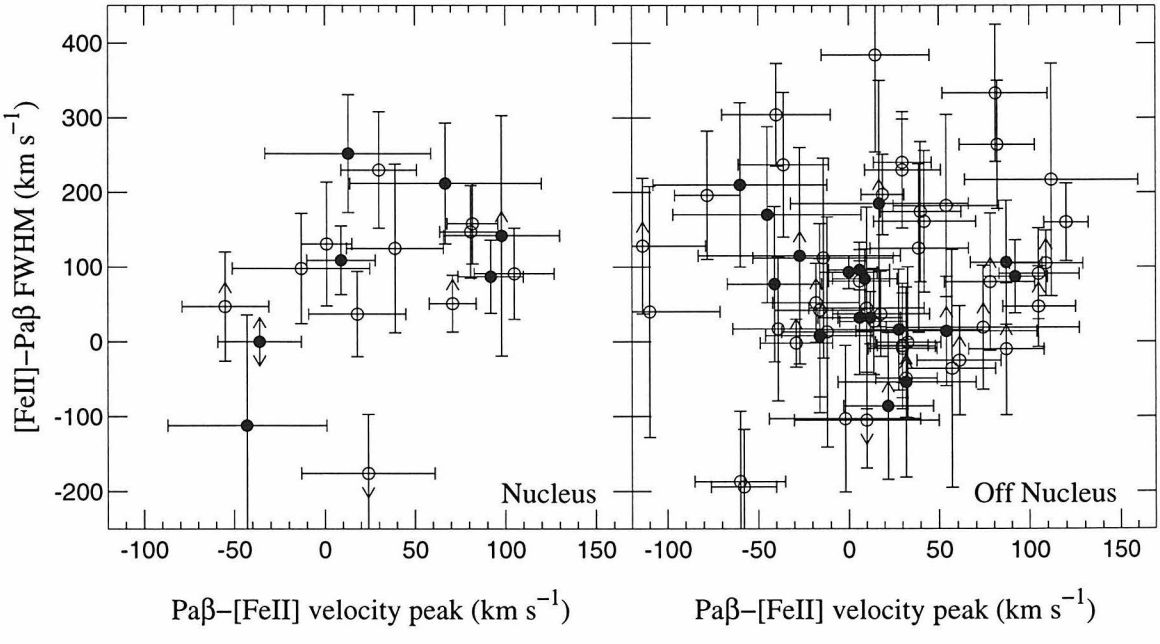

Figure 6.2: Difference in FWHM vs. difference in peak velocity for [FeII] and narrow Paβ on the nucleus. The left plot shows the nuclear data, and the right plot shows the data for all resolved off-nuclear positions. In both plots, open circles represent Seyfert 2 galaxies, and closed circles represent Seyfert 1.x galaxies.

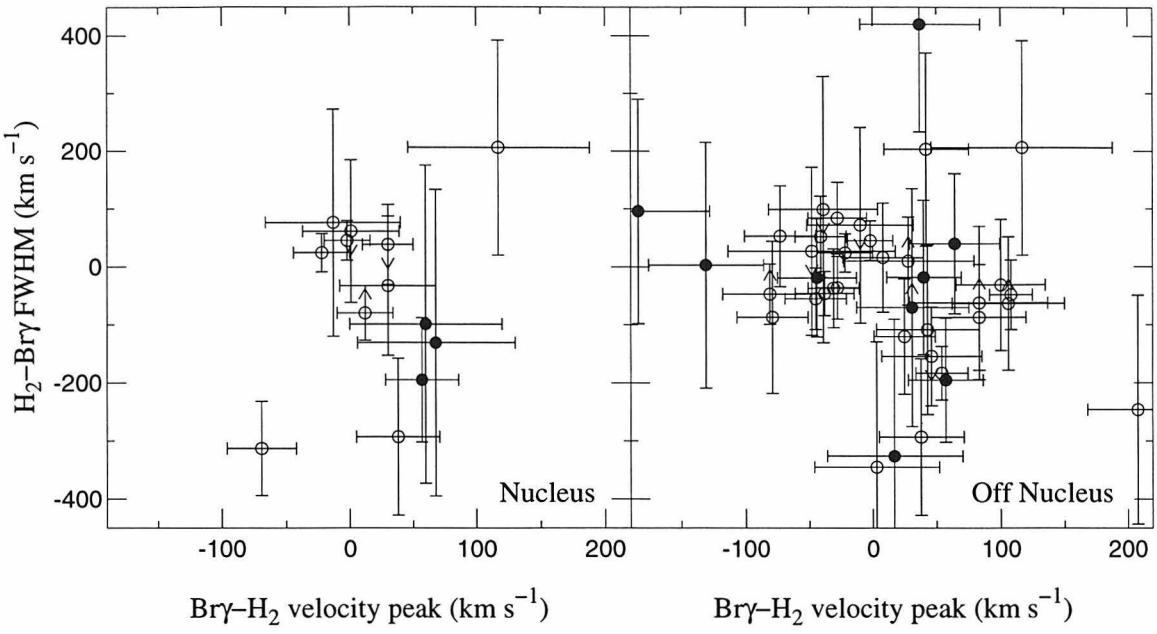

Figure 6.3: Difference in FWHM vs. difference in peak velocity for H_2 and narrow Brγ on the nucleus. Closed circles represent Seyfert 1.x galaxies and open circles represent Seyfert 2 galaxies.

difference between the widths or centroids of the H_2 and Brγ lines to the resolution of the data. Rather, for most of the objects, the two lines have the same width within 100 km s^{-1}, both on and off of the nucleus. Both Brγ and H_2 tend to have the same velocity centroid within 50 km s^{-1} on the nucleus, and within 100 km s^{-1} off of the nucleus.

6.2.2 Narrow Line Ratios

Flux ratios between infrared lines may be used as a diagnostic that can differentiate between different sorts of objects (e.g., Moorwood & Oliva 1988). The two most robust line ratios obtainable from these data are [FeII]/Paβ and H_2/Brγ. In each case, the two lines in question are observed simultaneously, so the fluxes originate from the same projected area on the sky, and the absolute positioning of the slit and possible variations in atmospheric seeing are not an issue. Additionally, the ratios of the line fluxes may be determined independently of the flux calibration.

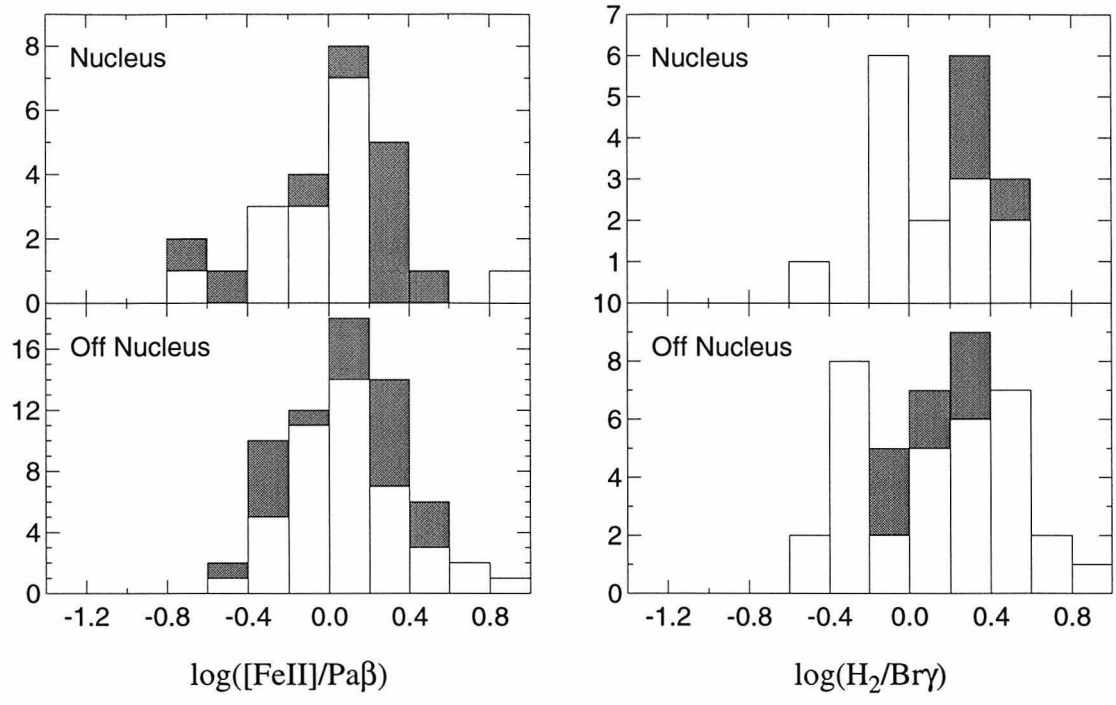

Figure 6.4: Histograms of the nuclear and off-nuclear [FeII]/Paβ and H_2/Brγ line flux ratios. Open bars represent values for Seyfert 2 galaxies and shaded bars represent values for Seyfert 1.x galaxies.

Figure 6.4 shows histograms of nuclear and off-nuclear [FeII]/Paβ and H_2/Brγ line flux ratios. (These nuclear flux ratios are tabulated in Chapter 5. For the nuclear ratios, the flux was integrated in a rectangular beam which is the width of the slit ($\sim$ 0.6″) by the FWHM of the psf along the slit (as tabulated in Table 5.1 in Chapter 5).) Off-nuclear flux ratios are from similarly sized beams. Each off-nuclear beam in each object was counted as a separate measurement, meaning that galaxies with spatially extended infrared line emission contribute multiple measurements. The histogram counts the total number of measurements within each flux ratio bin.

The nuclear and off-nuclear flux ratios are distributed within the same range, and share similar distributions. There are some small differences in the distributions. For instance, [FeII]/Paβ in Seyfert 2 galaxies appears to tend towards higher values off of the nucleus than on the nucleus. The variance weighted average of the [FeII]/Paβ ratio in Seyfert 2 galaxies off of the nucleus is 1.38$\pm$0.01, whereas on the nucleus it

is 1.22±0.02. Note, however, that any means of these distributions are going to be dominated by the small size of the sample. For example, if NGC 2110 with its large [FeII]/Paβ ratio is omitted from the sample, the mean of the [FeII]/Paβ distributions change by about 20%.

6.3 Discussion

6.3.1 The Extinction to the Broad Line Region

As at optical wavelengths, the broad components of the Paβ and Brγ lines in Seyfert 1.x galaxies are spatially unresolved. The broad line region is believed to be $\sim 10^{-2}$ pc (Osterbrock & Martel 1993), which is much smaller than the projected size of the seeing in these observations ($\sim 10^{2}$ pc). Consequently, one may correct observations of broad components of Paβ and Brγ for differences in the point spread function in order to derive a total broad line flux. These fluxes, and the Paβ/Brγ ratios, are tabulated in Table 6.1. The tabulated fluxes and ratios include the uncertainty in the flux calibration at each wavelength.

Table 6.1: Seeing-Corrected Fluxes of Broad Components

Object	Type	Paβ flux	Brγ flux	Paβ/Brγ	A_V
		10^{-15} erg cm^{-2} s^{-1}	10^{-15} erg cm^{-2} s^{-1}	flux ratio	
Mk993	1/1.9	8.6±2.4	2.4±0.8	3.62±1.65	3.3±2.9
Mk359	1.5	15.7±5.5	...	...	
NGC2992	2/1.9	17.1±4.4	14.4±3.7	1.19±0.43	10.4±2.3
NGC3227	1.5	51.3±51.3	10.2±10.3	5.02±7.11	1.2±9.1
NGC3516	1.5	384±96	28.9±7.3	13.3±4.7	...
NGC4051	1	53.4±53.4	24.2±24.2	2.21±3.13	6.4±9.1
NGC4151	1.5	2550±1290	...	...	
NGC5273	1.9	4.6±2.4	...	...	
NGC6814	1	< 3	< 10	...	
NGC7450	1.5	10.6±3.0	...	...	
NGC7469	1	121±61	27.6±13.9	4.40±3.13	2.0±4.6

For Case B recombination with T= 15,000K and $n_e = 10^9$ cm^{-3}, the Paβ/Brγ flux ratio is 6.0 (Storey & Hummer 1995). Assuming these conditions, the visual

extinction A_V to the broad line region is tabulated for the Seyfert 1.x galaxies where both a broad Paβ and Brγ line was detected, using the standard interstellar extinction law (Savage & Mathis 1979). The flux ratios are between the broad components of the lines, as discussed in section 5.3.1 and tabulated in Table 5.2. The broad Paβ/Brγ ratio in NGC 3516 is somewhat larger than 6, implying the possibility of an unphysical negative visual extinction under the assumed conditions. This may be the result of narrow line region Paβ emission with a FHWM of several times 100 km s^{-1} having been blended into the broad line flux used in the ratio in Table 6.1. Alternatively, it may suggest that Case B may not apply, and that optical depth effects are important in the broad line region of at least NGC 3516. The low values of the ratio in the other objects, most notably the Seyfert 2/1.9 galaxy NGC 2992, indicate that there are several magnitudes of extinction to the region wherein the observed broad line radiation arises.

6.3.2 The Extinction to the Narrow Line Region

It is difficult to draw direct conclusions from the ratio between narrow Paβ and Brγ fluxes in any spatial bin. The two lines are not observed simultaneously, so any changes in the atmospheric seeing will cause differing amounts of light from positions adjacent to the slit to pass into the spatial bin in question. Because the narrow infrared line emission is seen to be spatially extended in many objects, but the full two-dimensional distribution of that extended emission is not known, it becomes difficult to correct for the seeing. Even under the assumption that seeing differences are small and the spatial distribution of the two species are the same, the uncertainties in the flux calibrations will produce large uncertainties in the Paβ/Brγ ratio, as was the case with the broad line ratio in section 6.3.1. However, if the flux ratio is normalized to its nuclear value, yielding a value for ΔA_V but not an absolute value of A_V, the uncertainty in the flux calibration is not an issue.

Figure 6.5 shows a histogram of the log of the Paβ/Brγ ratio normalized to the nuclear value. Values greater than 0 in this histogram indicate points where Paβ is

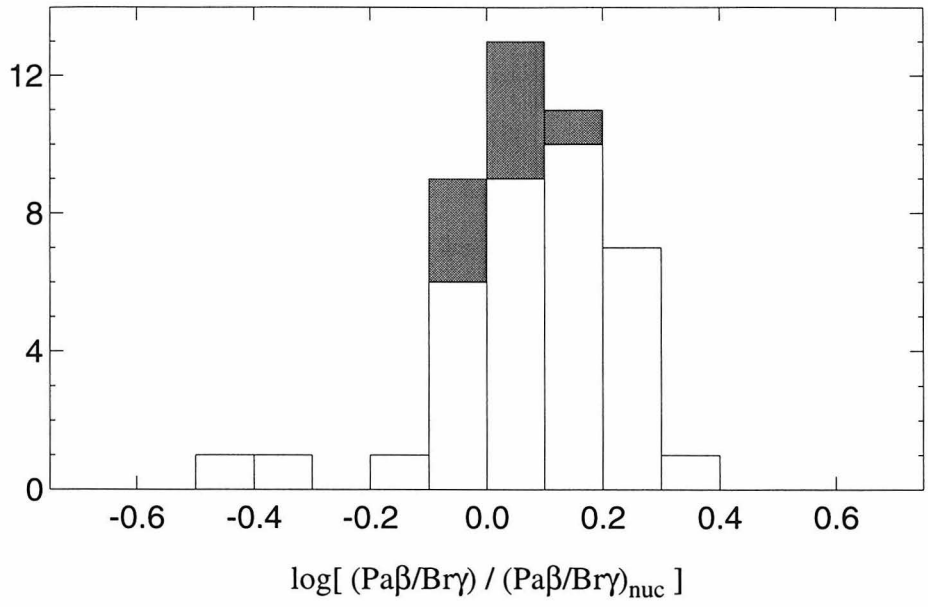

Figure 6.5: Histogram of the log of the Paβ/Brγ ratio normalized to its nuclear value. Higher values of this quantity indicate that Paβ is stronger relative to Brγ off of the nucleus than it is on the nucleus. Shaded bars are for Seyfert 1.x galaxies and open bars are for Seyfert 2 galaxies.

stronger relative to Brγ off of the nucleus than it is on the nucleus. While statistics are limited for Seyfert 1.x galaxies, Figure 6.5 indicates that on average the Paβ/Brγ ratio is higher off of the nucleus than it is on the nucleus. This in turn means that reddening, most likely due to dust extinction, is stronger in the narrow line region coincident with the nucleus than it is in the circumnuclear regions. The average ratio of nuclear to off-nuclear Paβ/Brγ of the data plotted in Figure 6.5 is 1.2. This corresponds to a greater extinction to the nucleus of $\Delta A_V \sim 1.2$ magnitudes.

6.3.3 The [FeII] to Radio Luminosity Correlation

Forbes and Ward (1993) found a correlation between infrared [FeII] luminosity and 6cm radio luminosity for supernova remnants (SNR) and starburst and Seyfert galaxies. In SNR and starburst galaxies, the correlation between radio and [FeII] emission is believed to be primary, as the synchrotron-emitting radio plasma causes fast shocks

which in turn destroy dust grains, releasing iron into the gas phase, and create partially ionized regions from which [FeII] emission can arise. Although Forbes and Ward (1993) plotted the correlation for different types of objects, Simpson *et al.* (1996b) confirm that a correlation exists between the integrated [FeII] luminosity and 6cm radio luminosity in Seyfert galaxies alone. The correlation for Seyfert galaxies, however, is not as tight as the correlation for starburst galaxies and composite objects.

Simpson *et al.* (1996b) also found a correlation between Paβ luminosity and 6cm luminosity in Seyfert galaxies. The [FeII]–6cm correlation was stronger than the Paβ–6cm correlation. Under the assumption that the Paβ-6cm correlation is secondary ("brighter objects are brighter"), and that Paβ is due to photoionization from the nuclear source, Simpson *et al.* (1996b) argue that $\sim 20\%$ of the [FeII] is due to shocks associated with the radio emission, with the bulk of the [FeII] arising from partially ionized regions created by x-ray photoionization.

Because our data are obtained using narrow slits, we cannot accurately measure the luminosity in any line. However, if the [FeII]-6cm correlation is tighter than the Paβ-6cm correlation, then the [FeII]/Paβ ratio ought to be correlated with 6cm luminosity. Figure 6.6 shows a log-log plot of the nuclear [FeII]/Paβ ratio vs. 6cm luminosity for the galaxies in our sample. No correlation is apparent for Seyfert 1.x galaxies; there is a weak correlation visible for Seyfert 2 galaxies. Off the nucleus, neither type of object shows a correlation between [FeII]/Paβ and 6cm luminosity. These results support the idea that if there is any direct relationship between the [FeII]/Paβ ratio and the 6cm luminosity, it is weak. The [FeII]-6cm relationship may be stronger in Seyfert 2 galaxies than in Seyfert 1.x galaxies, although the limited statistics render this conclusion suspect. Under the assumption that the bulk of the Paβ emission does not arise from processes associated directly with the radio plasma, only a small fraction of the [FeII] emission can arise from shocks created by the interaction of the radio plasma with the surrounding medium.

For many objects, we have claimed a correspondence between features which are enhanced in [FeII] relative to Paβ and radio emission, such as the galaxies discussed in Chapter 4 (see Section 4.4.1). In general, these features are differences in profiles,

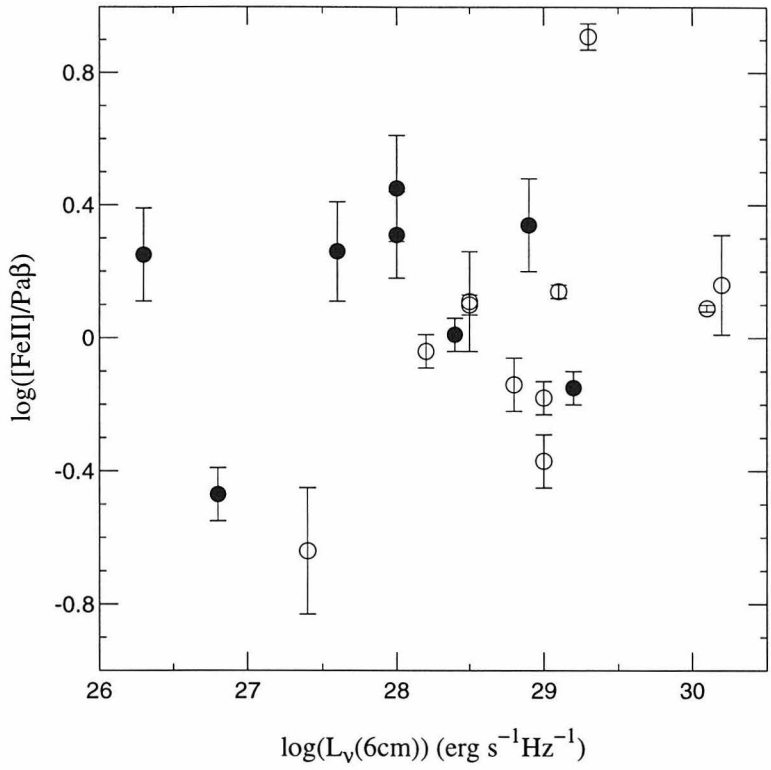

Figure 6.6: Log nuclear [FeII]/Paβ flux ratio vs. log 6cm radio luminosity for Seyfert 1.x (closed circles) and Seyfert 2 (open circles) galaxies. Radio luminosities are calculated assuming H_0=75 km s^{-1} Mpc^{-1}. Radio fluxes are from Ulvestad & Wilson (1989), Ulvestad & Wilson (1984a), Kukula *et al.* (1995), Baum *et al.* (1993), and Edelson (1987).

such as an enhanced wing on the [FeII] line, or a greater width of [FeII] relative to Paβ. If the bulk of the [FeII] arises from x-ray photoionized gas, these enhancements of wings of [FeII] associated with radio emission would be washed out in the total [FeII]/Paβ–6cm correlation plotted in Figure 6.6.

6.3.4 The [FeII]/Paβ–H_2/Brγ Correlation

Figure 6.7 shows log-log plots of the H_2/Brγ flux ratio versus the [FeII]/Paβ flux ratio. On the nucleus, there is a weak positive correlation, with a formal correlation coefficient (neglecting limits) of $r = 0.5$. The correlation is stronger in Seyfert 2

galaxies than it is in Seyfert 1.x galaxies. A line fit to the data has a slope of 0.5. However, the exact nature of this relationship is not well determined since the sample numbers only $\sim$ 20 objects. Extinction should not significantly affect this correlation, because both ratios are between lines close enough in wavelength that the differential extinction between them should be unimportant.

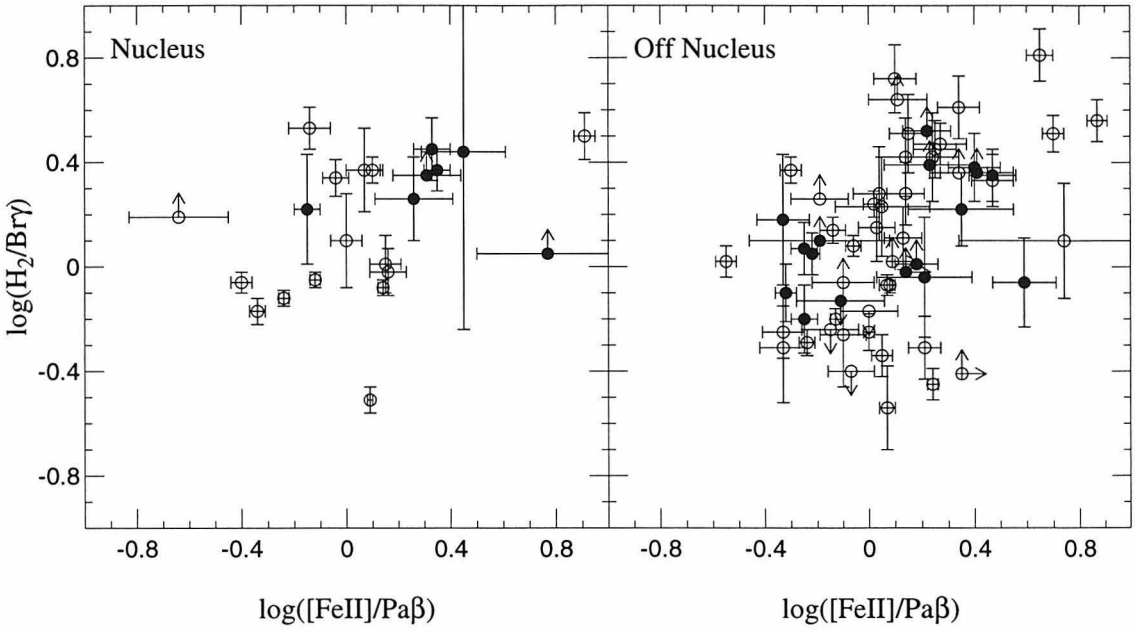

Figure 6.7: Log nuclear [FeII]/Paβ vs. log H_2/Brγ for Seyfert 1.x (closed circles) and Seyfert 2 (open circles) galaxies. The left plot shows the nuclear data, and the right plot shows the off-nuclear data.

Off of the nucleus, the correlation between H_2/Brγ and [FeII]/Paβ remains. The correlation is visible for both Seyfert 1.x and Seyfert 2 galaxies. Additionally, the slope of the relationship off of the nucleus is 0.6, somewhat higher than the slope of the relationship on the nucleus. This is consistent with the result seen in two galaxies in Chapter 4: in those positions off of the nucleus where both the [FeII]/Paβ and H_2/Brγ ratio rose with distance from the nucleus, the H_2/Brγ ratio rose faster. Note, however, that in some Seyfert galaxies the circumnuclear spatial distribution of infrared [FeII] and H_2 emission has been observed to be different (e.g., NGC 1068, Blietz *et al.* 1994).

Correlations have been seen in the past between [FeII] and H_2 with single-beam spectroscopy. In a sample including starburst, Seyfert, and composite galaxies, Green-

house *et al.* (1991) found a correlation between [FeII] ($\lambda = 1.644$) and H_2 v=1-0 S(1) luminosity. Similarly, Moorwood & Oliva (1988) saw a weak correlation between $H_2/Br\gamma$ and [FeII] $\lambda = 1.644\mu m/Br\gamma$ line ratios for starburst, Seyfert, and composite galaxies.

Because both lines originate from the same upper state, results for both the $\lambda = 1.644\mu$m and λ=1.2567μm lines of [FeII] may be directly compared. The aforementioned studies that found a correlation between [FeII] and H_2 only included a handful of Seyfert galaxies, the bulk of the samples being comprised of starburst and composite galaxies. This result shows that a larger sample of just Seyfert galaxies continues to show a correlation (albeit a weak one) between nuclear H_2 and [FeII] emission. Additionally, that correlation appears to be present for emission which is spatially distant from the nucleus, as well as for emission spatially unresolved from the nucleus.

6.3.5 The Origin of the [FeII] and H_2 Emission

[FeII] emission in supernova remnants (SNR) is strong, and SNR are thought to be the source of [FeII] emission in starburst galaxies (Moorwood & Oliva 1988). Similarly, H_2 emission may result from slow shocks created driven by mass outflows from young stars which propagate into dense molecular clouds, or it may originate in molecular clouds heated by young stars (Moorwood & Oliva). It is natural to question whether [FeII] emission in Seyfert galaxies results from the same processes and, as such, indicates the presence of circumnuclear star formation activity. Based on similarities in [FeII] and H_2 emission between Seyfert, composite, and starburst galaxies, Greenhouse *et al.* (1991) and Moorwood & Oliva (1988) suggested that these lines result primarily from SNR in all galaxies. Other studies (Kawara *et al.* 1990; Mouri *et al.* 1993; Simpson *et al.* 1996b) conclude that the [FeII] and H_2 emission is associated directly with the AGN activity, based on enhancements of the strength of these lines relative to hydrogen recombination lines in Seyfert galaxies, and on the fact that the lines are broader in Seyfert galaxies than they are in starburst galaxies,

showing widths characteristic of Seyfert narrow-line region (NLR) gas.

It is of interest to understand whether extended [FeII] and H_2 emission is also associated with the AGN or if it is indicative of circumnuclear star formation. The data presented here support the conclusion that the bulk of the spatially extended [FeII] and H_2 emission results from the nuclear activity rather than from starburst activity. The line ratios are more characteristic of Seyfert activity, and there are spatial and kinematic similarities between [FeII] and H_2 emission and optical and radio emission believed to result from the nuclear activity.

Simpson *et al.* (1996b) show histograms for the [FeII]/Paβ ratio in supernova remnants, Seyfert galaxies, composite systems, and starburst galaxies. Most systems with vigorous star formation (composite and starburst) tend to show [FeII]/Paβ ratios <1. Seyfert galaxies in their sample, in contrast, show ratios close to 1, with an average slightly greater than 1. The distribution of [FeII]/Paβ ratios for both nuclear and off-nuclear positions in our data as plotted in Figure 6.4 is consistent with the distribution of the ratio for Seyfert nuclei seen by Simpson *et al.* Because the distribution of nuclear and off-nuclear ratios is similar, it is probable that the nuclear and off-nuclear [FeII] result from similar excitation mechanisms. This argues against starburst activity as a significant contributor to off-nuclear [FeII] emission.

The arguements in favor of processes associated with the Sefyert nucleus being responsible for the excitation of H_2 are somewhat weaker than is the case for [FeII]. The H_2/Brγ ratio in most starburst galaxies varies between 0.1 and 1.0 (Mouri *et al.* 1993; Moorwood & Oliva 1990; Moorwood & Oliva 1988), with most galaxies having ratios $\lesssim 0.6$. Seyfert galaxies frequently show H_2/Brγ ratios > 1 both on and off the nucleus, with average values $\gtrsim 1.0$. The nuclear and off-nuclear distributions in Figure 6.4 are similar, suggesting a common source for the nuclear and off-nuclear H_2 emission. Additionally, the weak correlation between [FeII] and H_2 emission which Seyfert galaxies exhibit suggests that if the Seyfert nucleus itself is responsible for the [FeII] emission, then some process associated with the nuclear activity probably contributes to H_2 excitation in many Seyfert galaxies.

The other argument in favor of an AGN origin for the [FeII] and H_2 emission is

spatial and kinematic similarities between the emission in these lines and emission at other wavelengths associated with the nuclear activity. Again, these arguments are stronger for [FeII] than for H_2. For those objects where there is data along two slits, the [FeII] emission in particular is more extended (stronger at greater radii) along the slit that is aligned with the greatest extent of optical lines tracing ionized gas (e.g., [OIII]) and/or the greatest extent of anisotropic radio emission. In NGC4151, velocity components in the [FeII] line could be identified with components in the Paβ line, which in turn could be identified with components in optical [OIII] and Hα lines (Chapter 3). In other galaxies, enhanced wings in the [FeII] line profile could be associated with features in optical [OIII] or radio emission (Chapter 4; Chapter 5).

In the objects observed, the H_2 emission, although still concentrated on the nucleus, does not show as strong similarities in spatial and kinematic distribution to other emission associated with the Seyfert nucleus. While in some cases enhanced wings on the [FeII] line profile could be argued to result from a nuclear outflow (Chapter 4), in general the H_2 line profiles do not show these features. Rather, the H_2 emission generally seems to be confined to the disk of the galaxy. Additionally, in objects where data are available along two slit position angles, the H_2 emission is generally more extended (stronger at greater radii) than the other lines along the slit perpendicular to the anisotropy of the optical ionized gas. Narrow band images of NGC 1068 (Blietz *et al.* 1994) show that the [FeII] and H_2 emission have different distributions on spatial scales of $\sim 10^2$ pc.

If the [FeII] emission, and possibly the H_2 emission, is associated with the nuclear activity, the question remains as to the processes responsible for the emission. The [FeII] line is thermally excited, with an upper state at $\sim 10^4$ K. As Fe^+ has an ionization potential of 16.2 eV, the [FeII] line will only be strong where there are large partially ionized regions. X-rays which penetrate deeply into neutral clouds can create such regions. Alternatively, fast ($v > 100$ km s^{-1}) shocks can destroy dust grains which contain much of the iron in the local interstellar medium, and can create large partially ionized regions (Shull & Draine 1987), thereby enhancing [FeII] emission. The H_2 line may result from ultraviolet fluorescence, or may be thermally

excited in warm (T$\sim$ 5000 K) molecular gas. In the case of ultraviolet fluorescence, the ratio of the H_2 v=2-1S(1) ($\lambda = 2.247\mu$m) to the H_2 v=1-0S(1) line should be ~ 0.5 (Moorwood & Oliva 1990). Thermally excited H_2 may arise in molecular clouds which are heated by either X-rays or by shocks slow enough (v$<$ 25 km s^{-1}) not to dissociate the molecules (Shull & Draine 1987).

Blietz *et al.* (1994) calculated [FeII] intensities using the radiative lifetime of the upper state from Nussbaumer & Storey (1988), level energies from Johansson (1978), and collision strengths from Pradhan & Zhang (1993) and Nussbaumer & Storey. They perform a least squares fit to these numerical calcuations, and from this derive an expression for the [FeII] ($\lambda = 1.644\mu$m)/Brγ ratio under the assumption of solar abundances. This expression is easily modified for our [FeII]/Paβ ratio given the constant ratio between the intensities of the two [FeII] lines mentioned above and the Case B assumption that Paβ/Br$\gamma\sim$ 6. The resulting expression is

$$\frac{\text{[FeII]}\ (\lambda = 1.2567\mu\text{m})}{\text{Pa}\beta} = \left[\frac{23\ {T_4}^{0.07} e^{-1.54/T_4}}{1 + 4.2({T_4}^{0.69}/n_4)}\right]\ \delta\ \frac{n_{\text{Fe+}}/n_{\text{Fe}}}{n_{\text{H+}}/n_{\text{H}}} \qquad (6.1)$$

where T_4 is the electron temperature in units of 10^4K, n_4 is the electron density in units of 10^4cm^{-3}, n_{Fe} and n_{H} are the total gas phase densities of all ionization states of Fe and H respectively, and δ is the fraction of iron in the gas phase (so that $1-\delta$ represents the fraction of iron depleted onto dust grains). For typical physical conditions in the NLR of a Seyfert galaxy ($T_4 = 1$, $n_4 = 1$), the term in brackets in Equation 6.1 is approximately 1. The [FeII]/Paβ flux ratio of any homogeneous cloud of gas is the relative ionization fraction of iron to hydrogen times the fraction of iron in the gas phase. In the local ISM, the gas phase abundance of iron is $\delta \sim 0.02$ (Steenberg & Shull 1988).

A hard non-thermal spectrum of x-rays which penetrates deeply into clouds may produce regions where the relative ionization fraction of iron to hydrogen is 10–10^2 (Blietz *et al.* 1994; Simpson *et al.* 1996b). It is plausible then that x-rays could produce the observed [FeII]/Paβ ratios of ~ 1 without increasing the gas phase abundance of iron. Fast (v$\sim$ 100 km s^{-1}) shocks also produce large partially ionized regions having similar physical conditions. Behind these shocks, the relative ionization fractions of

iron and hydrogen can be in the range 2–10 (Mouri *et al.* 1993; Blietz *et al.* 1994). Fast shocks may also dissociate up to tens of percent of the interstellar dust grains (Seab & Shull 1983; Draine & McKee 1993), thereby increasing the gas phase abundance of iron to $\delta \sim 0.1$–0.6. Consequently, the [FeII]/Paβ ratio observed behind fast shocks in regions with $T_4 = 1$ and $n_4 = 1$ may be substantially larger than 1. Based on these arguments, we conclude that nuclear x-ray photoionization is primarily responsible for most of the [FeII] emission in the circumnuclear regions of Seyfert galaxies. This is consistent with the conclusion of Simpson *et al.* (1996b), who argue that the lack of a strong correlation between [FeII]/Paβ and 6cm radio emission indicates that only a small fraction of the [FeII] intensity can result from shocks at the interface between radio plasma and circumnuclear gas.

While the bulk of the [FeII] emission is due to photoionization, there is probably an additional contribution from shocked gas. Equation 6.1 implicitly assumes that the [FeII] and Paβ emission is arising from the same parcel of gas. However, in Chapters 3 through 5, [FeII] showed on the average greater velocity widths than Paβ, and [FeII] was stronger relative to the peak line intensity in secondary components seen in some line profiles. This indicates that although most of the [FeII] may be coming from the same physical regions as the Paβ, there are additional regions with higher [FeII]/Paβ ratios that give rise to these greater widths and additional components. Shocks that destroy dust grains are a natural mechanism which can produce these additional regions. This would further explain the additional wings and components seen for instance in Mk 1066 (Chapter 4) and other galaxies which correspond spatially and kinematically with sites of enhanced radio emission often associated with an outflow.

Figure 6.8 shows a simplified cartoon of a portion of a Seyfert NLR. The small central source emits a power-law spectrum of ionizing radiation. A circumnuclear torus allows that radiation to escape only over a restricted opening angle toward the direction of the ionization cones, where photoionized Paβ and [FeII] emission arises. These gas clouds are accelerated into an outflow, perhaps by radiation. Where this outflow interacts with ambient circumnuclear gas, shocks give rise to additional [FeII]

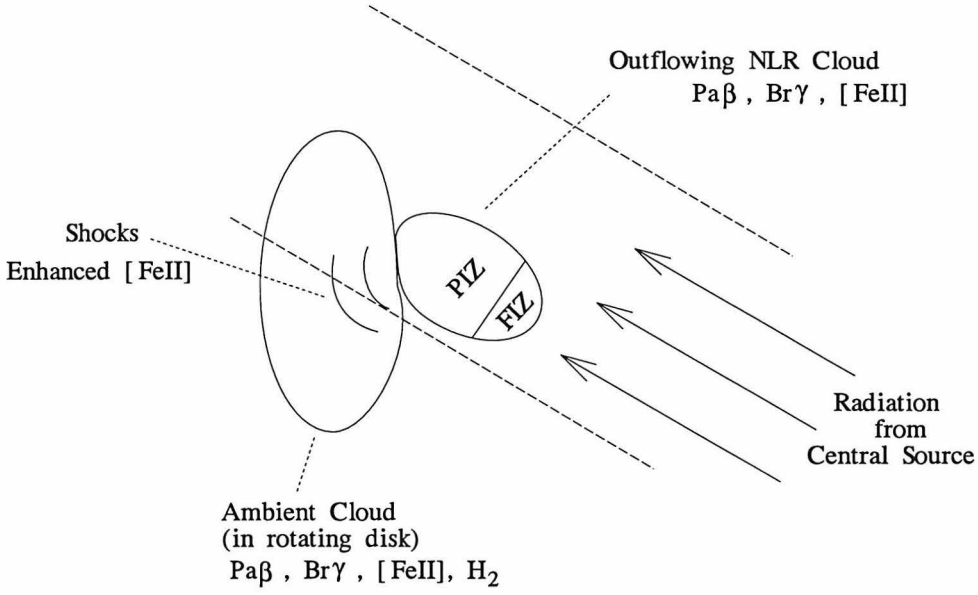

Figure 6.8: A simplified picture of a part of the narrow line region of a Seyfert galaxy. The NLR illuminated by ionizing radiation which escapes from the central source is delimited by dashes. Ambient clouds in the galaxy rotate into the disk and are ionized and heated by incident radiation, giving rise to line emission. Clouds in the NLR accelerated outward form an outflow; additional line emission arises in the outflow. (In the outflowing cloud, FIZ indicates a fully ionized zone and PIZ indicates a partially ionized zone.) Where outflowing clouds run into ambient clouds, shocks at the interface produce additional [FeII] emission.

emission.

It is unlikely that ultraviolet fluorescence contributes appreciably to the H_2 emission. The one object discussed in Chapter 5 that has observations in the wavelength range including H_2 v=2-1S(1) does not show strong enough emission in that line to allow for a significant contribution from this process. This is consistent with the results of Moorwood & Oliva (1990). The H_2 emission may be due more to x-ray heating of molecular clouds than to heating by shocks associated with the radio plasma which gives rise to the observed 6cm emission. The $H_2/Br\gamma$ ratio does not show any correlation with the 6cm luminosity, arguing against a direct relationship between 6cm emission and H_2 emission.

6.3.6 Implications for Unification Schemes

In unification models of AGN (e.g., Antounucci 1993), the difference between Seyfert 1.x and Seyfert 2 galaxies is orientation. In Seyfert 2 galaxies, the broad line region is obscured to our view. The same mechanism that prevents our seeing broad lines only allows the nuclear radiation to escape anisotropically, creating ionization cones observed in some Seyfert 1 and Seyfert 2 galaxies. If orientation effects do contribute significantly to the classification of an object as a Seyfert 1 or a Seyfert 2 galaxy, then the properties of the narrow line gas ought to be similar for the two different sorts of objects.

The [FeII]/Paβ and H_2/Brγ narrow line ratios plotted in Figure 6.4 show no convincing differences between Seyfert 1.x and Seyfert 2 galaxies, although statistics are limited particularly in the case of Sefyert 1.x galaxies. Kinematically, there are only marginal differences between Seyfert 1.x and Seyfert 2 galaxies in the comparison between [FeII] and Paβ. In both objects, the FWHM of the [FeII] line tends to be $\sim$ 100 km s^{-1}greater than that of the Paβ line (Figure 6.2). The scatter in this difference is larger for Seyfert 1.x galaxies than for Seyfert 2 galaxies. However, the uncertainties on the values for Seyfert 1.x galaxies are larger, and this difference may not be significant. Additionally, the marginal trend toward a blueshift of the [FeII] line relative to the Paβ line seen in Seyfert 2 galaxies is not apparent in Seyfert 1.x galaxies. This trend is marginal even in case of Seyfert 2 galaxies, and the difference is probably not significant.

No new broad lines were found in any galaxies not known previously to have broad lines in optical hydrogen recombination emission. According to unification schemes, the broad lines should be present, but subject to such high extinction in Seyfert 2 galaxies that the lines are invisible optically. That the lines were also not observed in the infrared indicates that, if there are broad lines present, the extinction must be high enough also to heavily suppress the infrared lines. However, because only weak broad lines were detected in those high-extinction galaxies such as NGC 2992 which also have only weak optical broad lines, the fact that the Paβ and Brγ lines are

intrinsically weaker than Hα and Hβ probably negates any advantage gained by the ability to look deeper into heavily extincted regions in infrared emission. In summary, the data presented in this thesis do not present startling evidence either in support or denial of Seyfert unification schemes. Similarities in the narrow-line properties of Seyfert 1.x and Seyfert 2 galaxies are consistent with the idea that they are similar types of objects. However, no new broad line regions were found in Seyfert 2 galaxies.

6.4 Summary

Spatially resolved observations of the near-infrared lines of [FeII], H_2, and H^+ in Seyfert 1.x and Seyfert 2 nuclei lead to the following conclusions:

1. Nuclear and off-nuclear [FeII] emission results from processes associated with the nuclear activity; the H_2 emission may be due to a combination of processes both associated and unassociated with the Seyfert nucleus. The [FeII]/Paβ and H_2/Brγ ratios both on and off of the nucleus are characteristic of Seyfert galaxies, and in both cases are higher than typical values for starburst galaxies.

2. [FeII] emission results primarily from x-ray photoionization. Additional contribution from shocks can explain the greater FWHM of the [FeII] line as compared to the Paβ line in many objects. Enhanced components seen in some [FeII] line profiles may be due to shocks associated with spatially coincident radio peaks.

3. The [FeII]/Paβ and H_2/Brγ line ratios appear to be correlated in Seyfert galaxies.

4. The coronal line [SIX] is visible in about 1/3 of the objects observed, and generally is less spatially extended than the other lines.

5. There is no strong difference in the infrared line ratios observed in Seyfert 1.x and Seyfert 2 galaxies. There may be marginal differences in the kinematical comparison of [FeII] and Paβ in the different types of objects.

References

Antonucci, R.J., 1993, ARAA, 31, 473

Antonucci, R.R.J., and Cohen, R.D., 1983, ApJ, 271, 564

Awaki, H., Koyama, K., Kunieda, A., and Tawara, Y., 1990, Nature, 346, 544

Balick, B., and Heckman, T., 1985, AJ, 90, 197

Baum, S.A., O'Dea, C.P., Dallacassa, D., de Bruyn, A.G., and Pedlar, A., 1993, ApJ, 419, 553

Bergeron, A., and Durret, F., 1987, A&A, 184, 93

Blietz, M., Cameron, M., Drapatz, S., Genzel, R., Krabbe, A., van der Werf, P., Sterberg, A., and Ward, M., 1994, ApJ, 421, 92

Bower, G., Wilson, A., Morse, J.A., Gelderman, R., Whittle, M., and Mulchaey, J., 1995, ApJ, 454, 106

Bower, G.A., Wilson, A.S., Mulchaey, J.S., Miley, G.K., Heckman, T.M., and Krolik, J.H., 1994, AJ, 107, 1686

Brodie, J., Willick, J.A., Bowyer, S., and Henry, J.P., 1987, AJ, 93, 1054

Capetti, A., Macchetto, F., Axon, D.J., Sparks, W.B., and Boksenberg, A., 1995, ApJ, 448, 600

Colina, L., Fricke, K.J., Kollatschny, W., and Perryman, M.A.C., 1987, A&A, 186, 39

Colina, L., Fricke, K.J., Kollatschny, W., and Perryman, M.A.C., 1987, A&A, 178, 51

Corben, M.R., Baldwin, J.A., and Wilson, A.S., 1988, ApJ, 334, 584

Cutri, R.M., Rudy, R.J., Rieke, G.H., Tokunaga, A.T., and Willner, S.P., 1984, AJ, 280, 521

Dahari, O., and De Robertis, M.M., 1988, ApJS, 67, 249

de Vaucoulers, G., de Vaucouleurs, A., Corwin Jr., H.G., Buta, R.J., Paturel, G., and Fouque, P., 1991, "Third Reference Catalogue of Bright Galaxies, Version 3.9," Springer-Verlag

Draine, B.T., and Woods, D.T., 1990, ApJ, 363, 464

Draine, B.T., and McKee, C.F., 1993, ARAA, 31, 373

Edelson, R.A., 1987, ApJ, 313, 653

Evans, I.N., Tsvetanov, Z., Kriss, G.A., Ford, H.C., Caganoff, S., and Koratkar, A.P., 1993, ApJ, 417, 82

Filippenko, A.V., and Sargent, W.L.W., 1985, ApJS, 57, 503

Fisher, K.B., Huchra, J.P., Strauss, M.A., Davis, M., Yahil, A., and Schlegel, D., 1995, ApJS, 100, 69

Forbes, D.A., and Ward, M.J., 1993, ApJ, 416, 150

Genzel, R., Weitzel, L., Tacconi-Garman, L.E., Blietz, M., Cameron, M., Krabbe, A., and Lutz, D., 1995 ApJ, 444, 129

Gezari, D.Y., Schmitz, M., Pitts, P.S., and Mead, J.M., 1993, "Catalog of Infrared Observations," NASA Reference Publication 1294

Goodrich, R.W., Veilleux, S., and Hill, G.J., 1994, ApJ, 422, 521

Graham, J.R., Wright, G.S., and Longmore, A.J., 1990, ApJ, 352, 172

Greenhouse, M.A., Woodward, C.E., Thronson, H.A., Jr., Rudy, R.J., Rossano, G.S., Erwin, P., and Puetter, R.C., 1991, ApJ, 383, 164

Haniff, C.A., Wilson, A.S., and Ward, M.J., 1988, ApJ, 334, 104

Hanson, C.G., Skinner, G.K., Eyles, C.J., and Willmore, A.P., 1990, MNRAS, 242, 262

Helou, G., Salpeter, E.E., and Krumm, N., 1979, ApJ, 228, L1

Huchra, J.P., Geller, M.J., and Corwin Jr., H.G., 1995, ApJS, 99, 391

Hummel, E., and Saikia, D.J., 1991, A&A, 249, 43

Johansson, S., 1978, Physica Scripta, 18, 217

Kawara, K., Nishida, M., and Gregory, B., 1990, ApJ, 352, 433

Kawara, K., Nishida, M., and Taniguchi, Y., 1988, ApJ, 328, L41

Keel, W.C., 1996, AJ, 111, 696

Knop, R.A., 1997, PhD thesis, in preparation

Knop, R.A., 1997, PhD thesis, Chapter 2

Knop, R.A., Armus, L., Larkin, J.E., Matthews, K., Shupe, D.L., and Soifer, B.T., 1996, AJ, 112, 81 (Chapter 3)

Knop, R.A., Armus, L., Matthews, K., and Soifer, B.T., 1997, in preparation (Chapter 4)

Knop, R.A., Arums, L., Matthews, K., Murphy Jr., T.W., and Soifer, B.T., 1997, in preparation (Chapter 5)

Knop, R.A., Armus, L., Matthews, K., Murphy, T.W., Jr., and Soifer, B.T., 1997, in preparation (Chapter 6)

Korista, K.T., and Ferland, G.J., 1989, ApJ, 343, 678

Kriss, G.A., Canizares, C.R., and Ricker, G.R., 1980, ApJ, 242, 492

Kuhn, J.R., Penn, M.J., and Mann, I., 1996, ApJ, 456, L67

Kukula, M.J., Ghosh, T., Pedlar, A., Schilizzi, R.T., Miley, G.K., de Bruyn, A.G., and Saikia, D.J., 1993, MNRAS, 264, 893

Kukula, M.J., Pedlar, A., Baum, S.A., and O'Dea, C.P., 1995, MNRAS, 276, 1262

Larkin, J.E., 1995, PhD Thesis, Caltech

Larkin, J.E., Knop, R.A., Lin, S., Matthews, K., and Soifer, B.T., 1996, PASP, 108, 211

Livingston, W., and Wallace, L., 1991, An Atlas of the solar spectrum in the infrared from 1850 to 9000 cm^{-1}, National Solar Observatory Technical Report 91-001

Maiolino, R., Rieke, G.H., and Rieke, M.J., 1996, AJ, 111, 537

Matt, G., Piro, L., Antonelli, L.A., Fink, H.H., Meurs, E.J.A., and Perola, G.C., 1994, A&A, 292, L13

Mazzarella, J.M., Voit, G.M., Soifer, B.T., Matthews, K., Graham, J.R., Armus, L., and Shupe, D., 1994, AJ, 107, 1274

McLeod, K.K., and Rieke, G.H., 1995, ApJ, 441, 96

Meixner, M., Puchalsky, R., Blitz, L., Wright, M., and Heckman, T., 1990 ApJ 354, 158

Miller, J.S., and Goodrich, R.W., 1990, ApJ, 355, 456

Moorwood, A.F.M., and Oliva, E., 1988, A&A, 203, 278

Moorwood, A.F.M., and Oliva, E., 1990, A&A, 239, 78

Moorwood, A.F.M., and Oliva, E., 1994, Infrared Phys. Technol, 35,349

Morse, J.A., Wilson, A.S., Elvis, M., and Weaver, K.A., 1996, ApJ, 439, 121

Mouri, H., Kawara, K., and Taniguchi, Y., 1993, ApJ, 406, 52

Mouri, H., Nishida, M., Taniguchi, Y., and Kawara, K., 1990, ApJ, 360,55

Mulchaey, J.S., Wilson, A.S., Bower, G.A., Heckman, T.M., Krolik, J.H., and Miley, G.K., 1994, ApJ, 433, 625

Mulchaey, J.S., Wilson, A.S., and Tsvetanov, Z., 1996, ApJS, 102, 309

Mundell, C.G., Holloway, A.J., Pedlar, A., Meaburn, J., Kukula, M.J., and Axon, D.J., 1995, MNRAS, 275, 67

Neugebauer, G., 1995, private communication

Neugebauer, G., 1996, private communication

Nussbaumer, H., and Storey, P.J., 1988, A&A, 193, 327

Oliva, E., Moorwood, A.F.M., and Danziger, I.J., 1989, A&A, 214, 307

Oliva, E., and Origlia, L., 1992, A&A, 254, 466

Oliva, E., Salvati, M., Moorwood, A.F.M., and Marconi, A., 1994, A&A, 288, 457

Osterbrock, D.E., 1988, "Astrophysics of Gaseous Nebulae and Active Galactic Nuclei," University Science Books

Osterbrock, D.E., 1993, ApJ, 404, 551

Osterbrock, D.E., and Koski, A.T., 1975, MNRAS, 176, 61P

Osterbrock, D.E., and Martel, A., 1993, ApJ, 414, 552

Osterbrock, D.E., and Pogge, R.W., 1985, ApJ, 297,166

Pedlar, A., Dyson, J.E., and Unger, S.W., 1985, MNRAS, 214, 463

Pedlar, A., Howley, P., Axon, D.J., and Unger, S.W., 1992, MNRAS, 259, 369

Penston, M.V., Fosbury, R.A.E., Boskenberg, A., Ward, M.J., and Wilson, A.S., MNRAS, 208, 347

Persson, E., private communication

Petitjean, P., and Durret, F., 1993, A&A, 277, 365

Pierce, M.J., and Tully, R.B., 1988, ApJ, 330, 579

Pogge, R.W., 1989, ApJ, 345, 730

Pogge, R.W., and de Robertis, M.M., 1993, ApJ, 404, 563

Pradhan, A.K., and Zhang, H.L., 1993, ApJ, 409, L77

Prestwich, A.H., Wright, G.S., and Joseph, R.D., 1992, ApJs, 80, 205

Reichert, G.A., Mushotzky, R.F., Petre, R., and Holt, S.S., 1985, ApJ, 296, 69

Rix, H.W., Carleton, N.P., Rieke, G., and Rieke, M., 1990, ApJ, 363, 480

Robbins, R.R., 1968, ApJ, 151, 497

Rudy, R.J., Cohen, R.D., Rossano, G.S., Erwin, P., Puetter, R.C., Greenhouse, M.A., and Woodward, C.E., 1993, ApJ, 414, 527

Ruiz, M., Rieke, G.H., and Schmidt, G.D., 1994, ApJ, 423, 608

Savage, B.D., and Mathis, J.S., 1979, ARAA, 17, 73

Schulz, H., 1990, AJ, 99, 1442

Seab and Shull, 1983, ApJ 275, 652

Sekiguchi, K., and Menzies, J.W., 1990, MNRAS, 245, 66

Shields, J.C., and Filippenko, A.V., 1988, ApJ, 332, L55

Shields, J.C., and Filippenko, A.V., 1996, A&A, 311, 393

Shuder, J.M., 1980, ApJ, 240, 32

Shull, J.M., and Draine, B.T., in Hollenbach, D.J., and Thronson, H.A., Jr., 1987, "Interstellar Processes", D. Reidel Publishing Company, 283

Simpson, C., Forbes, D.A., Baker, A.C., and Ward, M.J., 1996, HST preprint, to appear in MNRAS

Simpson, C., Mulchaey, J.S., Wilson, A.S., Ward, M.J., and Alonso-Herrero, A., 1996, ApJ, 457, L19

Smits, D.P., 1991, MNRAS, 248, 193

Steenberg, M.E., & Shull, J.M., 1988, ApJ, 330, 942

Sternberg, A., and Dalgarno, A., 1989, ApJ, 338, 197

Storey, P.J., and Hummer, D.G., 1995, MNRAS, 272, 41

Taylor, D., Dyson, J.E., and Axon D.J, 1992, MNRAS, 255, 351

Telesco, C.M., and Harper, D.A., 1980, ApJ, 235, 392

Thompson, R.I., 1995, ApJ, 445, 700

Thompson, R.I., 1996, ApJ, 459, L61r

Tran, H.D., Osterbrock, D.E., and Martel, A., 1992, AJ, 104, 2072

Ulrich, M., 1973, ApJ, 181, 51

Ulvestad, J.S., and Wilson, A.S., 1984, ApJ, 285, 439

Ulvestad, J.S., and Wilson, A.S., 1984, ApJ, 278, 544

Ulvestad, J.S., and Wilson, A.S., 1989, ApJ, 343, 659

Ulvestad, J.S., Wilson, A.S., and Sramek, R.A., 1981, 247, 419

Veilleux, S., 1991, ApJ, 369, 331

Veilleux, S., Tully, R.B., and Bland-Hawthorn, J., 1993, AJ, 105, 1318

Veron, P., Lindblad, P.O., Zuiderwijk, E.J., Veron, M.P., and Adam, G., 1980, A&A, 1980, 87

Weaver, K.A., Mushotzky, R.F., Serlemitsos, P.J., Wilson, A.S., Elivs, M., and Briel, U., 1995, ApJ, 442, 597

Wegner, G., Haynes, M.P., and Giovanelli, R., 1993, AJ, 105, 1251

Wehrle, A.E., and Morris, M., 1988, AJ, 95, 1689

West, R.C., Astle, M.J., and Beyer, W.H., eds., 1985, "CRC Handbook of Chemistry and Physics," 66th ed., CRC Press, Inc., Boca Raton, FL

Whittle, M., Haniff, C.A., Ward, M.J., Meurs, E.J.A., Pedlar, A., Unger, S.W., Axon, D.J., and Harrison, B.A., 1986, MNRAS, 222, 189

Whittle, M., Pedlar, A., Meurs, E.J.A., Unger, S.W., Axon, D.J., and Ward, M.J., 1988, ApJ 326, 125

Wilson, A.S., and Baldwin, J.A., 1985, ApJ, 289, 124

Wilson, A.S., Baldwin, J.A., and Ulvestad, J.S., 1985, ApJ, 291, 627

Wilson, A.S., Baldwin, J.A., Sun, S.D., and Wright, A.E., 1986 ApJ 310, 121

Wilson, A.S., and Tsvetanov, Z.I., 1994, AJ, 107, 1227